TEMPERATURE-DEPENDENT DIELECTRIC PROPERTIES OF TISSUE PHANTOMS AND TISSUE SAMPLES AT MICROWAVE FREQUENCIES

TEMPERATURE-DEPENDENT DIELECTRIC PROPERTIES OF TISSUE PHANTOMS AND TISSUE SAMPLES AT MICROWAVE FREQUENCIES

By

Yona Baskharoun, B.ENG.

A Thesis Submitted to the School of Graduate Studies

in Partial Fulfillment of the Requirements

for the Degree of Masters of Applied Science

McMaster University

MASTER OF APPLIED SCIENCE (2012) McMaster University

(Electrical and Computer Engineering) Hamilton, Ontario

TITLE: **Temperature-Dependent Dielectric Properties of Tissue Phantoms and Tissue Samples at Microwave Frequencies**

AUTHOR: Yona Baskharoun
B.Eng. (Electrical and Biomedical Engineering,
McMaster University, Hamilton, Canada)

SUPERVISORS: Natalia K. Nikolova, Professor,
Canada Research Chair in High-frequency Electromagnetics
Department of Electrical and Computer Engineering, McMaster University
Dipl.Eng. (Technical University of Varna)
Ph.D. (University of Electro-Communication)
P.Eng. (Province of Ontario)
Fellow Member, IEEE

NUMBER OF PAGES: 284

ABSTRACT

Accurate knowledge of the frequency- and temperature-dependent dielectric properties of biological tissues is crucial in the development of ultra-wideband diagnostic and therapeutic technologies such as microwave breast cancer detection and hyperthermia treatments. This work examines the temperature dependence of the dielectric properties of the five tissue phantom-types developed by our group as well as porcine fat, muscle and liver tissues for the frequency range from 3 GHz to 10 GHz and for the temperature range from 5 °C to 45 °C. A systematic and simple measurement procedure is developed to measure the continuous temperature dependence of the dielectric properties of the various phantom and tissue types. The temperature trends of the dielectric properties of the different phantoms and tissues are investigated.

Linear temperature coefficients at discrete frequencies are impractical and insufficient in ultra-wideband applications when realistic, non-linear numerical models of the dielectric properties are required. Therefore, a compact one-pole Cole-Cole model is used to model the frequency dependence of the dielectric properties of the measured samples at every temperature point. A second- or third-order polynomial is used to model the temperature dependence of the Cole-Cole parameters. The final model is a one-pole Cole-Cole model whose parameters are polynomial functions of temperature. This model enables the estimation of the relative permittivity and the conductivity of the measured phantom and tissue types at any temperature and frequency.

ACKNOWLEDGEMENTS

It is my pleasure to thank everyone who supported and assisted me in the past two years of my M.A.Sc. program. First and foremost, I will like to express my sincere appreciation and my profound gratitude to my M.A.Sc. supervisor, Dr. Natalia K. Nikolova, who has supported me and guided me throughout my MA.Sc. journey and my undergraduate capstone project. Throughout the past three years, Dr. Nikolova supported me academically, professionally and personally. She constantly offered great advice, constant encouragement and lots of great times. I would also like to thank her for giving me the opportunity to be a part of her team and the chance to work in an upcoming area of research. I can truly say that I would not be where I am at today without her guidance.

I am also grateful to Prof. Mohamed Bakr for his great teaching of the numerical techniques in Electromagnetics graduate course. Prof. Bakr was proficient in making some of the intimidating material related to numerical techniques more practical and understandable. This helped me with getting the grasp of numerical techniques as well as become efficient with MATLAB, which was crucial in completing this work. It is a pleasure to have him as a member on my committee as well.

I would also show my appreciation to thank Dr. Michael D. Noseworthy for being an outstanding mentor on medical imaging in my undergraduate and graduate courses. His profound knowledge of the physiological and medical aspects of imaging was invaluable and of great assistance in merging the biomedical and the engineering aspects

of my research. It is also a pleasure to have him as a member on my committee.

I am also grateful to Cheryl Gies for her continued efforts in always keeping me informed of all pertinent departmental matters.

I would also like to thank all my senior colleagues, Dr. Reza K. Amineh and Aastha Trehan from the Computational Electromagnetics Laboratory for helping me throughout the past two years. I am also grateful to my colleagues Sheng Tu, Yifan Zhang, Kaveh Moussakhani, Mohamed Negm and Osman Ahmed for all their helpful suggestions and moral support.

I am also grateful to all of my friends for their constant moral support and all the great times throughout my undergraduate and graduate years.

Last but not least, I would like to thank my family, especially my mother for her unwavering encouragement, support, motivation and always believing in me. Finally, I thank God for such a wonderful life and opportunities.

TABLE OF CONTENTS

LIST OF FIGURES

LIST OF TABLES

LIST OF SYMBOLS AND ACRONYMS

SYMBOLS

ω	Frequency in radians
ε_r or ε'	Relative permittivity
ε''	Dielectric Loss
ε^*	Complex permittivity
ε_o	Permittivity of free space
ε_∞	Infinite-frequency permittivity
ε_s	Static-frequency permittivity
$\Delta\varepsilon$	ε_s - ε_∞
μ	Permeability
σ	Conductivity
σ_s or σ_i	Ionic conductivity
δ	Loss angle
α	Distribution parameter
τ	Relaxation time
f_c	Relaxation frequency

ACRONYMS

BIRADS	Breast Imaging Reporting and Database System
DIW	De-ionized Water
DCIS	Ductal Carcinoma In Situ
EM	Electromagnetic
FDA	Food and Drug Administration
FDTD	Finite Difference Time Domain
FG	Fibro-glandular
HWCT	High Water Content Tissue
IDC	Invasive Ductal Carcinoma
IEEE	Institute of Electrical and Electronics Engineers
IWCT	Intermediate Water Content Tissue
LCIS	Lobular Carcinoma In Situ
LWCT	Low Water Content Tissue
MRI	Magnetic Resonance Imaging
NSF	Nephrogenic Systemic Fibrosis
RC	Resistor-Capacitor
RF	Radio Frequency
SAR	Specific Absorption Rate
TM	Tissue Mimicking
TMN	Tumor, Nodes and Metastases
UHF	Ulta-high frequency
UWB	Ultra-wideband

CHAPTER 1

INTRODUCTION

1.1 MOTIVATION

Cancer is increasingly becoming a burden on today's society. Breast cancer continues to be the leading form of cancer affecting women; with 22,700 new cases and 5,100 deaths expected in 2012, making up 26% of new cancer cases with 14% of cancer deaths among women in Canada [1]. Breast cancer ranks second after lung cancer in cancer mortalities among women [2]. In spite of the extensive amount of research and funds being geared towards finding a cure for cancer, current medicine can only hope to contain the cancerous cells rather than cure them. Although breast cancer remains one of the more manageable forms of cancer, early detection of tumors is necessary for current techniques to successfully halt or impede the spreading of cancerous cells and for managing the disease. As a result of increased breast screening and cancer therapies, breast cancer mortality rate is at its lowest since 1950, showing a decrease of almost 40% since its peak in 1986 [2].

Mammography is currently the gold standard in breast cancer screening. However, dense breasts are the main reason why screening mammograms have a high false-negative rate; missing 20% to 40% of breast tumors present at the time of screening. Mammography also has a high false-positive rate of 50% to 70% [3]. In addition, mammographs expose the patient to painful breast compression and possibly harmful ionizing radiation. Ultrasound, MRI and other breast cancer detection modalities are available; however, these modalities are either less effective or too expensive and time consuming [4]. Due to the lack of an accurate, comfortable, efficient, inexpensive and readily available imaging modality to detect breast cancer, there is need for a new imaging modality especially for the purpose of mass screening. Microwave imaging for breast cancer screening is a new technique that has the potential of fulfilling these requirements.

A great deal of research efforts have been employed towards developing microwave imaging systems for breast cancer detection [5]-[23]. Microwave imaging of the breast relies on sufficient contrast between the dielectric properties of normal breast tissues, especially fat, the tissue most abundant in the breast, and tumors. The dielectric properties of tissues determine how electromagnetic fields will interact with and propagate within the tissues. Thus extensive studies of the dielectric properties of tissues are a crucial part of developing microwave imaging techniques.

Numerous data have been reported on the dielectric properties of breast tissues [24]-[40]. Accurate knowledge of the dielectric properties of various tissues is not only valuable for imaging purposes, but is also used for many other applications such as

treating cancer using hyperthermia [41]-[44], determining how food products heat in a microwave oven [45], as well as characterizing and limiting human exposure to electromagnetic fields [41]. The dielectric properties of biological tissues, and most materials in general, are dependent on many variables, such as frequency and temperature.

Often, measurements that aim to determine the dielectric properties of human tissue are performed *ex vivo* because of the difficulty of performing *in vivo* measurements. In these cases, measurements are usually carried out at room temperature. Moreover, *in vivo* measurements require direct contact between the measurement probes and the tissue under test. As a result, even during *in vivo* measurements, the measurement temperature is often less than the normal body temperature. The temperature dependence of the dielectric properties of tissues has been investigated in various studies [46]-[59]. However, most of the measurements in these studies have been performed at discrete frequencies and varying temperatures with the final results presented as linear temperature coefficients (percent change in the relative permittivity or conductivity per degree Celsius). Primarily, due to the absence of validations, it is not clear that linear temperature coefficients are sufficient to model the temperature dependence of the dielectric properties of tissues at all temperatures and frequencies. Moreover, most biomedical applications of microwaves involve wide frequency ranges as well as numerical simulations that are designed to mimic the real-life scenario. Consequently, linear temperature coefficients at discrete frequencies are impractical and insufficient in ultra-wideband (UWB) applications when realistic numerical models of the dielectric

properties are required at every frequency and temperature in the range of interest.

1.2 CONTRIBUTIONS

The goals of this work are (i) to systematically measure the temperature dependence of the dielectric properties of five different physical phantom types developed by our group, as well as porcine fat, muscle and liver samples, over a wide frequency range (3 GHz to 10 GHz); (ii) to present a compact numerical model for all the measured phantom and tissue types over the measured frequency and temperature ranges. Namely, a one-pole Cole-Cole model is used to model the frequency dependence of the dielectric properties of the measured samples at every temperature point. Then, a second- or third-order polynomial is used to model the temperature dependence of the Cole-Cole parameters. The final model is a function of both frequency and temperature for every phantom and tissue type.

The availability of the temperature trends of the dielectric properties pertaining to phantoms used in this work allows for their use in testing microwave-induced acoustic imaging systems, in which thermo-acoustic tomography is used for image reconstruction. Temperature information is important for image reconstruction using thermo-acoustic tomography [60],[61]. The model can be used to calculate the dielectric properties of the measured phantom and tissue types at every frequency and temperature for the frequency range from 3 GHz to 10 GHz and for temperatures ranging from 5 °C to 45 °C.

The author's contributions can be summarized as follows:

1) The development of a systematic and simple measurement procedure to measure

the continuous temperature dependence of the dielectric properties of the various phantom and tissue types.

2) The investigation of the temperature trends of the different phantom types and more importantly, the temperature trends of fat, muscle and liver.
3) Providing compact numerical models for the frequency and the temperature dependence of the measured phantom and tissue types in the form of a one-pole Cole-Cole model, whose parameters are second- or third-order polynomial functions of temperature. These numerical models can be used to estimate the relative permittivity and the conductivity of the measured phantom and tissue types at every frequency and temperature for the frequency range from 3 GHz to 10 GHz and the temperatures range from 5 °C to 45 °C.
4) The publication of the work done on developing the breast tissue phantoms in an IEEE conference. A major journal paper that summarizes the work and the results of this thesis is also under preparation.

1.3 OUTLINE OF THESIS

Chapter 2 of this thesis includes some background information on breast caner, breast cancer screening, microwave imaging of the breast and physical breast phantoms. No contributions are made to these fields; however, they form the background that motivates this work.

Chapter 3 includes a review of the electromagnetic properties of tissues and the biological and physical mechanisms that govern these properties; the numerical models

of these mechanisms are also explained. Finally, a review of relevant studies published on the temperature dependence of tissues is presented. The properties of water and saline, two of the main constituents of tissues, and their temperature-dependent dielectric properties are also presented.

In chapter 4, the measurement setup and protocol, as well as hardware and the used materials are explained. The measured results for the LWCT (low-water content tissue), IWCT (intermediate-water content tissue), HWCT-1 (high-water content tissue), HWCT-2 and the alginate-based tumor phantoms are presented along with the measured data for the fat, muscle and liver tissue samples. The observed temperature trends of the different phantom and tissue types are also explained in this chapter.

In chapter 5 the developed numerical models used and their results are presented. In the first part of this chapter the data fitting procedure to the Cole-Cole model at every temperature for every phantom and tissue type is explained and the results are presented. In the second part, the data fitting of the Cole-Cole parameters (obtained in the first part) to a second- or third- order polynomial is shown, along with the resulting temperature parameters for the measured phantom and tissue types. An investigation of the differences between the measured and the modeled relative permittivities and conductivities for every phantom and tissue type is also provided in this chapter.

Chapter 6 concludes this thesis with a summary of the work and its results. Recommendations on possible ways of improving this work and suggestions for future work are discussed. For convenience, a complete bibliography of all the sources used is given at the end of the thesis.

REFERENCES

[1] (May 2012). Breast Cancer Statistics 2012. Canadian Cancer Society. [Online]. http://www.cancer.ca/canada-wide/about%20cancer/cancer%20statistics/stats%20at%20a%20glance/breast%20cancer.aspx.

[2] (May 2012). Cancer Statistics 2012. Canadian Cancer Society, pp. 11, 28. [Online]. http://www.cancer.ca/~/media/CCS/Canada%20wide/Files%20List/English%20files%20heading/PDF%20-%20Policy%20-%20Canadian%20Cancer%20Statistics%20-%20English/Canadian%20Cancer%20Statistics%202012%20-%20English.ashx.

[3] E. C. Fear, X. Li, S. C. Hagness, and M. A. Stuchly, "Confocal microwave imaging for breast cancer detection: Localization of tumors in three dimensions," *IEEE Trans. Biomed. Eng.*, vol. 49, pp. 812-822, August 2002.

[4] S. C. Hagness, A. Taflove, and J. E. Bridges, "Two-dimensional FDTD analysis of a pulsed microwave confocal system for breast cancer detection: Fixed-focus and antenna-array sensors," *IEEE Trans. Biomed. Eng.*, vol. 45, pp. 1470-1479, Dec. 1998.

[5] E. C. Fear, S. C. Hagness, P. M. Meaney, M. Okoniewski, and M. A. Stuchly, "Enhancing breast tumor detection with near field imaging," *IEEE Microw. Mag.*, vol.3, pp. 8-56, March 2002.

[6] N. K. Nikolova, "Microwave imaging for breast cancer," *IEEE Microw. Mag.*, vol. 12, no. 7, pp. 78-94, December 2011.

[7] B.Bocquet, J.C. van deVelde, A. Mamouni, Y. Leroy, G. Giaux, J. Delannoy, and D. DelValee, "Microwave radiometric imaging at 3 GHz for the exploration of breast tumors," *IEEE Trans. Microw. Theory Tech.*, vol. 38, pp. 791-793, June 1990.

[8] S. Mouty, B. Bocquet, R. Ringot, N. Rocourt, and P. Devos, "Microwave radiometric imaging for the characterisation of breast tumors," *Eur. Phys. J.: Appl. Phys.*, vol. 10, pp. 73-78, 2000.

[9] K.L. Carr, "Microwave radiometry: its importance to the detection of cancer," *IEEE Trans. Microw. Theory Tech.*, vol. 37, pp. 1862-1869, December 1989.

[10] K.L. Carr, P.Cevasco, P.Dunlea, and J. Shaeffer, "Radiometric sensing: An adjuvant to mammography to determine breast biopsy*," IEEE MTT-S Int. Microwave Symp.*

Dig., vol. 2, 2000, pp. 929-932.

[11] P. M. Meaney, M. W. Fanning, D. Li, S. P. Poplack, and K. D. Paulsen, "A clinical prototype for active microwave imaging for the breast," *IEEE Trans. Microw. Theory Tech.*, vol. 48, no. 11, pp. 1841-1853, November 2000.

[12] A. E. Bulyshev, S. Y. Semenov, A. E. Souvorov, R. H. Svenson, A. G. Nazarov, Y.E. Sizov and G. P. Tatsis, "Computational modeling of three-dimensional microwave tomography of breast cancer," *IEEE Trans. Biomed. Eng.*, vol. 48, no. 9, pp. 1053-1056, September 2001.

[13] Q. H. Liu, Z. Q. Zhang, T. T. Wang, J. A. Bryan, G. A. Ybarra, L. W. Nolte, and W. T. Joines, "Active microwave imaging I — 2-D forward and inverse scattering methods," *IEEE Trans. Microw. Theory Tech.*, vol. 50, no. 1, pp. 123-133, January 2002.

[14] Z. Q. Zhang, Q. H. Liu, C. Xiao, E. Ward, G. Ybarra, and W. T. Joines, "Microwave breast imaging: 3-D forward scattering simulation," *IEEE Trans. Biomed. Eng.*, vol. 50, no. 10, pp. 1180-1189, 2003.

[15] T. Rubæk, P. M. Meaney, P. Meincke, and K. D. Paulsen, "Nonlinear microwave imaging for breast-cancer screening using gauss–newton's method and the CGLS inversion algorithm," *IEEE Trans. Antennas Propagat.*, vol. 55, no. 8, pp. 2320-2331, 2007.

[16] X. Li, E. J. Bond, B. D. Van Veen and S. C. Hagness, "An overview of ultra-wideband microwave imaging via space-time beamforming for early- stage breast-cancer detection," *IEEE Antennas Propagat. Mag.*, vol. 47, pp. 19-34, February 2005.

[17] X. Li, S. K. Davis, S. C. Hagness, D. W. Weide and B. D. Van Veen, "Microwave imaging via space–time beamforming: experimental investigation of tumor detection in multilayer breast phantoms," *IEEE Trans. Microw. Theory Tech.*, vol. 52, pp. 1856-1865, August 2004.

[18] X. Li and S. C. Hagness, "A confocal microwave imaging algorithm for breast cancer detection," *IEEE Microwave Wireless Compon. Lett.*, vol. 11, no. 3, pp. 130-132, 2001.

[19] E. J. Bond, S. C. Hagness, and B. D. Van Veen, "Microwave imaging via space-time beamforming for early detection of breast cancer," *IEEE Trans. Antennas Propagat.*, vol. 51, no. 8, pp. 1690-1705, 2003.

[20] J. M. Sill and E. C. Fear, "Tissue sensing adaptive radar for breast cancer detection—experimental investigation of simple tumor models," *IEEE Trans. Microw. Theory Tech.*, vol. 53, pp. 3312-3319, November 2005.

[21] M. Elsdon, D. Smith, M. Leach, and S. J. Foti, "Experimental investigation of breast tumor imaging using indirect microwave holography," *Microwave Opt. Technol. Lett.*, vol. 48, no. 3, pp. 480-482, March 2006.

[22] M. Ravan, R. K. Amineh, and N. K. Nikolova, "Two-dimensional near-field microwave holography," *Inverse Prob.*, vol. 26, no. 5, May 2010.

[23] R. K. Amineh, M. Ravan, N. K. Nikolova, and A. Khalatpour, "Three-dimensional near-field microwave holography using reflected and transmitted signals," *IEEE Trans. Antennas Propagat.*, vol. 59, no. 12, pp. 4777-4789, December 2011.

[24] C. Gabriel, S. Gabriel and E. Corthout, "The dielectric properties of biological tissues: I. Literature survey," *Phys. Med. Biol.*, vol. 41, pp. 2231-2249, 1996.

[25] S. Gabriel, R. W. Lau, and C. Gabriel, "The dielectric properties of biological tissues: III. Parametric models for the dielectric spectrum of tissues," *Phys. Med. Biol*., vol. 41, pp. 2271-2293, April 1996.

[26] S. Gabriel, R. W. Lau and C. Gabriel, "The dielectric properties of biological tissues: II. Measurements in the frequency range 10 Hz to 20 GHz," *Phys. Med. Biol.*, vol. 41, pp. 2251-2269, 1996.

[27] T. S. England N. A. and Sharples, "Dielectric properties of the human body in the microwave region of the spectrum," *Nature*, vol. 163, pp. 487-488, 1949.

[28] S. S. Chaudhary, R. K. Mishra, A. Swarup and J. M. Thomas, "Dielectric properties of normal and malignant human breast tissues at radiowave and microwave frequencies," *Indian J. Biochem. Biophys.*, vol.21, pp. 76-79, 1984.

[29] A. J. Surowiec, S. S. Stuchly, J. R. Barr and A. Swarup, "Dielectric properties of breast carcinoma and the surrounding tissues," *IEEE Trans. Biomed. Eng.*, vol. 35, pp. 257-263, 1988.

[30] A. M. Campbell and D. V. Land, "Dielectric properties of female human breast tissue measured *in vitro* at 3.2 GHz," *Phys. Med. Biol.*, vol. 37, pp. 193-210, 1992.

[31] T. Morimoto *et al.*, "A study of the electrical bioimpedance of tumors," *J. Invest. Surg.*, vol. 6, pp. 25-32, 1993.

[32] W. T. Joines, Y. Zhang, C. Li and R. L. Jirtle, "The measured electrical properties

of normal and malignant human tissues from 50 to 900 MHz," *Med. Phys.*, vol. 21, pp. 547-550, 1994.

[33] J. Jossinet, "The impedivity of freshly excised human breast tissue," *Phys. Meas.*, vol. 19, pp. 61-75, 1998.

[34] J. da Silva, J. de Sa and J. Jossinet, "Classification of breast tissue by electrical impedance spectroscopy," *Med. Biol. Eng. Comput.*, vol. 38, pp. 26-30, 2000.

[35] J. W. Choi *et al.*, "Microwave detection of metastasized breast cancer cells in the lymph node; potential applications for sentinel lymphadenectomy," *Breast Cancer Res. Treat.*, vol. 86, pp. 107-115, 2004.

[36] S. P. Poplack *et al.*, "Electromagnetic breast imaging: average tissue property values in women with negative clinical findings," *Radiology*, vol. 231, pp. 571-580, 2004.

[37] M. Lazebnik, L. McCartney, D. Popovic, C. B. Watkins, M. J. Lindstorm, J. Harter, S. Sewall, A. Magliocco, J. H. Brooske, M. Okoniewski and S. C. Hagness, " A large - scale study of the ultra wideband microwave dielectric properties of normal breast tissue obtained from reduction surgeries*," Phys. Med. Biol.*, vol. 52, pp. 2637-2656, April 2007.

[38] M. Lazebnik, L. McCartney, D. Popovic, C. B. Watkins, M. J. Lindstorm, J. Harter, S. Sewall, A. Magliocco, J. H. Brooske, M. Okoniewski and S. C. Hagness, "A large-scale study of the ultrawideband microwave dielectric properties of normal, benign and malignant breast tissues obtained from cancer surgeries," *Phys. Med. Biol*., vol. 52, pp. 6093-6115, October 2007.

[39] M. Lazebnik, M. Okoniewski, J. H. Brooske, S. C. Hagness, "Highly accurate Debye models for normal and malignant breast tissue dielectric properties at microwave frequencies," *IEEE Microw. Wireless Comp. Lett.*, vol. 17, no. 12, pp. 822-824, December 2007.

[40] R. J. Halter *et al.*, "The correlation of in vivo and ex vivo tissue dielectric properties to validate electromagnetic breast imaging: initial clinical experience," *Physiol. Meas.*, vol. 30, pp. S121-S136, June 2009.

[41] A. Rosen, M. A. Stuchly and A. Vander Vorst, "Applications of RF/microwaves in medicine," *IEEE Trans. Microw. Theory Tech.*, vol. 50, no.3, pp. 963-74, 2002.

[42] M. C. Converse, E. J. Bond, S. C. Hagness and B. D. Van Veen "Ultrawideband microwave space-time beamforming for hyperthermia treatment of breast cancer: a computational feasibility study," *IEEE Trans. Microw. Theory Tech.,* vol. 52, no. 8, pp. 1876-89, 2004.

[43] M. D. Sherar, J. Trachtenberg, S. R. H. Davidson and M. R. Gertner, "Interstitial microwave thermal therapy and its application to the treatment of recurrent prostate cancer," *Int. J. Hyperthermia*, vol. 20, no. 7, pp. 757-68, 2004.

[44] D. Yang *et al.*, "A floating sleeve antenna yields localized hepatic microwave ablation," *IEEE Trans. Biomed. Eng.*, vol. 53, no. 3, pp. 533-7, 2005.

[45] O. Sipahioglu, S. A. Barringer and C. Bircan, "The dielectric properties of meats as a function of temperature and composition," *J. Microw. Power Electr. Energy*, vol. 38, pp. 161-9, 2003.

[46] H. P. Schwan and K. R. Foster, "Rf-field interactions with biological systems: electrical properties and biophysical mechanisms," *Proc. IEEE*, vol. 68, pp. 104-113, 1980.

[47] C. C. Johnson, A. W. Guy, "Nonionizing electromagnetic wave effects in biological materials and systems," *Proc. IEEE*, vol. 60, no. 6, pp. 692-718, 1972.

[48] H. P. Schwan, "Electrical properties of tissue and cell suspensions," *Adv. Biol. Med. Phys.*, vol. 5, pp. 147-209, 1957.

[49] K. R. Foster, J. L. Schepps, R. D. Stoy and H. P. Schwan, "Dielectric properties of brain tissue between 0.01 and 10 GHz," *Phys. Med. Biol.*, vol. 24, no. 6, pp. 1177-87, 1979.

[50] E. C. Burdette, F. L. Cain and J. Seals, "*In situ* tissue permittivity at microwave frequencies: perspective, techniques, results," *Medical Applications of Microwave Imaging ed. L. E. Larsen and J. H. Jacobi,* New York: IEEE, 1985, pp. 13-40.

[51] K. R. Foster and H. P. Schwan, "Dielectric properties of tissues and biological materials: a critical review," *Crit. Rev. Biomed. Eng.*, vol. 17, pp. 25-104, 1989.

[52] J. Kyber, H. Hansgen and F. Pliquett, "Dielectric properties of biological tissues at low temperatures demonstrated on fatty tissue," *Phys. Med. Biol.*, vol. 37, no. 8, pp. 1675-1688, 1992.

[53] S. Y. Semenov, R. H. Svenson and G. P. Tatsis, "Microwave spectroscopy of myocardial ischemia and infarction. 1. Experimental study," *Ann. Biomed. Eng.*, vol. 28, pp. 48-54, 2000.

[54] L. Chin and M. Sherar, "Changes in dielectric properties of ex vivo bovine liver at 915 MHz during heating," *Phys. Med. Biol.,* vol. 46, no. 1, pp. 197-211, 2001.

[55] F. Jaspard and M. Nadi, "Dielectric properties of blood: an investigation of temperature dependence," *Physiol. Meas.*, vol. 23, pp. 547-554, 2002.

[56] P. R. Stauffer, F. Rossetto, M. Prakash, D. G. Neuman and T. Lee, "Phantom and animal tissues for modeling the electrical properties of human liver," *Int. J. Hyperthermia*, vol. 19, no. 1, pp. 89-101, 2003.

[57] L. Chin and M. Sherar, "Changes in the dielectric properties of rat prostate ex vivo at 915 MHz during heating," *Int. J. Hyperthermia*, vol. 20, no. 5, pp. 517-27, 2004.

[58] C. L. Brace, "Temperature-dependent dielectric properties of liver tissue measured during thermal ablation: Toward an improved numerical model," *30th Annual IEEE EMBS Conference, Vancouver, British Columbia, Canada*, pp. 230-233, August 2008.

[59] M. Lazebnik, M. C. Converse, J. H. Booske and S. C. Hagness, "Ultrawideband temperature-dependent dielectric properties of animal liver tissue in the microwave frequency range," *Phys. Med. Biol.*, vol. 51, pp. 1941-1955, 2006.

[60] G. Ku and L. V. Wanga, "Scanning thermoacoustic tomography in biological tissue," *Med. Phys.*, vol. 27, no. 5, pp. 1195-1202, May 2000.

[61] R. A. Kruger, W. L. Kiser Jr, D. R. Reinecke, G. A. Kruger, R. L. Eisenhart, "Thermoacoustic Computed Tomography of the Breast at 434 MHz," *IEEE MlT-S Digest*, vol. 2, pp. 591-594, 1999.

CHAPTER 2

BACKGROUND

2.1 BREAST CANCER

Breast cancer refers to an uncontrollable cell growth that starts in the breast. The normal cycle of cell growth involves the formation of new cells when the body needs them and the death of old or damaged ones. When this process is disrupted, new cells grow uncontrollably while older, damaged ones do not die as necessary, resulting in a buildup of extra cells that form a mass commonly referred to as a tumor. Tumors can be either benign or malignant. Benign tumors are not cancerous and are therefore mostly not harmful because they do not invade surrounding tissue or body parts, can be easily removed, and do not grow back. On the other hand, malignant tumors are cancerous and are consequently a threat to the patient's life [1].

As shown in Figure 2.1, a breast consists of ducts that carry milk to the nipples and

lobules that produce the breast milk, and surrounding tissue such as fat, muscle and glandular tissue and connective tissue, together known as fibro-glandular tissue. Noninvasive breast cancer refers to cancer that remains within the milk ducts or lobules of the breast. Invasive ductal carcinoma (IDC) is the most common breast cancer that starts in a milk duct, breaks through its wall and invades the tissue of the breast. Ductal carcinoma is associated with random specks of calcium deposits, called micro-calcifications that occur in milk ducts. This cancer can further metastasize (or spread) into other body parts through the bloodstream or the lymphatic system. Once the cancer is metastasized to distant parts of the body it is impossible to cure. On the other hand, cancerous growth that is confined in the milk ducts is called ductal carcinoma in situ (DCIS), which is the most common type of noninvasive breast cancer. Early detection is crucial for the treatment of DCIS, which is usually lumpectomy, followed by radiation therapy. Similarly, if the cancer is confined to the lobes it is called lobular carcinoma in situ (LCIS). LCIS is not considered a true cancer because the growth does not further spread into breast tissue and thus it is not malignant and does not need to be treated. However, its presence increases a woman's risk of developing invasive breast cancer later; therefore, women with LCIS have to be regularly examined [2].

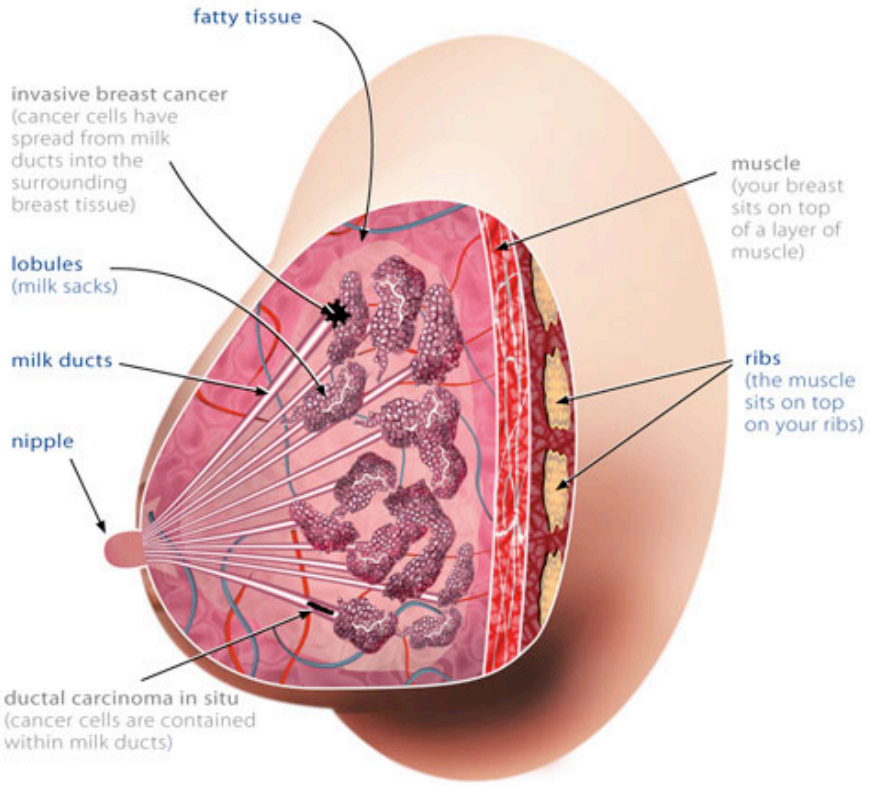

Figure 2.1: Illustration of a woman's breast showing ductal carcinoma in situ and invasive breast cancer (from [2]).

Once identified and diagnosed, the stage of the cancer is determined by the healthcare professional in order to identify whether breast cancer is at an early, locally advanced or metastatic stage. The TNM system stands for Tumor, Nodes and Metastases, is most commonly used to identify the stage of the cancer taking into consideration the size of the tumor, the number of affected lymph nodes, if any, and the metastasizing of the cancer to other body parts, if any. These three factors are combined to give an overall stage between I and IV. The higher the stage the more advanced the cancer is and the harder it is to control or cure [3].

2.2 BREAST CANCER SCREENING

It is evident that early detection plays an essential role in the treatment and management of DCIS and IDC. It is also necessary for women with LCIS in order to ensure proper awareness and regular screening. Early detection is also important in diagnosing the cancer at an early stage before it has significantly increased in size, affected lymph nodes or metastasized to other body parts. It is also crucial for treatments. Population-wide breast cancer screening programs that began in Canada in the late 1980's have helped to reduce breast cancer mortality by more than 35% [3].

Risk Categories

Risk categories help inform a woman and her health care provider about her breast screening options. Age (over 50 years old) and gender (female) are the key risk factors in developing breast cancer. Various other risk factors are used to assess the breast cancer risk category a woman belongs to. The risk categories divide women into three risk groups: average, intermediate, and high risk of developing breast cancer.

Approximately 80% of Canadian women are at average risk of developing breast cancer in their lifetime. Average risk means that over their lifetime they have 11% risk of developing breast cancer. Women at an average risk of developing breast cancer do not have any additional risk factors, apart from age and gender, associated with high or intermediate risk of breast cancer [4]. Women aged 50 to 69 with an average risk of developing breast cancer are encouraged to undergo regular breast screening, namely once every two years. For younger and older women, the balance of benefits and harms is

not so clear, however it is still recommended that they remain aware of breast cancer [5],[6]. Recent analyses by the Canadian Task Force on Preventive Health Care found that routine examinations had no significant benefit with the potential for harm from over-diagnosis and unnecessary biopsy for women aged 40 to 49 with an average risk of developing breast cancer [6]. On the other hand, the National Cancer Institute recommends that all women aged 40 and above should have mammograms every one to two years [7].

Approximately 18% of Canadian women are at intermediate risk of developing breast cancer in their lifetime. Intermediate risk means that they have at least 15% up to 25% risk of developing breast cancer in their lifetime. Women are considered to be at intermediate risk if they have a personal history of breast cancer (with no known/suspected genetic mutation), and an intermediate family history of breast cancer. Women at an intermediate risk of developing breast cancer are encouraged to discuss with their health care provider their breast screening options [4].

A small number of Canadian women (approximately 1% to 2%) are at high risk of developing breast cancer in their lifetime. These women have a 25% or higher risk of developing breast cancer in their lifetime. In the case of rare genetic mutations, this risk can be as high as a 50% possibility of developing breast cancer. A woman is at a high risk of developing breast cancer if she has one or a combination of the risk factors associated with breast cancer. The main risk factors include: a known, personal or in immediate family, genetic alteration associated with breast cancer such as mutations of the BRCA1, BRCA2 genes; a known personal or immediate family history of breast

cancer; and a personal history of radiation exposure to the chest before the age of 30 [4]. These risk factors place some younger women (younger than 50) at a high risk of developing breast cancer. Unfortunately, these women face the greatest challenge in diagnosis through mammograms.

Breast Cancer Screening Modalities

Mammography is currently the main screening tool for breast cancer. A mammogram is an x-ray picture of the breast that is used to detect and evaluate breast changes. The type of x-ray machine used for mammograms produces lower energy x-rays that do not go through tissue as easily as other x-ray machines, resulting in an improved contrast of the image. Mammograms today expose the breast to much lower radiation doses than devices used in the past. There are two types of mammograms used today depending on the purpose: a screening mammogram and a diagnostic mammogram. The screening mammogram is used for women who have had no prior breast concerns and show no signs of symptoms of breast cancer. The goal of this mammogram is the early detection of the tumor while it is small and before it shows any signs or symptoms in order to increase a woman's chance for treatment and survival. Diagnostic mammograms are used to further investigate a breast that has been identified as containing an abnormality. This mammogram can be used to focus on the area of question and evaluate the type of tumor. The results of diagnostic mammograms may finally identify that a biopsy, in which a cell sample is taken from the lump and studied under the microscope, is needed to identify if the abnormality is cancerous [8].

Even though mammography is currently the gold standard in breast cancer screening, it is not perfect in detecting breast cancer. The density of the breast also affects the ability of mammography to detect tumors. According to BI-RADS® (Breast Imaging-Reporting and Data System) the following pattern should be used for the consistent classification of the breast composition for all patients [9]:

1. The breast is almost entirely fat (< 25 % glandular).
2. There are scattered fibro-glandular densities (approximately 25%-50% glandular).
3. The breast tissue is heterogeneously dense (approximately 51%-75% glandular), which could obscure detection of small masses.
4. The breast tissue is extremely dense (>75% glandular), which may lower the sensitivity of mammography.

Mammograms do not work well in younger women, whose breasts are usually dense and can hide tumors. The same may also be true for pregnant women and women who are breast-feeding [10]. In a recent study, the sensitivity of mammograms, or the measure of true-positive results, increases from 63% for women with extremely dense breasts to 87% in women with mostly fatty breasts. Sensitivity also increases from 69% in women aged 40 to 49 to 83% in women aged 80 to 89 [11]. Therefore, dense breasts are the main reason why screening mammograms have a high false-negative rate, missing 20% to 40% of breast tumors present at the time of screening. Mammography also has a high false-positive rate of 50% to 70%. False-positive results occur when radiologists decide that there is an abnormality in the breast when no cancer is truly present. False-positive results lead to over-diagnosis and over-treatment of non-cancerous tumors [12].

Moreover, although the radiation exposure in mammograms is low, repeated exposure to x-rays has the potential of causing cancer. Pregnant women should also not be exposed to x-rays [7]. However, those in the mammography community argue that the benefits of regular breast screening using mammography outweigh the possible harms with an estimated benefit-to-harm ratio of 48.5 lives saved per 1 life lost due to radiation exposure [11]. Mammography also subjects women to uncomfortable and usually painful breast compression. As a result, in addition to attempting to improve on current mammography techniques, radiologists have turned to other imaging modalities such as MRI, ultrasound and other technologies that are still under testing.

In early 2011, the U.S. Food and Drug Administration (FDA) approved the first x-ray mammography machine that provides three-dimensional (3-D) images of the breast for cancer screening and diagnosis. The device provides a combined output of 2-D and 3-D images that roughly doubles the amount of radiation a patient receives. However, the increase in cancer risk from having both a 2-D and 3-D exam is expected to be less than 1.5% more than the natural cancer risk, and less than 1% compared to the risk from conventional 2-D mammography [13]. Initial studies performed on 3-D mammograms estimate that they could drop the false-positive rate of mammograms by up to 50% [14].

For certain women at high risk for breast cancer, screening magnetic resonance imaging (MRI) is recommended along with a yearly mammogram. MRI is not generally recommended as a screening tool by itself, because it does not detect all cancerous tumors and is very sensitive to breast abnormalities resulting in a high incidence of negative biopsies. MRI may also be used to further examine suspicious areas found by a

mammogram and to better determine the actual size of the cancer and to look for any other cancers in the breast. However, MRI machines are limited and result in very long wait times. MRI is also very time consuming and costly. Breast imaging using an MRI also requires the injection of a contrast material (called gadolinium) in the arm before or during the exam [10],[15]. FDA-accumulated data indicates that gadolinium-based contrast agents increase the risk to develop a systemic fibrosis disease called nephrogenic systemic fibrosis (NSF) among patients with severe renal insufficiency or renal dysfunction due to the hepato-renal syndrome or in the preoperative liver transplantation period [16]. As a result MRI cannot be used as a general screening method and can only be used for screening special cases, mainly younger women with a higher risk of developing breast cancer.

Breast ultrasound is sometimes used to further evaluate breast problems that are found during a screening or diagnostic mammogram, or a physical exam. Combining ultrasound and mammography has been suggested for screening high-risk women with dense breasts. Breast ultrasounds are also used to help the doctor guide the biopsy needle into the examined area in the breast. Although the ultrasound is less sensitive than the MRI, it is used more often because it is widely available, non-invasive, does not expose the patient to radiation and costs less. Ultrasounds are also highly operator dependable, resulting in a high rate of false negatives that are confirmed during biopsies. More studies are needed to figure out if ultrasound should be added to routine screening mammograms for some groups of women. However, the performance of the breast ultrasound alone does not grant it a position as a routine screening tool for breast cancer [8].

2.3 MICROWAVE IMAGING OF THE BREAST

Due to the lack of a comfortable, efficient, inexpensive and readily available imaging modality to detect breast cancer, there is need for a new imaging modality to detect breast tumors early. Microwave imaging for breast cancer screening is a new technique that has the potential to fulfill those requirements. Microwave imaging of the breast relies on sufficient contrast between the dielectric properties, namely permittivity and conductivity, of breast tissue, especially fat, the tissue most abundant in the breast, and tumors [17]-[24]. Malignant regions in the breast gather calcium ions from breast milk. Malignant cells also develop their own blood supply system to provide nutrients to the fast growing cancer cells. The unique properties that make tumor vessels different from normal ones are the high vascular density, high vascular permeability, chaotic vasculature and impaired lymphatic clearance from their interstitial space that take place in the tumor. These characteristics result in the enhanced permeability and retention (EPR) effect in tumors. These features allow malignant cells to develop their own blood supply system to provide nutrients to growing cancer cells. Consequently, there is a high ionic flow through malignant tissue that results in contrast in dielectric properties between normal and malignant breast tissue [25]. Many groups have therefore decided to take advantage of this contrast and develop a new breast screening technique using microwave imaging.

A microwave imaging system for breast cancer detection comprises an acquisition surface, sensors (antennas), a coupling liquid if necessary, and a reconstruction algorithm that translates signals measured by the sensors into images. This results in a system that is

relatively cheap and compact compared to current breast screening modalities. Microwaves are also non-ionizing, allowing frequent patient examinations. Painful breast compression is also not required for microwave imaging of the breast. Microwave imaging techniques for the breast are also being designed to offer high sensitivity, to compete with mammography, and specificity, to compete with MRI machines. Thus microwave imaging for the breast can offer an alternate, more efficient method for mass breast screening.

Microwave imaging techniques are divided into passive, active and hybrid systems [26],[27]. Passive systems use the principles of radiometry, which rely on the increased tumor temperature compared to normal breast tissue [28]-[31]. These systems effectively produce an image from the natural microwave radiation of human tissue. On the other hand, active breast imaging microwave systems involve the illumination of the tissue with microwave transmitters and the fields scattered by or transmitted through the tissue are measured [26]. Active microwave imaging systems are divided into microwave tomography systems [32]-[36], ultra-wideband radar systems [37]-[41] and holography systems [42]-[44]. Tomography involves the slice-by-slice image reconstruction using nonlinear optimization. The reconstructed images are maps of the permittivity and conductivity of the imaged object. The pulsed radar systems are time-domain systems in which the breast is illuminated with an ultra-wide band pulse and the scattered field is measured in order to identify the tumor signature (*the scattered field component due to the tumor*). Microwave holography is a fast inversion technique that relies on the measurement of the magnitude and phase of the wave scattered from the imaged target.

Knowledge of the magnitude and phase across an aperture allows Fourier transform (FT)-based reconstruction of the target's reflectivity [42]-[47].

Hybrid technologies, such as microwave-induced acoustic imaging, use microwaves to illuminate the breast [26],[27]. A small temperature rise can be produced when a microwave pulse irradiates a biological tissue, and the heated tissue thermally expands and contracts, becoming a source of acoustic waves. More energy is deposited in tumors due to their higher conductivity [48]. Cancerous breast tissues are two to five times more absorbing than surrounding normal breast tissues, which is attributed to an increase in bound water and sodium within malignant cells. Thermo-acoustic tomography is used for image reconstruction [49]. Temperature information is important for image reconstruction using thermo-acoustic tomography. Temperature measurements on tissue-equivalent phantoms are sometimes used to determine breast tissue heating [50].

2.4 BREAST PHANTOMS IN MICROWAVE IMAGING

The Need for Physical Breast Phantoms

Quantitative validation is crucial for microwave imaging systems for breast cancer detection. Clinical studies with human subject would be the ideal testing situation. However, clinical studies involve many complications related to performing studies on human subjects. Moreover, such experimentation is challenging due to the fact that the true *in vivo* properties of breast tissues are not completely known. As a result, realistic physical breast phantoms with known dielectric properties that mimic those of breast tissues are necessary in preclinical validation studies. Physical phantoms are used in the

testing of all imaging modalities in addition to the studies of interactions between certain technologies and the human body, such as specific absorption rate (SAR) measurements of the body when exposed to radiofrequency (RF) fields. Physical phantoms may be solid, liquid or semi-solid (gel). The heterogeneity of the human breast is difficult to achieve using a single phantom recipe. Therefore, most phantom recipes mimic the dielectric properties of a single tissue in the breast (skin, fat, fibroglandular (FG) tissue, muscle or tumor). A mixture of those phantom recipes can be used to achieve a structure that is heterogeneous.

Physical Breast Phantoms in the Literature

Physical phantoms of the breast are used to test and validate microwave-imaging setups for breast cancer detection [51]-[53]. Table 2-1 summarizes the materials and the properties of some of the numerous breast phantoms presented in the literature. The shape and structural complexity of the phantoms vary significantly across the literature, ranging from simple geometric volumes with predominantly homogeneous interiors to realistically shaped volumes with heterogeneous interiors. The materials used in these phantoms range from those with dielectric properties which approximate breast tissue properties at certain frequencies to tissue-mimicking (TM) materials [54] that mimic the dielectric properties of certain breast tissues over a wide frequency range [55]. Our group has also developed physical breast phantoms that are used to test the various components of a microwave imaging system for breast cancer detection [64].

Table 2-1: Summary of published work on breast phantoms for microwave imaging applications (from **[55]**).

Materials used	Breast shape	ε_r and σ (S/m) of constituents				Frequency (GHz)	References
		Skin	Fat	Fibroglandular	Tumor		
Oil-in-gelatin	Realistic	ε_r = 40–34 σ = 0.62–4.25	ε_r = 8–6 σ = 0.01–0.5	ε_r = 40–35 σ = 0.6–4	NA	1–6	[55]
Corn syrup, NaCl, agar	Cylinder	NA	NA	ε_r = 23 σ = 0.2	ε_r = 53.5 σ = 1.2	1.35	[56]
Corn syrup, agar	Cylinder	NA	NA	ε_r = 42 σ = 0.67	ε_r = 74 σ = 1.6	0.9	[41]
Silicone sheet, dough, alginate	Cylinder	$\varepsilon_r \approx$ 34.3 σ = 2–4	ε_r = 4.5–5 σ = 0.67	NA	$\varepsilon_r \approx$ 43.7 σ = 5–8	1–7	[57]
Oil-in-gelatin	Realistic	ε_r = 40–30 σ = 0.6–10.5	ε_r = 8–7.1 σ = 0.05–1.1	NA	NA	1–11	[58]
Liquid, gelatin, polythene	Hemi-sphere	ε_r = 35 σ NA	ε_r = 10 σ NA	ε_r = 27 σ NA	ε_r = 50 σ NA	3	[59]
Dough, water	Truncated cone	NA	NA	ε_r = 80–64 σ = 0.1–15	ε_r = 50–27 σ = 0.1–9	1–9	[60]
Isoparaffin, salt, sugar, water	Realistic	ε_r = 40.8 σ = 1.79	ε_r = 5.3 σ = 0.13	NA	NA	2.5	[61]
Oil-in-gelatin	Realistic	ε_r = 34–21 σ = 0.5–10	ε_r = 7.5–5.5 σ = 0.01–1.8	ε_r = 25.5–22.5 σ = 0.5–10	ε_r = 47.5–30 σ = 0.5–15	0.05–13.51	[62]
Oil-in-gelatin	Cylinder	ε_r = 46–35 σ = 12.5–18	ε_r = 5–4.5 $\sigma \approx$ 1	ε_r = 26–20 σ = 2.5–5	ε_r = 26–20 σ = 2.5–5	0.5–8	[63]

REFERENCES

[1] (October 2009). Breast Cancer. WebMD Health News. [Online]. http://www.medicinenet.com/script/main/art.asp?articlekey=150356.

[2] (March 2010). National Breast and Ovary Cancer Center, Australia. [Online]. http://canceraustralia.nbocc.org.au/breast-cancer/about-breast-cancer/about.

[3] (June 2012). Breast Cancer Information. Canadian Breast Cancer Foundation, Toronto, ON. [Online]. http://www.cbcf.org/central/AboutBreastCancerMain/AboutBreastCancer/Pages/default.aspx.

[4] (June 2012). Detecting Breast Cancer Earlier. Canadian Breast Cancer Foundation, Toronto, ON. [Online]. http://www.cbcf.org/central/AboutBreastHealth/EarlyDetection/Pages/default.aspx.

[5] (January 2010). Information on Mammography for Women Aged 40 and Older - A Decision Aid for Breast Cancer Screening in Canada. Public Health Agency of Canada. [Online]. http://www.phac-aspc.gc.ca/cd-mc/mammography-mammographie-eng.php.

[6] The Canadian Task Force on Preventive Health Care, "Recommendations on screening for breast cancer in average-risk women aged 40–74 years," *CMAJ*, vol. 183, no. 17, pp. 1991-2001, November 2011.

[7] (September 2010). Mammograms. National Cancer Institute (NCI). [Online]. http://www.cancer.gov/cancertopics/factsheet/detection/mammograms.

[8] (December 2011). Mammograms and Other Breast Imaging Procedures. American Cancer Society (ACS). [Online]. http://www.cancer.org/Healthy/FindCancerEarly/ExamandTestDescriptions/MammogramsandOtherBreastImagingProcedures/index.

[9] (November 2011). The American College of Radiology BI-RADS® ATLAS and MQSA: Frequently Asked Questions. American College of Radiology (ACR). [Online]. http://www.acr.org/~/media/ACR/Documents/PDF/QualitySafety/Resources/BIRADS/BIRADSFAQs.pdf.

[10] (March 2011). Breast Cancer: Early Detection. National Cancer Institute. [Online]. http://www.cancer.org/Cancer/BreastCancer/MoreInformation/BreastCancerEarlyD

etection/breast-cancer-early-detection-toc.

[11] J. G. Elmore, K. Armstrong, C. D. Lehman, S.W. Fletcher, "Screening for breast cancer," *JAMA*, vol. 293, no. 10, pp. 1245-1256, 2005.

[12] E. C. Fear, X. Li, S. C. Hagness, and M. A. Stuchly, "Confocal microwave imaging for breast cancer detection: Localization of tumors in three dimensions," *IEEE Trans. Biomed. Eng.*, vol. 49, pp. 812-822, August 2002.

[13] (February 2011). FDA approves first 3D mammogram device. Bloomberg Business Week, New York, USA. [Online]. http://www.businessweek.com/lifestyle/content/healthday/649867.html.

[14] M. Kerr. (November 2007). 3-D mammography cuts false-positive rates by half. Reuter Health, Chicago. [Online]. http://www.reuters.com/article/healthNews/idUSCOL97439820071129.

[15] J. Reichman. (April 2007). MRI vs. Mammography: Which is better for screening women at high risk of breast cancer? National Cancer Institute (NCI). [Online]. http://www.cancer.gov/clinicaltrials/results/mri-vs-mammography0603.

[16] (August 2009). Questions and Answers on Gadolinium-Based Contrast Agents. FDA Drug Safety Newsletter, Maryland, USA. [Online]. http://www.fda.gov/Drugs/DrugSafety/DrugSafetyNewsletter/ucm142889.htm.

[17] S. S. Chaudhary, R. K. Mishra, A. Swarup, and J. M. Thomas, "Dielectric properties of normal and malignant human breast tissues at radiowave and microwave frequencies," *Indian J. Biochem. Biophys.*, vol. 21, pp. 76-79, February 1984.

[18] J. Surowiec, S. S. Stuchly, J. R. Barr, and A. Swarup, "Dielectric properties of breast carcinoma and the surrounding tissues," *IEEE Trans. Biomed. Eng.*, vol. 35, pp. 257-263, April 1988.

[19] S. Gabriel, R. W. Lau, and C. Gabriel, "The dielectric properties of biological tissues: II. Measurements on the frequency range 10 Hz to 20 GHz," *Phys. Med. Biol.*, vol. 41, no. 11, pp. 2251-2269, November 1996.

[20] W. T. Joines, Y. Zhang, C. Li, and R. L. Jirtle, "The measured electrical properties of normal and malignant human tissues from 50 to 900 MHz," *Med. Phys.*, vol. 21, pp. 547-550, April 1994.

[21] M. Lazebnik, L. McCartney, D. Popovic, C. B. Watkins, M. J. Lindstorm, J. Harter, S. Sewall, A. Magliocco, J. H. Brooske, M. Okoniewski and S. C. Hagness, " A large – scale study of the ultra wideband microwave dielectric properties of normal

breast tissue obtained from reduction surgeries," *Phys. Med. Biol.*, vol. 52, pp. 2637-2656, April 2007.

[22] M. Lazebnik, L. McCartney, D. Popovic, C. B. Watkins, M. J. Lindstorm, J. Harter, S. Sewall, A. Magliocco, J. H. Brooske, M. Okoniewski and S. C. Hagness, "A large-scale study of the ultrawideband microwave dielectric properties of normal, benign and malignant breast tissues obtained from cancer surgeries," *Phys. Med. Biol*., vol. 52, pp. 6093-6115, October 2007.

[23] L. Sha, E. R. Ward, B. Story, "A review of dielectric properties of normal and malignant breast tissue," *Proc. IEEE Southeast Conf.*, pp. 457-462, 2002.

[24] M. Lazebnik, M. Okoniewski, J. H. Brooske, S. C. Hagness, "Highly accurate Debye models for normal and malignant breast tissue dielectric properties at microwave frequencies," *IEEE Microw. Wirel. Comp. Lett.*, vol. 17, no. 12, pp. 822-824, December 2007.

[25] H. Maeda, "The enhanced permeability and retention (EPR) effect in tumor vasculature: the key role of tumor selective macromolecular drug targeting," *Advan. Enzyme Regul.,* vol. 41, pp. 189-207, 2001.

[26] E. C. Fear, S. C. Hagness, P. M. Meaney, M. Okoniewski, and M. A. Stuchly, "Enhancing breast tumor detection with near field imaging," *IEEE Microw. Mag.*, vol.3, pp. 8-56, March 2002.

[27] N. K. Nikolova, "Microwave imaging for breast cancer," *IEEE Microw. Mag.*, vol. 12, no. 7, pp. 78-94, December 2011.

[28] B.Bocquet, J.C. van deVelde, A. Mamouni, Y. Leroy, G. Giaux, J. Delannoy, and D. DelValee, "Microwave radiometric imaging at 3 GHz for the exploration of breast tumors," *IEEE Trans. Microw. Theory Tech.*, vol. 38, pp. 791-793, June 1990.

[29] S. Mouty, B. Bocquet, R. Ringot, N. Rocourt, and P. Devos, "Microwave radiometric imaging for the characterisation of breast tumors," *Eur. Phys. J.: Appl. Phys.*, vol. 10, pp. 73-78, 2000.

[30] K. L. Carr, "Microwave radiometry: its importance to the detection of cancer," *IEEE Trans. Microw. Theory Tech.*, vol. 37, pp. 1862-1869, December 1989.

[31] K. L. Carr, P.Cevasco, P.Dunlea, and J. Shaeffer, "Radiometric sensing: An adjuvant to mammography to determine breast biopsy*," IEEE MTT-S Int. Microwave Symp. Dig.*, vol. 2, 2000, pp. 929-932.

[32] P. M. Meaney, M. W. Fanning, D. Li, S. P. Poplack, and K. D. Paulsen, "A clinical prototype for active microwave imaging for the breast," *IEEE Trans. Microw. Theory Tech.*, vol. 48, no. 11, pp. 1841-1853, November 2000.

[33] A. E. Bulyshev, S. Y. Semenov, A. E. Souvorov, R. H. Svenson, A. G. Nazarov, Y.E. Sizov and G. P. Tatsis, "Computational modeling of three-dimensional microwave tomography of breast cancer," *IEEE Trans. Biomed. Eng.*, vol. 48, no. 9, pp. 1053-1056, September 2001.

[34] Q. H. Liu, Z. Q. Zhang, T. T. Wang, J. A. Bryan, G. A. Ybarra, L. W. Nolte, and W. T. Joines, "Active microwave imaging I — 2-D forward and inverse scattering methods," *IEEE Trans. Microw. Theory Tech.*, vol. 50, no. 1, pp. 123-133, January 2002.

[35] Z. Q. Zhang, Q. H. Liu, C. Xiao, E. Ward, G. Ybarra, and W. T. Joines, "Microwave breast imaging: 3-D forward scattering simulation," *IEEE Trans. Biomed. Eng.*, vol. 50, no. 10, pp. 1180-1189, 2003.

[36] T. Rubæk, P. M. Meaney, P. Meincke, and K. D. Paulsen, "Nonlinear microwave imaging for breast-cancer screening using gauss–newton's method and the CGLS inversion algorithm," *IEEE Trans. Antennas Propagat.*, vol. 55, no. 8, pp. 2320-2331, 2007.

[37] X. Li, E. J. Bond, B. D. Van Veen and S. C. Hagness, "An overview of ultra-wideband microwave imaging via space-time beamforming for early- stage breast-cancer detection," *IEEE Antennas Propagat. Mag.*, vol. 47, pp. 19-34, February 2005.

[38] X. Li, S. K. Davis, S. C. Hagness, D. W. Weide and B. D. Van Veen, "Microwave imaging via space–time beamforming: experimental investigation of tumor detection in multilayer breast phantoms," *IEEE Trans. Microw. Theory Tech.*, vol. 52, pp. 1856-1865, August 2004.

[39] X. Li and S. C. Hagness, "A confocal microwave imaging algorithm for breast cancer detection," *IEEE Microwave Wireless Compon. Lett.*, vol. 11, no. 3, pp. 130-132, 2001.

[40] E. J. Bond, S. C. Hagness, and B. D. Van Veen, "Microwave imaging via space-time beamforming for early detection of breast cancer," *IEEE Trans. Antennas Propagat.*, vol. 51, no. 8, pp. 1690-1705, 2003.

[41] J. M. Sill and E. C. Fear, "Tissue sensing adaptive radar for breast cancer detection—experimental investigation of simple tumor models," *IEEE Trans. Microw. Theory Tech.*, vol. 53, pp. 3312-3319, November 2005.

[42] M. Elsdon, D. Smith, M. Leach, and S. J. Foti, "Experimental investigation of breast tumor imaging using indirect microwave holography," *Microwave Opt. Technol. Lett.*, vol. 48, no. 3, pp. 480-482, March 2006.

[43] M. Ravan, R. K. Amineh, and N. K. Nikolova, "Two-dimensional near-field microwave holography," *Inverse Prob.*, vol. 26, no. 5, May 2010.

[44] R. K. Amineh, M. Ravan, N. K. Nikolova, and A. Khalatpour, "Three-dimensional near-field microwave holography using reflected and transmitted signals," *IEEE Trans. Antennas Propagat.*, vol. 59, no. 12, pp. 4777-4789, December 2011.

[45] S. C. Hagness, A. Taflove, and J. E. Bridges, "Two-dimensional FDTD analysis of a pulsed microwave confocal system for breast cancer detection: Fixed-focus and antenna- array sensors," *IEEE Trans. Biomed. Eng.*, vol. 45, pp. 1470-1479, December 1998.

[46] E. C. Fear, J. Sill, and M. A. Stuchly, "Experimental feasibility study of confocal microwave imaging for breast tumor detection," *IEEE Trans. Microw. Theory Tech.*, vol. 51, no. 3, pp. 887-892, March 2003.

[47] M. Klemm, J. A. Leendertz, D. Gibbins, I. J. Craddock, A. Preece, and R. Benjamin, "Microwave radar-based differential breast cancer imaging: imaging in homogeneous breast phantoms and low contrast scenarios," *IEEE Trans. Antennas Propagat.*, vol. 58, no. 7, pp. 2337-2344, July 2010.

[48] L. Nie, D. Xing, Q. Zhou, D. Yang, and H. Guo, "Microwave-induced thermoacoustic scanning CT for high-contrast and noninvasive breast cancer imaging," *Med. Phys.*, vol. 35, no. 9, pp. 4026-4032, September 2008.

[49] G. Ku and L. V. Wanga, "Scanning thermoacoustic tomography in biological tissue," *Med. Phys.*, vol. 27, no. 5, pp. 1195-1202, May 2000.

[50] R. A. Kruger, W. L. Kiser Jr, D. R. Reinecke, G. A. Kruger, R. L. Eisenhart, "Thermoacoustic Computed Tomography of the Breast at 434 MHz," *IEEE MIT-S Digest*, vol. 2, pp. 591-594, 1999.

[51] X. Li, S. K. Davis, S. C. Hagness, D. W. van der Weide and B. D. Van Veen, "Microwave imaging via space–time beamforming: Experimental investigation of tumor detection in multilayer breast phantoms," *IEEE T. Microw. Theory*, vol. 52, no. 8, pp. 1856-1865, August 2004.

[52] E. Porter, A. Santorelli, A. Bourdon, D. Coulibaly, M. Coates, M. Popovi, "Time-domain microwave breast cancer detection: Experiments with comprehensive

glandular phantoms," *Proceedings of the Asia-Pacific Microwave Conference*, pp. 203-206, 2011.

[53] J. C. Y. Lai, C. B. Soh, E. Gunawan, and K. S. Low, "UWB microwave imaging for breast cancer detection – experiments with heterogeneous breast phantoms," *Prog. Electromagn. Res.M.*, vol. 16, pp. 19-29, 2011.

[54] M. Lazebnik, E.L. Madsen, G.R. Frank, and S.C. Hagness, "Tissue-mimicking phantom materials for narrowband and ultrawideband microwave applications," *Phys. Med. Biol.*, vol. 50, pp. 4245-4258, 2005.

[55] A. Mashal, F. Gao, and S. C. Hagness, "Heterogeneous anthropomorphic phantoms with realistic dielectric properties for microwave breast imaging experiments," *Microw. Opt. Techn. Let.*, vol. 53, no. 8, pp. 1896-1902, August 2011.

[56] P. M. Meaney, N. K. Yagnamurthy, and K. D. Paulsen, "Pre-scaled two-parameter Gauss-Newton image reconstruction to reduce property recovery imbalance," *Phys. Med. Biol.*, vol. 47, pp. 1101-1119, 2002.

[57] D. Li, P. M. Meaney, T. D. Tosteson, S. Jiang, T. E. Kerner, T. O. McBride, B. W. Pogue, A. Hartov, and K. D. Paulsen, "Comparisons of three alternative breast modalities in a common phantom imaging experiment," *Med. Phys.*, vol. 30, pp. 2194-2205, 2003.

[58] D. W. Winters, J. D. Shea, E. L. Madsen, G. R. Frank, B. D. Van Veen, and S. C. Hagness, "Estimating the breast surface using UWB microwave monostatic backscatter measurements," *IEEE Trans. Biomed. Eng.*, vol. 55, pp. 247-256, 2008.

[59] M. Klemm, J. A. Leendertz, D. Gibbins, I. J. Craddock, A. Preece, and R. Benjamin, "Microwave radar-based breast cancer detection: Imaging in inhomogeneous breast phantoms," *IEEE Antennas Wireless Propag. Lett.*, vol. 8, pp. 1349-1352, 2009.

[60] S. M. Salvador and G. Vecchi, "Experimental tests of microwave breast cancer detection on phantoms," *IEEE Trans. Antennas Propag.*, vol. 57, pp. 1705-1712, 2009.

[61] M. Miyakawa, S. Takata, and K. Inotsume, "Development of non-uniform breast phantom and its microwave imaging for tumor detection by CP-MCT," *Proceedings of the Annual International Conference of the IEEE Engineering in Medicine and Biology Society*, pp. 2723-2726, 2009.

[62] J. Croteau, J. Sill, T. Williams, and E. Fear, "Phantoms for testing radar-based microwave breast imaging," *Presented at the 13th International Symposium on Antenna Technology and Applied Electromagnetics and Canadian Radio Sciences*

Meeting, 2009.

[63] M. Ostadrahimi, R. Reopelle, S. Noghanian, S. Pistorius, A. Vahedi, and F. Safari, "A heterogeneous breast phantom for microwave breast imaging," *Proceedings of the Annual International Conference of the IEEE Engineering in Medicine and Biology Society*, pp. 2727-2730, 2009.

[64] Y. Baskharoun, A. Trehan, N. K. Nikolova, and M. D. Noseworthy, "Physical phantoms for microwave imaging of the breast," *IEEE Conference on BioWireLess*, pp. 73-76, January 2012.

CHAPTER 3

LITERATURE REVIEW

3.1 GENERAL ELECTROMAGNETIC PROPERTIES OF TISSUES

The main driving force behind microwave imaging of the breast is the sufficient contrast in dielectric properties between normal and malignant breast tissue. This conclusion was achieved from extensive studies of the dielectric properties of different body tissues. The electromagnetic properties of body tissues result from the interaction of its constituents, at a cellular and molecular level, with an applied electromagnetic field [1]. The knowledge of the biological effects of electromagnetic fields is useful for many applications such as electrocardiography (ECG), muscle contraction, nerve transmission, cancer hyperthermia, and medical imaging [2].

The electrical properties of materials include the conductivity σ, and the dielectric permittivity ε. The conductivity is defined as the conductance of a unit volume of matter. The dielectric permittivity is defined as the capacitance of a unit volume of matter

divided by the permittivity of free space $\varepsilon_0 = 8.8541\times 10^{-12}$ F/m [3]. In physical terms, the conductivity of a material can be regarded as a measure of the ability of its charge to be transported throughout its volume by an applied electric field. Similarly, its permittivity is a measure of the ability of its dipoles to rotate or its charge to be stored in the presence of an applied external field [4]. The complex permittivity is defined as:

$$\varepsilon^* = \varepsilon' - j\varepsilon'', \text{ where } \varepsilon' = \varepsilon \text{ and } \omega\varepsilon''\varepsilon_0 = \sigma \,. \tag{1}$$

The real part of the complex permittivity represents the dielectric constant of the material ε_r while the imaginary part is a measure of the dielectric losses. Losses are often defined as the tangent of the loss angle δ:

$$\tan\delta = \frac{\varepsilon''}{\varepsilon'} = \frac{\sigma}{\omega\varepsilon'\varepsilon_0} \,. \tag{2}$$

The magnetic properties of biological tissue are rarely discussed since their magnetic permeability is equal to that of free space and thus magnetic losses are negligible [3].

The interaction of the electromagnetic waves with the body tissues depends on their dielectric properties. Tissues are composed of cells containing intracellular fluid that contains various salt ions, polar protein molecules, and polar water molecules that are surrounded by thin membranes. Outside the cells, the extracellular fluid has similar concentrations of ions and polar molecules although some of the elements are different. Two types of effects control the dielectric behavior of tissues: the oscillation of free charges and ions and the rotation of dipole molecules at the frequency of the applied

field. The oscillation of free charges gives rise to conduction currents with an energy loss caused by the electrical resistance of the medium. On the other hand, the rotation of dipole molecules affects the displacement current though the medium with a dielectric loss due to viscosity [5]. The total current is thus the sum between the conduction current and the displacement current, which are 90 degrees apart in phase [4].

Interaction Mechanisms

The permittivity and conductivity of biological tissues, like most other materials, are frequency dependent or dispersive. The orientation of the dipoles and the motion of the charge carriers can explain the dispersion of tissues. At relatively low frequencies, dipoles can easily orient in response to the change in the applied field, whereas the charge carriers travel longer distances allowing for a greater opportunity of trapping at a defect or interface. As a result, the permittivity is relatively high and the conductivity is relatively low. As the frequency increases, the dipoles are less able to follow the rapid changes in the applied field and the resultant polarization disappears. In contrast, the charge carriers travel shorter distances and are less likely to be trapped. Therefore, the permittivity decreases and the conductivity increases [4]. The change in electric polarization following the application of an electric field is termed dielectric relaxation. The lag between the change in polarization of the material and the applied electric field results in the dispersion of the material. Dispersions can be characterized by their relaxation frequencies f_c or relaxation times $\tau = 1/f_c$ [6].

The dielectric properties of the various components of tissue govern the effective interaction between the electromagnetic fields and the biological matter. The main components of biological tissues are water, protein solutions and membranes.

A. Water

A single relaxation process centered near 20 GHz characterizes the dielectric properties of pure water. Three parameters characterize the electrical and viscous properties of water: (a) the relaxation frequency $f_c \approx 20$ GHz, (b) a static-frequency relative permittivity $\varepsilon_s \approx 78$ at frequencies much smaller than f_c and an infinite-frequency relative permittivity $\varepsilon_\infty \approx 5$ at room temperature, and (c) the conductance of ions in water. Researchers have also concluded that the mobility of ions in the tissue fluids is not significantly different from their mobility in water. They have also realized that there is no noticeable difference between the relaxation frequency of tissue water and pure water. The dielectric properties of electrolytes (*water-based solutions that have free ions which makes the solution electrically conductive*) are almost identical to those of water with the addition of a conductivity term σ_i due to the conductance of the dissolved ions. The static dielectric permittivity of electrolytes is about two units lower than that of pure water. There is also evidence of the presence of water bound to macromolecules, mostly proteins, in tissues. Bound water molecules do not rotate freely at microwave frequencies. Thus their dielectric dispersion occurs at a lower frequency range than the dispersion of free water, and bound water has higher permittivity and conductivity values than free water.

B. Protein Solutions

Protein solutions are formed of protein macromolecules that form a main part of the intracellular fluid. Protein solutions exhibit three major dispersion ranges. The first is at radio frequencies (RF's) and arises from macromolecular rotation in the applied electric field. The high frequency dielectric permittivity of this dispersion is lower than that of water because of the low dielectric permittivity of proteins. This dispersion is most noticeable in pure protein solutions; however, in tissues it only contributes to the dispersion at RF. At microwave frequencies, the dielectric properties of tissues are dominated by water relaxation; however, the presence of proteins in the solution displaces the corresponding water volume and thus diminishes the magnitude of the water dispersion by around 20 dielectric units. Between those two noticeable dispersions, at frequencies between a few hundreds to a few thousands of MHz, exists a less evident dispersion with a considerably smaller magnitude termed the δ dispersion. This dispersion is caused by the corresponding dispersion of the protein-bound water and the partial rotation of polar subgroups. The conductivity of protein bound water is higher than that of water and electrolytes in this frequency range.

C. Membranes

Membranes govern the dielectric properties of tissues at radio frequencies. The principal mechanism behind dielectric polarization at and below RF is the accumulation of charges from intra- and extracellular fluid at membranes. Thus, dispersion at RF's disappears if cell membranes are destroyed resulting in dispersions only at higher and lower frequencies that are governed by the intra- and extracellular ionic strengths. All

biological membranes, including cellular and subcelluar membranes, have a capacitance in the order of 1 μF/cm^2 independent of the frequency in the RF range. At lower frequencies, the capacitance of membranes increases with decreasing frequencies due to additional relaxation mechanisms in or near the membranes. As a result, the cell membrane acts as an insulating layer at lower frequencies causing current to flow only in the extracellular medium and resulting in a lower conductivity. As frequency increases, the capacitive reactance of the cell membrane decreases, allowing more currents to flow in the intracellular medium, resulting in an increase in the conductivity of the tissue. At sufficiently low frequencies, the cell membrane charging time constant is small enough to allow for the complete charging and discharging of the membrane in a single cycle. This behavior results in a high capacitance and thus a high relative permittivity. The increase in frequency prevents the cell membrane from charging completely during a single cycle, resulting in a decrease in the relative permittivity. At higher frequencies, the membrane behaves electrically like a short circuit [3].

Thus, the decrease in relative permittivity and increase in conductivity with increasing frequency for tissues with high water content is due to an interfacial polarization across the cell membrane. The frequency dispersion of tissues with low water content is similar to that of tissues with high water content. However, the behavior of water molecules in those tissues plays a bigger role in determining their dielectric permittivity. Since the relative permittivity and conductivity of water is significantly higher compared to tissues with low water content, small changes in water content can considerably affect the dielectric properties of tissues with low water content [5].

The above mechanisms govern the effective dielectric behavior of tissues at different frequency ranges. are three major relaxation mechanisms associated with body tissues, the α dispersion, the β dispersion and the γ dispersion [7]. The mechanisms that determine the electric behavior of biological tissues at different frequencies are described next [2]:

- At very low frequencies, below several hundred hertz, the conductivity of the tissue is dominated by the conduction in the electrolytes in the extracellular space. The relative permittivity of tissues reaches very high values, up to 10^6 and 10^7.
- At low frequencies, centered in the low kilohertz range, the tissue exhibits α dispersion. The α dispersion is very evident in the permittivity of the tissue but hardly in its conductivity. The α dispersion occurs due to the polarization of counterions (*ions that accompany an ionic species in order to maintain electric neutrality*) near charged surfaces in the tissue and the polarization of large membrane-bound structures in the tissue. The α dispersion has little significance for engineering applications.
- At RF, centered in the range from 0.1 MHz to 10 MHz, tissues exhibit β dispersion. The β dispersion is evident in both the permittivity and conductivity. The β dispersion occurs due to the charging of the cell membrane by the intracellular and extracellular electrolytes that introduces dispersion known as the Maxwell-Wager polarization effect. Hence the membrane charging time constant varies inversely with the conductivity of the electrolytes. Above the β dispersion, the cell membrane has

negligible impedance, thus current can pass though intracellular and extracellular media.

- At microwave frequencies, above 1 GHz, centered at 20 GHz, the tissue exhibits γ dispersion. The γ dispersion is due to the rotational relaxation of tissue water. At these frequencies, where the capacitive shorting-out effects of the cell membrane resistances begins to take effect, the dielectric characteristics of tissues can be expected to reflect the properties of the inter- and extracellular electrolytes and, in particular, to exhibit dielectric dispersion associated with the relaxation of water dipoles [8].
- Tissues also exhibit a small dispersion between 0.1 GHz and 3 GHz called the δ dispersion or ultrahigh frequency (UHF) relaxation. This relaxation is caused by a combination of mechanisms: bipolar relaxation of the water of hydration "bound" to proteins; a small Maxwell-Wager contributions due to ions and organelles in the cytoplasm; and the rotation of polar side-chains on the protein surface [9],[10].

Other smaller dispersions occur in tissues due to rotational relaxation of bound water or tissue proteins, charging of membranes of intracellular organelles and other effects. These dispersions overlap in frequency resulting in a broad and featureless dispersion in tissue [2]. Tissues also have finite ionic conductivities dictated by the nature and extent of their ionic content and ionic mobility [1].

Water Content

As mentioned earlier, the dielectric properties of tissues at frequencies above 1 GHz reflect the dielectric relaxation of tissue water, which is well described by the Debye equations with a relaxation frequency of 20 GHz at room temperature and 25 GHz at 37°C. Thus, the dielectric properties of tissue at these frequencies are highly dependent on their free water content [11]. The dielectric behavior of free water at constant temperature is shown in Figure 3.1. ε_∞ and ε_s are around 4.3 and 80, respectively, at room temperature. Higher values have been also been reported for ε_∞. Saline solutions are made up of salt dissolved in water. Salts dissolved in aqueous solutions act as conductors in an electromagnetic field. They therefore decrease the permittivity and increase the dielectric loss factor of solutions when compared to pure water. The decrease in ε' is caused by the binding of the free water molecules to counter-ions of the dissolved salts. The increase in ε'' results from the addition of conductive charge carriers caused by the ions of the dissolved salts. The dielectric loss of an aqueous ionic solution can be expressed as the sum of the ε'' $\left(\varepsilon_d''\right)$ caused by the dipole rotation and ε'' caused by the conductive (ionic) charge migration $\left(\varepsilon_\sigma''\right)$. This simple addition is realistic only when there are no other loss mechanisms and no mutual effects in the total dielectric loss [12].

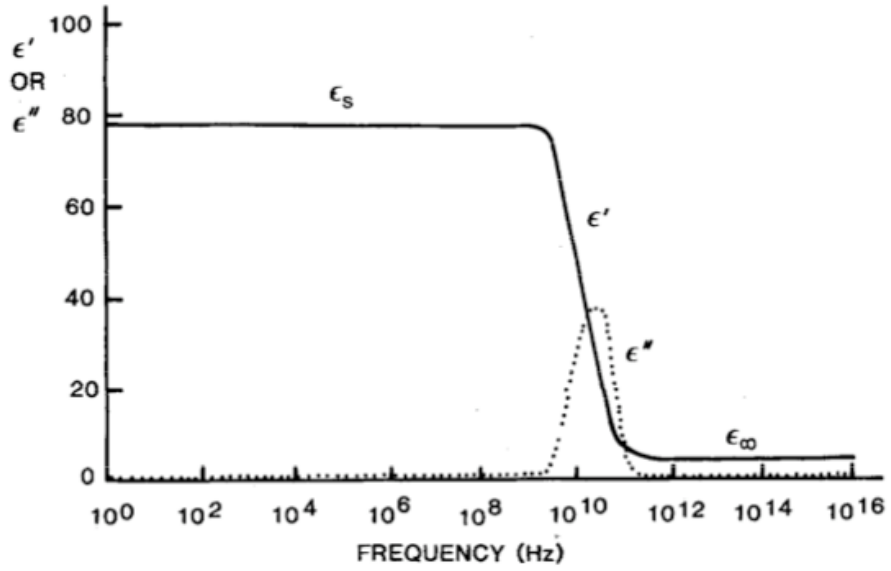

Figure 3.1: Dielectric behavior of free water at room temperature (from [12], with permission from Elsevier Limited).

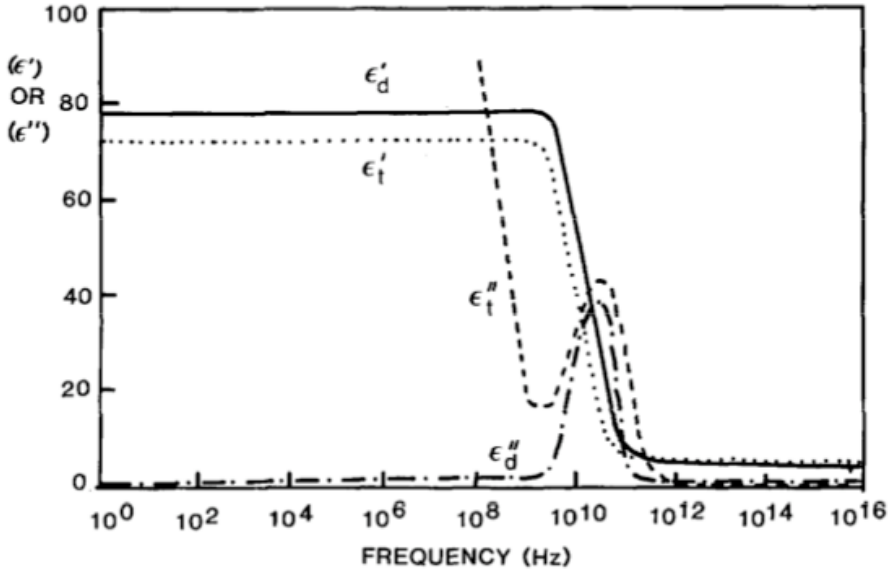

Figure 3.2: Behavior of an aqueous ionic solution at constant temperature. *d* indicates the dipole component and *t* indicates the total (dipole and ionic) effect (from [12], with permission from Elsevier Limited).

3.2 EM PROPERTIES OF BREAST TISSUES

The tissues available in a normal breast are fat, fibroglandular (FG) tissue (connective and glandular tissue) and muscle with the possibility of a benign or malignant tumor for diseased breasts. Fat is a low-water-content tissue; skin and FG tissue are intermediate-water-content tissues, and muscle and tumors are high-water-content tissues. The estimated water percentage by weight of different tissue types as well as benign and malignant tumors is shown in Table 3-1. The dependence of the dielectric properties of tissue on water content can be confirmed by observing Figure 3.3 and Figure 3.4, in the *in vivo* relative permittivity and resistivity ($\rho = 1/\sigma$) values of rat brain (a high-water-content tissue), muscle and canine fat for frequencies above 100 MHz compared to those of 0.9% saline solution, which corresponds to the ionic strength of cellular fluid [8].

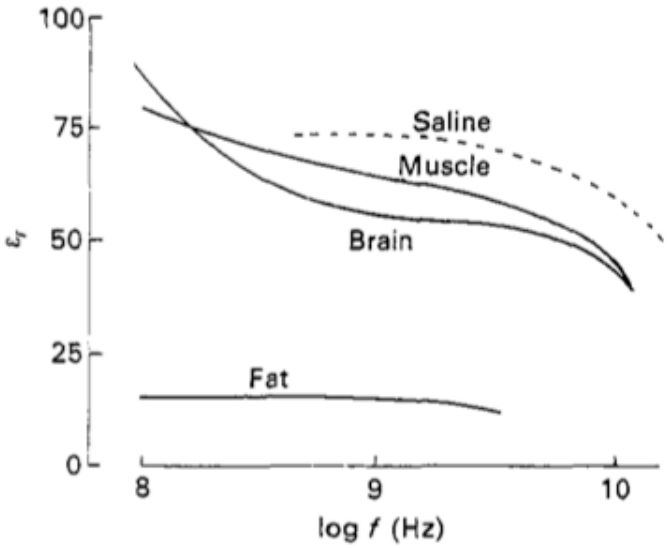

Figure 3.3: *In vivo* relative permittivity values of rat brain, muscle and canine fat for frequencies above 100 MHz compared to those of 0.9% saline solution (from [8], with permission from IOPscience).

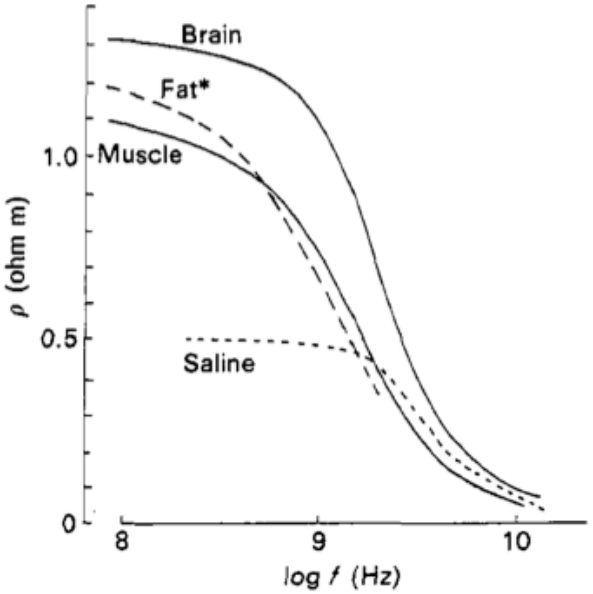

Figure 3.4: *In vivo* resistivity values of rat brain, muscle and canine fat for frequencies above 100 MHz compared to those of 0.9% saline solution *The values for canine fat are scaled down by one-fifth (from [8] , with permission from IOPscience).

Table 3-1. The water content of various tissue types present in normal and cancerous breast (from [13],[14]).

Tissue type	Percent water by weight
Fat	11 – 31 %
FG tissue	41 – 76 %
Skin	57 – 71 %
Muscle	71 – 76 %
Benign tumor	62 – 84 %
Malignant tumor	66 – 79 %

Malignant Tissue Mechanisms

Malignant tumors have higher relative permittivity and conductivity values than normal breast tissue. These values can be as high as 10 times for adipose fat, but drop to a contrast of around 10%, mainly in conductivity, for FG tissue. This contrast has posed a challenge for the microwave imaging community as FG tissue is where most breast tumors originate [15]. Understanding the mechanisms that result in the high permittivity and hyper-conductivity of tumors is therefore a crucial part of breast cancer imaging. A variety of factors have been associated with the difference in dielectric properties between normal and malignant tissues:

A. Necrosis

Inflammation and necrosis usually exist in malignant breast tissue. Necrosis leads to the breakdown of cell membranes and thus a larger fraction of tissue can carry current at low frequencies, decreasing the capacitance of the tumor.

B. Cell membrane

In breast carcinoma, fat lobules are replaced with fibroblastic proliferation and epithelial cells accompanied by various transformations at the new cell surface. Cancer cell membranes have a reduced potential and have the ability to absorb positive ions because they have a higher negative surface charge. As a result, the conductivity of the malignant tissue is increased because of the displacement and rotations of this mobile charge by the microwave field.

C. Relaxation times

The relaxation times in malignant tissues are larger than those in normal tissues

resulting from the increased motional freedom of water.

D. Sodium concentration and water content

The sodium concentration in cancer cells is higher than that in normal cells. The higher sodium concentration alone yields higher permittivity and conductivity values for malignant tissue. This higher sodium concentration also affects the cell membrane potential and causes the malignant tissue to retain more fluid. This retained fluid is in the form of bound water, which has higher permittivity and conductivity values. Malignant tissue thus has significantly higher water content [9].

F. Elasticity and stiffness

Under small deformation conditions, the elastic modulus of normal breast fat and fibro-glandular tissues are similar while benign tumors feature approximately twice the stiffness. Malignant tumors exhibit three- to six-fold increase in stiffness, with advanced invasive ductal carcinoma (IDC) exhibiting up to a thirteen-fold increase in stiffness compared to fibro- glandular tissue. The higher stiffness in malignant regions is attributed to higher interstitial pressure in malignant tissue due to rapid multiplication of cells and angiogenesis that increases blood and ionic flow to malignant regions. The lack of a dedicated lymphatic system to rid malignant regions of waste materials also adds to the pressure in this region and increases its stiffness. Elasticity and stiffness contrast between normal and malignant tissues is used in breast imaging using elastography [16].

Numerical Models

The polarization mechanisms that govern the different relaxation regions can be characterized in the simplest form by a single time constant τ. This simple representation results in a Debye-type response of the complex permittivity ε^* as a function of the angular frequency ω, which corresponds to parallel *RC* elements:

$$\varepsilon^* = \varepsilon_\infty + \frac{\varepsilon_s - \varepsilon_\infty}{1 + j\omega\tau} \tag{3}$$

where the time constant is $\tau = 1/RC$, ε_∞ is the relative permittivity at very high frequencies where $\omega\tau$ is much greater than 1, ε_s is the relative permittivity at very low frequencies where $\omega\tau$ is much smaller than 1, and the magnitude of the dispersion is $\Delta\varepsilon = \varepsilon_s - \varepsilon_\infty$.

However, the complexity of the structure, composition and the resultant dispersion of biological materials cannot be readily described by a single term or a summation of terms of Debye relaxations. The widths of the dispersion are particularly broader than those of simple *RC* elements because each dispersion region is broadened by multiple contributions to it. As a result, a distribution parameter, α, is introduced to account for this broadening to yield the Cole-Cole response:

$$\varepsilon^*(\omega) = \varepsilon_\infty + \frac{\Delta\varepsilon}{1 + (j\omega\tau)^{(1-\alpha)}} + \frac{\sigma_i}{j\omega\varepsilon_0} \tag{4}$$

where σ_i is the static ionic conductivity or the conductivity at very low frequencies and α is a parameter that depends on the nature of the material (being equal to 1 for Debye-type

dispersions). The width of the dispersion increases as α becomes smaller. Researchers attribute two physical interpretations to the distribution parameter. Some regard a wide dispersion as an indication of numerous Debye-type dispersions with a distribution of simple relaxation times. Other researchers regard the spread as an indication that the fundamental charge-transport and dipole-reorientation processes are essentially cooperative in nature and that, as the degree of cooperation increases, α becomes smaller than one.

The spectrum of a tissue can therefore be represented by a summation of multiple Cole-Cole dispersion terms:

$$\varepsilon^*(\omega) = \varepsilon_\infty + \sum_n \frac{\Delta\varepsilon_n}{1 + (j\omega\tau_n)^{(1-\alpha_n)}} + \frac{\sigma_i}{j\omega\varepsilon_0} \tag{5}$$

in which the choice of parameters for each tissue can be used to predict its dielectric behavior over a certain frequency range [4],[17].

Measurements of the EM Properties of Breast Tissues

Measurements of the EM properties of tissues date back to the 1930s. There is a wide range of published measurements of dielectric properties of different tissues at various frequency ranges. The measurements are performed *in vivo* and *ex vivo*, at various temperatures, on human as well as animal tissues [1].

Various data have been reported on the average dielectric properties of breast tissue [17]-[32]. Two groups have performed the most comprehensive and relevant studies on dielectric properties of human tissues: in 1996 the group of Gabriel *et al.* performed

measurements on biological tissues from 10 Hz to 20 GHz [1],[17],[18],[33] and in 2007 the group of Lazebnik *et al.* performed measurements on normal, benign and malignant breast tissues from 0.5 to 20 GHz [29]-[31]. Also, Halter *et al.* performed *in vivo* measurements of the dielectric properties of breast tissue during mastectomy procedures in the operating room followed by *ex vivo* measurements on the same freshly excised breast tissue over the frequency range 100 Hz – 8.5 GHz in order to compare the results and validate electromagnetic breast imaging [32].

Gabriel *et al.* measured the dielectric properties of a wide range of biological tissues; however, only the results of tissues found in the breast, such as adipose tissue, muscle and skin will be presented. Also, the relevant results for liver will be given as a representative of high-water-content tissues. Three techniques were used to measure the dielectric properties of tissue in the frequency range from 10 Hz to 20 GHz. The dielectric measurements were carried out using automatic swept-frequency network and impedance analyzers. An HP4192A impedance analyzer was used to cover the frequency range from10 Hz to 10 MHz. An HP8753C network analyzer was used for the frequency range from 300 KHz to 3 GHz, and an HP8720 network analyzer was used from 130 MHz to 20 GHz. The overlap between the three sets of measurements was deemed sufficient to demonstrate the consistency of the results. Open-ended coaxial probes were used to link the measuring equipment with the tissue samples. A detailed explanation of the techniques used to determine the dielectric properties of the samples using the

impedance analyzer and the HP8700 network analyzers are explained in [17] and [33], respectively. Three sources of samples were used: (i) ovine and porcine excised animal tissue, from freshly killed animals; (ii) human autopsy materials and (iii) human skin and tongue *in vivo*. All animal tissues were used mostly within 2 hours of the animal's death. Human materials were obtained within 24 to 48 hours after death. The measurement technique used for the impedance analyzer at low frequencies required at least a cube of 5 cm linear dimension; therefore, not all samples were measured at those frequencies [17].

The measurement technique as well as the instrumentation yielded a 1% uncertainty. The inhomogeneity of biological tissues resulted in about ±5 – 10% spread of the dielectric properties above 100 MHz to ±15 – 25% at lower frequencies. Corrections for the measurement technique below 1 KHz may also be under-corrected, while permittivity values below 100 Hz may have an error of up to a factor of two or three. The results of human tissues were compared to their animal equivalents. Comparisons were also made between *in vivo* and *in vitro* measurements of accessible body parts. Measurement results using the three techniques are shown in Figure 3.5 (*a*) – (*d*) for skin, muscle and liver tissues. The dielectric properties of muscle are known to be anisotropic. Measurements were performed on the paravertebral muscle twice, first with a transverse section against the probe (Figure 3.5 (*b*)) and again cut along the muscle fibre (Figure 3.5 (*c*)). Because of the radial nature of the fringing field of the co-axial probe, these measurements do not represent the true limits of the dielectric properties with the field

along and across the fibre. However, they show the effect of fibre direction and the parts of the spectrum influenced by it.

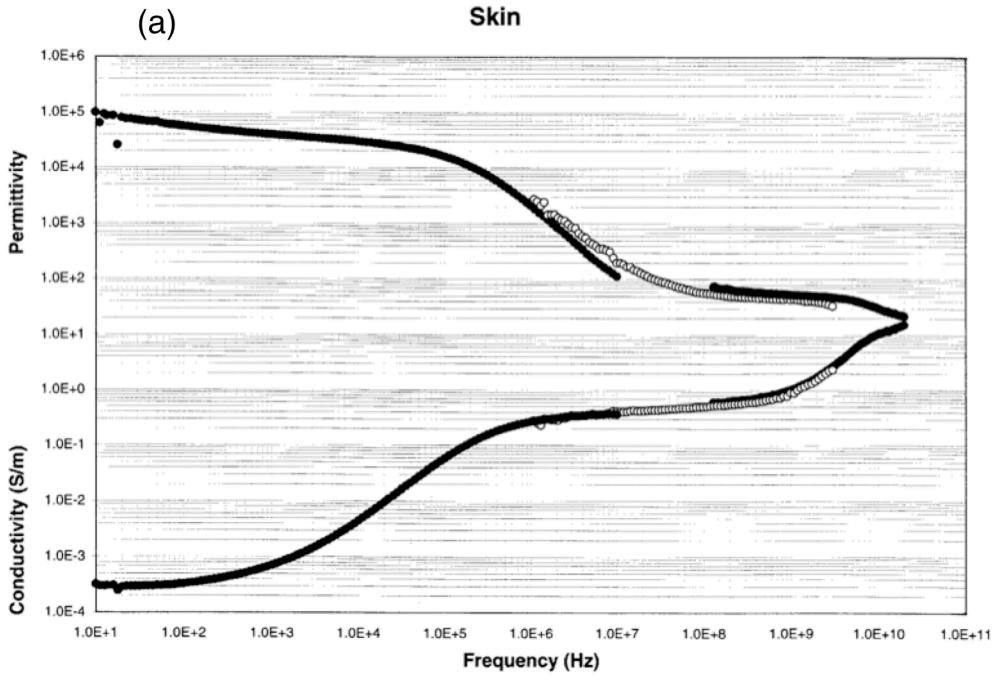

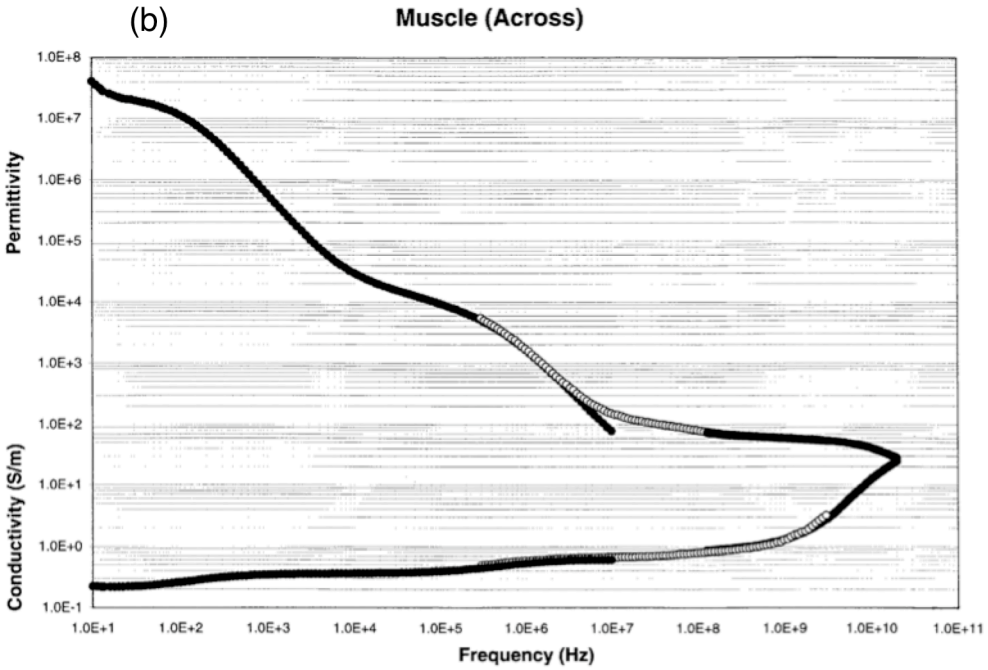
(b)
Muscle (Across)
Permittivity
Conductivity (S/m)
1.0E+8
1.0E+7
1.0E+6
1.0E+5
1.0E+4
1.0E+3
1.0E+2
1.0E+1
1.0E+0
1.0E-1
1.0E+1
1.0E+2
1.0E+3
1.0E+4
1.0E+5
1.0E+6
1.0E+7
1.0E+8
1.0E+9
1.0E+10
1.0E+11
Frequency (Hz)

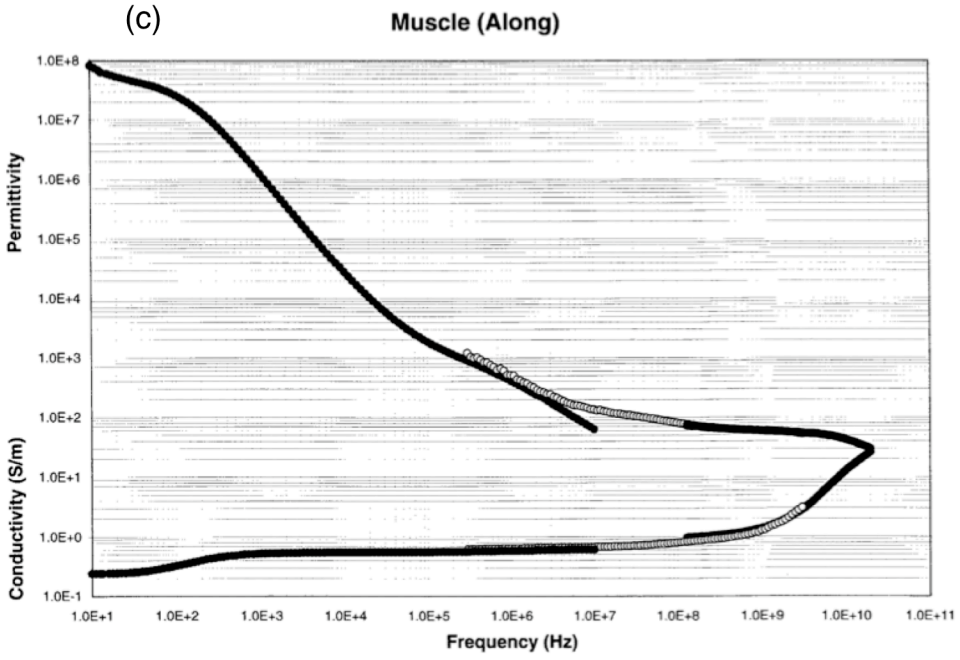
(c)
Muscle (Along)
Permittivity
Conductivity (S/m)
1.0E+8
1.0E+7
1.0E+6
1.0E+5
1.0E+4
1.0E+3
1.0E+2
1.0E+1
1.0E+0
1.0E-1
1.0E+1
1.0E+2
1.0E+3
1.0E+4
1.0E+5
1.0E+6
1.0E+7
1.0E+8
1.0E+9
1.0E+10
1.0E+11
Frequency (Hz)

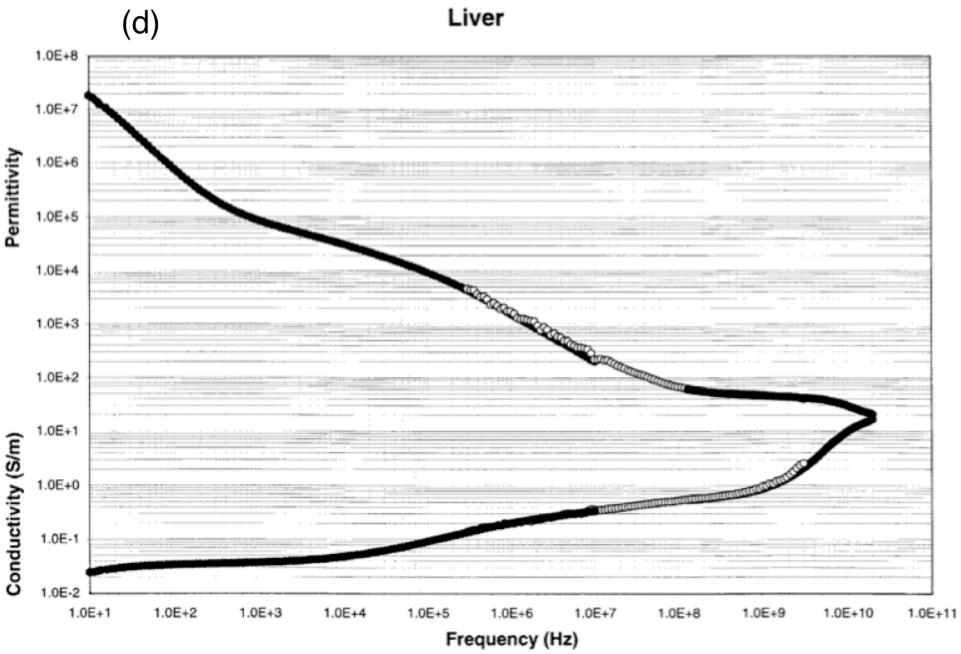

Figure 3.5: The permittivity and conductivity of various tissues from measurements using the three techniques with overlapping frequency coverage. (*a*) skin (ventral forearm), (*b*) muscle (paravertebral cut across the fibres), (*c*) muscle (paravertebral cut along the fibres), and (*d*) liver. (*a*) is from a human post-mortem sample, (*a*) – (*d*) are of bovine origin and (*b*) is human *in vivo*. All measurements were at body temperature (from [17], with permission from IOPscience).

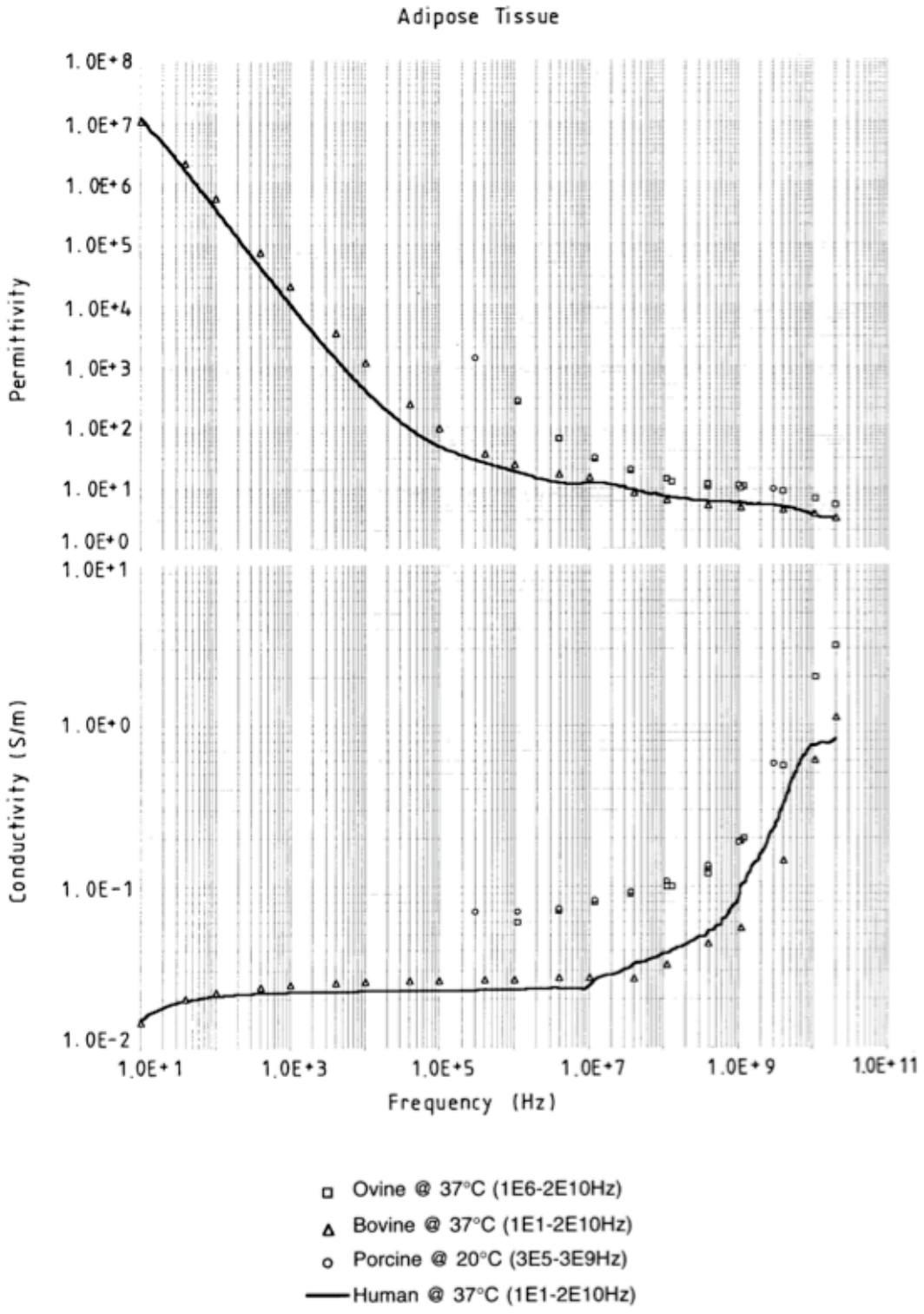

Figure 3.6: Comparisons between species and between *in vivo* and *in vitro* measurements of adipose tissue (from [17]**,** with permission from IOPscience).

Figure 3.6 shows the wide spread of data for adipose tissue from measurements on human and animal samples. Two limiting values are observed in the data, corresponding to pure fatty tissue of low water content and little infiltration with blood, in contrast to the data corresponding to tissue of higher water content and more blood infiltration. The resulting data was also shown to fall well within the range of the data published in other literature [17].

Using the data measured in [17] along with data from other literature sources, Gabriel *et al.* modeled the dielectric properties of tissues from 10 Hz to 100 GHz to four Cole-Cole dispersion regions $(n = 4)$:

$$\varepsilon^*(\omega) = \varepsilon_\infty + \sum_{n=1}^{4} \frac{(\varepsilon_s)_n - \varepsilon_\infty}{1 + (j\omega\tau_n)^{(1-\alpha_n)}} + \frac{\sigma_i}{j\omega\varepsilon_0}. \quad (6)$$

The parameters of equation (6) were determined to fit the dielectric data. Numerical least-square minimization techniques were not feasible to fit this data since the data spans several order of magnitude, creating a bias toward fitting the low-frequency data. The modeling parameters are also intercorellated, resulting in the absence of a unique solution. As a result analysis was carried out using a Microsoft Excel spreadsheet. 22 sets of data from measurements performed in [17] as well as data compiled from the literature were used. Graphs were produced to display the full range of data as well as a representation of the fitting equation generated from a parameter list. This presentation allowed for the continuous monitoring of the contribution of the fitting parameters. Using a systematic

procedure, the main parameters of the equation were fitted visually from high to low frequencies. The fitting procedure is terminated when positive and negative changes to the parameters produce no visible difference. The value of ε_∞ was fixed at 2.5 and 4 for low-water-content and high-water-content tissues, respectively. These values were chosen based on the knowledge that ε_∞ for water is 5. Three main dispersions are found in the frequency range from 10 Hz to 100 GHz; however, a four-pole Cole-Cole model provided more flexibility to achieve a better fit to the data. Figure 3.7 (*a*) – (*f*) shows the graphical prediction of the model using the parameters in Table 3-2.

Table 3-2: Parameters of equation (6) used to predict the dielectric properties of tissues in Figure 3.7 (*a*) – (*f*) (from [18]).

	Dry skin	**Wet skin**	**Muscle**	**Infiltrated fat**	**Not infiltrated fat**	**Liver**
ε_∞	4	4	4	2.5	2.5	4
$\Delta\varepsilon_1$	32	39	50	9	3	39
τ_1 (ps)	7.96	7.23	7.23	7.96	7.96	8.84
α_1	0.0	0.10	0.1	0.2	0.2	0.1
$\Delta\varepsilon_2$	1100	280	7000	35	15	6000
τ_2 (ns)	32.48	79.58	353.68	15.92	15.92	530.52
α_2	0.2	0.0	0.1	0.1	0.1	0.2
$\Delta\varepsilon_3$	0.0	3e4	1.2e6	3.3e4	3.3e4	5e4
τ_3 (μs)	NA	1.59	318.12	159.15	159.15	22.74
α_3	NA	0.16	0.1	0.05	0.05	0.2
$\Delta\varepsilon_4$	0.0	3e4	2.5e7	1e7	1e7	3e7
τ_4 (ms)	NA	1.592	2.274	15.915	7.958	15.915
α_4	NA	0.2	0.0	0.01	0.01	0.05
σ_i (S/m)	0.0002	0.0004	0.2	0.035	0.01	0.02

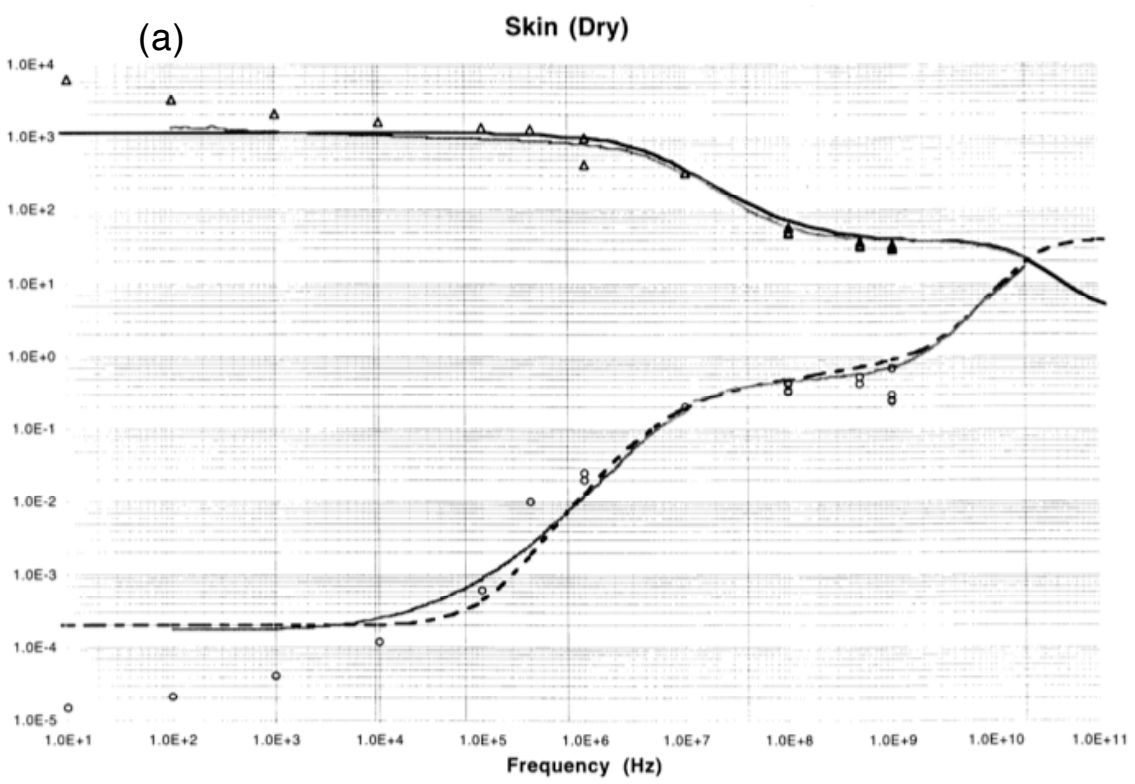
(a)
Skin (Dry)
1.0E+4
1.0E+3
1.0E+2
1.0E+1
1.0E+0
1.0E-1
1.0E-2
1.0E-3
1.0E-4
1.0E-5
1.0E+1
1.0E+2
1.0E+3
1.0E+4
1.0E+5
1.0E+6
1.0E+7
1.0E+8
1.0E+9
1.0E+10
1.0E+11
Frequency (Hz)

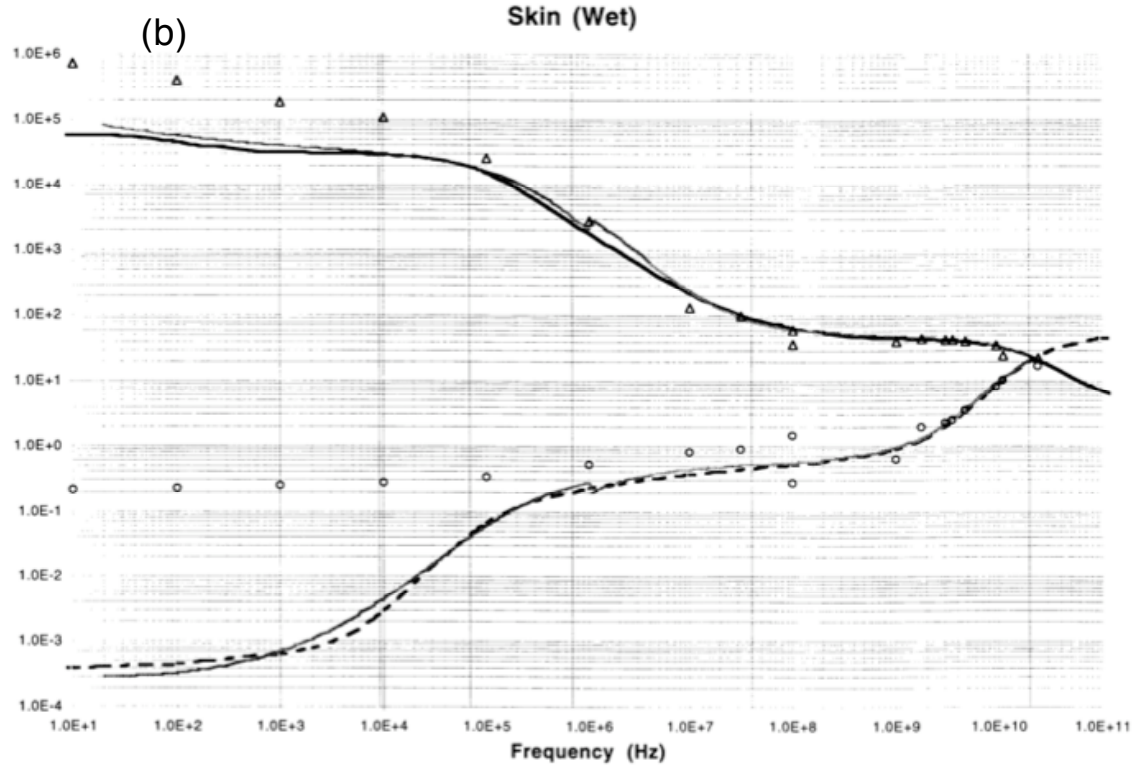
(b)
Skin (Wet)
1.0E+6
1.0E+5
1.0E+4
1.0E+3
1.0E+2
1.0E+1
1.0E+0
1.0E-1
1.0E-2
1.0E-3
1.0E-4
1.0E+1
1.0E+2
1.0E+3
1.0E+4
1.0E+5
1.0E+6
1.0E+7
1.0E+8
1.0E+9
1.0E+10
1.0E+11
Frequency (Hz)

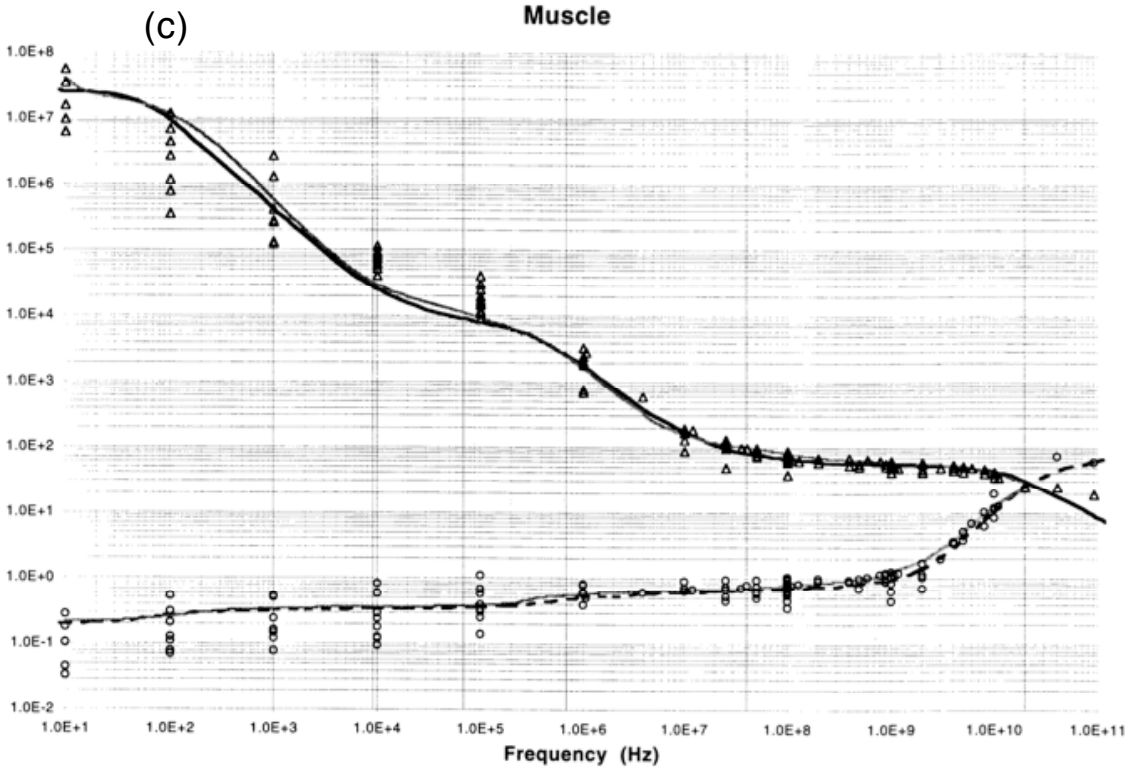
(c)
Muscle
1.0E+8
1.0E+7
1.0E+6
1.0E+5
1.0E+4
1.0E+3
1.0E+2
1.0E+1
1.0E+0
1.0E-1
1.0E-2
1.0E+1
1.0E+2
1.0E+3
1.0E+4
1.0E+5
1.0E+6
1.0E+7
1.0E+8
1.0E+9
1.0E+10
1.0E+11
Frequency (Hz)

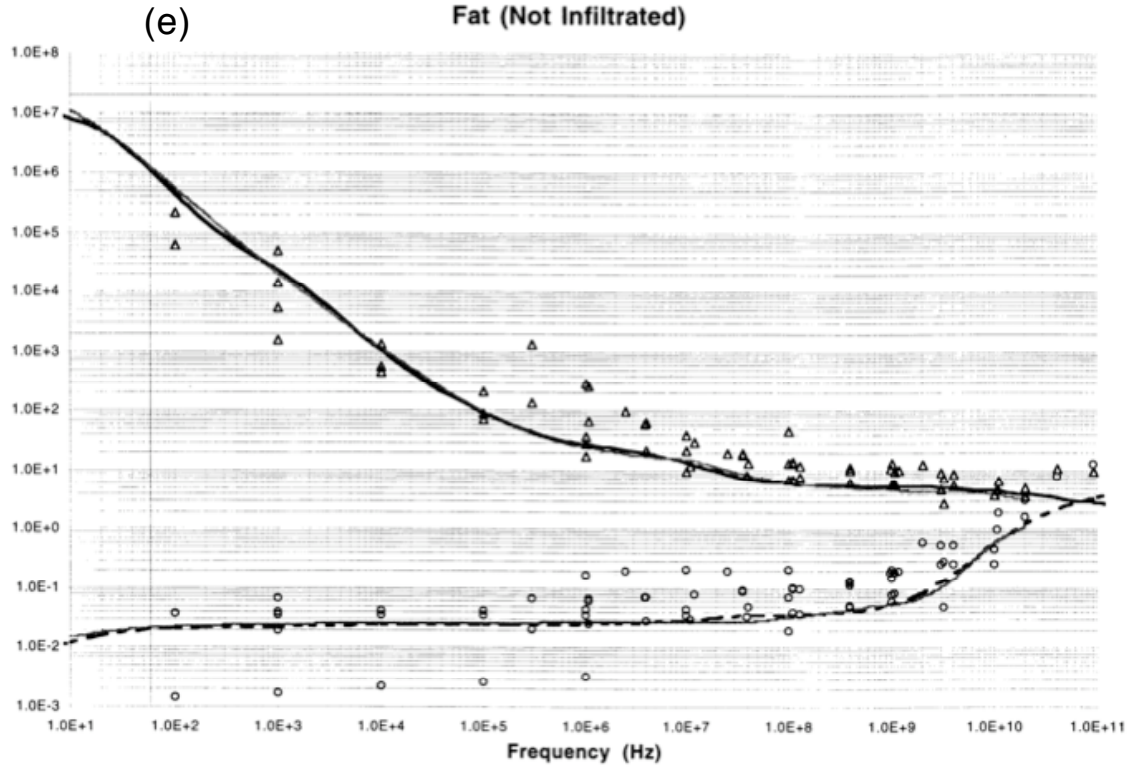
(e)
Fat (Not Infiltrated)
1.0E+8
1.0E+7
1.0E+6
1.0E+5
1.0E+4
1.0E+3
1.0E+2
1.0E+1
1.0E+0
1.0E-1
1.0E-2
1.0E-3
1.0E+1
1.0E+2
1.0E+3
1.0E+4
1.0E+5
1.0E+6
1.0E+7
1.0E+8
1.0E+9
1.0E+10
1.0E+11
Frequency (Hz)

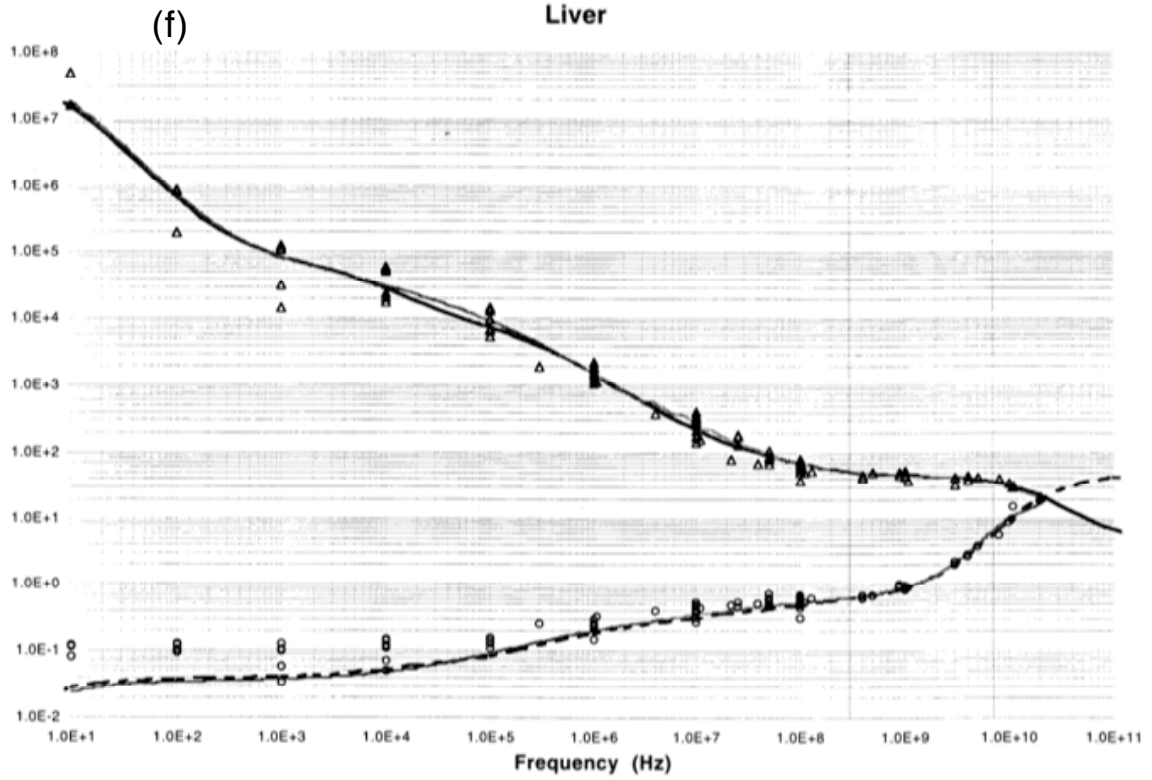

Figure 3.7: Permittivity and conductivity of tissues: prediction of the model (black filled and dotted curves), experimental data at 37°C (grey filled and dotted curves) and data from the literature (triangles and circles). (*a*) Skin (dry), (*b*) Skin (wet), (*c*) Muscle, (*d*) Fat (average infiltrated (with blood)), (*e*) Fat (not infiltrated (with blood)), and (*f*) Liver (from [18], with permission from IOPscience).

This analysis has been performed in order to find a model that is in line with data from literature and predicts the dielectric properties of tissues at different frequencies. However, due to the nature of the model, the obtained parameters are not unique. Therefore, the model as a whole should not be used to compare the dielectric parameters to the structure and composition of the various tissues. However, parts of the spectrum and their underlying mechanisms can be compared. For example, at frequencies above a few hundred MHz, the dipolar orientation of the water molecules is the dominant

polarization mechanism. The high frequency data (above 400 MHz) was fitted to a one-pole Cole-Cole model using a least-squares minimization procedure. Therefore, the resulting dispersion parameters may be used to understand the dielectric response of tissue water given each tissue's water content. The authors compare three kinds of tissues, aqueous humour (body fluid), retina and cortical bone, with > 95%, > 85% and < 20% water content, respectively with water at 37°C. ε_s increases, to a limiting value equal to that of water as tissue water content increases. The distribution parameter α is significant for most tissues and decreases with increased water content to become negligible for body fluids and zero for water. The relaxation time τ is generally longer than its value for water, which is an indication of a restriction in the rotational ability of some of the water molecules due to the organic environment. Body fluids with a low organic environment do not have this effect on τ and thus have values comparable to that of water. This model therefore offers a 'best estimate' based on the knowledge available; however, it is crucial to understand the limitations of the model especially due to the lack of definite data to support its predictions [18].

The group of Lazebnik *et al.* performed two large-scale studies of the ultrawideband microwave dielectric properties of normal breast tissue from reduction surgeries [29] and of normal, benign and malignant tissue from cancer surgeries [30]. Breast tissue has the greatest uncertainty in dielectric properties among human tissues because of its greater heterogeneity as well as the variability in the procedures and protocols used in different studies. Therefore, Lazebnik *et al.* used methodological experimentation and measurement and described them in great detail in order to overcome the inconsistencies

of previous studies.

The same experimental procedure was used for measuring both the samples from reduction surgeries and those from cancer surgeries. Measurements were carried out on samples from surgeries at the University of Wisconsin and the University of Calgary hospitals. Details of tissue collection and handling protocol for samples taken from breast reduction surgeries and samples taken from cancer surgeries at both hospitals are shown in Table 3-3 and Table 3-4, respectively. The dielectric spectroscopy measurements were carried out from 0.5 to 20 GHz using a small (3 mm) diameter precision open-ended coaxial cable placed in direct contact with an unperturbed sample. The flange-free precision probe offered a small sensing volume, thus enabling the reliable identification of the measurement site and the precise assessment of the tissue composition within the sensing volume. The expected measurement uncertainty of the technique used was verified in [34] to be no greater than 10%. Histological analysis was performed to determine the tissue composition within the probe's sensing volume by making histology slides taken from a medial cross-section directly underneath the site of the probe's contact with the tissue. 118 out of 488 samples from breast-reduction surgeries and 159 out of 319 samples from cancer surgeries were excluded using a histology-based criterion, in which samples with poor histology slides were excluded from further analysis [29],[30].

Table 3-3: Details of tissue collection and handling protocol for samples taken from breast reduction surgeries (from [29], with permission from IOPscience).

Total number of patients	93
Total number of measurements	488
Patient age	17–64 years (UW)
	17–65 years (UC)
Time from excision to measurement	5–80 min (UW)
	5–320 min (UC)
Tissue temperature during measurement	18.0–25.7 °C (UW)
	19.5–26.6 °C (UC)

Table 3-4: Details of tissue collection and handling protocol for samples taken from cancer surgeries (from [30], with permission from IOPscience).

Total number of patients	196
Total number of samples	319
Patient age	35–87 years (UW)
	19–90 years (UC)
Time from excision to measurement	20–221 min (UW)
	11–240 min (UC)
Tissue temperature during measurement	18.0° C–25.7° C (UW)
	19.9° C–27.2° C (UC)

The complex permittivity ε^* data of each sample in [29] and [30] was fit to a one-pole Cole-Cole model:

$$\varepsilon^*(\omega) = \varepsilon_\infty + \frac{\varepsilon_s - \varepsilon_\infty}{1 + (j\omega\tau)^{(1-\alpha)}} + \frac{\sigma_i}{j\omega\varepsilon_0} \tag{7}$$

where ω is the angular frequency and ε_∞, $\Delta\varepsilon$, α, τ and σ_i are the model parameters as discussed in (4) The parameter values for each complex-permittivity data set corresponding to each characterized tissue sample were obtained by minimizing the following criterion:

$$e = \frac{\sum_{i=1}^{N}\left(\frac{\varepsilon'(\omega)_i - \hat{\varepsilon}'(\omega)}{\text{median}[\varepsilon'(\bar{\omega})]}\right)^2 + \sum_{i=1}^{N}\left(\frac{\varepsilon''(\omega)_i - \hat{\varepsilon}''(\omega)}{\text{median}[\varepsilon''(\bar{\omega})]}\right)^2}{N} \quad (8)$$

where N is the number of frequency points in the 0.5 GHz to 20 GHz range. This number was set to N = 50 equally spaced frequency points. Median dielectric constants and effective conductivity dispersion curves were obtained by calculating the fitted values for each sample at the 50 frequency points. The Cole-Cole model was fit to these median values. The upper and lower quartiles (25^{th} and 75^{th} percentiles) of the fitted curves were calculated at 5, 10 and 15 GHz to summarize the spread of the results and allow for further analysis. All fitting and data analysis was accomplished using a statistical software package [29].

Some samples were also excluded due to a physics-based exclusionary criterion in which measurements that suffer from inevitable experimental errors are determined. Data sets that do not obey the Kramers-Kronig relation between the real and imaginary parts of the complex were identified when their best fitting Cole-Cole model did not match the frequency dependence of the measured data set within a certain threshold. 16 out of the remaining 370 samples from breast reduction surgeries and 5 out of the remaining 160 samples from cancer surgeries were disqualified using this criterion, making the final number of samples analyzed 354 and 155, respectively [29],[30].

A. Normal Breast Tissue from Reduction Surgeries [29]

The histological analysis of the samples obtained from reduction surgeries quantified tissue composition in terms of percentages of adipose, glandular and fibroconnective tissues. The samples in this study were divided into three groups based

on adipose tissue content: 99 samples in group 1 contained 0 – 30% adipose tissue (the high-water content group), 84 samples in group 2 contained 31 – 84% adipose tissue and 171 samples in group 3 contained 85 – 100% adipose tissue (the low-water content group). Curve fitting and data analysis were performed, as described above, for samples of each of the three groups separately.

Figure 3.8 shows the Cole-Cole fits for the 354 tissue samples characterized and analyzed in the reduction surgery study. This figure clearly illustrates the important finding that the normal breast tissue dielectric properties span a large range. The dielectric property curves are color-coded by their tissue composition. In order of highest to lowest adipose content, the colors are red, purple, blue, cyan and green. It can be observed that as the dielectric constant and effective conductivity of the samples increase, the adipose content decreases and the fibroconnective and/or glandular contents increase. The dielectric parameters of the median Cole-Cole model for the three adipose-defined groups are given in Table 3-5, Table 3-6 and Table 3-7. ε_∞, $\Delta\varepsilon$, and σ_i monotonically decrease as the percent of adipose tissue increases (as water percentage decreases). The median τ values of group 1 and group 2 differ from this trend because of the large heterogeneity of the samples in group 2. Group 2 also had the largest median α values, corresponding to the largest spread of intrinsic τ values. The resulting median Cole-Cole fits of the dielectric properties and the variability bars that represent the 25^{th} – 75^{th} percentiles of the three groups are shown in Figure 3.9. Group 3 shows the smallest variation around the median due to the dominance of adipose tissue and thus relative homogeneity of the sample. Group 2 displays the greatest variability in dielectric

properties due to the high heterogeneity of the tissues in this group.

Table 3-5: Cole-Cole parameters for group 1 of normal samples from reduction surgeries (from [30]).

Percentile	ε_∞	$\Delta\varepsilon$	τ (ps)	α	σ_i (S/m)
25th	9.941	26.60	10.90	0.003	0.462
50th	7.821	41.48	10.66	0.047	0.713
75th	6.151	48.26	10.26	0.049	0.809

Table 3-6: Cole-Cole parameters for group 2 of normal samples from reduction surgeries (from [30]).

Percentile	ε_∞	$\Delta\varepsilon$	τ (ps)	α	σ_i (S/m)
25th	8.718	17.51	13.17	0.077	0.293
50th	5.573	34.57	9.149	0.095	0.524
75th	5.157	45.81	8.731	0.091	0.766

Table 3-7: Cole-Cole parameters for group 3 of normal samples from reduction surgeries (from [30]).

Percentile	ε_∞	$\Delta\varepsilon$	τ (ps)	α	σ_S (S/m)
25th	2.908	1.2	16.88	0.069	0.020
50th	3.140	1.708	14.65	0.061	0.036
75th	4.031	3.654	14.12	0.055	0.083

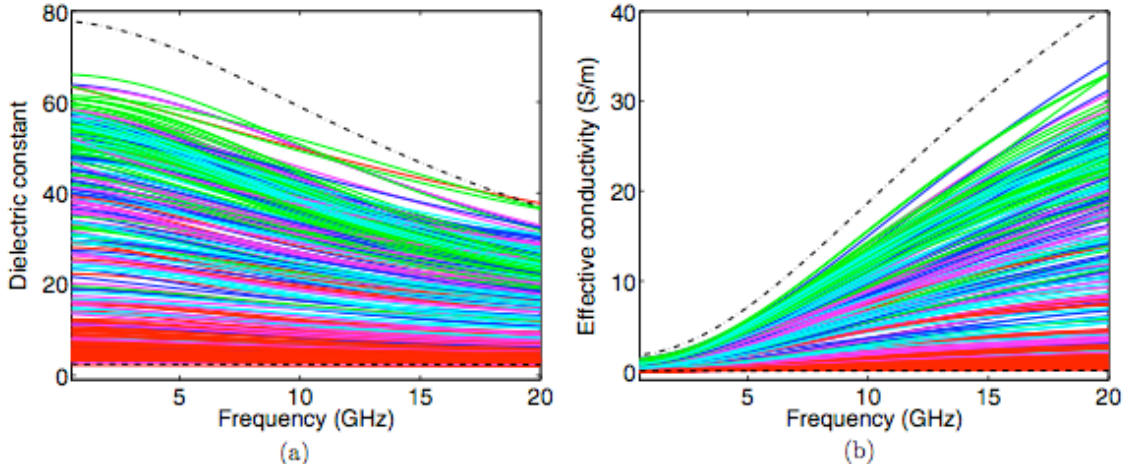

Figure 3.8: One-pole Cole-Cole fits to 354 dielectric properties data sets of reduction surgery study: (a) dielectric constant; (b) effective conductivity. The dashed (lower) black curve corresponds to the dielectric properties of lipid, and the dash-dot (upper) black curve corresponds to the dielectric properties of physiological saline (from [29], with permission from IOPscience).

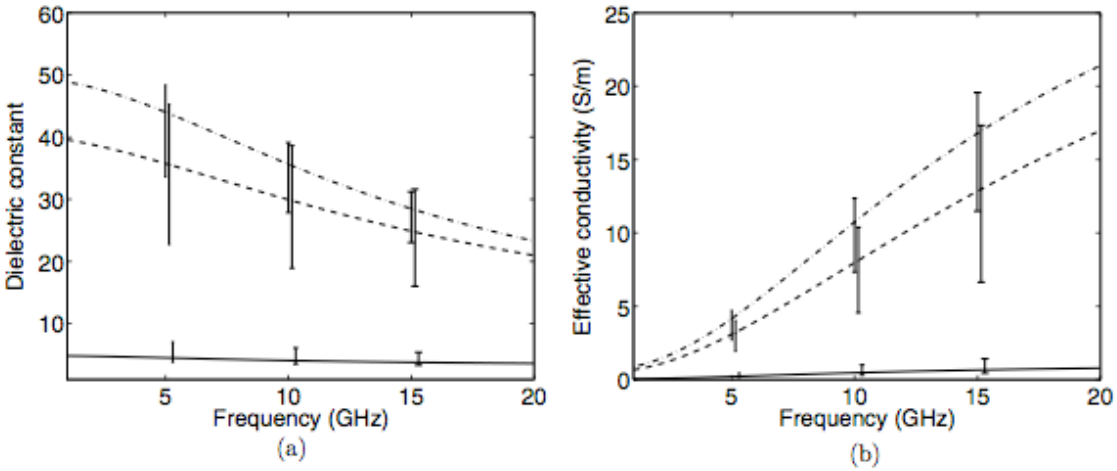

Figure 3.9: Median dielectric properties of the three adipose-defined tissue groups. The variability bars show the 25th – 75th percentiles of the fitted values. Dash-dot line: group 1 (0 – 30% adipose), dashed line: group 2 (31 – 84% adipose), solid line: group 3 (85 – 100% adipose) (from [29], with permission from IOPscience).

After analyzing the dielectric properties of the tissue samples, large variability in the dielectric properties was found due to substantial tissue heterogeneity in the breast. It

was also determined that tissue dielectric properties are bound by those of lipids at the low end and by those of physiological saline at the high end. The tissue dielectric properties do not, as expected, reach those of saline because even the highest-water content tissue contains less than about 80% water. The authors also concluded that there is no statistically significant variability due to the use of samples from different breasts and the variability due to the samples within the breast. A statistically significant trend was found between the dielectric properties and the time between excision and measurement for the 85 – 100% adipose tissue group (group 3). The dielectric constant and the effective conductivity decreased as the time between excision and measurement increased. Even though the trend was statistically significant, the magnitude of the change is negligible compared to the much larger range of properties spanned by all tissue groups. This trend was not observed for the other two groups with higher water contents. Since extracellular water is more dominant than intracellular water in adipose tissue, while the opposite is true for non-adipose tissue, most of the extracellular water in the samples with a dominant content of adipose tissue was lost due to desiccation faster than the intracellular water that is contained in the non-adipose tissue. Patient age, sample temperature and time between excision and measurement had no statistically significant trend or identifiable pattern effect on the dielectric properties.

B. Normal, Benign and Malignant Breast Tissue from Cancer Surgeries [30]

In the cancer surgery study, the samples were first diagnosed as either normal, benign or cancer. The normal tissue samples were divided into three groups as in the reduction surgery study. The type of benign tissue and the grade of the cancer were

determined in benign or malignant samples. The samples diagnosed as benign were categorized based on the percentages of benign tissue. The tissue samples diagnosed as cancerous were categorized in terms of percentages of invasive ductal carcinoma (IDC), invasive lobular carcinoma (ILC), ductal carcinoma *in situ* (DCIS) and lobular carcinoma *in situ* (LCIS). In total there were 85 normal samples, 10 benign samples and 60 cancer samples. In cancer samples, the adipose and glandular tissue content was very low such that 83% of them contained 0 – 20% adipose tissue, and all 60 cancer samples contained 10% or less glandular tissue. This is because the vast majority of cancer tissues analyzed in this study originated within the glandular region of the breast, so it is to be expected that these tumors contain very little adipose and normal (non-malignant) glandular tissues.

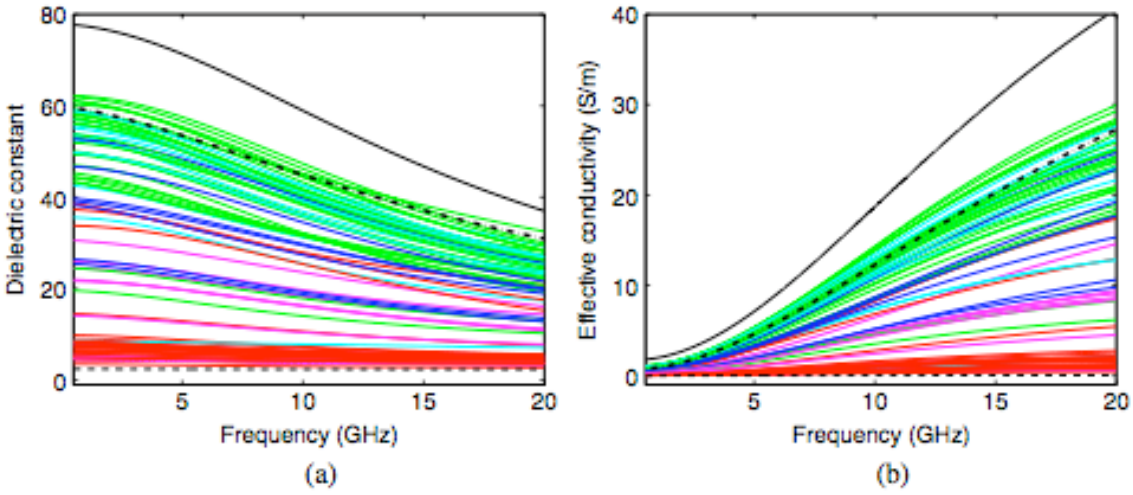

Figure 3.10: One-pole Cole-Cole fits to the 85 normal data sets. The curves are color-coded based on the amount of adipose tissue present in each sample. The solid black (upper) curve represents the dielectric properties of saline, the dashed black (lower) curve represents the dielectric properties of lipids, and the dash-dot black (middle) curve represents the dielectric properties of blood (from [30], with permission from IOPscience).

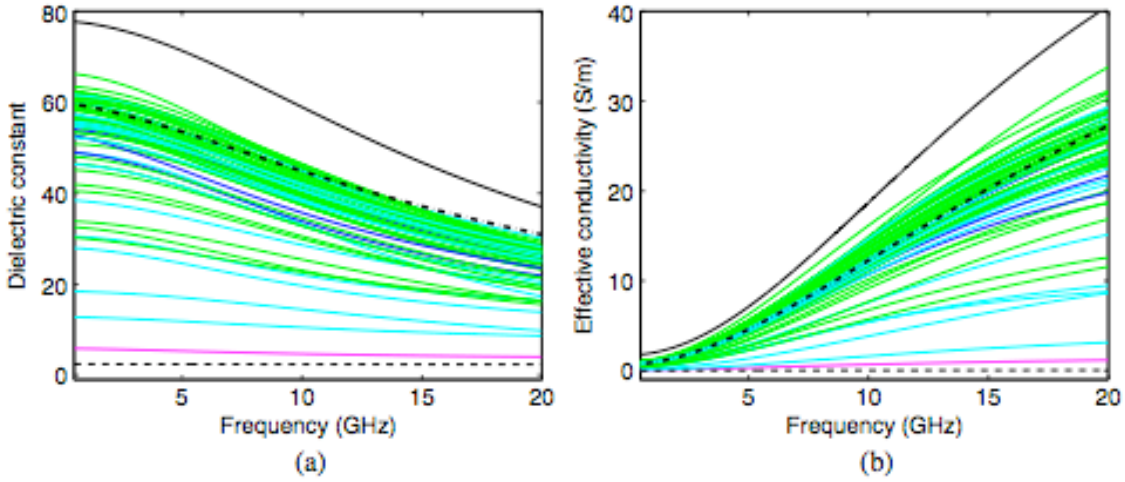

Figure 3.11: One-pole Cole-Cole fits to the 60 cancer data sets. The curves are color-coded based on the amount of adipose tissue present in each sample. The solid black (upper) curve represents the dielectric properties of saline, the dashed black (lower) curve represents the dielectric properties of lipids, and the dash-dot black (middle) curve represents the dielectric properties of blood (from [30], with permission from IOPscience).

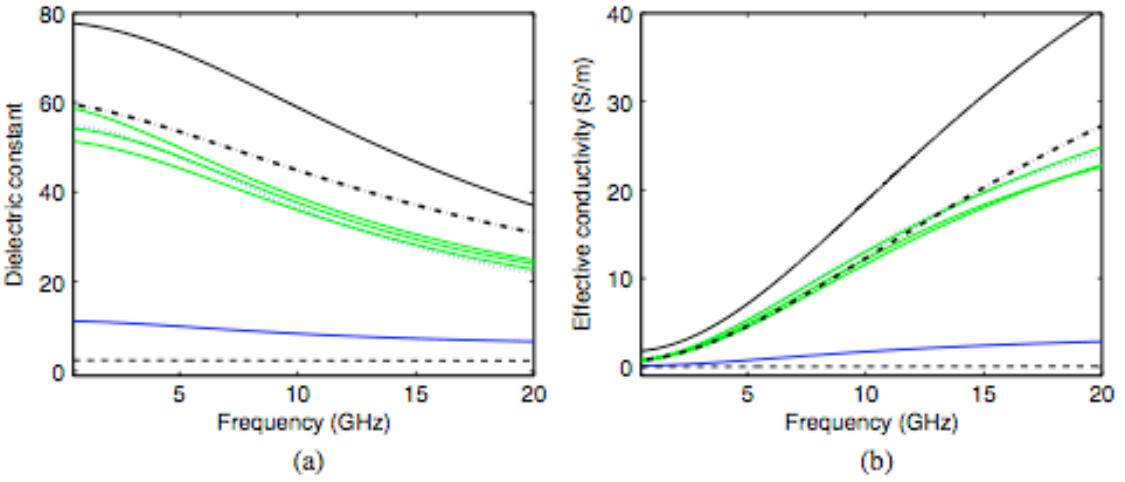

Figure 3.12: One-pole Cole-Cole fits to the five UW benign data sets (four cystic cases, solid lines, and one ductal hyperplasia case, dotted lines). The curves are color-coded based on the amount of adipose tissue present in each sample. The solid black (upper) curve represents the dielectric properties of saline, the dashed black (lower) curve represents the dielectric properties of lipids, and the dash-dot black (middle) curve represents the dielectric properties of blood (from [30], with permission from IOPscience).

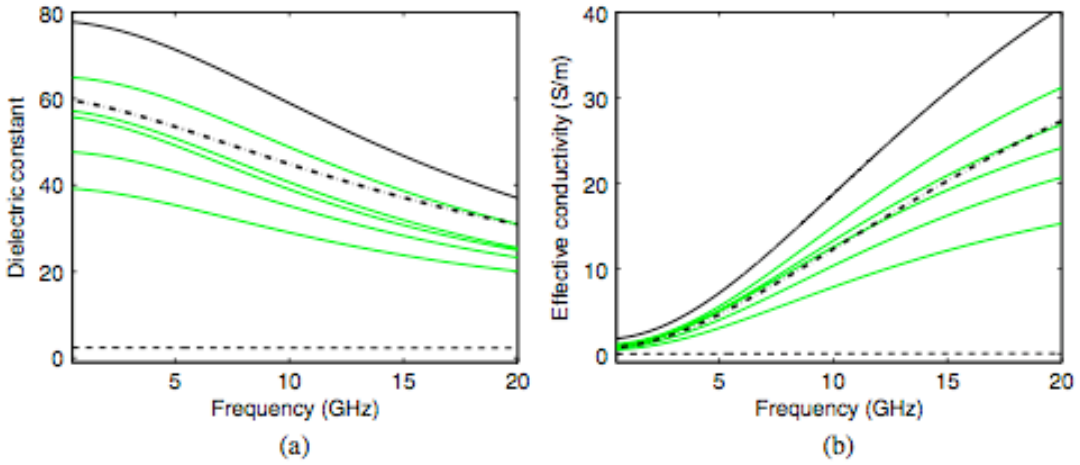

Figure 3.13: One-pole Cole-Cole fits to the five UC benign data sets (four cystic cases, solid lines, and one ductal hyperplasia case, dotted lines). The curves are color-coded based on the amount of adipose tissue present in each sample. The solid black (upper) curve represents the dielectric properties of saline, the dashed black (lower) curve represents the dielectric properties of lipids, and the dash-dot black (middle) curve represents the dielectric properties of blood (from [30], with permission from IOPscience).

The one-pole Cole-Cole curves of the 85 normal samples in this study, shown in Figure 3.10, were similar to the results of the normal samples from the breast reduction surgery study. Table 3-8, Table 3-9 and Table 3-10 show the Cole-Cole parameters of the curves corresponding to the 25th, 50th, and 75th percentiles for the three adipose-content defined groups. Figure 3.11 shows the one-pole Cole-Cole curves for the 60 cancer samples, and Figure 3.12 and Figure 3.13 show the one-pole Cole-Cole curves for the 5 UW benign samples and 5 UC benign samples, respectively. In all figures, the curves are color-coded based on the adipose tissue content of each sample. In order of highest to lowest adipose content, the colors are red, purple, blue, cyan and green. The Cole-Cole parameters of the curves corresponding to the 25th, 50th, and 75th percentiles for cancer samples containing 30% or greater malignant tissue content are shown in Table 3-11.

Table 3-8: Cole-Cole parameters for group 1 of normal samples from cancer surgeries (from [30]).

Percentile	ε_∞	$\Delta\varepsilon$	τ (ps)	α	σ_S (S/m)
25th	5.013	40.6	10.16	0.091	0.607
50th	7.237	46.0	10.3	0.049	0.808
75th	7.816	50.21	10.47	0.055	0.889

Table 3-9: Cole-Cole parameters for group 2 of normal samples from cancer surgeries (from [30]).

Percentile	ε_∞	$\Delta\varepsilon$	τ (ps)	α	σ_S (S/m)
25th	3.891	4.113	13.83	0.038	0.082
50th	6.080	19.26	11.47	0.057	0.297
75th	6.381	32.30	10.41	0.081	0.561

Table 3-10: Cole-Cole parameters for group 3 of normal samples from cancer surgeries (from [30]).

Percentile	ε_∞	$\Delta\varepsilon$	τ (ps)	α	σ_S (S/m)
25th	3.122	2.133	14.27	0.099	0.034
50th	3.581	3.337	15.21	0.052	0.053
75th	3.882	5.020	12.92	0.059	0.103

Table 3-11: Cole-Cole parameters for 49 of cancer samples from cancer surgeries that contain 30% or greater malignant tissue content (from [30]).

Percentile	ε_∞	$\Delta\varepsilon$	τ (ps)	α	σ_S (S/m)
25th	7.670	43.92	10.70	0.028	0.748
50th	6.749	50.09	10.5	0.051	0.794
75th	9.058	51.31	10.84	0.022	0.899

Figure 3.14 shows the median Cole-Cole curves for the dielectric properties of three adipose-defined tissue groups for the normal breast tissue samples obtained from reduction surgeries (dashed lines) and cancer surgeries (solid lines). The variability bars represent the 25^{th} – 75^{th} percentiles. The difference between the normal samples obtained from reduction surgeries and those obtained from cancer surgeries are attributed to two factors. First, there are 84 normal samples from the breast reduction surgeries and 16 samples from the cancer surgeries study. The median estimated from a smaller number of samples is likely to be less accurate than the median estimated from a larger number of samples. Secondly, the distribution of tissue compositions for the samples obtained from reduction and cancer surgeries are skewed. Three-fourths of all normal samples obtained from cancer surgeries contain 51% – 84% adipose tissue make up, while only half of all normal samples obtained from reduction surgeries contain 51% – 84% adipose tissue. Since all of the breast cancers considered in the study arise in the glandular tissue, the normal tissue samples characterized in cancer surgery study had higher adipose contents than the normal tissue samples characterized in the reduction surgery study because measurements collected on normal samples in cancer surgery study were away from the site of the tumor. Since more of the samples in the intermediate group obtained from cancer surgeries have higher adipose contents than the samples obtained from reduction surgeries, it is expected that the median dielectric properties of these samples is lower.

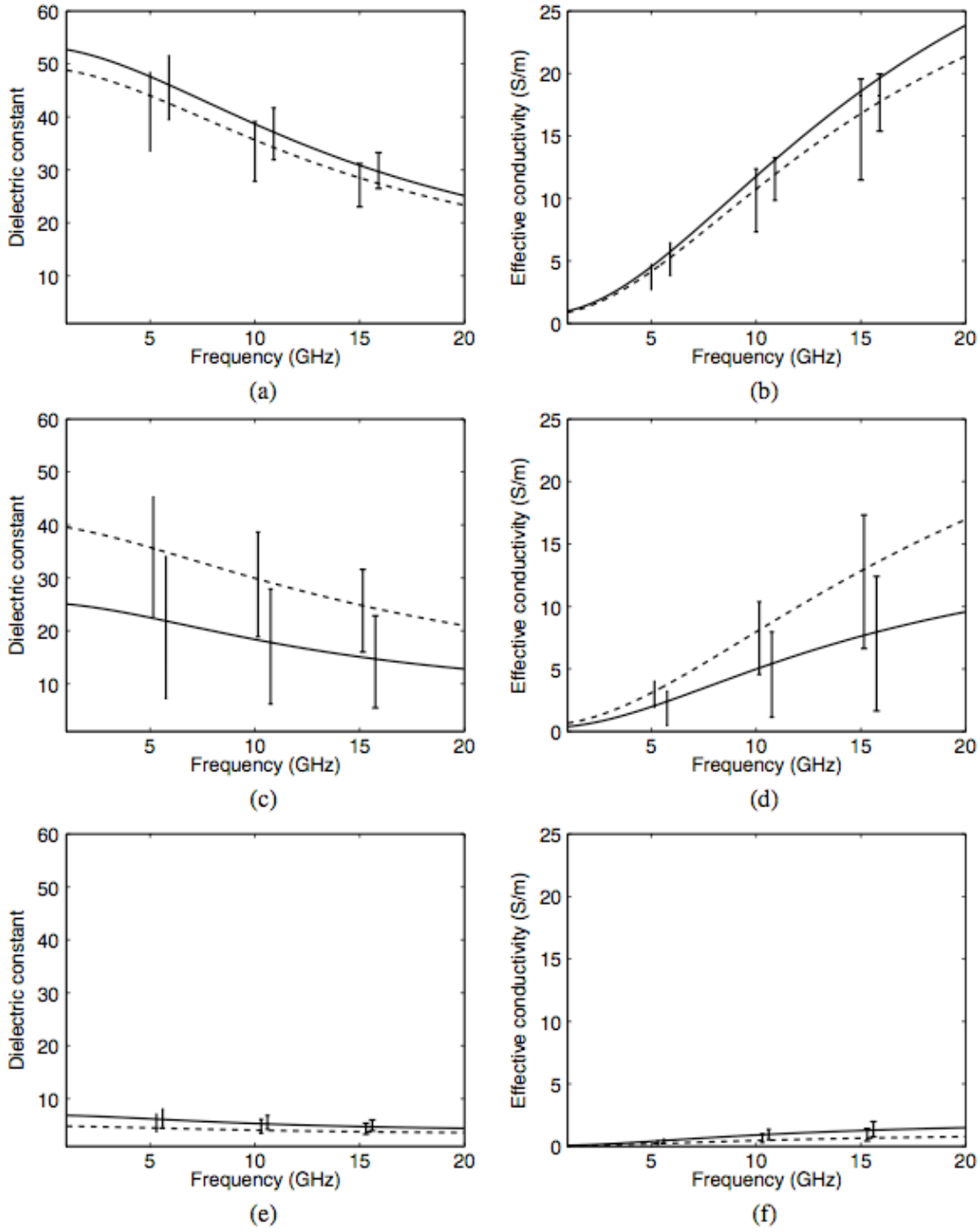

Figure 3.14: Median Cole-Cole curves for the dielectric properties of three adipose-defined tissue groups for the normal breast tissue samples obtained from reduction surgeries (dashed lines) and cancer surgeries (solid lines): (*a*) and (*b*) group 1 dielectric

constant and effective conductivity; (*c*) and (*d*) group 2; (*e*) and (*f*) group 3 (from [30], with permission from IOPscience).

Further data analysis was conducted to analyze the sources of variability in the study and to compare the dielectric properties of normal and malignant breast samples. No statistically significant differences were found in the variability due to the use of samples from different beasts and the variability due to the samples within the breast. The effect of tissue temperature on the dielectric properties of the normal samples was statistically significant. However, the temperature range of the samples in this study was relatively small and the magnitude of the change dielectric properties was small compared to the overall range of the dielectric properties of normal tissue samples. Thus this trend was deemed insignificant for engineering applications. Patient age, sample temperature and time between excision and measurement had no statistically significant trend or identifiable pattern effect on the dielectric properties.

Three statistical analysis techniques were used to compare the dielectric properties of cancer samples containing more than 30% malignant tissue with those of normal samples obtained from cancer surgeries. In the first technique, adipose tissue content was adjusted for in all samples by only comparing the mean dielectric properties of samples that contained 0 – 10% adipose content. Second, *Lazenbik et al.* adjusted for the content of both adipose and fibroconnective tissues in all samples. Finally, the mean dielectric properties of all malignant samples containing more than 30% malignant tissue with those of all normal samples were used without any adjustments. The results of this analysis indicated that the contrast in dielectric properties at the microwave frequency range between malignant breast tissue and normal adipose breast tissue can be as large as

10:1. On the other hand, the contrast in the dielectric properties between malignant breast tissue and normal fibroconnective/glandular breast tissues is no more than about 10%.

Lazebnik et al. were therefore able to create a database of the microwave-frequency dielectric properties of normal, benign and malignant breast tissues based on methodological experimentation and systemized data analysis. The provided compact Cole-Cole representation of the wideband dielectric properties of breast tissues allows for these numerical models to be readily and accurately incorporated into numerical and experimental breast phantoms used in the development of microwave breast cancer detection systems. The authors have also determined that the measured dielectric properties in both studies in [29] and [30] agree well with previously published data.

Because the one-pole Cole-Cole dispersion model in [29] and [30] has a high computational complexity when embedded into the finite-difference time-domain (FDTD) method, *Lazebnik et al.* [31] decided to investigate the accuracy of simpler one- and two-pole Debye models for fitting the data they measured in [30]. The Debye model is defined as:

$$\varepsilon_d^*(\omega) = \varepsilon_\infty + \sum_{n=1}^{N} \frac{\Delta\varepsilon_{d,n}}{1 + j\omega\tau_n} + \frac{\sigma_i}{j\omega\varepsilon_0} \tag{9}$$

where N is the number of poles and the subscript d refers to "Debye." One- and two-pole Debye models were fit to the original single-pole Cole-Cole model in equation (7) from 0.5 GHz to 20 GHz. In addition, single-pole Debye models were fit to the data from 3.1 GHz to 10.6 GHz. This fitting was accomplished by minimizing the error function

$$e = \frac{\sum_{i=1}^{M} \left(\frac{\varepsilon'_{i,c}(\omega) - \varepsilon'_{i,d}(\omega)}{\text{median}[\varepsilon'_{i,d}(\overline{\omega})]} \right)^2 + \left(\frac{\varepsilon''_{i,c}(\omega) - \varepsilon''_{i,d}(\omega)}{\text{median}[\varepsilon''_{i,d}(\overline{\omega})]} \right)^2}{M} \tag{10}$$

where M is the number of frequency points used in the fit (M = 104 for both frequency ranges). ε_{dn} and τ_{dn} were allowed to vary while σ_i and ε_∞ were kept constant. The errors in the real and imaginary parts of the complex permittivity were also calculated as

$$\begin{aligned} e_r(\omega) &= \varepsilon'_c(\omega) - \varepsilon'_d(\omega) \\ e_i(\omega) &= \varepsilon''_c(\omega) - \varepsilon''_d(\omega) \end{aligned} \tag{11}$$

where $\varepsilon^*_c(\omega) = \varepsilon'_c - j\varepsilon''_c$ is the complex permittivity from the single-pole Cole-Cole model. The total error e and the frequency-dependent errors in the real and imaginary parts, $e_r(\omega)$ and $e_i(\omega)$, were computed as a function of N, and used to determine the number of poles required in the Debye model for the frequency range of interest.

The one- and two-pole Debye model parameters for the three adipose-defined normal breast tissues and the malignant breast tissues are given in Table 3-12 (*a*) and (*b*), respectively. For both models, the values of ε_∞ are: 7.82 (group 1), 5.57 (group 2), 3.14 (group 3), and 6.75 (malignant), and the values of σ_s are: 0.71 S/m (group 1), 0.52 S/m (group 2), 0.036 S/m (group 3), and 0.79 (malignant). Figure 3.15 (*a*) and (*b*) show the errors in the real and imaginary parts of the relative permittivity from 0.5 to 20 GHz for the three adipose-defined normal tissue groups as defined in equation (11) for the one- and two-pole Debye models, respectively. The maximum errors for the one-pole Debye fit for groups 1 and 2 are no greater than about two units of the real part of the relative

permittivity and one unit of the imaginary part. For the two-pole Debye models, the maximum errors are less than approximately 0.5 units. Similar errors were obtained for the malignant tissue properties. Figure 3.15 (*c*) shows the errors for the one-pole Debye models for the three adipose-defined normal tissue groups in the frequency range from 3.1GHz to 10.6 GHz. Table 3-13 shows the total error as defined in equation (10) for the three adipose-defined normal breast tissues and the malignant breast tissues of the one-pole (N = 1) and the two-pole (N = 2) Debye models. Therefore, *Lazebnik et al.* demonstrated that, for normal and malignant breast tissues, a two-pole Debye model could be used to replace the one-pole Cole-Cole model in the frequency range from 0.5 GHz to 20 GHz, while a one-pole Debye model is sufficient for the frequency range from 3.1 GHz to 10.6 GHz [31]

Table 3-12: Parameters of (*a*) 0.5 – 20 GHz one- and two-pole Debye models and (*b*) 3.1 – 10.6 GHz one-pole Debye model for normal tissue groups 1, 2 and 3 (N1, N2, N3) and malignant tissue group (M) (from [31]).

(a)	**N1**	**N2**	**N3**	**M**
$\Delta\varepsilon_d$	39.80	32.08	1.60	47.91
τ_d **(ps)**	10.28	8.68	13.56	10.10
$\Delta\varepsilon_{d1}$	20.81	19.64	0.58	25.61
$\Delta\varepsilon_{d2}$	20.22	14.23	1.09	23.91
τ_{d1} **(ps)**	7.39	5.81	8.07	7.22
τ_{d2} **(ps)**	15.18	16.49	19.25	15.30

(b)	**N1**	**N2**	**N3**	**M**
$\Delta\varepsilon_d$	40.14	32.56	1.61	48.35
τ_d **(ps)**	10.62	9.24	14.11	10.47

Table 3-13: Total error, e ($\times 10^{-4}$), for one-pole (N = 1) and two-pole (N = 2) Debye model approximations of the dielectric properties of groups 1, 2 and 3 of normal breast tissues: N1, N2 and N3 and of malignant tissue, M3 (from [31]).

	N1	**N2**	**N3**	**M**
***N* = 1 (0.5-20 GHz)**	11.2	43.2	19.1	13.5
***N* = 2 (0.5-20 GHz)**	0.23	0.90	0.49	0.28
***N* = 1 (3.1-10.6 GHz)**	4.64	17.8	8.01	5.55

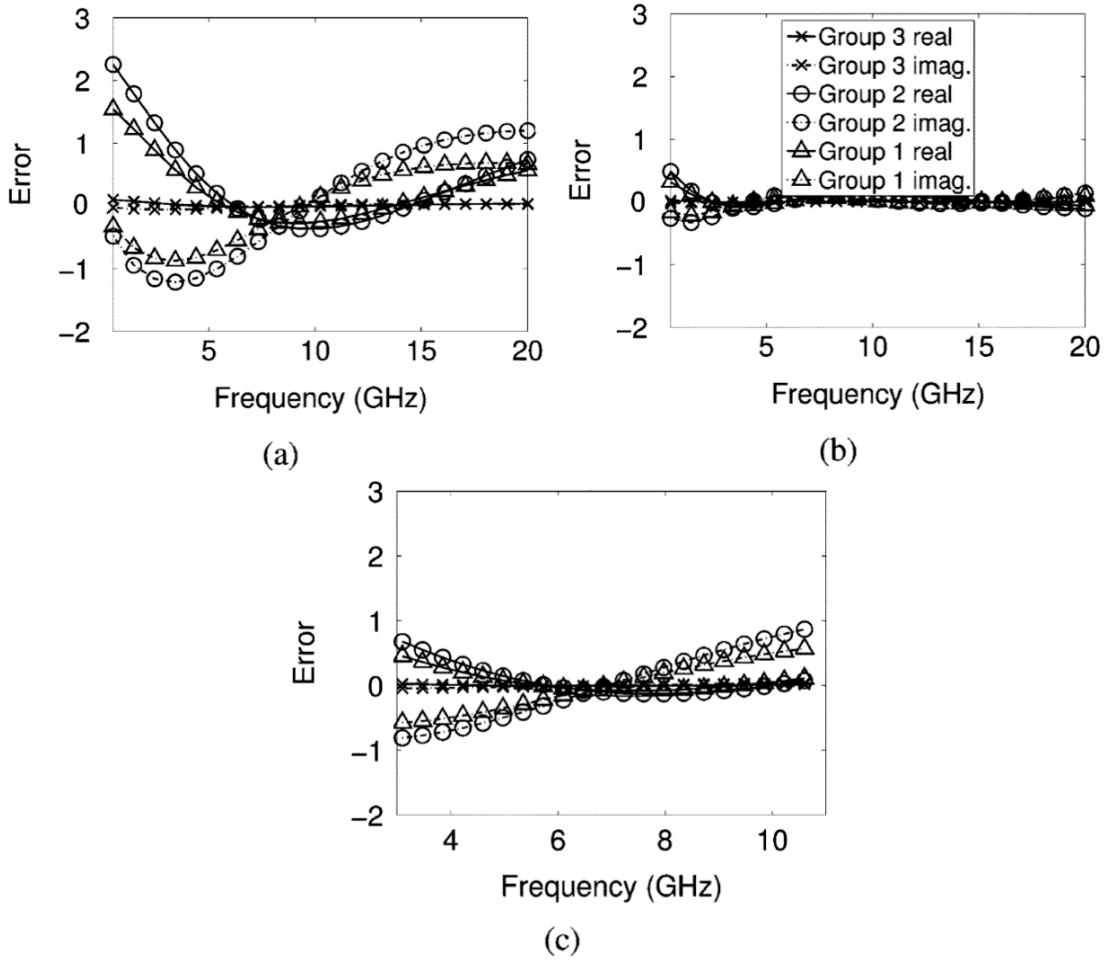

Figure 3.15: Errors in the real and imaginary parts of the complex dielectric constant for the three adipose-defined tissue groups for (*a*) one- and (*b*) two-pole Debye models 0.5–20 GHz, and (*c*) one-pole Debye models from 3.1–10.6 GHz (from [31]).

Halter *et al.* performed *in vivo* measurements of the dielectric properties of breast tissue during mastectomy procedures in the operating room followed by *ex vivo* measurements on the same freshly excised breast tissue over the frequency range 100 Hz–8.5 GHz in order to compare the results and to validate electromagnetic breast imaging. The study involved recording the dielectric properties of the breast tissue using three procedures: (i) *in vivo* electromagnetic (EM) imaging, (ii) *in vivo* point dielectric spectroscopy probing and (iii) *ex vivo* point dielectric spectroscopy probing. Four dielectric probes were used in this study: (i) an *in vivo* electrical impedance spectroscopy (EIS) probe, (ii) an *ex vivo* EIS probe, (iii) an *in vivo* microwave impedance spectroscopy (MIS) probe and (iv) and *ex vivo* MIS probe. Data was recorded from the six patients. 15 *ex vivo* dielectric spectra were recorded using the EIS probe and ten dielectric spectra with the MIS probe. The tissue types probed by EIS included ten intraductal carcinoma (IDCa) mixed with ductal carcinoma in situ (DCIS), one DCIS, one adipose and three fibrocystic disease (FCD), while those probed by MIS included six IDCa mixed with DCIS, one DCIS, one adipose, and two FCD.

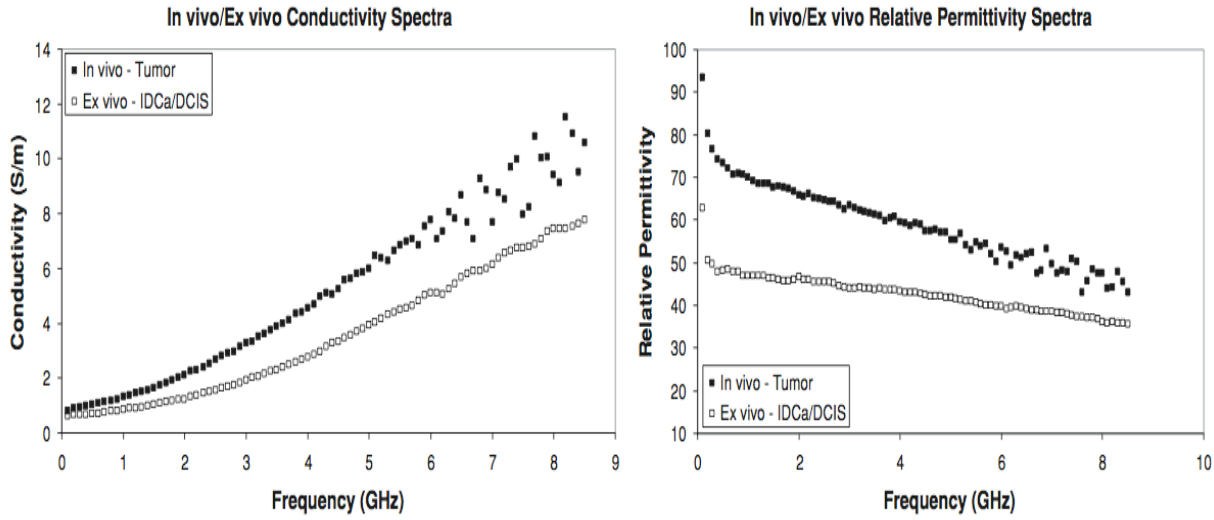

Figure 3.16: *In vivo* versus *ex vivo* average MIS dielectric spectra (from [32], with permission from IOPscience).

The difference between *in vivo* and *ex vivo* MIS measurements is illustrated in Figure 3.16. *Ex vivo* relative permittivities and effective conductivities were less than their *in vivo* counterparts for both the low frequency (EIS) measurements and the high frequency (MIS) measurements. Specifically, the conductivity decreased by 36, 39 and 20% at 1, 4 and 8.5 GHz, respectively, while the relative permittivity decreased by 33, 27 and 21% at the same frequencies. These changes arise from the decrease in temperature and from the metabolic breakdown of cellular regulation after tissue excision. Metabolic resources are also depleted when the tissue is devascularized which leads to cellular swelling and a decreased volume of extracellular fluid available for current flow. This study is crucial because the largest property changes in tissue occur immediately following its removal and stabilize over hours, with comparably small changes occurring 5 minutes to 5 hours after excision, the period in which Lazebnik *et al*. [29],[30] conducted their *ex vivo*

measurements. Therefore, further investigations need to be performed in correlating *in vivo* and *ex vivo* dielectric properties of breast tissues [32].

3.3 TEMPERATURE-DEPENDENT DIELECTRIC PROPERTIES OF TISSUES

A number of studies have reported the dependence of the dielectric properties of tissues on temperature [3],[5],[35]-[45], in order to facilitate the development of microwave technologies such as UWB microwave breast cancer detection and hyperthermia treatment. Similar studies have been conducted for the temperature effects in the dielectric properties of meats [12],[46]-[48], in order to predict how they behave in a microwave oven, and of tumors [49],[50], to predict how they behave under hyperthermia and ablation procedures. However, as shown in Table 3-14, most of the measurements in these studies are performed at discrete frequencies and varying temperatures with the final results presented as linear temperature coefficients (percent change in permittivity or conductivity per degree Celsius).

Table 3-14: Chronological summary of published temperature-dependent dielectric properties of tissues (from [45]).

Tissue Type	Frequency Range	Temperature coefficient (% C)	Reference
Various Tissues	50, 200, 400, 900 MHz	See reference	[35]
Biological Tissues (not specified)	Microwave (not specified)	$\frac{\Delta\sigma}{\sigma}$= 2, $\frac{\Delta\varepsilon}{\varepsilon}$= -0.5	[5]
Brain	<0.1 GHz <2 GHz 7 GHz	$\frac{\Delta\sigma}{\sigma}$= 2, $\frac{\Delta\varepsilon}{\varepsilon}$= 2 $\frac{\Delta\sigma}{\sigma}$= 2, $\frac{\Delta\varepsilon}{\varepsilon}$: small $\frac{\Delta\sigma}{\sigma}$= -1, $\frac{\Delta\varepsilon}{\varepsilon}$=: small	[36]
Biological Tissues (not specified)	Microwave (not specified)	$\frac{\Delta\sigma}{\sigma}$=: varies from 1 to 2 $\frac{\Delta\varepsilon}{\varepsilon}$: varies from -0.3 to 2	[3]
Biological Tissues (not specified)	Microwave (not specified)	~2	[37]
Barnacle muscle fibres	0.1, 2.2, 9.5 GHz	$\frac{\Delta\sigma}{\sigma}$: 2 to -2 Cross-over point near 2 GHz $\frac{\Delta\varepsilon}{\varepsilon}$=: small	[38]
Myocardium	0.2, 1.1, 2.5 3.0, 4.0, 5.0, 6.0, GHz	See reference	[40]
Bovine Liver	915 MHz	$\frac{\Delta\sigma}{\sigma}$= 1.82±0.28, $\frac{\Delta\varepsilon}{\varepsilon}$= -0.13±0.059	[41]
Animal and human liver	0.3–3 GHz	Porcine $\frac{\Delta\sigma}{\sigma}$= 1.1, $\frac{\Delta\varepsilon}{\varepsilon}$= -0.17 Bovine: $\frac{\Delta\sigma}{\sigma}$= 2.0, $\frac{\Delta\varepsilon}{\varepsilon}$= -0.04	[43]
Rat prostate	915 MHz	$\frac{\Delta\sigma}{\sigma}$= 1.10±0.11 $\frac{\Delta\varepsilon}{\varepsilon}$= -0.31±0.05	[44]

Temperature-Dependent Dielectric Properties of Tissues – Relevant Study 1 [45]

Linear temperature coefficients at discrete frequencies are impractical for UWB applications because the dielectric properties need to be available at every frequency and temperature in the range of interest. Moreover, according to *Lazebnik et al.* [45], it is not clear that linear temperature coefficients are sufficient for all temperatures and frequencies. As a result, *Lazebnik et al.* demonstrate a novel method to characterize the temperature-dependent dielectric properties of animal liver in the frequency range of 0.5 GHz to 20 GHz. They report their data in a compact manner that allows the estimation of the dielectric properties at any frequency and temperature. A single-pole Cole-Cole model of the form:

$$\varepsilon^*(\omega) = \varepsilon_\infty + \frac{\Delta\varepsilon}{1+(j\omega\tau)^{1-\alpha}} + \frac{\sigma_i}{j\omega\varepsilon_0} \tag{12}$$

was used to fit the dielectric properties as a function of frequency, and a second-order polynomial:

$$\begin{aligned} \varepsilon_\infty(T) &= A_1T^2 + B_1T + C_1 \\ \Delta\varepsilon(T) &= A_2T^2 + B_2T + C_2 \\ \tau(T) &= A_3T^2 + B_3T + C_3 \\ \sigma_i(T) &= A_4T^2 + B_4T + C_4 \end{aligned} \tag{13}$$

where T is the temperature and A_n, B_n and C_n are fitting parameters, was used to fit the Cole-Cole parameters as a function of temperature. Sipahioglu *et al.* [48] noted the quadratic behavior by measuring the dielectric properties of various meats as a function

of temperature. This trend may possibly be explained by the fact that the total dielectric loss is a sum of ionic and dipole losses, and since the dipole loss decreases with temperature, and the ionic loss increases with temperature, the total dielectric loss will first decrease then increase with temperature [48]. Measurements were performed starting at room temperature to about 60 °C.

Materials and Experimental Setup

Liver was chosen as a representative high-water content tissue since previous studies have shown that there is little inter-species difference between the dielectric properties of tissues. In this study, thirteen 5 × 10 × 3 cm samples from 7 livers (6 bovine and 1 porcine) were used. Bovine and porcine tissues were used because of their ease of accessibility. Measurements started within 2 hours of excision. To avoid excessive desiccation, each sample was wrapped in aluminum foil leaving only the top surface exposed. An acrylic plate with holes for the measurement probes covered about 75% of the exposed top surface. The experimental setup is illustrated in Figure 3.17. According to the authors, it is assumed that soon after excision, cell death is insignificant. There is however some fluid loss, as well as changes in oxygen tension, pH and temperature. Of these, only fluid loss and temperature have an effect on the dielectric properties at microwave frequencies. The authors claim that their experimental conditions aim to decrease the difference between their *ex vivo* measurements and possible *in vivo* results. They also argue that since their experimental conditions were controlled to prevent excessive fluid loss, the temperature change would be the only dominant effect on the *ex vivo* tissue dielectric properties.

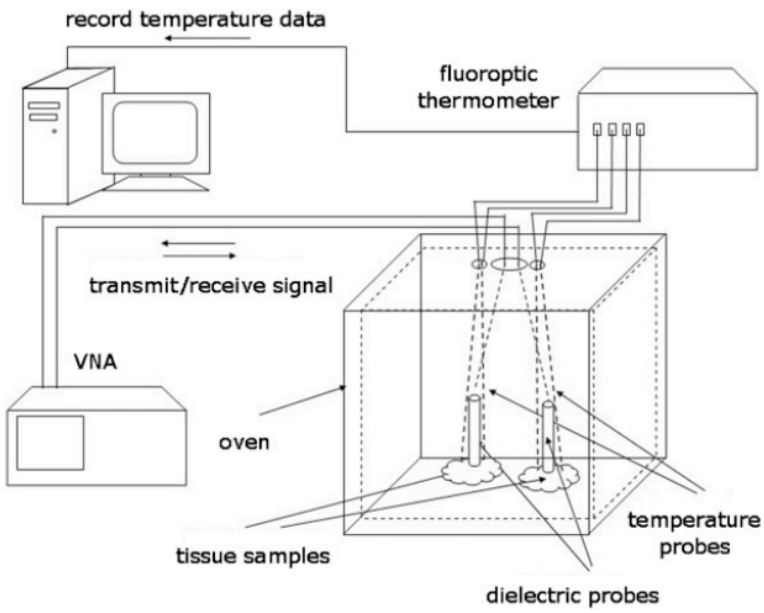

Figure 3.17: Diagram of the experimental setup for two samples simultaneously (from [45], with permission from IOPscience).

Data Recording

Measurements of tissue temperature and dielectric properties over the frequency range were recorded every 5 minutes during a heating and a cooling phase. Heating the samples was performed using the oven, while in the cooling phase the samples were allowed to cool back to room temperature. Tissue temperature in the area under the probe was assumed to be equal to the average of the two surrounding temperature probes. Approximately half of the samples were heated to about 37 °C (body temperature) and the other half was heated to 60 °C. Data was recorded at 401 frequency points and approximately 30 different temperatures.

Heating and Cooling Cycles

There were distinct and repeatable differences between the dielectric properties measured during the heating cycle and those measured during the cooling cycle. The permittivities and conductivities measured at different temperatures during the cooling cycle were well-behaved, easily fit to the Cole-Cole model and consistent with expected results. On the other hand, measurements performed during the heating cycle had unexpected but repeatable anomalies that were not amenable to modeling by the Cole-Cole equation. The consistency of these anomalies lead to the hypothesizing that they are a consequence of non-equilibrium effects in the tissue that occur during the heating cycle but not during the cooling cycle. Chin and Sherar [41] have also claimed that irreversible structural changes occur during tissue heating but these are negligible during tissue cooling. However, *Lazebnik et al.* have argued that irreversible structural changes that occur below around 60°C are not expected to affect the tissue's dielectric properties. This was demonstrated by conducting experiments in which the tissue was heated to ~40 °C, cooled to ~25 °C, reheated to ~60 °C, and cooled back down to room temperature. Since the dielectric properties measured during both cooling and heating transients, including the same anomalies, were repeatable, the authors concluded that: (i) the processes occurring during the heating cycle that produce the anomalous dielectric properties measurements are not due to irreversible structural changes of the tissue, and (ii) those same processes are absent during the cooling cycle. Therefore, *Lazebnik et al.* were not able to explain the heating cycle and only the results from the cooling cycle were reported.

Results

The experimental data of the liver dielectric properties and their Cole-Cole fits are shown at three distinct temperatures in Figure 3.18. The plots demonstrate that the one-pole Cole-Cole fit is sufficient to model this experimental data. The plots also show that the temperature trend of the complex permittivity changes over frequency. There are also 'cross-over' points, which are the frequencies where the permittivity and conductivity do not change with temperature. The dielectric constant curve has a cross-over point at about 4 GHz. Below this point, the permittivity decreases slowly as temperature increases. Above the cross-over point, the relative permittivity increases with a higher rate as temperature increases. The conductivity curve shows two cross-over points: one near 2–3 GHz and one near 16 GHz. Below the first cross-over point, the conductivity increases slowly as temperature increases. Between the two cross-over points the conductivity decreases as temperature increases. Above about 15 GHz, the conductivity again increases as temperature increases. These trends are consistent with those of water [51].

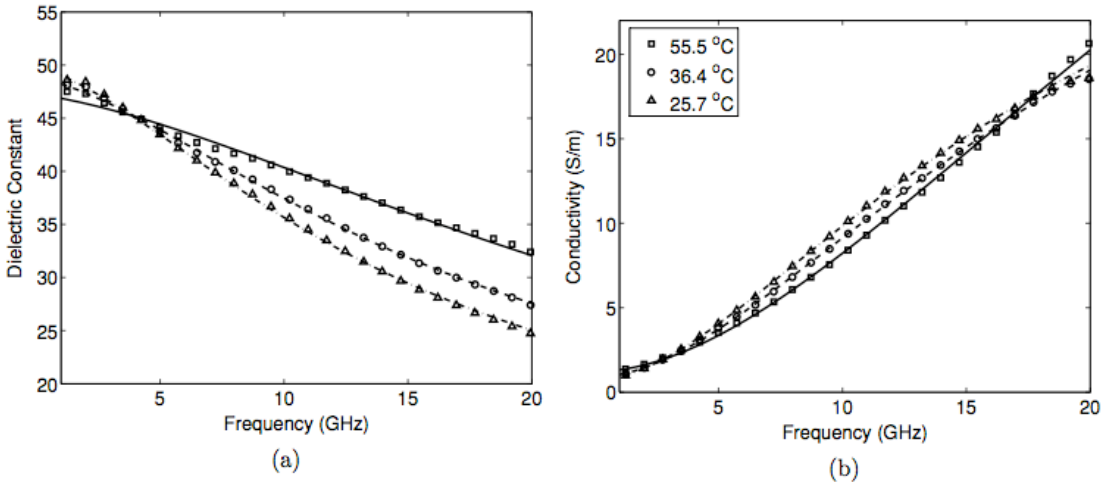

Figure 3.18: Example of (*a*) dielectric constant and (*b*) conductivity of liver tissue as a function of frequency at three temperatures. The symbols and the lines represent the experimental data and their one-pole Cole-Cole fits, respectively (from [45], with permission from IOPscience).

Wideband Analysis

A single-pole Cole-Cole model was used to fit the dielectric properties as a function of frequency, and a second-order polynomial was used to fit the Cole-Cole parameters as a function of temperature. A single-pole Cole-Cole model was used because only one pole with a pico-second-time-constant dominates the tissue dielectric response over the frequency range of interest. A MATLAB fitting function that performs the Nelder-Mead direct search optimization was used to fit the data at each temperature for each experiment to the single-pole Cole-Cole model in equation (12) over the frequency range from 0.5 GHz to 20 GHz. It was assumed that α, which is an empirical parameter that accounts for the observed broad distribution of relaxation time constants in tissue, does not change with temperature and is consistent with the value of 0.1 reported by Gabriel *et al*. [17] for liver. Limits were set on the parameters so that they would remain within

physical ranges (e.g., a lower bound of 1 on ε_∞). A MATLAB function that performs a least-squares polynomial fit was used to fit the 'super-set' of the Cole-Cole parameters from all experiments to the second-order polynomials in (13). The temperature-dependent Cole–Cole parameters for the cooling cycles of all experiments are shown in Figure 3.19 (*a*)–(*d*). The circles represent the Cole-Cole coefficients of a fit of a measurement to a single-pole Cole-Cole function. The solid curves are the quadratic fits to the 'super-set' of the parameters from all experiments. Therefore, the quadratic curves represent an average fit to all the temperature-dependent Cole-Cole parameters. The quadratic coefficients corresponding to the solid curves in Figure 3.19 (*a*)–(*d*) are shown in Table 3-15. In addition, Figure 3.19 (*e*) and (*f*) show the difference between the raw data and the reconstructed data obtained by using the second-order polynomials. The differences are expressed as absolute differences rather than percents because the conductivity values are very small at low frequencies possibly resulting in very large, though insignificant, percent errors. The maximum difference due to the reconstruction was approximately 5.6 units for permittivity and 5.4 S/m for conductivity.

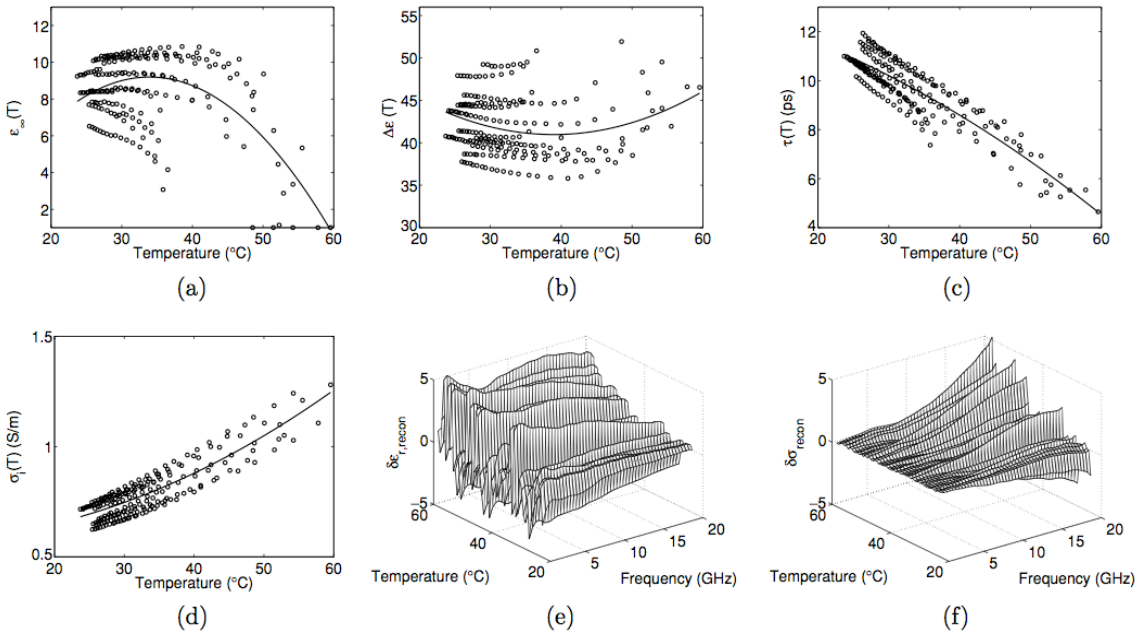

Figure 3.19: Cole-Cole parameters as a function of temperature (O), and quadratic fits (solid lines) to (*a*) ε_∞, (*b*) $\Delta\varepsilon$, (*c*) τ, and (*d*) σ_i. Differences as a function of frequency and temperature between the reconstruction and measured data for (*e*) dielectric constant and (*f*) conductivity (from [45], with permission from IOPscience).

Table 3-15: Coefficients of the quadratic fits to the temperature-dependent Cole-Cole parameters (from [45], with permission from IOPscience).

	n	A_n	B_n	C_n
ϵ_∞	1	−0.0127	0.8610	−5.4119
$\Delta\epsilon$	2	0.0115	−0.8933	58.3598
$\tau(\times 10^{-12})$	3	−0.0014	−0.0640	13.3749
$\sigma_i(\times 10^{-2})$	4	0.0185	0.0349	56.9673

Comparison with Data from Gabriel et al. for Liver [17]

The difference between the experimental data and the Cole-Cole fit presented in Gabriel *et al.* for a variety of animal and human tissues, including liver, is on the order of 1–10 units for permittivity and 1–10 S/m for conductivity, over the frequency range of

interest. As a result, the differences of approximately 5.6 units for permittivity and 5.4 S/m for conductivity reported by *Lazebnik et al.* were deemed reasonable. Table 3-16 shows the one-pole Cole-Cole parameters of *Lazebnik at al.* compared with the most relevant pole of the four-pole Cole-Cole fit presented by Gabriel *et al.* The two sets are reasonably comparable with two main differences: (i) Gabriel *et al.* set ε_∞ to 4.0, while *Lazebnik et al.* used it as a fitting parameter and (ii) since Gabriel *et al.* used a four-pole Cole-Cole model to fit their data over a very wide frequency range, the value of σ_i, which is an inherently DC quantity, is very different.

Table 3-16: Comparison between the Cole-Cole parameters at 37°C of *Lazebnik et al.* [45] (our data) and of Gabriel *et al.* [17] for liver (from [45], with permission from IOPscience).

	Our data	Gabriel data
ϵ_∞	9.1	4.0
$\Delta\epsilon$	41.1	39.0
$\tau(\times 10^{-12})$	9.09	8.84
σ_i	0.84	0.02

Single-Frequency Analysis

Lazebnik *et al.* also calculated linear temperature coefficients at 915 MHz and 2.45 GHz separately for the heating and cooling cycles. This analysis proved that linear temperature coefficients are not appropriate over large temperature ranges. Average linear coefficients for both the heating and cooling cycles were also found to be within the range of data presented in previous literature [45].

Temperature-Dependent Dielectric Properties of Tissues – Relevant Study 2 [53]

Microwave tumor ablation systems aim to remove the tumor cells by heating it with microwave power delivered by antennas. This procedure is also known as hyperthermia. The development of these systems is largely dependent on numerical simulations. However, these simulations can fall short of the actual systems because of the lack of accurate numerical models that describe the dielectric behavior of the target tissue with the changes induced by the ablation procedure. Changes in temperature, cellular makeup and water content during thermal ablation affect the dielectric properties of the tissue. Also, according to Brace [53], most temperature measurements include tissue samples that are immersed in saline or placed in a closed system to prevent dehydration. Such methods neglect the phenomena that occur during ablation, which includes water vaporization and dehydration.

Materials, Experimental Setup and Data Recording

Brace [53] measured the relative permittivity and the conductivity of five bovine livers from different animals from 5 to 100 °C over the frequency range from 500 MHz to 5 GHz. The excised organs were directly cooled and stored at 5 °C until measurement time, which was 2 to 48 hours post excision. Tissue samples were approximately 10 × 10 × 10 cm. Unlike in previous studies, no attempt was made to inhibit water transport, dehydration or otherwise adjust tissue water content during the measurement process. Therefore, measurements were allowed to reflect changes induced both by cellular breakdown and water vaporization. Complex reflection coefficients measured using an

open-ended coaxial probe technique with open, short and water calibration were used to calculate the dielectric permittivity and the conductivity of the sample. A clinical multiple-electrode RF ablation system that delivers energy at 500 kHz was used to heat the tissue. Temperature at the coaxial probe tip was measured using a fiber optic temperature probe that does not interfere with the ablation or the measurement systems. Measurements were taken several times before heating the sample. They were then recorded at 10-second intervals for the first minute of ablation, 15-second intervals for the next 2-minutes and 30-second intervals thereafter. Total ablation time was 10 minutes. Measurements were taken at 1-minute intervals after ablation until the tissue temperature returned to 35 °C. Water content in ablation zones and normal liver were also measured for comparison. The mean reflection coefficients from the five measured liver samples was used to calculate the relative permittivity and conductivity at each temperature and frequency points.

Results

Both the relative permittivity and the conductivity dropped sharply as temperatures approached 100 °C, and continued to decrease with exposure time as in Figure 3.20. These decreases are a result of both irreversible thermal damage (protein denaturation) and local tissue dehydration. However, the fact that property changes were not substantial until nearly 100 °C was achieved supports the hypothesis that measured changes are due primarily to dehydration. Protein denaturation occurs at ~60 °C and significant effects caused by protein denaturation should have been evident in the 60 – 80 °C range. Even

though measured data supports this hypothesis, additional tests are still needed to identify any correlations.

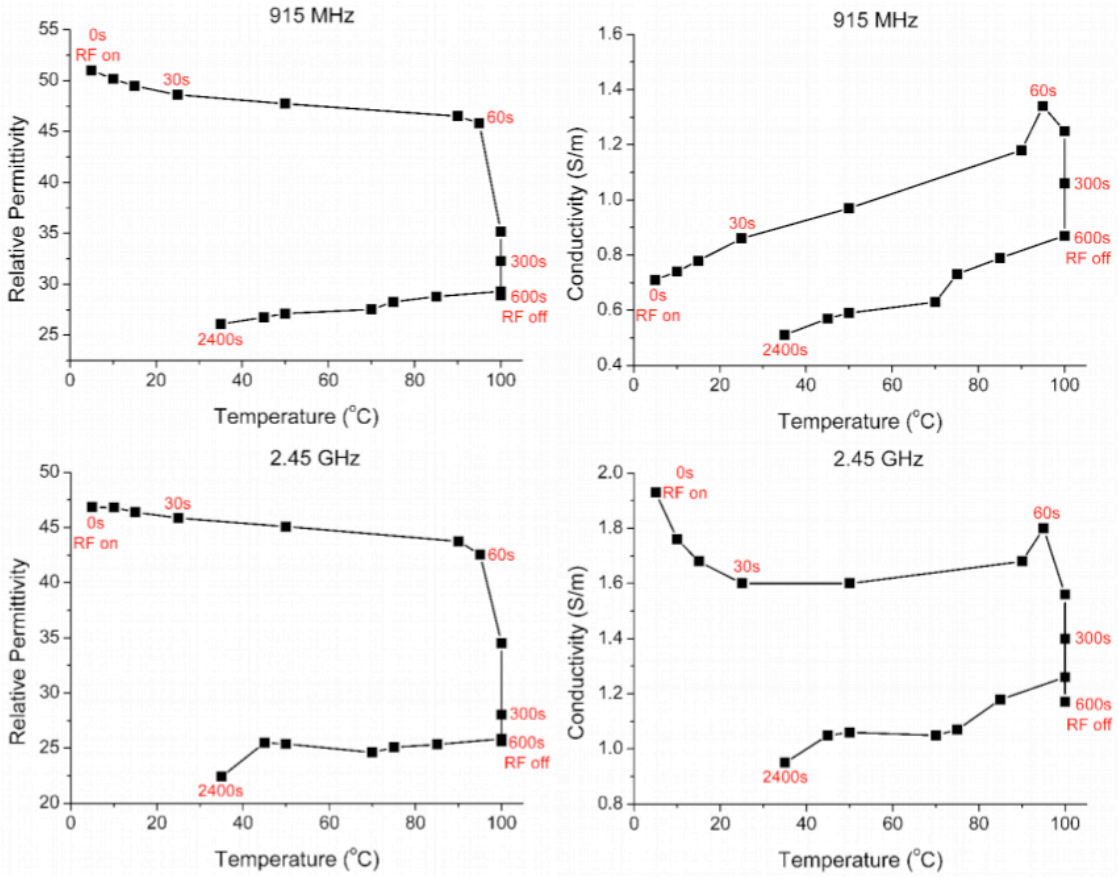

Figure 3.20: Relative permittivity and conductivity measurements made at 915 MHz and 2.45 GHz during thermal ablation. Accumulated ablation times noted on each figure to identify temporal variations (from [53]).

Once heating was removed, both the relative permittivity and the conductivity continued to decrease slightly over time. As shown in Figure 3.21, these changes in properties are irreversible, likely due to permanent cellular damage caused by temperatures near 100 °C and dehydration inside the ablation zone. Post ablation measurements of the ablation zone confirmed that water content near the measurement

point was around 25% less than its original value. Additional dehydration caused by microwave heating is expected to create more difference between pre- and post-ablation measurements.

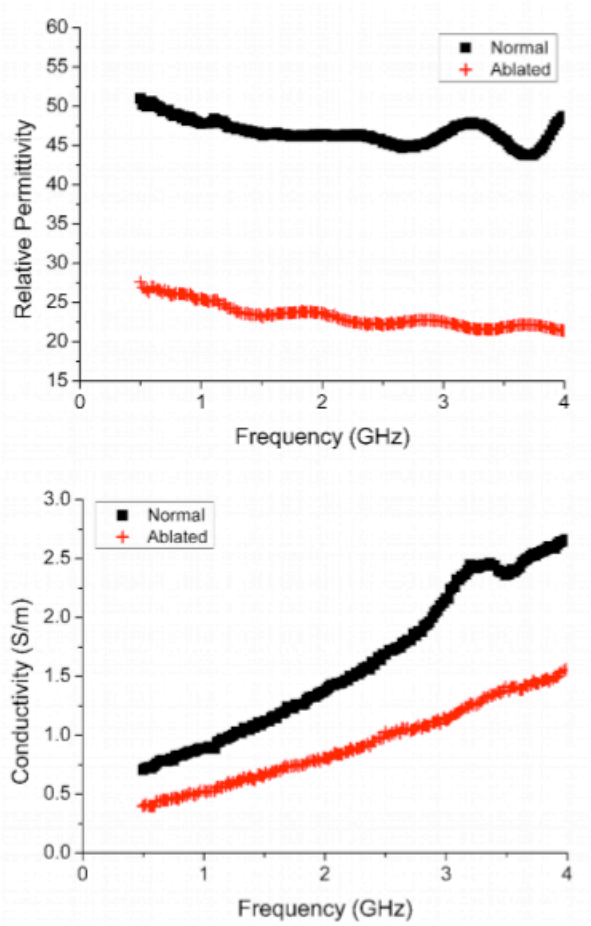

Figure 3.21: Frequency dependence of the dielectric properties of normal tissue at 35 °C and ablated tissue cooled to 35 °C (from [53]).

The measured dielectric permittivity and conductivity values at 37 °C in [53] matched well with data from previous studies as shown in Table 3-17. The linear temperature coefficients also agreed well with the previously published data, as shown in Table 3-18, with the exception of the conductivity coefficient at 2.45 GHz. The

coefficients in the 2 – 4 GHz range followed this same trend. So, the author is unsure whether this discrepancy with previous data is aberrant or is caused by differences in the heating techniques. The 5 – 25 °C measurements account for the negative temperature coefficient. When only the 30 – 50 °C measurements are considered, the temperature coefficient at 2.45 GHz is nearly zero. This result is consistent with the "cross-over" region of near-zero temperature dependence reported by Lazebnik *et al.* [45]. Temperature coefficients were also slightly lower than in previous studies; however, the author is unclear whether this observation is significant. Such differences could be due to local water transport, either from dehydration or internal pressure gradients. However, this hypothesis is speculative since significant dehydration, causing a decrease in permittivity and conductivity, is not expected until temperatures reach above 90 °C. Brace [53] concludes that approximated linear temperature coefficients are sufficient to describe the temperature-dependent changes in the dielectric properties of tissues when temperatures are not expected to rise significantly above 60 °C. However, these linear coefficients are insufficient to predict the changes that occur during high-temperature thermal ablation.

Table 3-17: Dielectric properties comparison at 37 °C (from [53]).

Frequency	ε_r	σ	Reference
915 MHz	48.0	0.94	This work [53]
2.45 GHz	45.3	1.62	
915 MHz	49.5	0.99	Lazebnik *et al.* [45]
2.45 GHz	47.6	1.77	
915 MHz	46.76	0.86	Gabriel *et al.* [18]
2.45 GHz	43.04	1.69	

Table 3-18: Temperature coefficients comparison (5–50 °C) (from [53]).

Frequency	ε_r	σ	Reference
915 MHz	-0.22	1.29	This work [53]
2.45 GHz	-0.18	-0.2	
915 MHz	-0.2	1.33	Lazebnik *et al.* [45]
2.45 GHz	-0.17	0.2	
915 MHz	-0.2	1.4	Duck [52]
2.45 GHz	-0.1	0.2	

The lack of temperature data above 100 °C as well as the small number of samples and the exclusive use of *ex vivo* samples are the limitations of this study. Brace [53] states that similar results would be expected for *in vivo* measurements of tissue properties during ablation. Additional measurements are required to validate his results and confirm this statement.

Temperature-Dependent Dielectric Properties of Water and Saline

Since the dielectric properties of tissue at frequencies above 1 GHz reflect the dielectric relaxation of tissue water and water content governs these properties, the temperature dependence of the dielectric properties of water and saline need to be reviewed as well. A single-pole Debye model is sufficient to describe the frequency dependence of the dielectric properties of water and aqueous solutions. Hill [54] reported a 7% decrease in ε_∞ from 4.35 to 4.05 in the temperature range 0 to 60 °C, a change that is much smaller than might be expected for a quantity depending on a hydrogen bonding structure. At the same time, Ryynanen [12] reported that the permittivity for infinite frequency ε_∞ is independent of temperature at a constant value of 4.3, while the structure of bound water appears to be between those of ice and free water. Hydrogen bonds restrict the free movement of water molecules, thus affecting its permittivity. Since the relaxation frequency is due to the mobility of the molecules, bound molecules have a lower relaxation frequency than free water molecules. This explains the fact that the static permittivity ε_s for most tightly bound molecules has a value of the same order as that for ice. Also, the relaxation frequency of ice is much lower than that of free water, being in the kHz instead of the GHz region. Since the dielectric properties of water and ice differ significantly, high water content substances show a large increase in ε' and ε'' with temperature while thawing. Those values again decrease with increasing temperature after thawing. The effect of temperature on the dielectric properties of water is shown in Figure 3.22 [12]. Hill [54] calculated the values of $(\varepsilon_s - \varepsilon_\infty)$ for temperatures from 0 to 60°C from values of ε_s, ε' and ε'' reported in the literature. His results are shown in Table

3-19. Tabulated values of ε' and ε'' of water and ¼ N and ½ N saline at seven equally spaced temperatures from 0 to 60°C for three distinct frequencies (23.67, 9.14 and 3.25 GHz) are reported in [55]. N is the normality of the saline solution. It is the concentration of a solution expressed in gram equivalent weights of solute per liter of solution. ¼ N and ½ N saline are commonly used concentrations. For water, Hasted and El Sabeh [55] reported similar values and trend for ε_s as those in Table 3-19; however, they reported an increase in ε_∞ from a value of 5.0±0.5 to 5.9±0.5. Their reported values of ε_∞, ε_s and the relaxation τ at different temperatures is shown in Table 3-20.

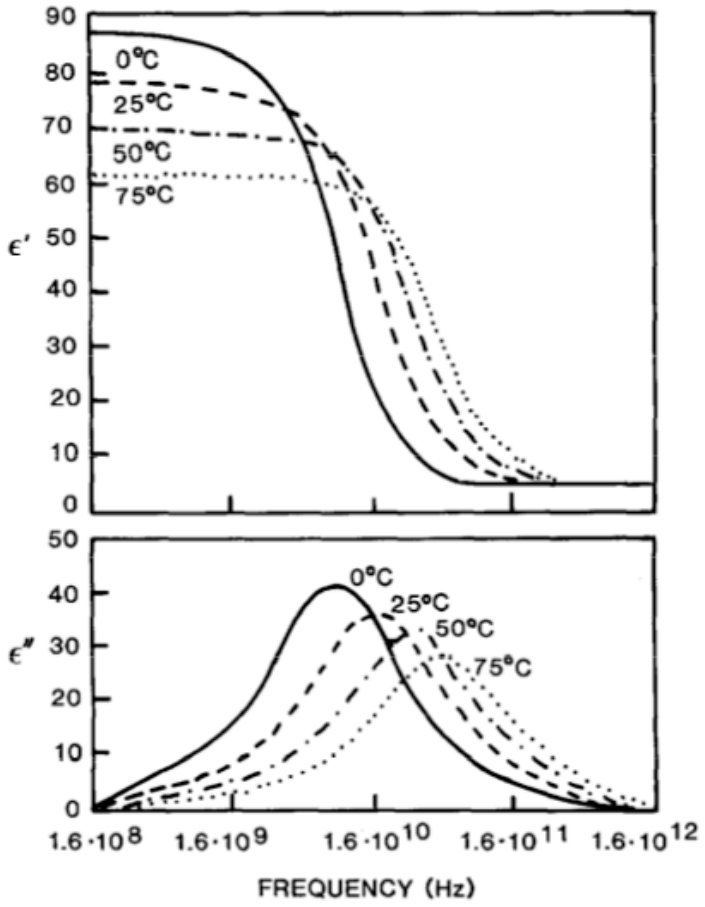

Figure 3.22: Effect of temperature on ε' and ε'' of water (from [12], with permission from Elsevier Limited).

Table 3-19: Values of **(ε_s - ε_∞)** at different temperatures (from [54], with permission from IOPscience).

t (°C)	$\epsilon_s - \epsilon_\infty$ experimental	ϵ_s	ϵ_∞	$\epsilon_s - \epsilon_\infty$ calculated
0	84·2 ± 2·8	87·90	4·35	83·55
10	79·4 ± 1·4	83·95	4·32	79·63
20	75·5 ± 2·4	80·18	4·28	75·90
30	72·1 ± 3·5	76·58	4·23	72·35
40	70·5 ± 3·0	73·15	4·17	68·98
50	66·6 ± 2·0	69·88	4·11	65·77
60	62·0 ± 2·1	66·76	4·05	62·71

Table 3-20: Temperature dependence of the Debye parameters of water (from [55]).

Temperature (°C)	**τ (ns)**	**ε_∞±0.5**	**ε_s±1**
0	1.7719	5.0	88.2
10	1.2891	5.0	84.0
20	0.9443	5.2	80.4
30	0.7215	5.2	76.5
40	0.58356	5.6	73.1
50	0.48276	5.8	70.7
60	0.40319	5.9	66.2

An ionic solution is formed when salts are dissolved in water to form saline. The dielectric loss of an aqueous ionic solution can be expressed as the sum of (ε_d'') caused by the dipole rotation and the value of (ε_σ'') caused by conductive (ionic) charge migration. These mechanisms vary inversely with temperature. The dipole loss component decreases while the ionic loss component increases with temperature. The resulting temperature dependent effect is shown in Figure 3.23 [12]. Tabulated values of

ε' and ε'' for ¼ N (0.22% w/v NaCl) and ½ N (0.45% w/v NaCl) saline at seven equally spaced temperatures from 0 to 60°C for three distinct frequencies (23.67, 9.14 and 3.25 GHz) are reported in [55]. The results are shown in Table 3-21, ε_∞ does not change much, varying from 5.7±0.5 at 0°C to 5.3±0.5 at 60°C. The estimated value for ε_∞ at 25°C is 6±1 [55].

Table 3-21: Temperature dependence of the Debye parameters of saline solutions (from [55]).

Temperature (°C)	**¼ N NaCl**		**½ N NaCl**	
	τ (ns)	**ε_s±1**	**τ (ns)**	**ε_s±1**
0	1.6870	83.0	1.6976	80.0
10	1.1777	79.0	1.2148	75.8
20	0.90718	77.2	0.9018	71.0
30	0.7268	73.8	0.7268	69.5
40	0.6260	70.7	0.6313	66.8
50	0.5199	66.5	0.5199	63.0
60	0.4615	63.0	0.4615	58.7

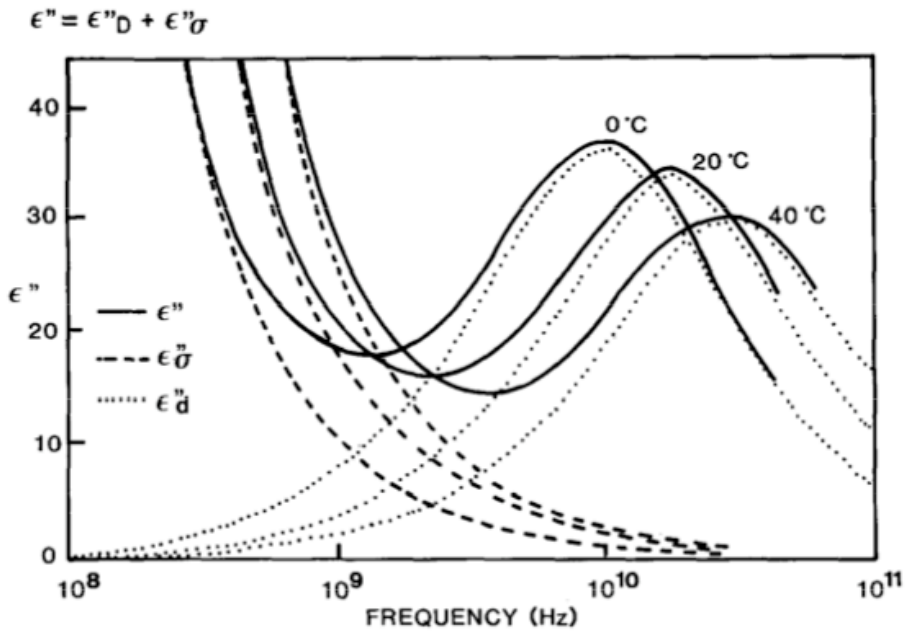

Figure 3.23: Temperature effects on ε'' of aqueous ionic solutions (from [12], with permission from Elsevier Limited).

Stogryn [56] reported equations for the parameters of the Debye model as functions of water salinity and temperature. These equations offer reasonable estimates:

$$\begin{aligned} \varepsilon_{\circ}(T,N) &= \varepsilon_{\circ}(T,0)a(N) \\ 2\pi\tau(T,N) &= 2\pi\tau(T,0)b(N,T) \end{aligned} \tag{14}$$

where T is the water temperature in °C and N is the normality of the solution. By fitting the data reported in [57] for $0 \le N \le 3$ and $0 \le T \le 40$°C, the following parameters were obtained by Stogryn [56]:

$$\begin{aligned} a(N) &= 1.000 - 0.2551N + 5.151\times10^{-2}N^2 - 6.889\times10^{-3}N^3 \\ b(N,T) &= 0.1463\times10^{-2}NT + 1.000 - 0.04896N - 0.02967N^2 5.644\times10^{-3}N^3. \end{aligned} \tag{15}$$

The relaxation time of pure water was also fit to the data in [58]:

$$2\pi\tau(T,0) = 1.1109\times10^{-10} - 3.824\times10^{-12}T + 6.938\times10^{-14}T^2 - 5.096\times10^{-16}T^3 . \quad (16)$$

$\varepsilon_\circ$ for pure water was given by Malmberg and Maryott [59] as a function of temperature to be:

$$\varepsilon_\circ(T,0) = 87.74 - 4.008T + 9.398\times10^{-4}T^2 + 1.410\times10^{-6}T^3 . \quad (17)$$

Stogryn [56] did not fit ε_∞ to a temperature model based on Hasted and El Sabeh's [55] results that report very small changes in ε_∞ with temperature.

The values of the complex permittivity and the Debye parameters for pure water and saline as well as their temperature trends may be used as a reference to verify the behavior of tissues at microwave frequencies. However, the values and trends reported in the literature are not all in agreement because they are mainly based on measurements acquired by different techniques and numerical fittings that can easily yield variable results that span large ranges.

REFERENCES

[1] C. Gabriel, S. Gabriel and E. Corthout, "The dielectric properties of biological tissues: I. Literature survey," *Phys. Med. Biol.*, vol. 41, pp. 2231-2249, 1996.

[2] J. D. Bronzino, *The Biomedical Engineering Handbook.* 2nd ed, vol. 1, Florida: CRC Press, 2000, pp. 89.

[3] H. P. Schwan and K. R. Foster, "Rf-field interactions with biological systems: electrical properties and biophysical mechanisms," *Proc. IEEE*, vol. 68, pp. 104-113, 1980.

[4] D. Miklavčič, N. Pavšelj, and F. X. Hart, Electric Properties of Tissues. Wiley Encyclopedia of Biomedical Engineering, 2006.

[5] C. C. Johnson, A. W. Guy, "Nonionizing electromagnetic wave effects in biological materials and systems," *Proc. IEEE*, vol. 60, no. 6, pp. 692-718, 1972.

[6] W. E. Vaughan, "Dielectric relaxation," *Ann. Rev. Phys. Chem.*, vol. 30, pp. 103-124, October 1979.

[7] Beau Lambert. (April 2008). Dr. K. A. Mauritz Research Group - Dielectric spectroscopy. [Online]. http://www.psrc.usm.edu/mauritz/dilect.html.

[8] R. Pethig, "Dielectric properties of body tissues," *Clin. Phys. Physol. Meas.*, vol. 8, suppl. A., pp. 5-12, 1987.

[9] L. Sha, E. R. Ward, B. Story, "A review of dielectric properties of normal and malignant breast tissue," *Proc. IEEE Southeast Conf.*, pp. 457-462, 2002.

[10] H. P. Schwan, "Electrical properties of tissues and cell suspensions: mechanisms and models," *Engineering in Medicine and Biology Society. Engineering Advances: New Opportunities for Biomedical Engineers. Proceedings of the 16th Annual International Conference of the IEEE*, vol. 1, pp. A70-A71, November 1994.

[11] J. L. Schepps and K. R. Foster, "The UHF and microwave dielectric properties of normal and tumour tissues: variation in dielectric properties with tissue water content," *Phys. Med. Biol.*, vol. 25, no. 6, pp. 1149-1160, 1980.

[12] S. Ryynanen, "The electromagnetic properties of food materials: a review of basic properties" *J. Food Eng.*, vol. 26, pp. 409-429, 1995.

[13] A. M. Campbell, and D. V. Land, "Dielectric properties of female human breast tissue measured in vitro at 3.2 GHz," *Phys. Med. Biol.*, vol. 37, pp. 193-210, 1992.

[14] R. F. Reinoso, B. A. Telfer and M. Rowland, "Tissue water content in rats measured by dessication," *J. Pharmacol. Toxicol. Methods*, vol. 38, pp. 87-92, 1997.

[15] N. K. Nikolova, "Microwave imaging for breast cancer," *IEEE Microw. Mag.*, vol. 12, no. 7, pp. 78-94, December 2011.

[16] A. Samani, J. Zubovits, D. Plewes, "Elastic moduli of normal and pathological human breast tissues: an inversion-technique-based investigation of 169 samples," *Phys. Med. Biol.*, vol. 52, pp. 1565-1576, February 2007.

[17] S. Gabriel, R. W. Lau, and C. Gabriel, "The dielectric properties of biological tissues: III. Parametric models for the dielectric spectrum of tissues," *Phys. Med. Biol*., vol. 41, pp. 2271-2293, April 1996.

[18] S. Gabriel, R. W. Lau and C. Gabriel, "The dielectric properties of biological tissues: II. Measurements in the frequency range 10 Hz to 20 GHz*," Phys. Med. Biol.*, vol. 41, pp. 2251-2269, 1996.

[19] T. S. England N. A. and Sharples, "Dielectric properties of the human body in the microwave region of the spectrum," *Nature*, vol. 163, pp. 487-488, 1949.

[20] S. S. Chaudhary, R. K. Mishra, A. Swarup and J. M. Thomas, "Dielectric properties of normal and malignant human breast tissues at radiowave and microwave frequencies," *Indian J. Biochem. Biophys.*, vol.21, pp. 76-79, 1984.

[21] A. J. Surowiec, S. S. Stuchly, J. R. Barr and A. Swarup, "Dielectric properties of breast carcinoma and the surrounding tissues," *IEEE Trans. Biomed. Eng.*, vol. 35, pp. 257-263, 1988.

[22] A. M. Campbell and D. V. Land, "Dielectric properties of female human breast tissue measured *in vitro* at 3.2 GHz," *Phys. Med. Biol.*, vol. 37, pp. 193-210, 1992.

[23] T. Morimoto *et al.*, "A study of the electrical bioimpedance of tumors," *J. Invest. Surg.*, vol. 6, pp. 25-32, 1993.

[24] W. T. Joines, Y. Zhang, C. Li and R. L. Jirtle, "The measured electrical properties of normal and malignant human tissues from 50 to 900 MHz," *Med. Phys.*, vol. 21, pp. 547-550, 1994.

[25] J. Jossinet, "The impedivity of freshly excised human breast tissue," *Phys. Meas.*, vol. 19, pp. 61-75, 1998.

[26] J. da Silva, J. de Sa and J. Jossinet, "Classification of breast tissue by electrical impedance spectroscopy," *Med. Biol. Eng. Comput.*, vol. 38, pp. 26-30, 2000.

[27] J. W. Choi *et al.*, "Microwave detection of metastasized breast cancer cells in the lymph node; potential applications for sentinel lymphadenectomy," *Breast Cancer Res. Treat.*, vol. 86, pp. 107-115, 2004.

[28] S. P. Poplack *et al.*, "Electromagnetic breast imaging: average tissue property values in women with negative clinical findings," *Radiology*, vol. 231, pp. 571-580, 2004.

[29] M. Lazebnik, L. McCartney, D. Popovic, C. B. Watkins, M. J. Lindstorm, J. Harter, S. Sewall, A. Magliocco, J. H. Brooske, M. Okoniewski and S. C. Hagness, " A large - scale study of the ultra wideband microwave dielectric properties of normal breast tissue obtained from reduction surgeries*," Phys. Med. Biol.*, vol. 52, pp. 2637-2656, April 2007.

[30] M. Lazebnik, L. McCartney, D. Popovic, C. B. Watkins, M. J. Lindstorm, J. Harter, S. Sewall, A. Magliocco, J. H. Brooske, M. Okoniewski and S. C. Hagness, "A large-scale study of the ultrawideband microwave dielectric properties of normal, benign and malignant breast tissues obtained from cancer surgeries," *Phys. Med. Biol*., vol. 52, pp. 6093-6115, October 2007.

[31] M. Lazebnik, M. Okoniewski, J. H. Brooske, S. C. Hagness, "Highly accurate Debye models for normal and malignant breast tissue dielectric properties at microwave frequencies," *IEEE Microw. Wireless Comp. Lett.*, vol. 17, no. 12, pp. 822-824, December 2007.

[32] R. J. Halter *et al.*, "The correlation of in vivo and ex vivo tissue dielectric properties to validate electromagnetic breast imaging: initial clinical experience," *Physiol. Meas*., vol. 30, pp. S121 - S136, June 2009.

[33] C. Gabriel, T. Y. A. Chan and E. H. Grant, "Admittance models for open ended coaxial probes and their place in dielectric spectroscopy," *Phys. Med. Biol.*, vol. 39, pp. 2183-2200, 1994.

[34] D. Popovic, L. McCartney, C. Beasley, M. Lazebnik, M. Okoniewski, S. C. Hagness and J. Booske, "Precision open-ended coaxial probes for *in vivo* and *ex vivo* dielectric spectroscopy of biological tissues at microwave frequencies," *IEEE Trans. Microw. Theory Tech.*, vol. 53, pp. 1713-1722, 2005.

[35] H. P. Schwan, "Electrical properties of tissue and cell suspensions," *Adv. Biol. Med. Phys.*, vol. 5, pp. 147-209, 1957.

[36] K. R. Foster, J. L. Schepps, R. D. Stoy and H. P. Schwan, "Dielectric properties of brain tissue between 0.01 and 10 GHz," *Phys. Med. Biol.*, vol. 24, no. 6, pp. 1177-87, 1979.

[37] E. C. Burdette, F. L. Cain and J. Seals, "*In situ* tissue permittivity at microwave frequencies: perspective, techniques, results," *Medical Applications of Microwave Imaging ed. L. E. Larsen and J. H. Jacobi,* New York: IEEE, 1985, pp. 13-40.

[38] K. R. Foster and H. P. Schwan, "Dielectric properties of tissues and biological materials: a critical review," *Crit. Rev. Biomed. Eng.*, vol. 17, pp. 25-104, 1989.

[39] J. Kyber, H. Hansgen and F. Pliquett, "Dielectric properties of biological tissues at low temperatures demonstrated on fatty tissue," *Phys. Med. Biol.*, vol. 37, no. 8, pp. 1675-1688, 1992.

[40] S. Y. Semenov, R. H. Svenson and G. P. Tatsis, "Microwave spectroscopy of myocardial ischemia and infarction. 1. Experimental study," *Ann. Biomed. Eng.*, vol. 28, pp. 48-54, 2000.

[41] L. Chin and M. Sherar, "Changes in dielectric properties of ex vivo bovine liver at 915 MHz during heating," *Phys. Med. Biol.,* vol. 46, no. 1, pp. 197-211, 2001.

[42] F. Jaspard and M. Nadi, "Dielectric properties of blood: an investigation of temperature dependence," *Physiol. Meas.*, vol. 23, pp. 547-554, 2002.

[43] P. R. Stauffer, F. Rossetto, M. Prakash, D. G. Neuman and T. Lee, "Phantom and animal tissues for modeling the electrical properties of human liver," *Int. J. Hyperthermia*, vol. 19, no. 1, pp. 89-101, 2003.

[44] L. Chin and M. Sherar, "Changes in the dielectric properties of rat prostate ex vivo at 915 MHz during heating," *Int. J. Hyperthermia*, vol. 20, no. 5, pp. 517-27, 2004.

[45] M. Lazebnik, M. C. Converse, J. H. Booske and S. C. Hagness, "Ultrawideband temperature-dependent dielectric properties of animal liver tissue in the microwave frequency range," *Phys. Med. Biol.*, vol. 51, pp. 1941-1955, 2006.

[46] V. N. Tran and S. S. Stuchly, "Dielectric properties of beef, beef liver, chicken and salmon at frequencies from 100 to 200 MHz," *J. Microw. Power*, vol. 22, pp. 29-33, 1987.

[47] C. Bircan and S. A. Barringer, "Determination of protein denaturation of muscle foods using the dielectric properties," *J. Food Sci.*, vol. 67, pp. 202-205, 2002.

[48] O. Sipahioglu, S. A. Barringer and C. Bircan, "The dielectric properties of meats as

a function of temperature and composition," *J. Microw. Power Electr. Energy*, vol. 38, pp. 161-9, 2003.

[49] R. Peloso, D. T. Tuma and R. K. Jain, Dielectric properties of solid tumors during nonhyperthermia and hyperthermia," *IEEE Trans. Biomed. Eng.*, vol. BME-31, no. 11, pp. 725-728, November 1984.

[50] D. A. McRae and M. A. Esrick, "The dielectric parameters of excised EMT-6 tumours and their change during hyperthermia," *Phys. Med. Biol.*, vol. 37, no. 11, pp. 2045-2058, 1992.

[51] V. Komarov, S. Wang and J. Tang, "Permittivity and measurements" *Encyclopedia of RF and Microwave Engineering* ed K. Chang, New York: Wiley, 2005.

[52] F. A. Duck, *Physical Properties of Tissue: A Comprehensive Reference Book.* London: Academic Press, 1990.

[53] C. L. Brace, "Temperature-dependent dielectric properties of liver tissue measured during thermal ablation: Toward an improved numerical model," *30th Annual IEEE EMBS Conference, Vancouver, British Columbia, Canada*, pp. 230-233, August 2008.

[54] N. E. Hill, "The temperature dependence of the dielectric properties of water," *J. Phys. C: Solid State Phys.*, vol. 3, pp. 238-239, 1970.

[55] J. B. Hasted and S. H. M. El Sabeh, "The dielectric properties of water in solutions," *Trans. Faraday. Soc.*, vol. 49, pp. 1003-1011, 1953.

[56] A. Stogryn, "Equations for calculating the dielectric constant of saline water," *IEEE Trans. Microw. Theory and Tech.*, vol. , pp. 733-376, August 1971.

[57] J. Lane and J. Saxon, "Dielectric dispersion in pure polar liquids at very high frequencies. III. The effect of electrolytes in solution, " *Proc. Roy. Sot.*, vol. A213, pp. 531-545, 1952.

[58] E. Grant, T. Buchanan, and H. Cook, "Dielectric behavior of water at microwave frequencies," *J. Chem. Phys.*, vol. 26, pp. 156-161, 1957.

[59] C. Malmberg and A. Maryott, "Dielectric constant of water from 0° to 100 °C," *J. Res. Nat. Bur. Stand.*, vol. 56, pp. 1-8, 1956.

CHAPTER 4

MEASUREMENT METHODS FOR THE TEMPERATURE-DEPENDENT DIELECTIC PROPERTIES OF PHANTOMS AND TISSUES

4.1 MATERIALS

Measurement Hardware

The dielectric properties of the tested samples measured at different temperatures over the frequency range from 3 GHz to 10 GHz. In order to acquire the measured data, the following hardware was used:

- *Agilent E8363B Performance Network Analyzer (PNA) [1]*
- *Agilent 85070E Dielectric Slim Probe Kit [1]*

The probe transmits a signal into the material under test (MUT). The network analyzer measures the material's response to RF or microwave energy as the complex

reflection coefficient S_{11}. A high quality coaxial cable interfaces the probe with the network analyzer (Agilent E8363B PNA). The included software controls the network analyzer and guides the user through calibration and measurement steps. It calculates and displays the complex permittivity (ε' and ε'') of the MUT. A "three standard" calibration (open, short, water) is performed at the end of the probe. The short standard is provided with the kit. A "one standard" (water) refresh calibration feature is available to be used between measurements to remove errors due to test port cable movement. No special fixtures or containers are required to use the probe. Measurements are non-destructive and can be made in real time. This system can be used with liquids or semi-solids. Measurement of materials can be performed from 10 MHz to 40 GHz. Three dielectric probes are available with this kit.

The Slime Form Probe (Figure 4.1) was chosen because of its small diameter and additional features, which allow for the use of small samples in the frequency and temperature ranges of interest. This probe allows for temperatures from 0 °C to 125 °C. The MUT is assumed to be "infinite" and non-magnetic, isotropic and homogeneous. For heterogeneous materials the measured complex permittivity is an average of the area detected by the probe. The area in direct contact with the probe has the most effect on the measurement results. A minimum insertion of 5 mm and 5 mm around the tip of the probe are required for the sample of the MUT. The resultant complex permittivity has an accuracy of $\varepsilon' = \varepsilon' \pm 0.05|\varepsilon^*|$ and $\varepsilon'' = \varepsilon'' \pm 0.05|\varepsilon^*|$.

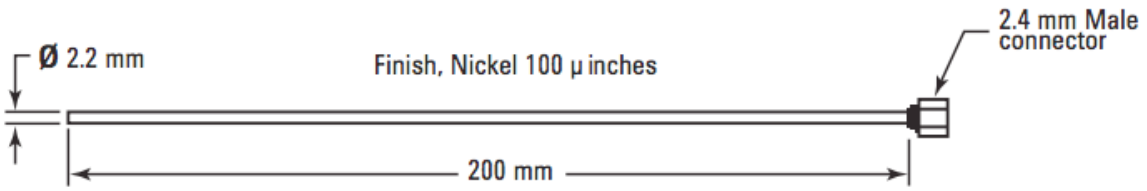

Figure 4.1: Slim Form Probe.

- *ThermoWorks Two-Channel TW8060 Thermocouple [2]*

  The thermocouple allows for the measurement of temperatures from -200 °C to 1300 °C with a resolution of 0.1 °C below 1000 °C and 1 °C above 1000 °C. The accuracy of the measurement for the temperature range of interest (5 °C to 45 °C) is ±0.1% reading + 0.7°C which results in a maximum error of ±0.745 °C at 45 °C. The sampling rate for this thermocouple is 1 sample per second. Two 5-inch penetration temperature probes from ThermoWorks are used with the two-channel thermocouple. These probes work in the temperature range from -50 °C to 250 °C. The probes have 1/8-inch diameters with sharp tips that allow for the penetration of semi-solids. The probes have a response time of 7 seconds and an accuracy of ±0.5 °C for the temperature range from 0 °C to 100 °C.

- Heating Apparatus

  Hot steam was used to heat the tissue samples. A water pot on a hot plate was used to provide the steam. The setup used directed the steam from the pot to the sample. The tissue sample was insulated to ensure proper heating. Water and 0.9% w/v saline were heated by simply placing the liquid in a Pyrex beaker on the hot plate.

Physical Phantoms

Glycerin based physical phantoms have been developed by our group to be used in the testing of a microwave imaging system for breast cancer detection [3],[4]. They have the following features: (i) high mechanical and shape stability as opposed to jelly and liquid phantoms which are messy to work with and are prone to air bubbles, (ii) non-toxicity – expensive protective or safety equipment is not required, (iii) fabrication simplicity – easily available ingredients and apparatus, (iv) wideband electrical properties from 3 to 10 GHz, (v) ease of maintenance – prolonged and stable mechanical and electrical properties, and (vi) low cost – suitable for pre-clinical studies where many experiments are needed.

The phantoms are made of glycerin, polyethelene powder (PEP), agar, ethythene glycol and double distilled/de-ionized water (DIW). The percentages of agar and glycerin are adjusted to achieve a balance between moisture and good mechanical strength. The ratio of water and PEP is used to control the loss (or conductivity) of the phantom. Agar is a polymer that provides mechanical strength necessary to preserve the phantom's shape. The materials required for malignant tumor phantoms are DIW, salt (NaCl) and alginate powder or gelatin. Salt is used only to raise the conductivity in the malignant tissue recipe. Table 4-1 to Table 4-5 show the percentages of materials, on a weight per weight basis, used for the different healthy breast-tissue phantoms. Glycerin-based recipes present 100 g of glycerin as the percentage base value. Other ingredients are variants whose weight percentages change to model the range of tissues. The recipes for healthy tissues are broadly divided according to water content as:

- HWCT-1 (High-Water-Content-Tissue-1) for muscle
- HWCT-2 (High-Water-Content-Tissue-2) for FG tissue
- IWCT (Intermediate-Water-Content-Tissue) for skin and transitional tissue
- LWCT (Low-Water-Content-Tissue) for adipose tissue
- Alginate powder in 0.9% w/v saline and gelatin in 0.9% w/v saline for tumors

Table 4-1: Recipe ratio for HWCT-1 phantom

Materials	Weight % Based on Glycerine
Glycerine	100
DIW	180
PEP	15
Agar	12

Table 4-2: Recipe ratio for HWCT-2 phantom

Materials	Weight % Based on Glycerine
Glycerine	100
DIW	140
PEP	14
Agar	11

Table 4-3: Recipe ratio for IWCT phantom

Materials	Weight % Based on Glycerine
Glycerine	100
DWI	100
PEP	8
Agar	8

Table 4-4: Recipe ratio for LWCT phantom

Materials	Weight % Based on Glycerine
Glycerine	100
DIW	8
Ethylene Glycol	52
PEP	10
Agar	11.5

Table 4-5: Recipe ratio for malignant tumor phantom

Materials	Quantity
Alginate Powder	23 g
DIW	100 g
NaCl	0.7 g

If the total volume of phantom mixture is below 800 mL, the following procedure can be used to make the phantoms.

1. Follow standard laboratory safety regulations.
2. Pour DIW into a glass flask and put on a burner with a low flame or on a digital plate.
3. Pour all liquids needed in the recipe and stir to form a clear solution. Heat the solution to approximately 46 °C.
4. Add a few drops of a bactericide, such as Bactine spray.
5. Add the powder reagents, as a mixture of PEP and agar in the recipe. The powder mixture is added in tiny amounts to the liquid. The mixture is stirred continuously and gently to form a homogenous solution with minimal bubbles.
6. Once the mixture is homogeneous and thick, pour into a suitable mould. Initially, the temperature is about 68 °C to 75 °C. Allow the phantom to cool down to room temperature then place it at 5 °C for solidification.
7. Use high quality plastic wraps, such as parafilm, to store the phantom after solidification to prevent dehydration.

If a phantom batch is above 800 mL, it is recommended to use an automatic blender to mix the solution. Steps 3 and 5 are changed to (a) and (b), respectively. The remaining steps are the same as in the case of a small batch.

(a) Heat the solution to 88 °C. High temperature is required as there cannot be any heat supply to the blender.

(b) Pour the liquid mixture into the blender. Add the powder mixture in tiny amounts and start churning the mixture at slow rotation speed – about 40 rpm to 60 rpm.

The procedure for malignant tissue phantoms requires a 0.9% w/v saline solution as per the given ratio. For gelatin-based tumor phantoms, gelatine powder is dissolved in hot 0.9% w/v saline (about 60 °C) and set to solidify. For alginate-based tumor phantoms, alginate is dissolved in cooled 0.9% w/v saline and immediately set in a mould, as alginate powder solidifies rapidly.

The measurement of the dielectric properties of the phantoms was performed using Agilent 85070E Dielectric Slim Form Probe Kit at room temperature. The measured properties are shown in Figure 4.2 and Figure 4.3 [4]. Measurements were performed on all phantom types described above. Phantom samples were cut into blocks of approximately 25 mm × 25 mm × 25 mm. The samples needed to be big enough to satisfy the assumptions of the Slim Form probe, yet small enough to be easily heated and have an approximately even temperature throughout.

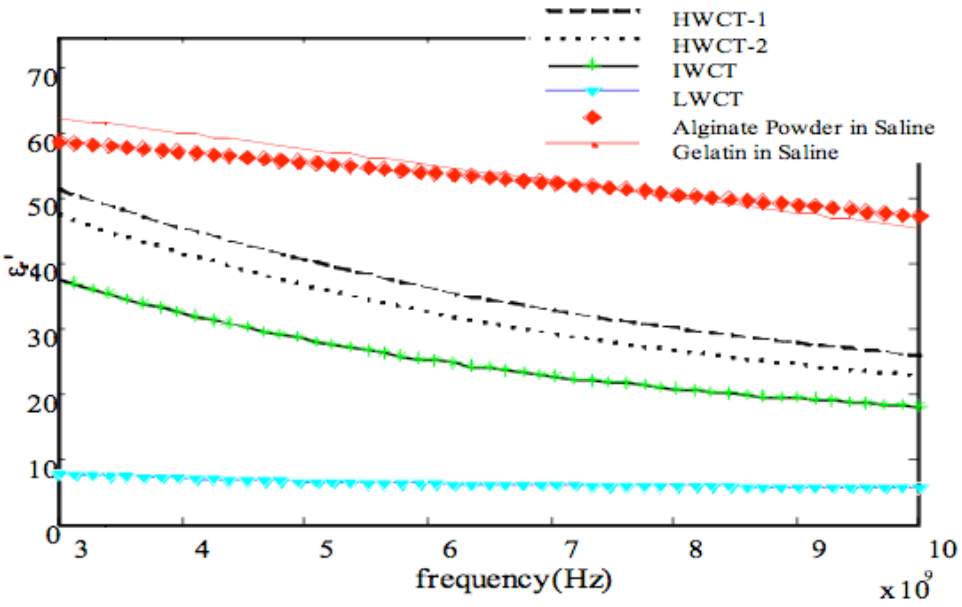

Figure 4.2: Measured relative permittivities ε' of breast tissue phantoms (from [4]).

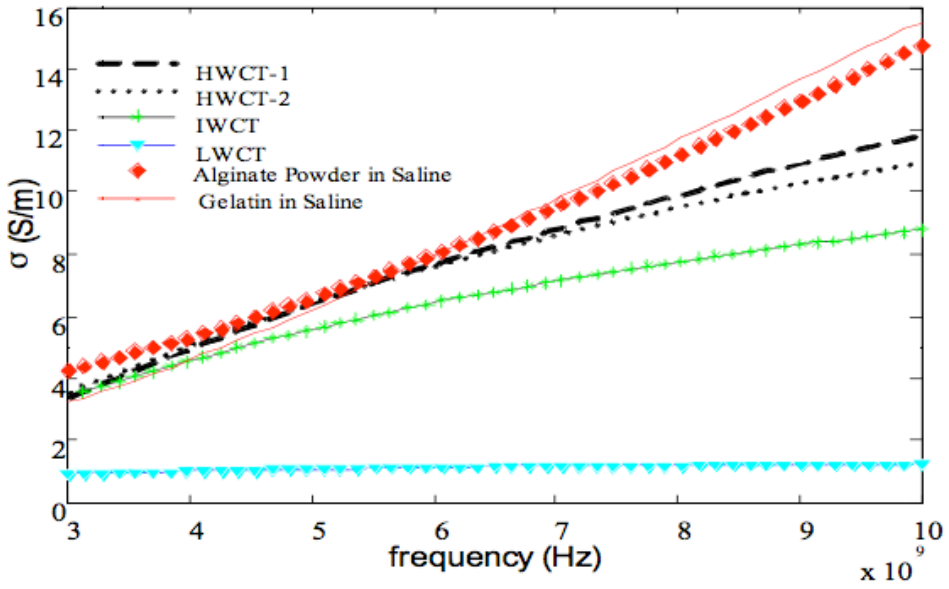

Figure 4.3: Measured conductivities σ of breast tissue phantoms (from [4]).

Animal Samples

Five porcine tissue samples from excised animal sections were obtained from a local slaughterhouse. The excised part consisted of a surface section of the slaughtered animal that was made up of a skin layer, a layer of fat under the skin, and a layer of muscle. This kind of sectioning was chosen in order to be as close as possible to the fat and muscle tissues of the breast. The liver samples were obtained from a porcine liver as well. The tissues were obtained from the slaughterhouse directly following excision and immediately cooled and stored at a temperature of 5 °C until the time of measurement, which was 2–72 hours after excision. Tissue samples were cut into approximately 25 mm × 25 mm × 25 mm. Great care was taken to ensure the homogeneity of the tissue sample for the tissue under test (fat, muscle or liver). The tissue samples needed to be big enough to satisfy the assumptions of the Slim Form probe, yet small enough to be easily heated and have an approximately even temperature throughout. Most temperature measurements of the dielectric properties of tissues are performed on tissues that are immersed in 0.9% w/v saline or in a closed system to prevent dehydration; however these setups neglect phenomena that occur during heating, namely water molecule motion which plays a major role in the dielectric properties of tissues at microwave frequencies [5].

4.2 METHODS

Measurement Setup

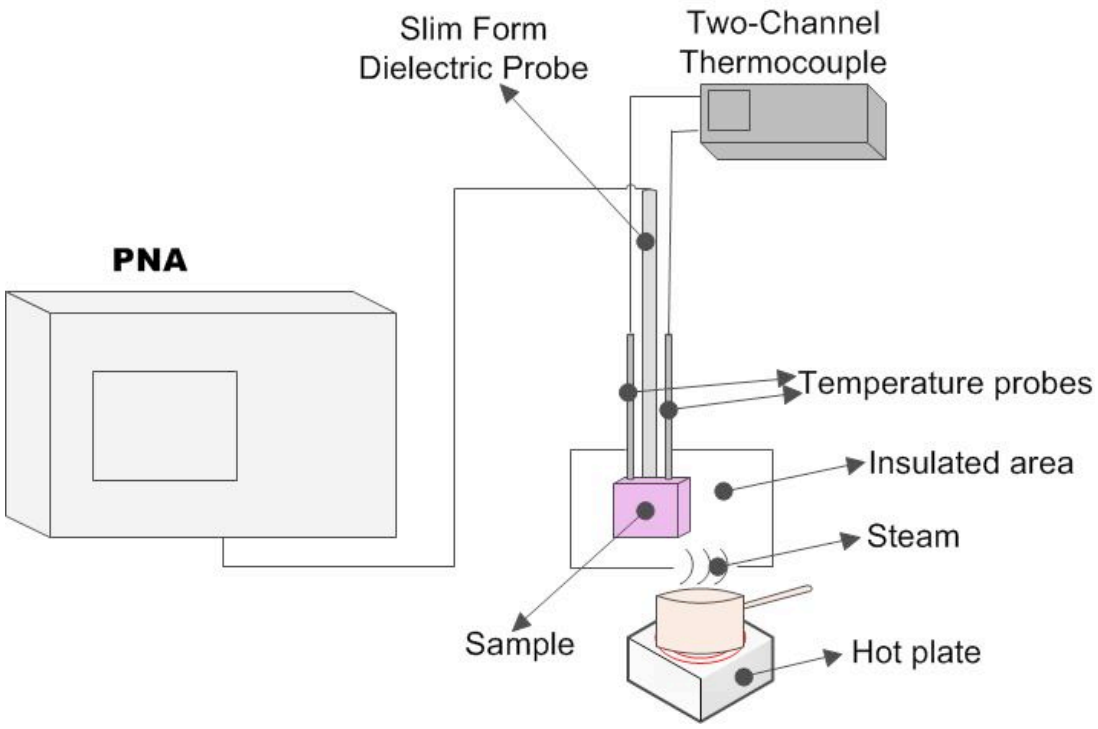

Figure 4.4: Measurement setup.

The measurement setup is shown in Figure 4.4. The PNA is connected to the Slim Form Dielectric Probe, which is inserted in the sample. Two temperature probes connected to a thermocouple are inserted in the sample on both sides of the dielectric probe. Hot steam is used to heat the sample, which is in an insulated area. The sample was not moved with respect to the probes between measurements to ensure that the difference in dielectric properties is due to the change in temperature rather than the heterogeneity of the sample.

Measurement Protocol

Measurements begin with the calibration of the Slim Form Dielectric Probe using the "three standard" calibration (open, short, water). A refresh calibration using water was performed between the measurements of each sample. Measurements are conducted by inserting the Slim Probe into the solid phantom or tissue sample. The samples were pressed against the dielectric probe in order to minimize the air gap between the probe and the sample to diminish this source of error. Great care was taken to minimize measurement error. However, variations due to cable motion, material adhesion to the probe's aperture, local sample heterogeneity and instrument (Johnson) noise, etc., are unavoidable. Measurements were carried out at 21 temperature points for the range from 5 °C to 45 °C with a 2 °C increment and in the frequency range from 3 GHz to 10 GHz with 51 linearly spaced frequency points. This temperature range was chosen based on the fact that this is the range within which the temperature of live tissues may change without resulting in permanent damage. This is true for very short duration of temperature change for temperatures higher than 41 °C. The recorded temperature was taken as the average of the two temperatures recorded by both temperatures probes on either side of the dielectric probe. The samples were cooled to 5 °C then heated to 45 °C using the hot steam. The dielectric probe and the PNA were used to perform a frequency sweep from 3 GHz to 10 GHz of ε' and ε'' at every temperature. Five measurements were carried out for every tissue and phantom type. Visual inspection of the temperature and frequency trends was used to eliminate inconsistent measurements.

4.3 MEASURED DATA

Permittivity and conductivity were measured at every temperature point in the frequency range from 3 GHz to 10 GHz. Five measurements were carried out with each of the LWCT, IWCT, HWCT-1, HWCT-2, alginate tumor phantom, fat, muscle, and liver samples. The results are summarized below in two ways for each phantom or tissue type. The results are first displayed at different temperatures for a single frequency. Then, they are shown as a series of frequency-dependent curves at every temperature. Only the two measurements that are chosen for further analysis are shown in the second manner. The two measurements are chosen based on their representation of the five measurements and their obedience of the Cole-Cole model. The trends and magnitudes of change in the relative permittivities and conductivities of the different phantom and tissue types are discussed below. It is important to note that those trends only apply to the frequency range from 3 GHz to 10 GHz and do not necessarily apply at other frequencies. Comparisons are made with previously reported only at frequencies in this frequency range.

Phantoms

A. LWCT Phantom

Figure 4.5 *(a) – (j)* shows the temperature trends of the relative permittivity ε_r and the conductivity σ of the LWCT phantoms at 3, 5.1, 7.06, 9.02 and 10 GHz. Each curve represents one of the five measurements carried out with the LWCT phantom.

Figure 4.6 *(a) – (f)* and Figure 4.7 *(a) – (f)* show the frequency trends at different temperatures of the second and the third measurements, respectively. Each curve displays the relative permittivity and the conductivity of the LWCT phantoms from 3 GHz to 10 GHz at each temperature. The figures are divided into three temperature ranges, 5 – 17 °C, 19 – 31 °C and 33 – 45 °C, for easier readability. The figures show an increase in both the relative permittivity and the conductivity of the LWCT phantoms with increasing temperature. The relative permittivity increases at a higher rate at lower frequencies, almost tripling at 3 GHz. The increase is less pronounced at higher frequencies, increasing by less than twice at 10 GHz. Most of the increase in the relative permittivity of the LWCT phantom occurs at the higher temperature range starting at around room temperature. This increase after room temperature is most likely a result of applying heat to the phantom. Conductivity increases almost constantly with the increase of temperature. The increase in conductivity is fairly consistent across the frequency range with a slightly higher rate at higher frequencies.

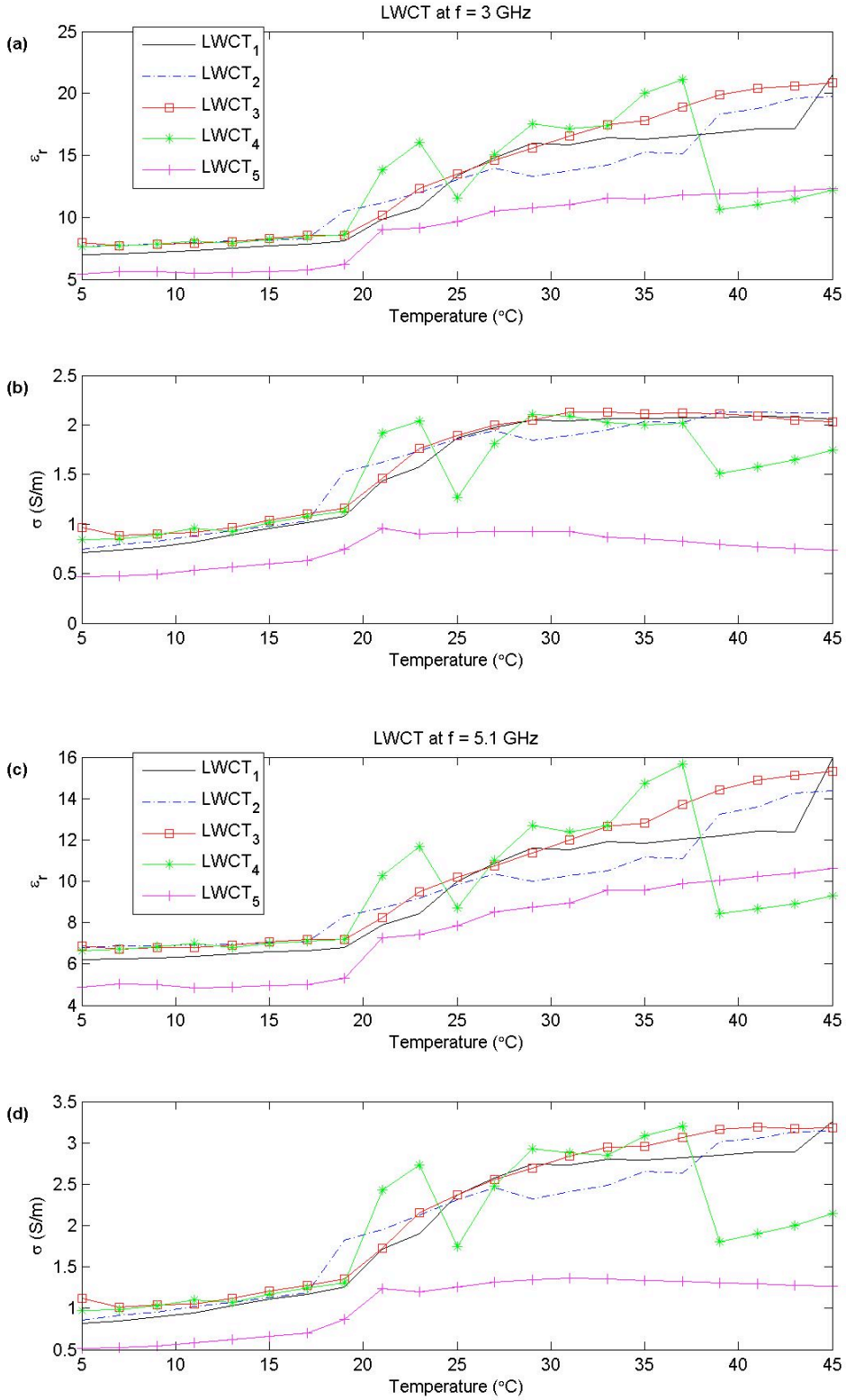
LWCT at f = 3 GHz
(a)
LWCT1
LWCT2
LWCT3
LWCT4
LWCT5
εr
Temperature (°C)
(b)
σ (S/m)
Temperature (°C)
LWCT at f = 5.1 GHz
(c)
LWCT1
LWCT2
LWCT3
LWCT4
LWCT5
εr
Temperature (°C)
(d)
σ (S/m)
Temperature (°C)

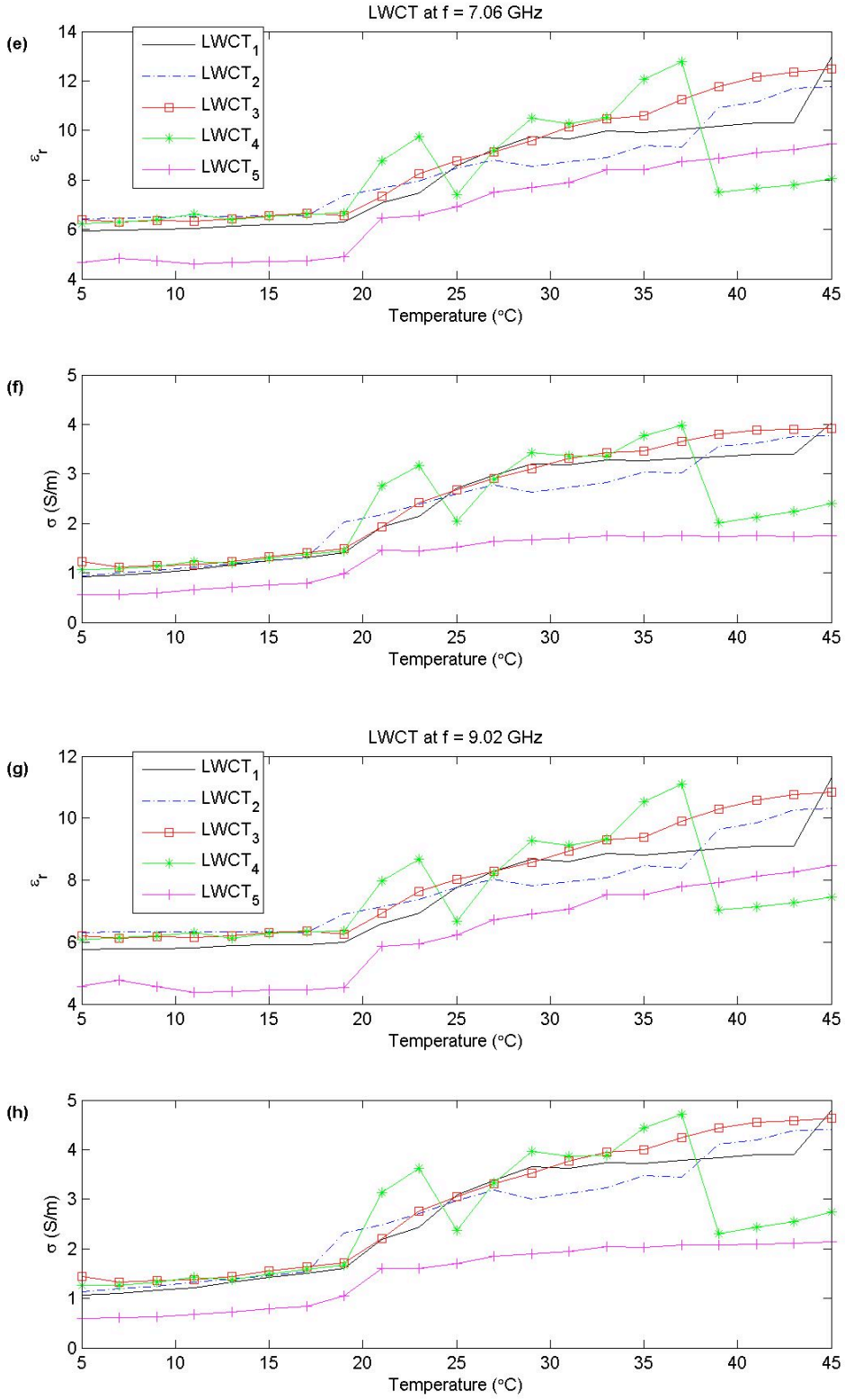
(e)
LWCT at f = 7.06 GHz
LWCT1
LWCT2
LWCT3
LWCT4
LWCT5
εr
Temperature (°C)
(f)
σ (S/m)
Temperature (°C)
(g)
LWCT at f = 9.02 GHz
LWCT1
LWCT2
LWCT3
LWCT4
LWCT5
εr
Temperature (°C)
(h)
σ (S/m)
Temperature (°C)

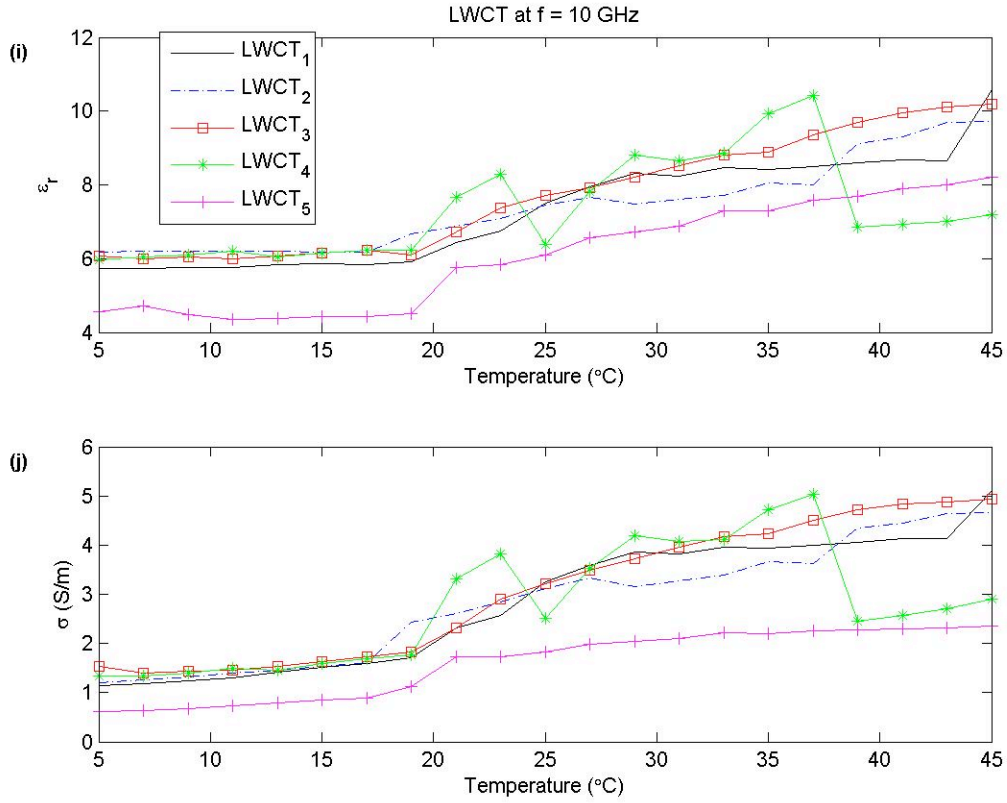

Figure 4.5: Measurements of the LWCT phantoms; temperature trends of permittivity ε_r at: *(a)* 3 GHz, *(c)* 5.01 GHz, *(e)* 7.06 GHz, *(g)* 9.02 GHz and *(i)* 10 GHz; and of conductivity σ at: *(b)* 3 GHz, *(d)* 5.01 GHz, *(f)* 7.06 GHz, *(h)* 9.02 GHz and *(j)* 10 GHz. The five curves represent the results of the measurements, which were repeated five times.

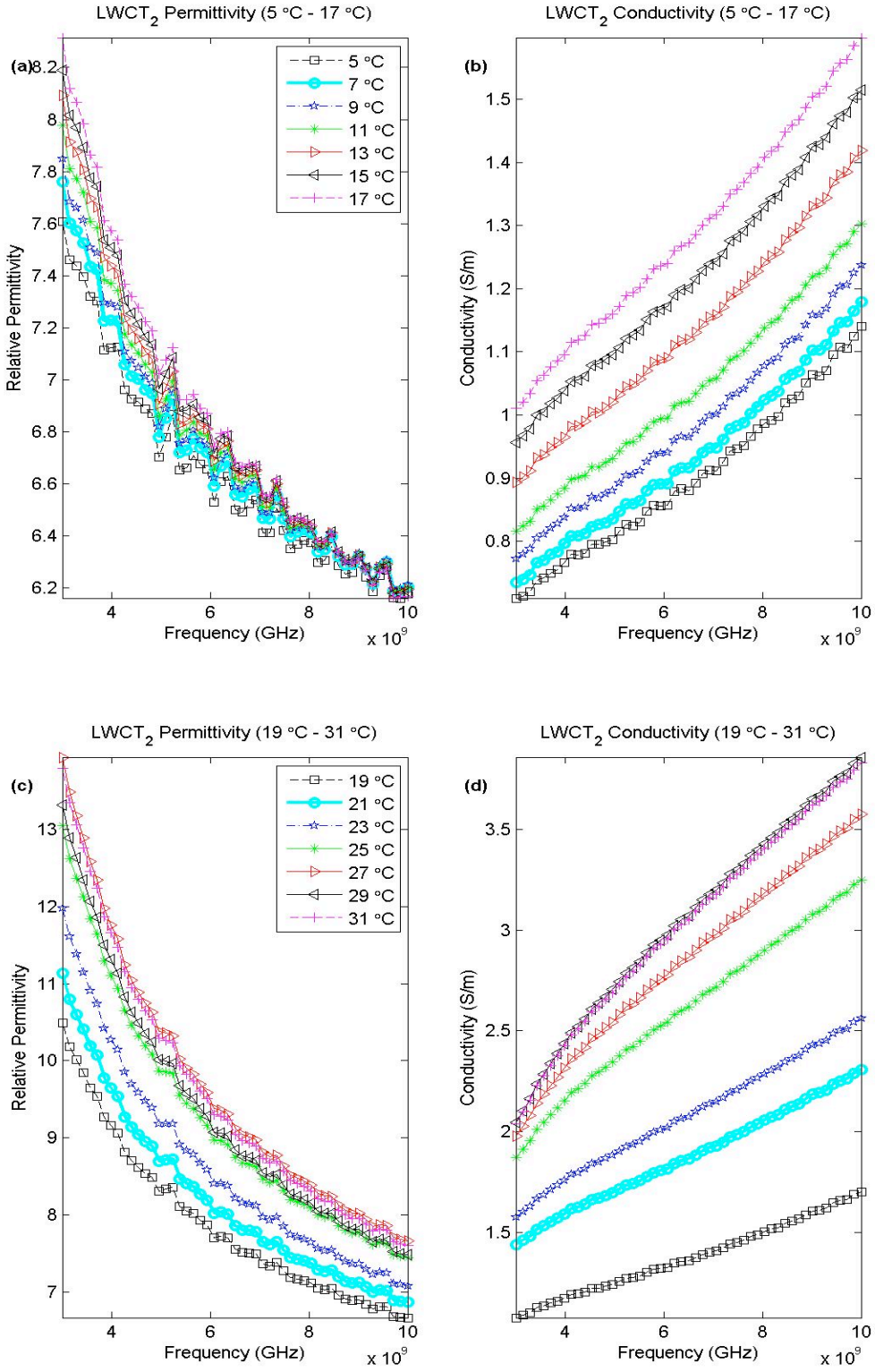
LWCT2 Permittivity (5 °C - 17 °C)
(a)
5 °C
7 °C
9 °C
11 °C
13 °C
15 °C
17 °C
Relative Permittivity
Frequency (GHz)
x 10^9
LWCT2 Conductivity (5 °C - 17 °C)
(b)
Conductivity (S/m)
Frequency (GHz)
x 10^9
LWCT2 Permittivity (19 °C - 31 °C)
(c)
19 °C
21 °C
23 °C
25 °C
27 °C
29 °C
31 °C
Relative Permittivity
Frequency (GHz)
x 10^9
LWCT2 Conductivity (19 °C - 31 °C)
(d)
Conductivity (S/m)
Frequency (GHz)
x 10^9

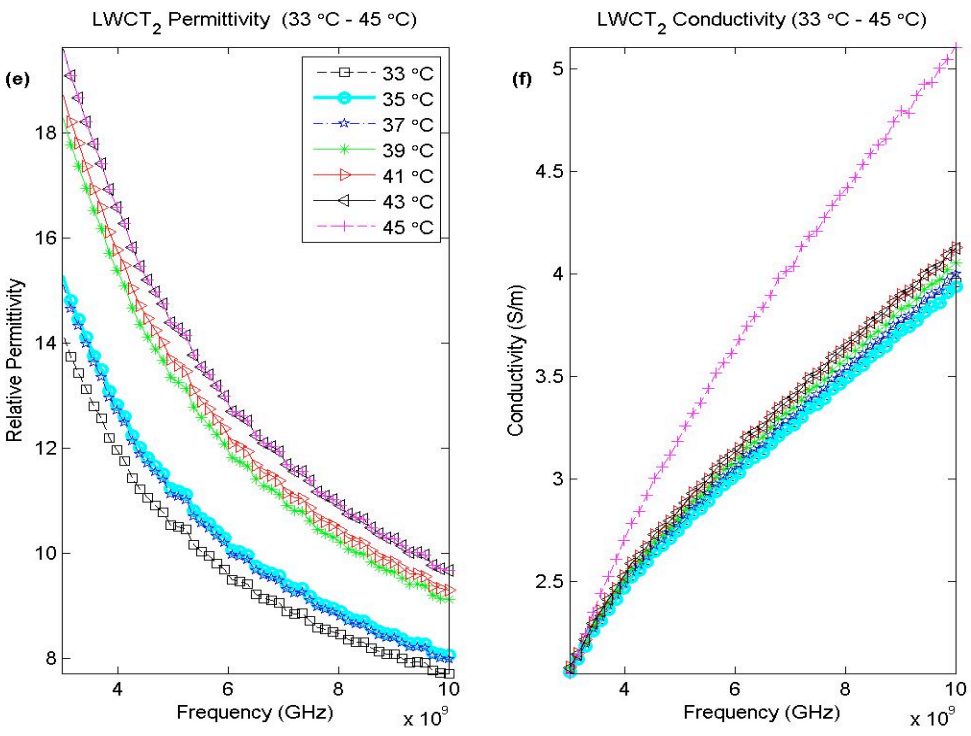

Figure 4.6: Second measurement of LWCT phantoms ($LWCT_2$); frequency trends of permittivity ε_r at: *(a)* 5 - 17 °C, *(c)* 19 - 31 °C and *(e)* 33 - 45 °C; and of conductivity σ at: *(b)* 5 - 17 °C, *(d)* 19 - 31 °C and *(f)* 33 - 45 °C.

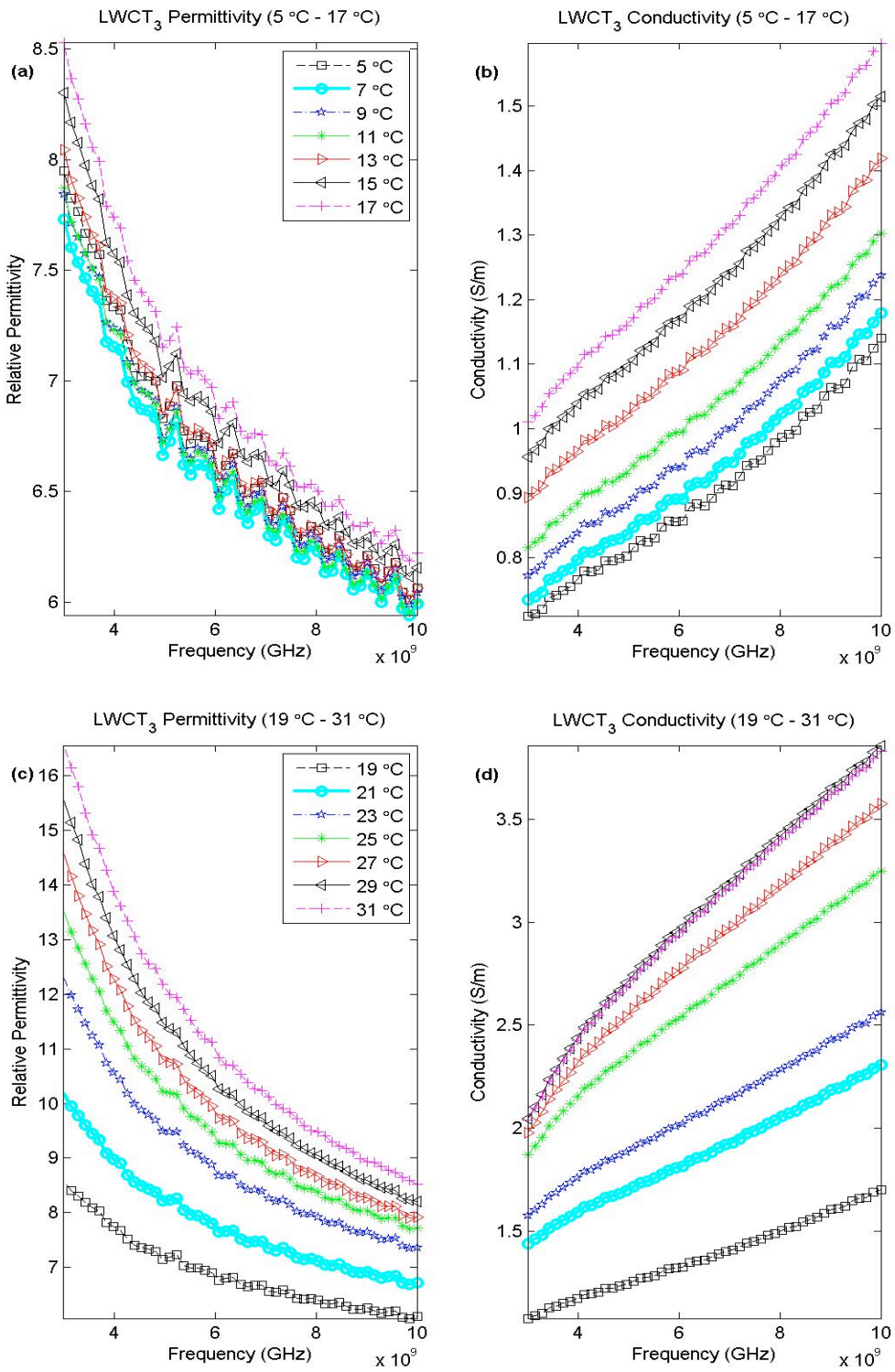
LWCT3 Permittivity (5 °C - 17 °C)
(a)
5 °C
7 °C
9 °C
11 °C
13 °C
15 °C
17 °C
Relative Permittivity
Frequency (GHz)
x 10^9
LWCT3 Conductivity (5 °C - 17 °C)
(b)
Conductivity (S/m)
Frequency (GHz)
x 10^9
LWCT3 Permittivity (19 °C - 31 °C)
(c)
19 °C
21 °C
23 °C
25 °C
27 °C
29 °C
31 °C
Relative Permittivity
Frequency (GHz)
x 10^9
LWCT3 Conductivity (19 °C - 31 °C)
(d)
Conductivity (S/m)
Frequency (GHz)
x 10^9

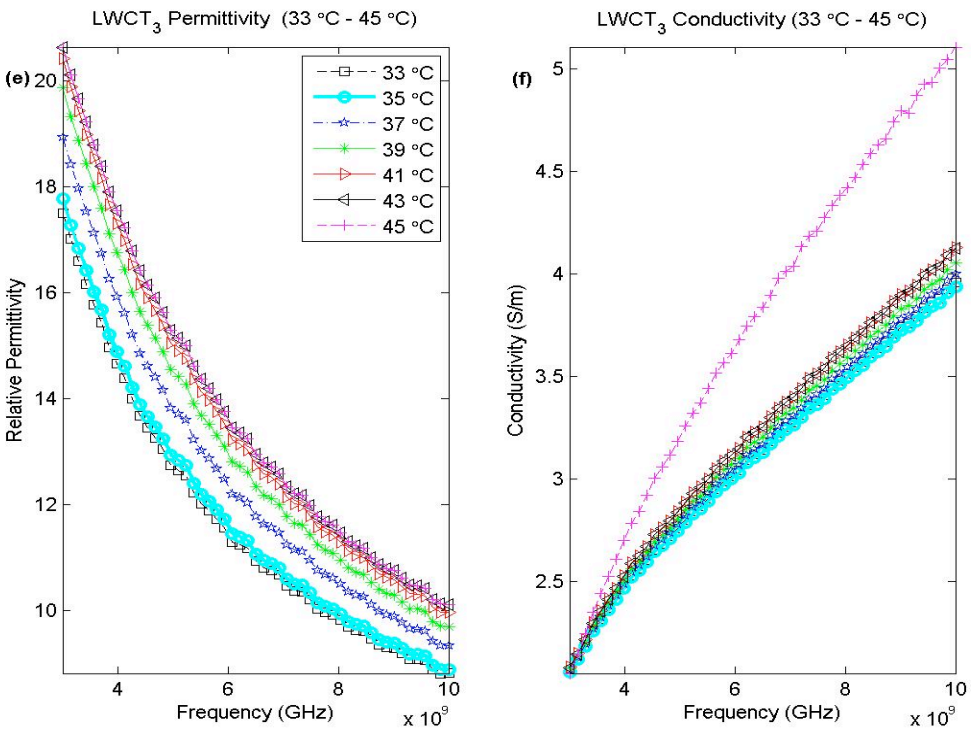

Figure 4.7: Third measurement of LWCT phantoms ($LWCT_3$); frequency trends of permittivity ε_r at: *(a)* 5 - 17 °C, *(c)* 19 - 31 °C and *(e)* 33 - 45 °C; and of conductivity σ at: *(b)* 5 - 17 °C, *(d)* 19 - 31 °C and *(f)* 33 - 45 °C.

B. IWCT Phantom

Figure 4.8 *(a)* – *(j)* shows the temperature trends of the relative permittivity ε_r and the conductivity σ of the IWCT phantoms at 3, 5.1, 7.06, 9.02 and 10 GHz. Each curve represents one of the five measurements carried out with the IWCT phantom. Figure 4.9 *(a)* – *(f)* and Figure 4.10 *(a)* – *(f)* show the frequency trends at different temperatures of the second and the third measurements, respectively. Each curve displays the relative permittivity and the conductivity of the IWCT phantoms from 3 GHz to 10 GHz at each temperature. The figures are divided into three temperature ranges 5 – 17 °C, 19 – 31 °C

and 33 – 45 °C for easier readability. The figures show that the relative permittivity of the IWCT phantom increases with temperature. It increases by a total of around 20 permittivity units for the frequency range. The relative permittivity increases at a slightly higher rate at frequencies above room temperature. The highest increase occurs around room temperature, probably as a result of the applying heat. The conductivity of the IWCT phantom decreases with temperature at lower frequencies and increases with temperature at higher frequencies. However, the change in conductivity is small and falls within the range of the measurements indicating a fairly constant conductivity with a slight change around room temperature due to heating.

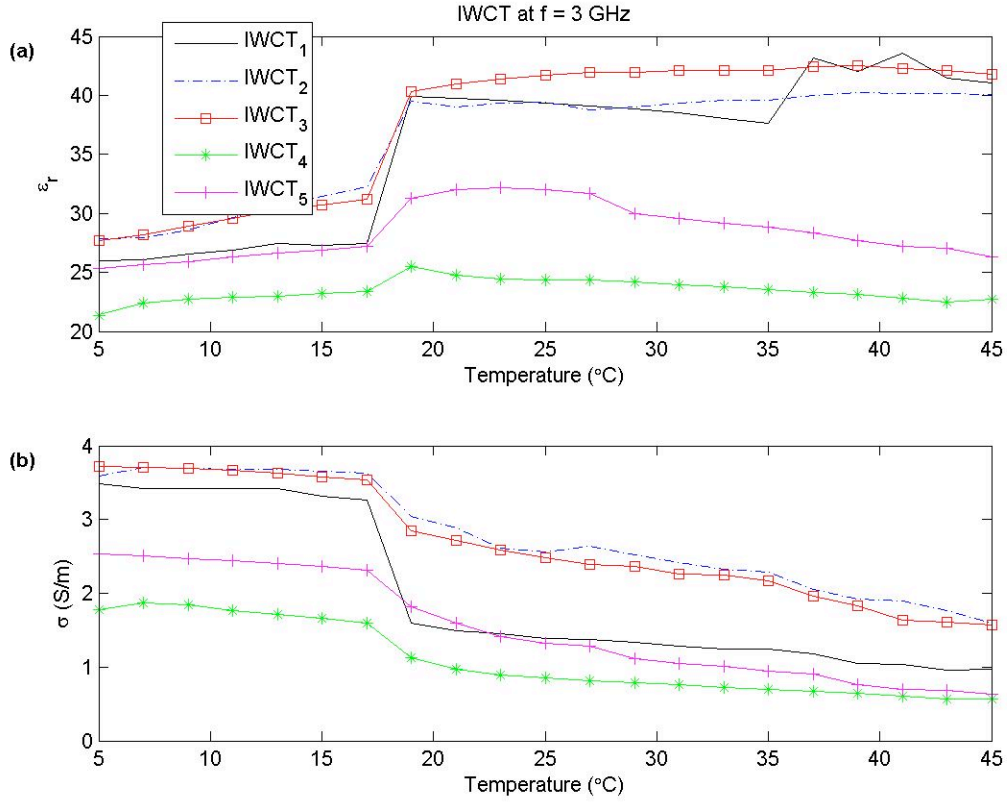

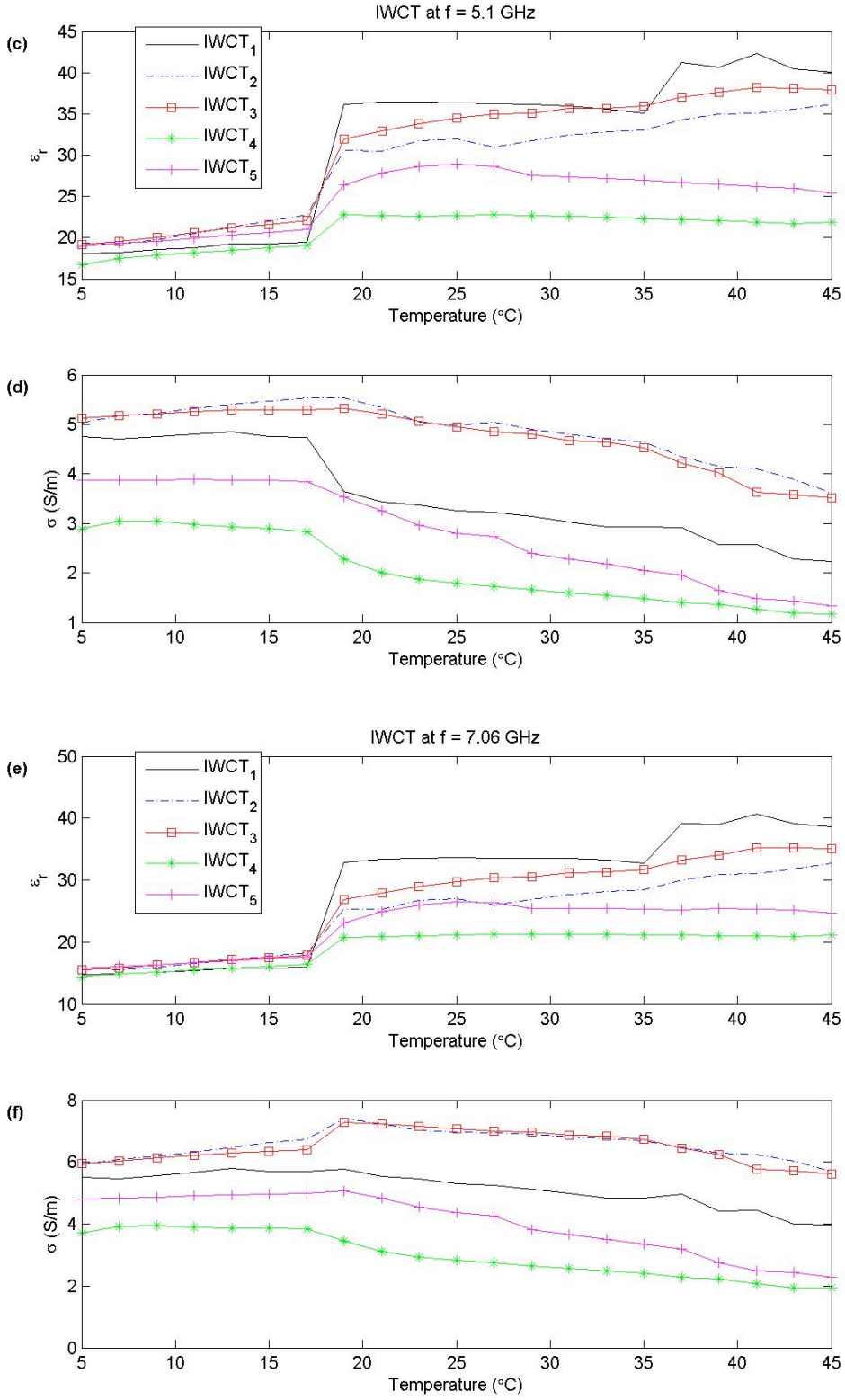
(c)
IWCT at f = 5.1 GHz
IWCT1
IWCT2
IWCT3
IWCT4
IWCT5
εr
Temperature (°C)
(d)
σ (S/m)
Temperature (°C)
(e)
IWCT at f = 7.06 GHz
IWCT1
IWCT2
IWCT3
IWCT4
IWCT5
εr
Temperature (°C)
(f)
σ (S/m)
Temperature (°C)

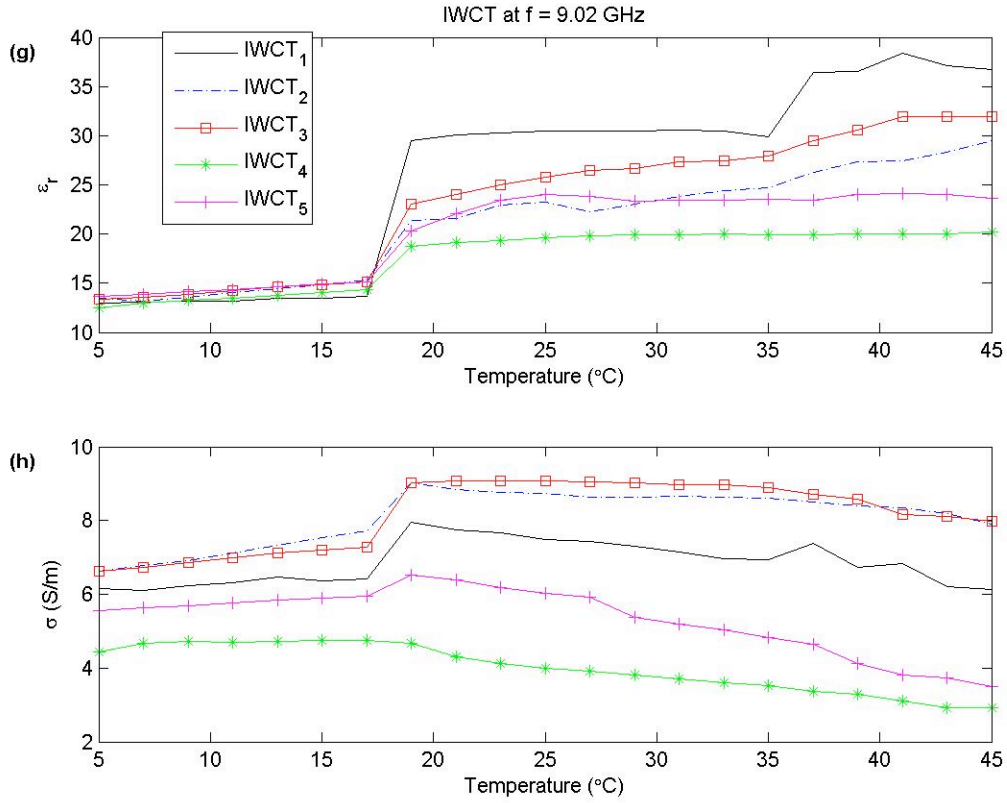
(g)
IWCT at f = 9.02 GHz
IWCT1
IWCT2
IWCT3
IWCT4
IWCT5
εr
Temperature (°C)
(h)
σ (S/m)
Temperature (°C)

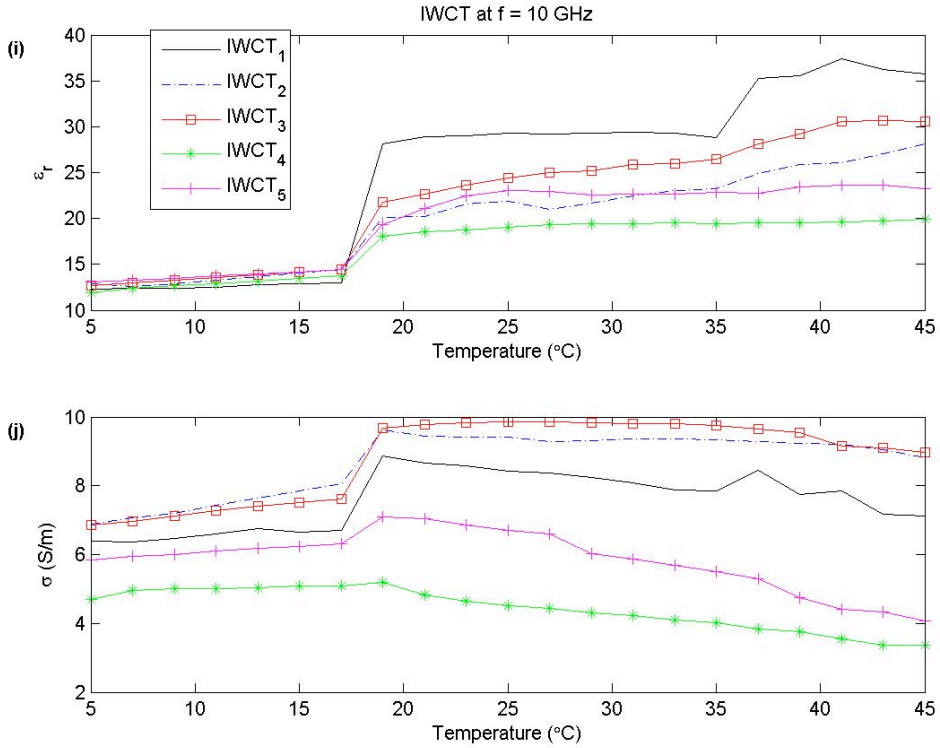

Figure 4.8: Measurements of the IWCT phantoms; temperature trends of permittivity ε_r at: *(a)* 3 GHz, *(c)* 5.01 GHz, *(e)* 7.06 GHz, *(g)* 9.02 GHz and *(i)* 10 GHz; and of conductivity σ at: *(b)* 3 GHz, *(d)* 5.01 GHz, *(f)* 7.06 GHz, *(h)* 9.02 GHz and *(j)* 10 GHz. The five curves represent the results of the measurements, which were repeated five times.

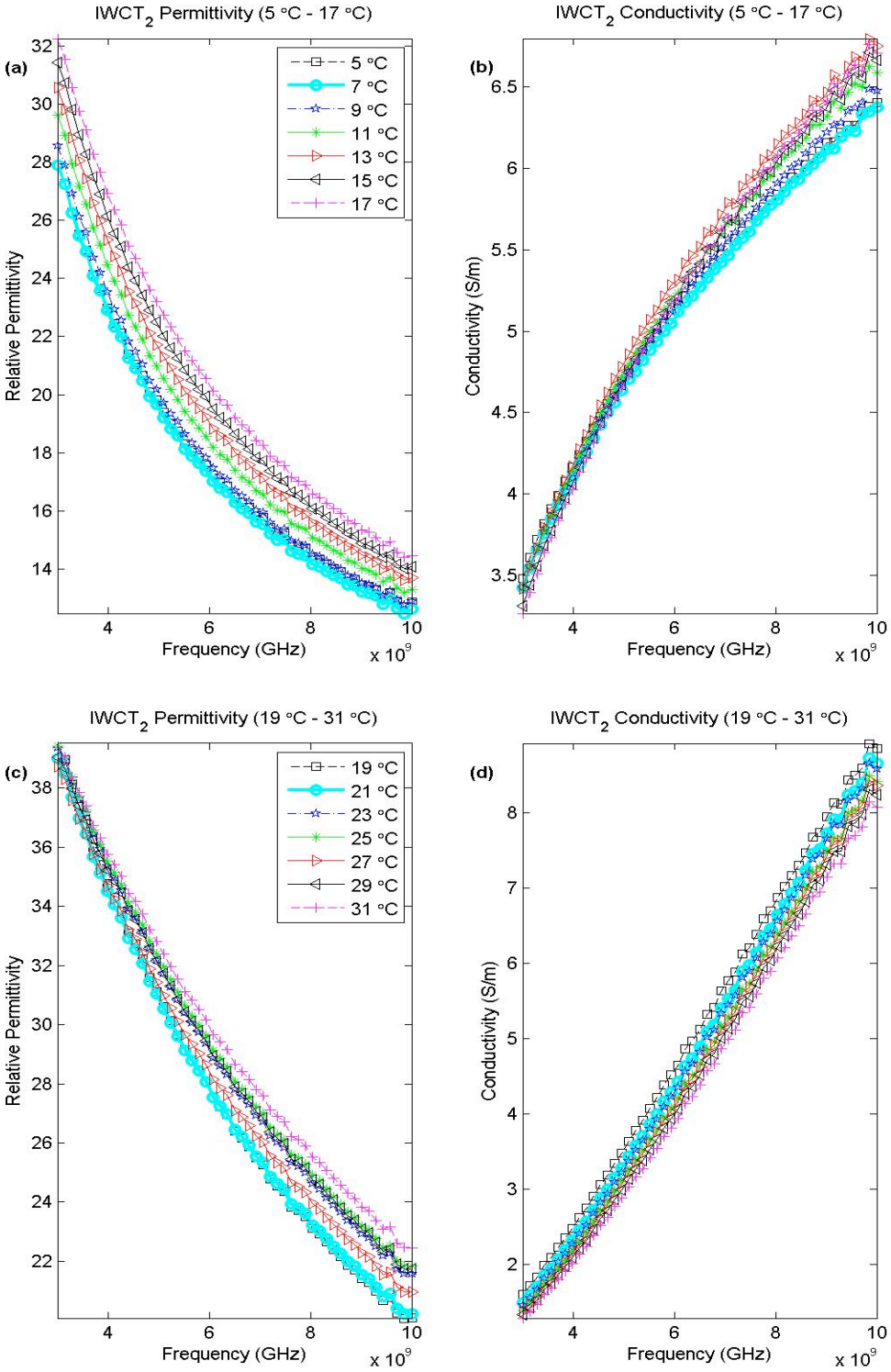
IWCT2 Permittivity (5 °C - 17 °C)
(a)
5 °C
7 °C
9 °C
11 °C
13 °C
15 °C
17 °C
Relative Permittivity
Frequency (GHz)
x 10^9
IWCT2 Conductivity (5 °C - 17 °C)
(b)
Conductivity (S/m)
Frequency (GHz)
x 10^9
IWCT2 Permittivity (19 °C - 31 °C)
(c)
19 °C
21 °C
23 °C
25 °C
27 °C
29 °C
31 °C
Relative Permittivity
Frequency (GHz)
x 10^9
IWCT2 Conductivity (19 °C - 31 °C)
(d)
Conductivity (S/m)
Frequency (GHz)
x 10^9

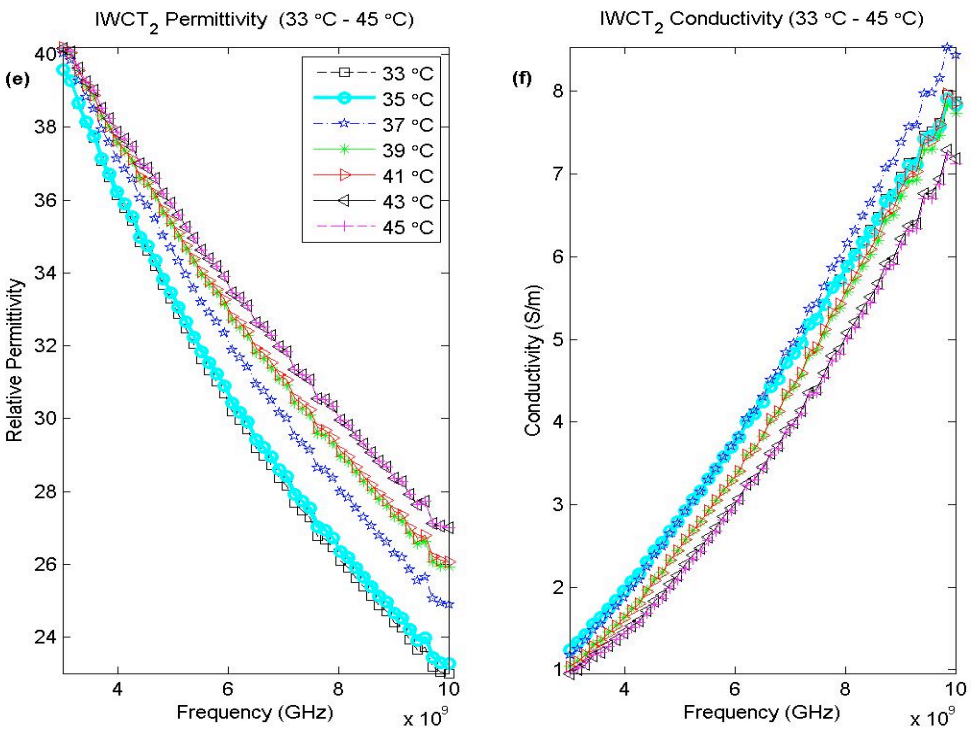

Figure 4.9: Second measurement of IWCT phantoms ($IWCT_2$); frequency trends of permittivity ε_r at: *(a)* 5 - 17 °C, *(c)* 19 - 31 °C and *(e)* 33 - 45 °C; and of conductivity σ at: *(b)* 5 - 17 °C, *(d)* 19 - 31 °C and *(f)* 33 - 45 °C.

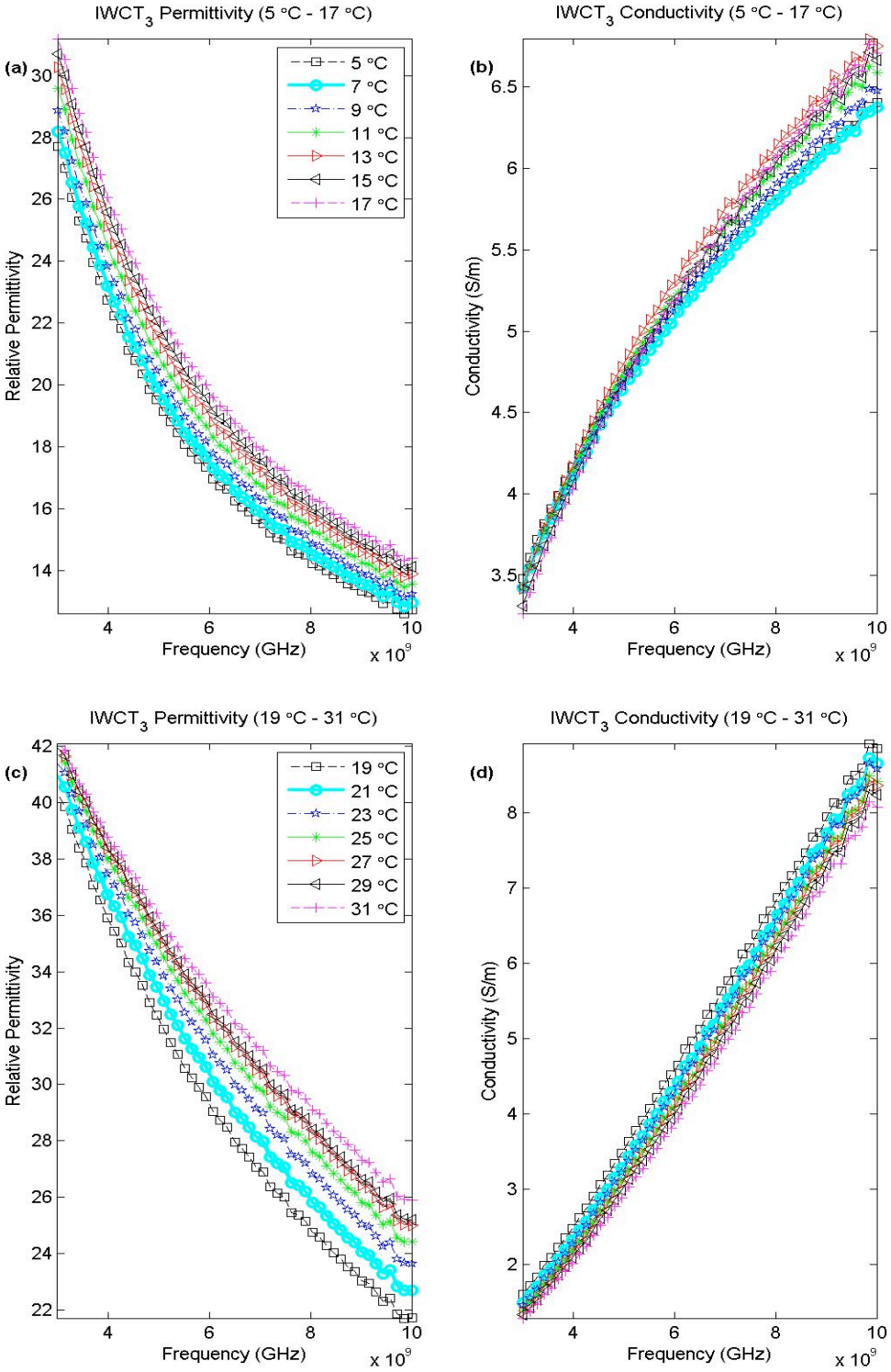
IWCT3 Permittivity (5 °C - 17 °C)
(a)
5 °C
7 °C
9 °C
11 °C
13 °C
15 °C
17 °C
Relative Permittivity
Frequency (GHz)
x 10^9
IWCT3 Conductivity (5 °C - 17 °C)
(b)
Conductivity (S/m)
Frequency (GHz)
x 10^9
IWCT3 Permittivity (19 °C - 31 °C)
(c)
19 °C
21 °C
23 °C
25 °C
27 °C
29 °C
31 °C
Relative Permittivity
Frequency (GHz)
x 10^9
IWCT3 Conductivity (19 °C - 31 °C)
(d)
Conductivity (S/m)
Frequency (GHz)
x 10^9

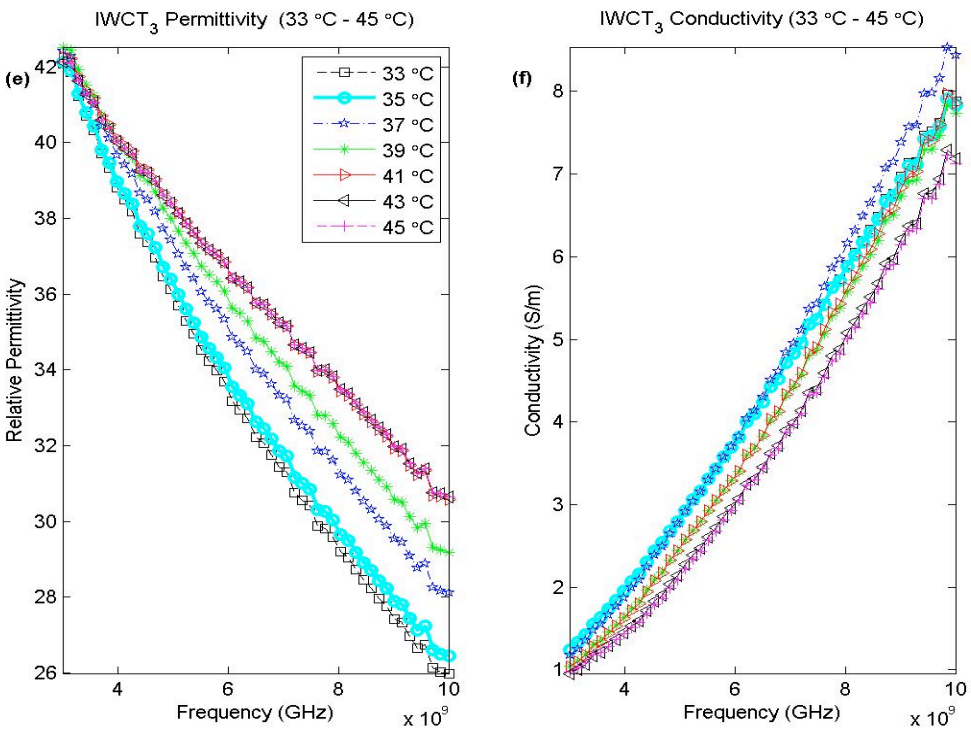

Figure 4.10: Third measurement of IWCT phantoms ($IWCT_3$); frequency trends of permittivity ε_r at: *(a)* 5 - 17 °C, *(c)* 19 - 31 °C and *(e)* 33 - 45 °C; and of conductivity σ at: *(b)* 5 - 17 °C, *(d)* 19 - 31 °C and *(f)* 33 - 45 °C.

C. HWCT-1 Phantom

Figure 4.11 *(a)* – *(j)* shows the temperature trends of the relative permittivity ε_r and the conductivity σ of the HWCT-1 phantoms at 3, 5.1, 7.06, 9.02 and 10 GHz. Each curve represents of one of the five measurements carried out with the HWCT-1 phantom. Figure 4.12 *(a)* – *(f)* and Figure 4.13 *(a)* – *(f)* show the frequency trends at different temperatures of the second and the third measurements, respectively. Each curve displays the relative permittivity and the conductivity of the HWCT-1 phantoms from 3 GHz to 10 GHz at each temperature. The figures are divided into three temperature ranges 5 – 17

°C, 19 – 31 °C and 33 – 45 °C for easier readability. The figures show a fairly constant relative permittivity at lower frequencies. The relative permittivity increases by around 10 – 15 units thereafter. The conductivity of the HWCT-1 decreases constantly with temperature by a total of around 3 S/m at lower frequencies. It decreases at a slightly lower rate at higher frequencies and it is constant at around 10 GHz.

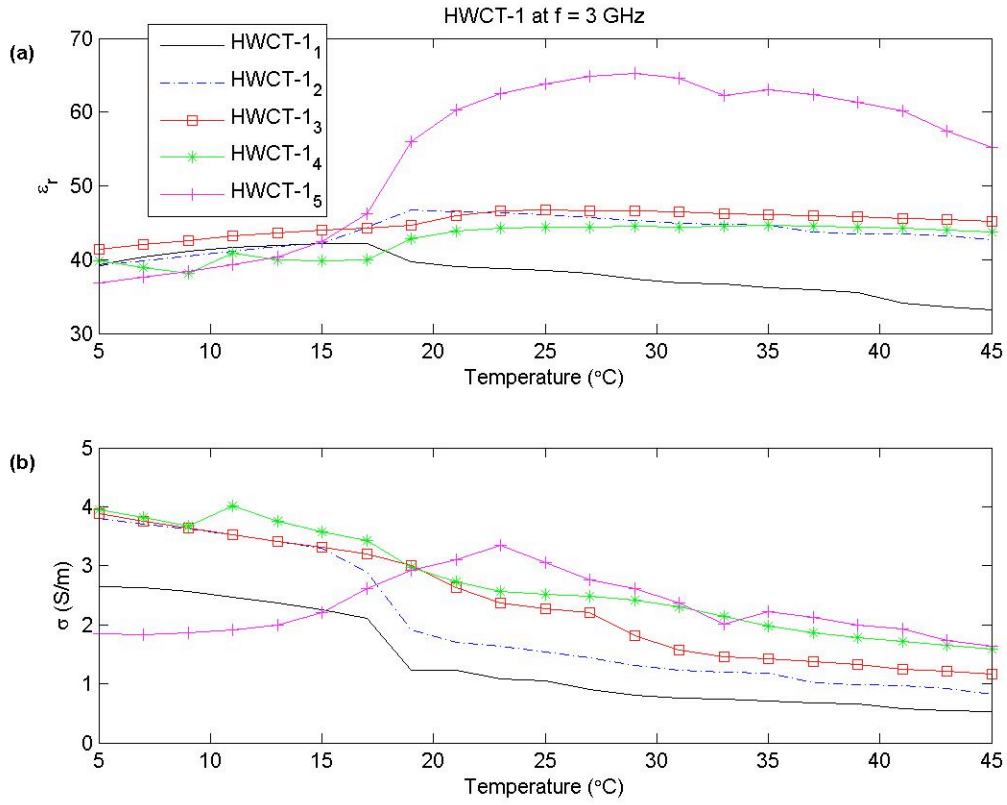

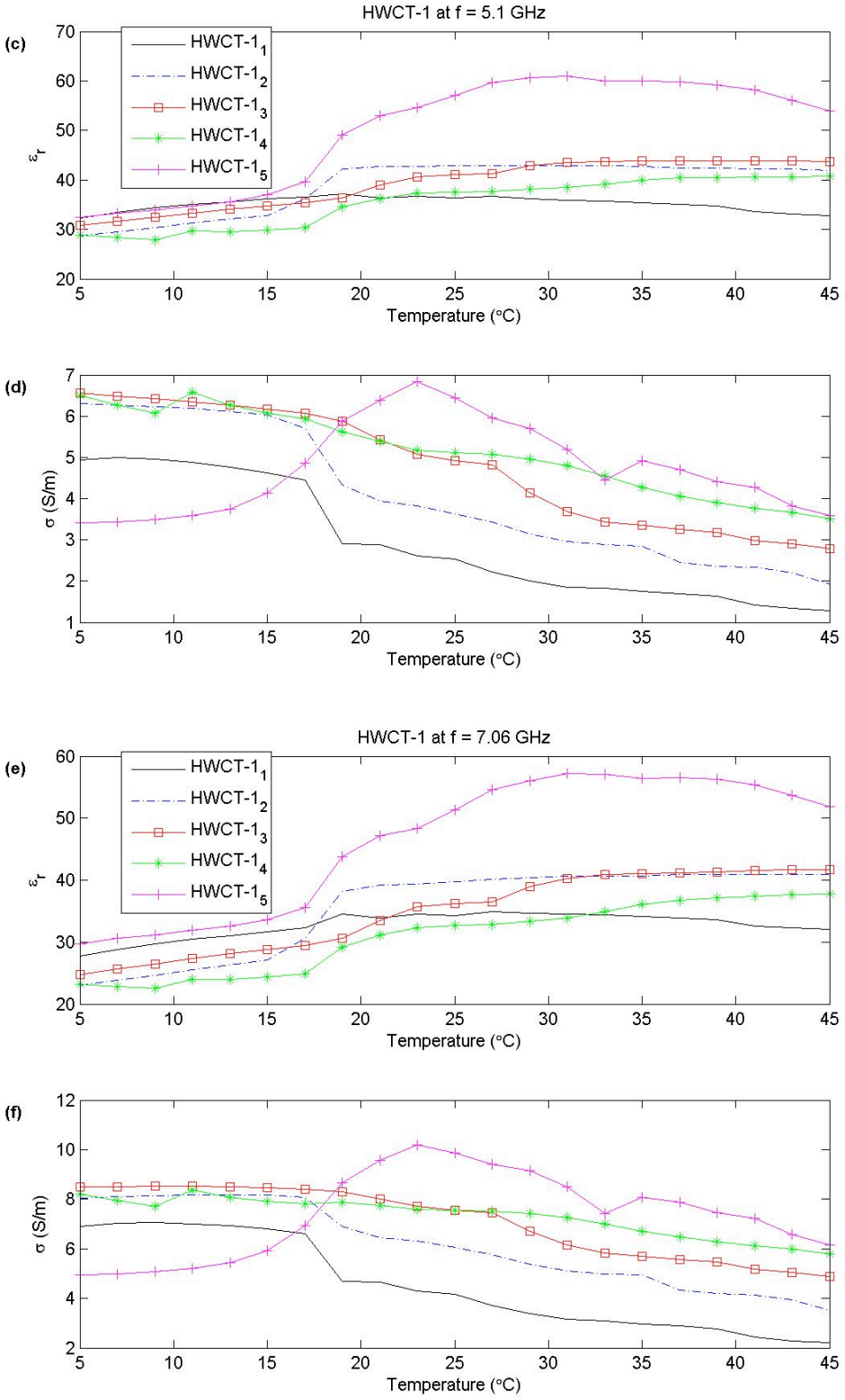
HWCT-1 at f = 5.1 GHz
(c)
HWCT-1$_1$
HWCT-1$_2$
HWCT-1$_3$
HWCT-1$_4$
HWCT-1$_5$
ε_r
Temperature (°C)
(d)
σ (S/m)
Temperature (°C)
HWCT-1 at f = 7.06 GHz
(e)
HWCT-1$_1$
HWCT-1$_2$
HWCT-1$_3$
HWCT-1$_4$
HWCT-1$_5$
ε_r
Temperature (°C)
(f)
σ (S/m)
Temperature (°C)

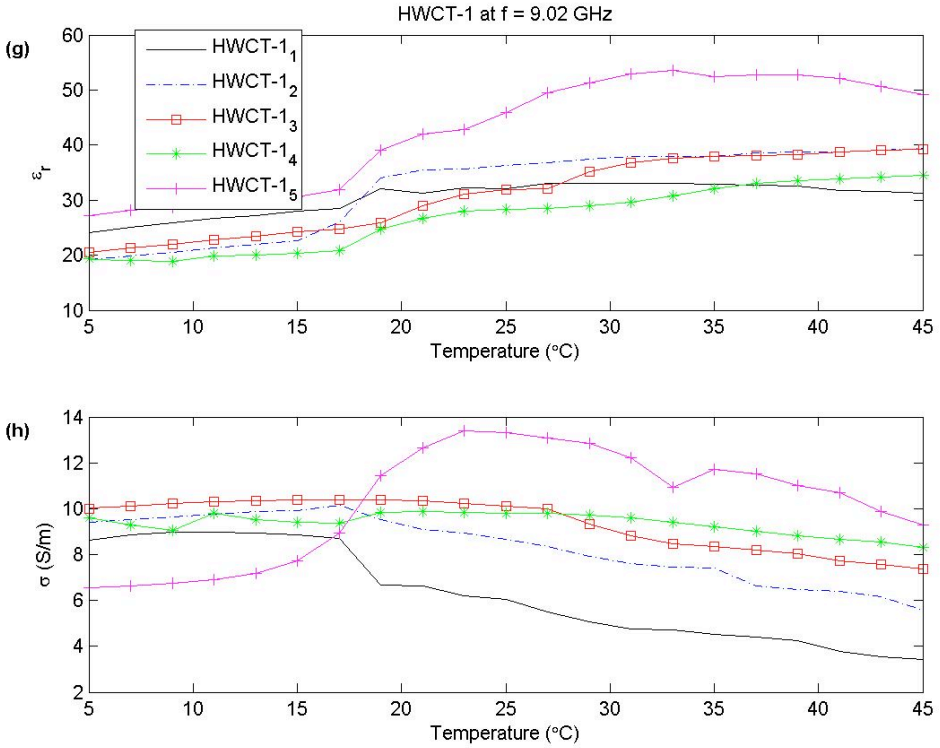
HWCT-1 at f = 9.02 GHz
(g)
HWCT-1$_1$
HWCT-1$_2$
HWCT-1$_3$
HWCT-1$_4$
HWCT-1$_5$
ε_r
Temperature (°C)
(h)
σ (S/m)
Temperature (°C)

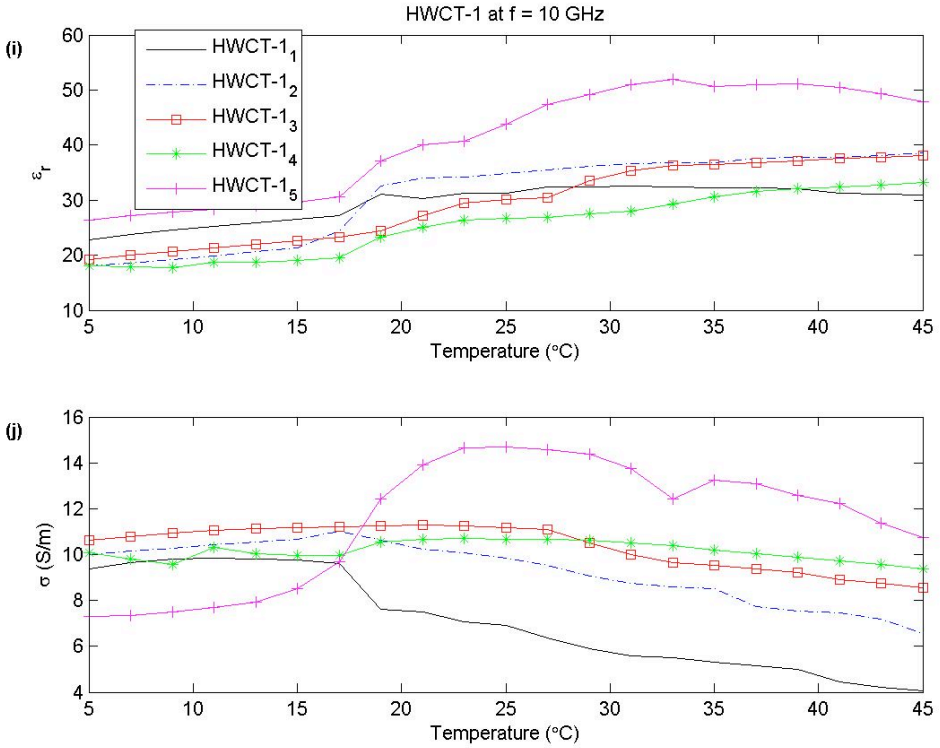

Figure 4.11: Measurements of the HWCT-1 phantoms; temperature trends of permittivity ε_r at: *(a)* 3 GHz, *(c)* 5.01 GHz, *(e)* 7.06 GHz, *(g)* 9.02 GHz and *(i)* 10 GHz; and of conductivity σ at: *(b)* 3 GHz, *(d)* 5.01 GHz, *(f)* 7.06 GHz, *(h)* 9.02 GHz and *(j)* 10 GHz. The five curves represent the results of the measurements, which were repeated five times.

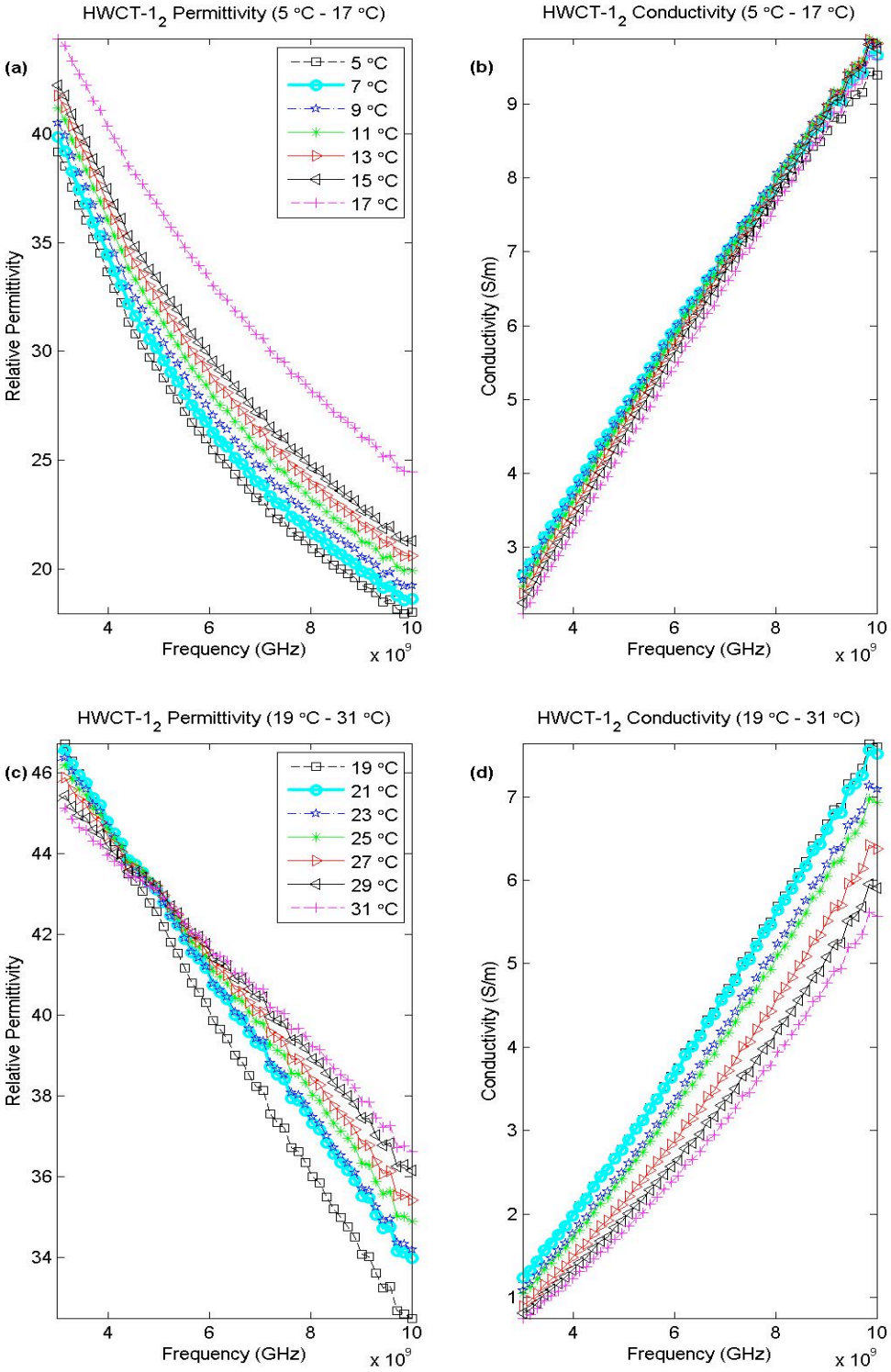
HWCT-1$_2$ Permittivity (5 °C - 17 °C)
(a)
5 °C
7 °C
9 °C
11 °C
13 °C
15 °C
17 °C
Relative Permittivity
Frequency (GHz)
x 10^9
HWCT-1$_2$ Conductivity (5 °C - 17 °C)
(b)
Conductivity (S/m)
Frequency (GHz)
x 10^9
HWCT-1$_2$ Permittivity (19 °C - 31 °C)
(c)
19 °C
21 °C
23 °C
25 °C
27 °C
29 °C
31 °C
Relative Permittivity
Frequency (GHz)
x 10^9
HWCT-1$_2$ Conductivity (19 °C - 31 °C)
(d)
Conductivity (S/m)
Frequency (GHz)
x 10^9

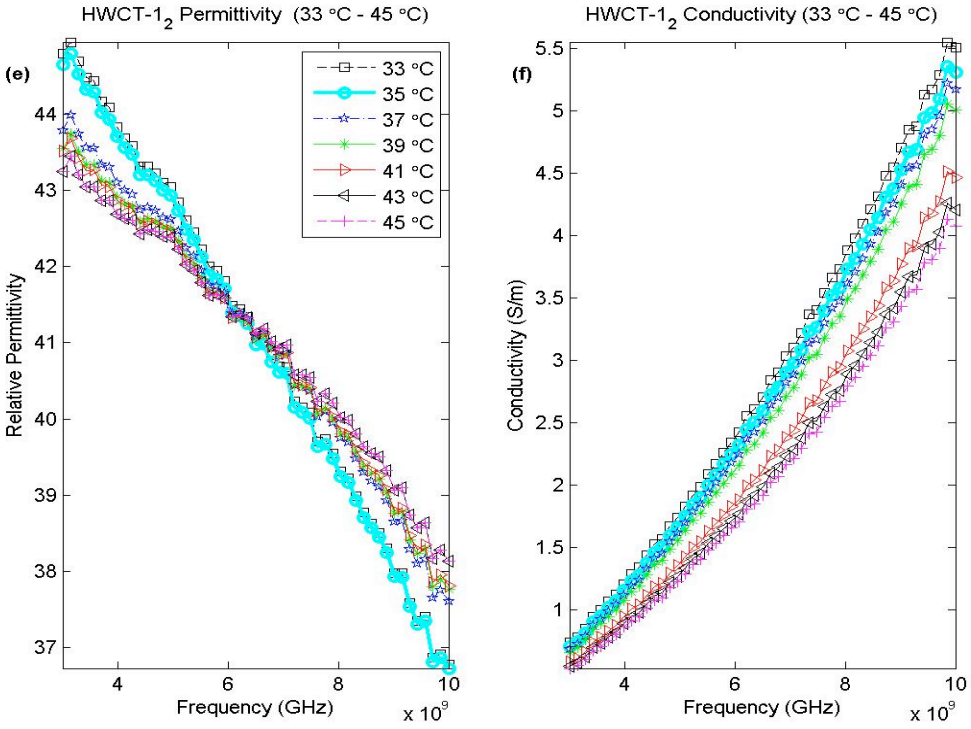

Figure 4.12: Second measurement of HWCT-1 phantoms (HWCT-1_2); frequency trends of permittivity ε_r at: *(a)* 5 - 17 °C, *(c)* 19 - 31 °C and *(e)* 33 - 45 °C; and of conductivity σ at: *(b)* 5 - 17 °C, *(d)* 19 - 31 °C and *(f)* 33 - 45 °C.

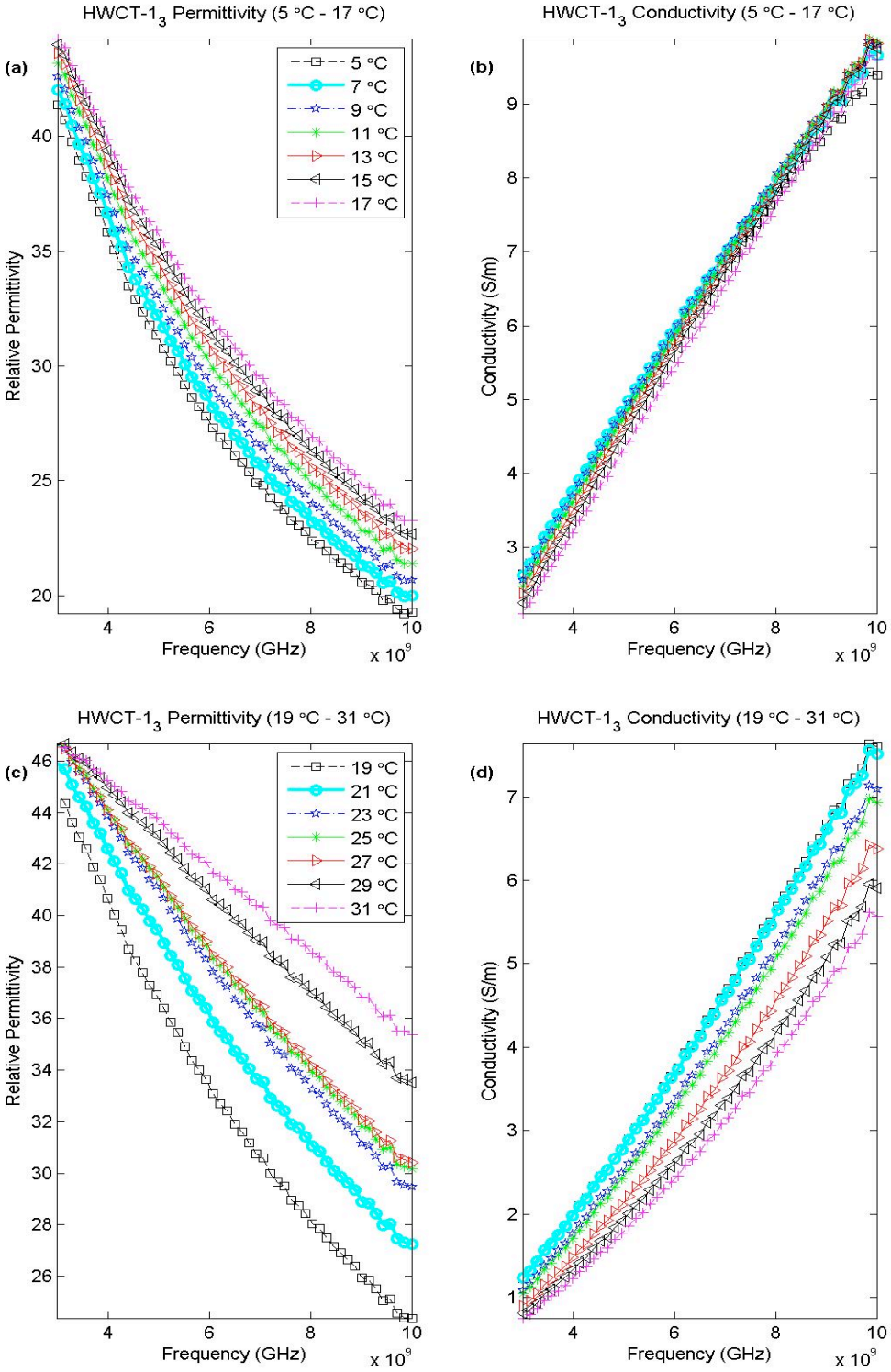
HWCT-1$_3$ Permittivity (5 °C - 17 °C)
(a)
5 °C
7 °C
9 °C
11 °C
13 °C
15 °C
17 °C
Relative Permittivity
Frequency (GHz)
x 10^9
HWCT-1$_3$ Conductivity (5 °C - 17 °C)
(b)
Conductivity (S/m)
Frequency (GHz)
x 10^9
HWCT-1$_3$ Permittivity (19 °C - 31 °C)
(c)
19 °C
21 °C
23 °C
25 °C
27 °C
29 °C
31 °C
Relative Permittivity
Frequency (GHz)
x 10^9
HWCT-1$_3$ Conductivity (19 °C - 31 °C)
(d)
Conductivity (S/m)
Frequency (GHz)
x 10^9

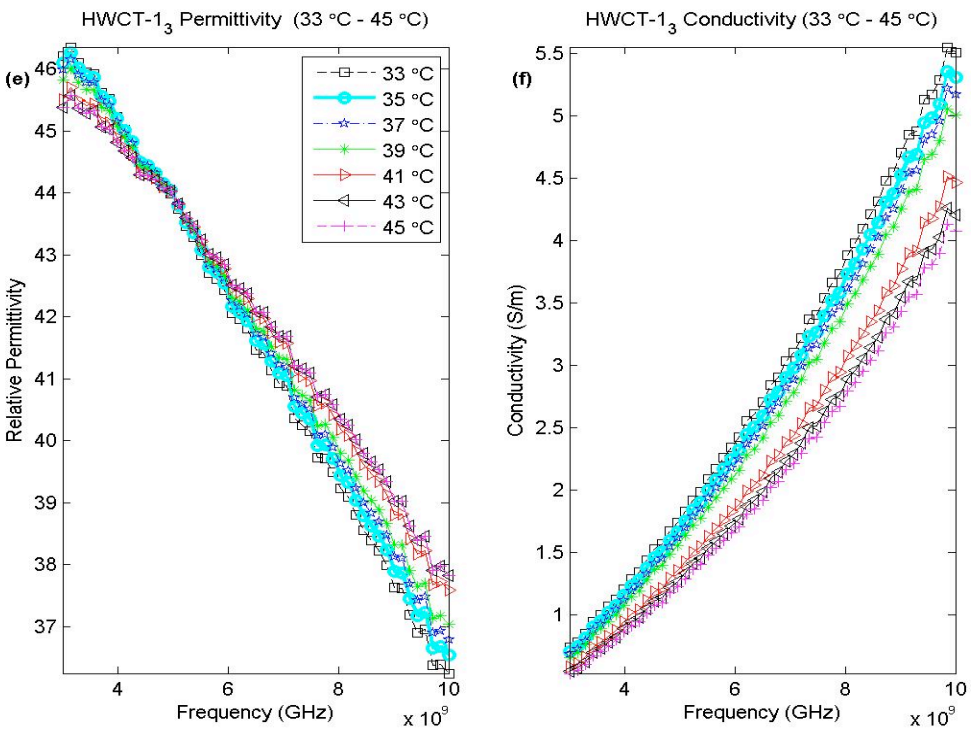

Figure 4.13: Third measurement of HWCT-1 phantoms (HWCT-1_3); frequency trends of permittivity ε_r at: *(a)* 5 - 17 °C, *(c)* 19 - 31 °C and *(e)* 33 - 45 °C; and of conductivity σ at: *(b)* 5 - 17 °C, *(d)* 19 - 31 °C and *(f)* 33 - 45 °C.

D. HWCT-2 Phantom

Figure 4.14 *(a) – (j)* show the temperature trends of the relative permittivity ε_r and the conductivity σ of the HWCT-2 phantoms at 3, 5.1, 7.06, 9.02 and 10 GHz. Each curve represents one of the five measurements carried out with the HWCT-2 phantom. Figure 4.15 *(a) – (f)* and Figure 4.16 *(a) – (f)* show the frequency trends at different temperatures of the first and the fifth measurements, respectively. Each curve displays the relative permittivity and the conductivity of the HWCT-2 phantoms from 3 GHz to 10 GHz at each temperature. The figures are divided into three temperature ranges 5 – 17

°C, 19 – 31 °C and 33 – 45 °C for easier readability. The relative permittivity of the HWCT-2 phantom increases by around 10 – 20 units with temperature. It increases at a higher rate at higher frequencies, showing very little increase at higher temperatures and lower frequencies. The conductivity of the HWCT-2 phantom decreases by a total of around 2 S/m with temperature at lower frequencies. It increases by around 2 S/m at higher frequencies. The HWCT-2 phantom thus has a cross-over point at around 5.5 GHz.

For all the gelatin-based phantoms the relative permittivity increases with temperature. On the other hand, the conductivity increases for the LWCT phantom and remains constant or decreases for the other three phantoms. The different properties of the LWCT phantom from the others can be explained by the fact that the main solvent in this phantom is ethylene glycol instead of water. Applying heat to the phantoms caused a significant change in properties that can be observed around room temperature for the LWCT and the IWCT phantoms. These phantoms that have a lower water content seem to have a less stable change in the dielectric properties, which leads to the assumption that water plays a role in the change of the dielectric properties of synthesized materials.

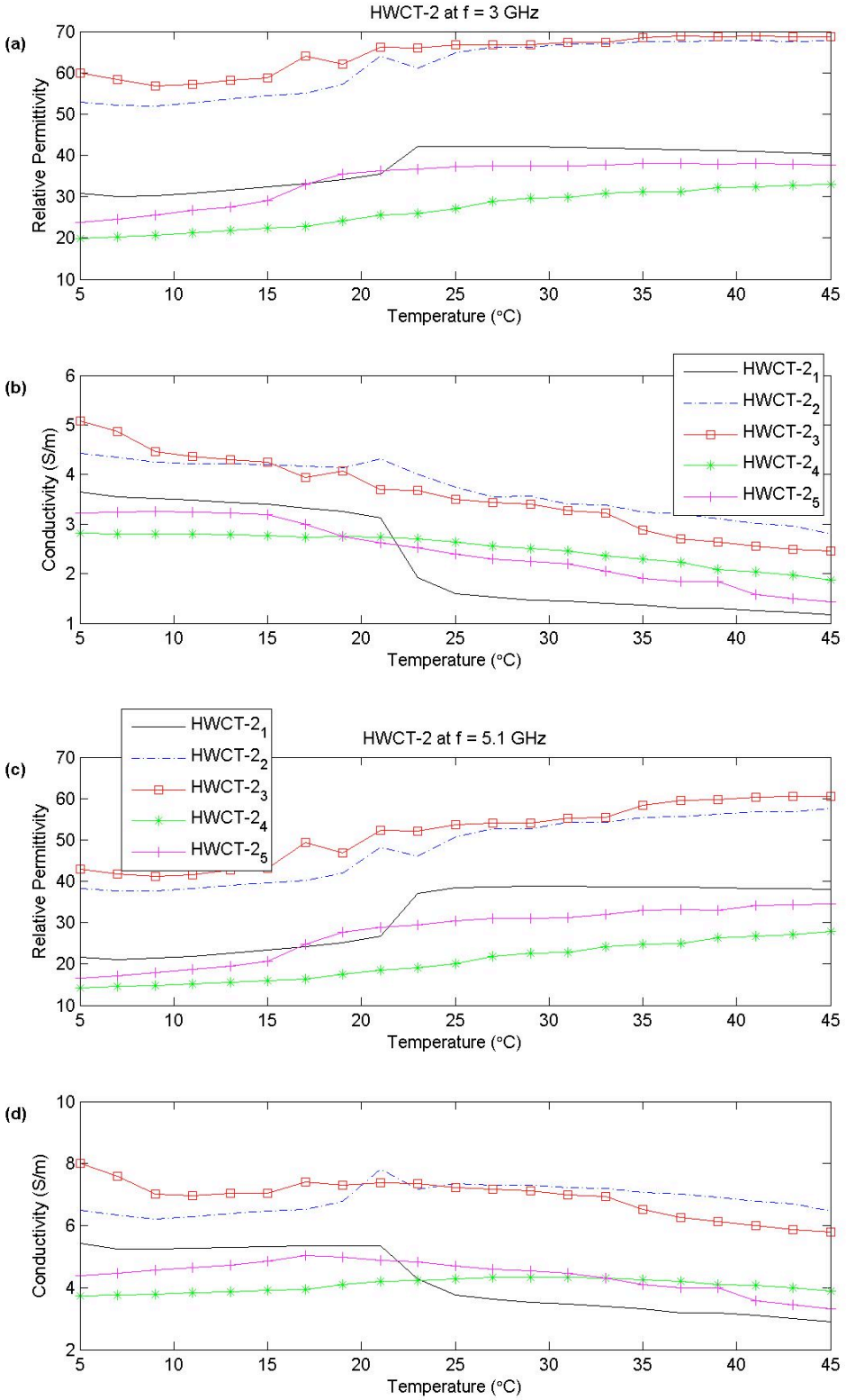
HWCT-2 at f = 3 GHz
(a)
Relative Permittivity
Temperature (°C)
(b)
Conductivity (S/m)
Temperature (°C)
HWCT-2 at f = 5.1 GHz
(c)
Relative Permittivity
Temperature (°C)
(d)
Conductivity (S/m)
Temperature (°C)
HWCT-2$_1$
HWCT-2$_2$
HWCT-2$_3$
HWCT-2$_4$
HWCT-2$_5$

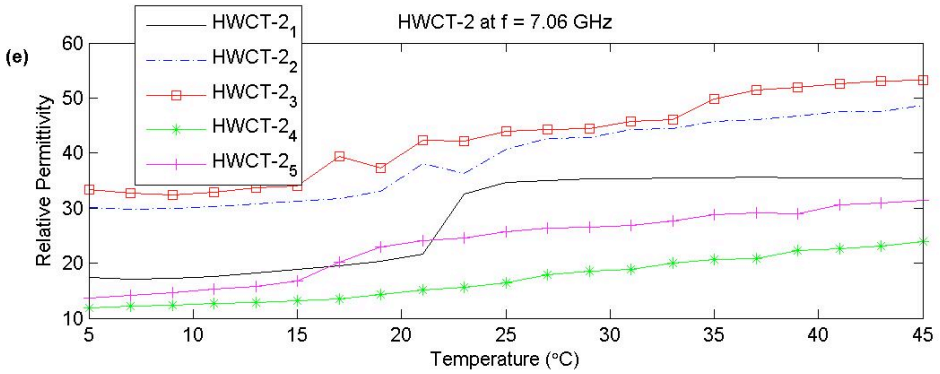
(e)
HWCT-2 at f = 7.06 GHz
HWCT-2$_1$
HWCT-2$_2$
HWCT-2$_3$
HWCT-2$_4$
HWCT-2$_5$
Relative Permittivity
Temperature (°C)

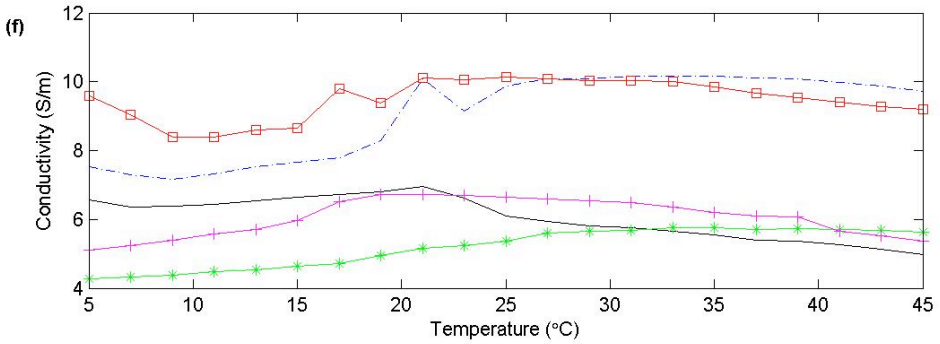
(f)
Conductivity (S/m)
Temperature (°C)

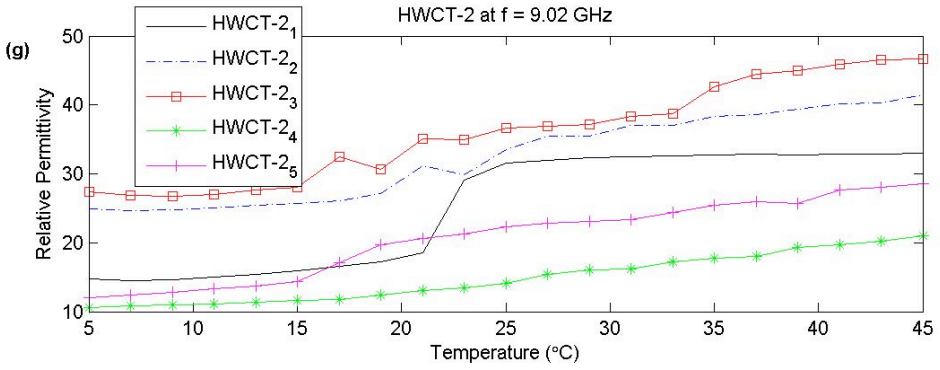
(g)
HWCT-2 at f = 9.02 GHz
HWCT-2$_1$
HWCT-2$_2$
HWCT-2$_3$
HWCT-2$_4$
HWCT-2$_5$
Relative Permittivity
Temperature (°C)

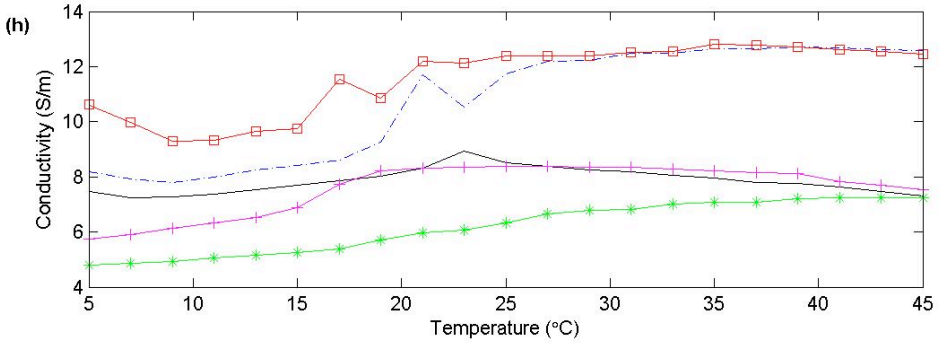
(h)
Conductivity (S/m)
Temperature (°C)

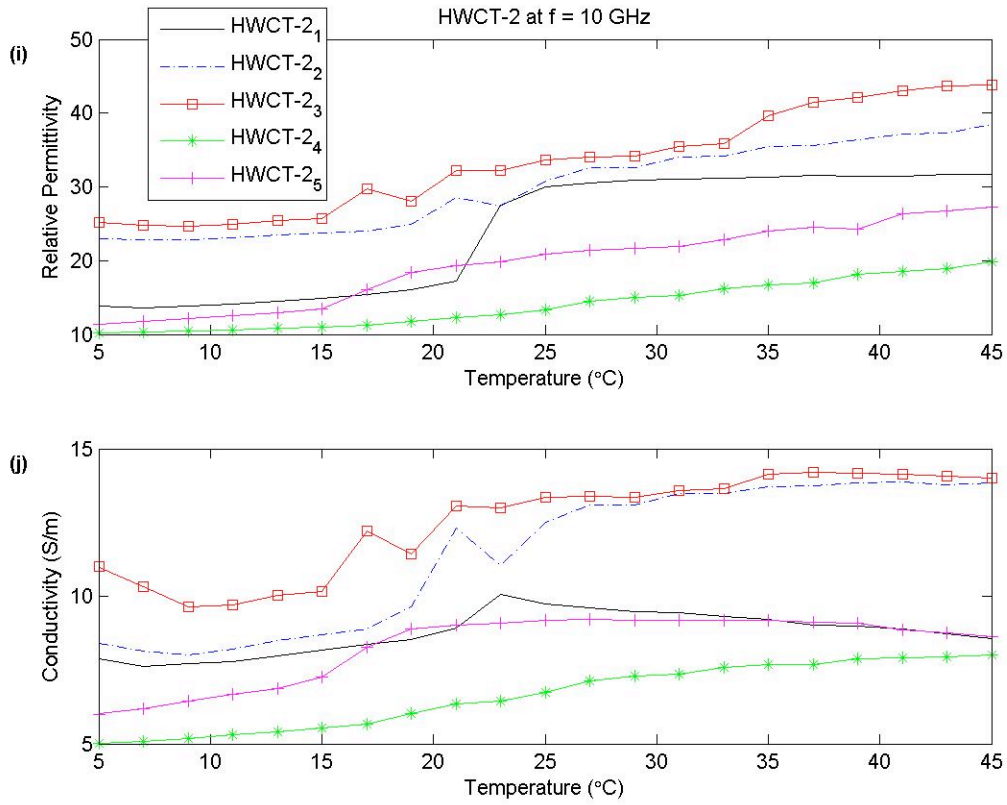

Figure 4.14: Measurements of the HWCT-2 phantoms; temperature trends of permittivity ε_r at: *(a)* 3 GHz, *(c)* 5.01 GHz, *(e)* 7.06 GHz, *(g)* 9.02 GHz and *(i)* 10 GHz; and of conductivity σ at: *(b)* 3 GHz, *(d)* 5.01 GHz, *(f)* 7.06 GHz, *(h)* 9.02 GHz and *(j)* 10 GHz. The five curves represent the results of the measurements, which were repeated five times.

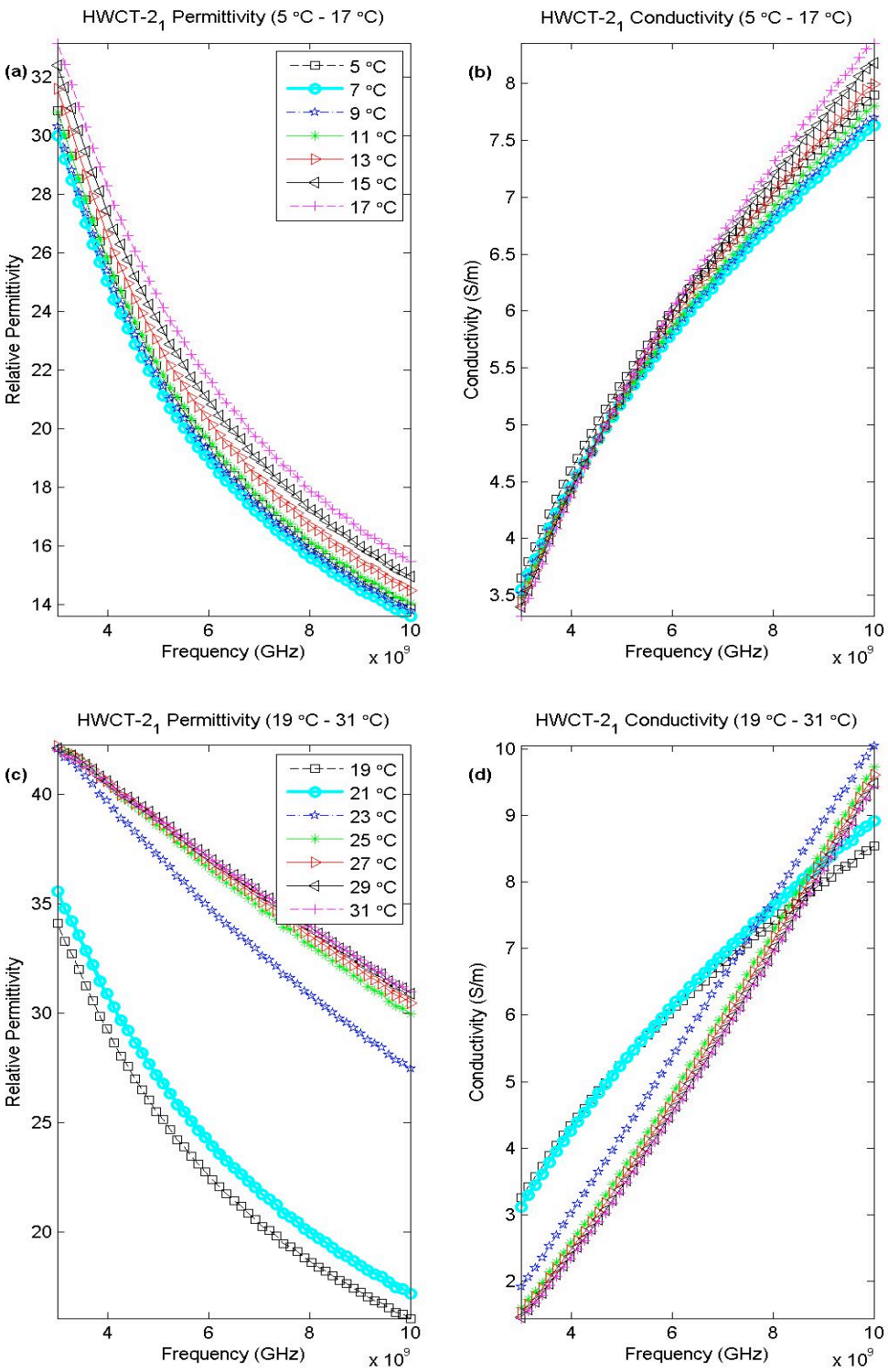
HWCT-2$_1$ Permittivity (5 °C - 17 °C)
(a)
5 °C
7 °C
9 °C
11 °C
13 °C
15 °C
17 °C
Relative Permittivity
Frequency (GHz)
x 10^9
HWCT-2$_1$ Conductivity (5 °C - 17 °C)
(b)
Conductivity (S/m)
Frequency (GHz)
x 10^9
HWCT-2$_1$ Permittivity (19 °C - 31 °C)
(c)
19 °C
21 °C
23 °C
25 °C
27 °C
29 °C
31 °C
Relative Permittivity
Frequency (GHz)
x 10^9
HWCT-2$_1$ Conductivity (19 °C - 31 °C)
(d)
Conductivity (S/m)
Frequency (GHz)
x 10^9

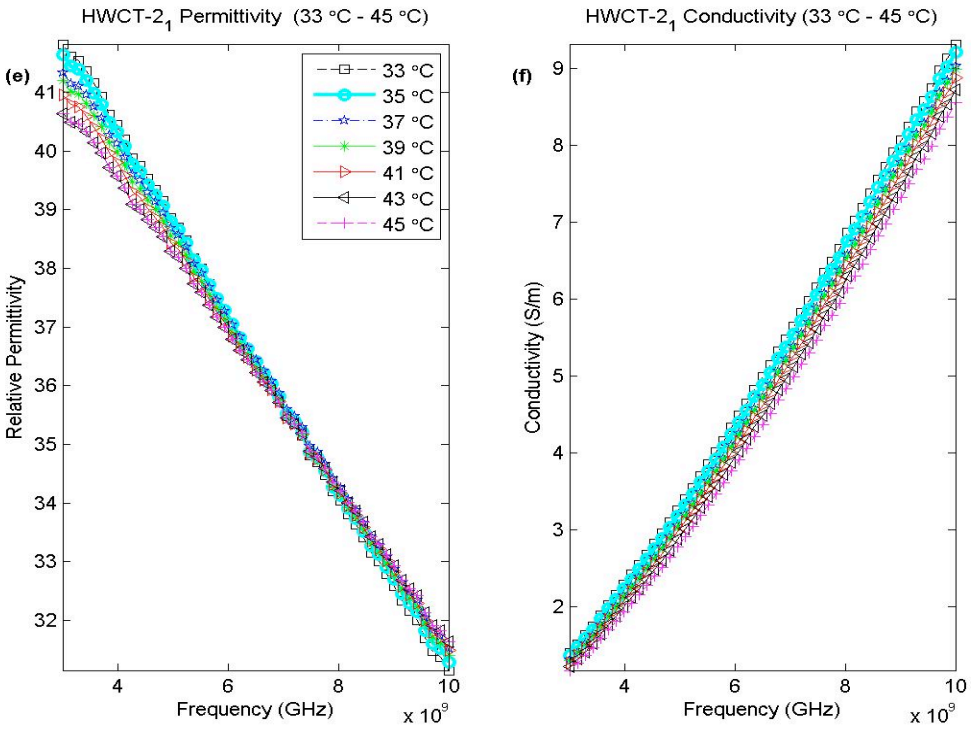

Figure 4.15: First measurement of HCWT-2 phantoms (HWCT-2$_1$); frequency trends of permittivity ε_r at: *(a)* 5 - 17 °C, *(c)* 19 - 31 °C and *(e)* 33 - 45 °C; and of conductivity σ at: *(b)* 5 - 17 °C, *(d)* 19 - 31 °C and *(f)* 33 - 45 °C.

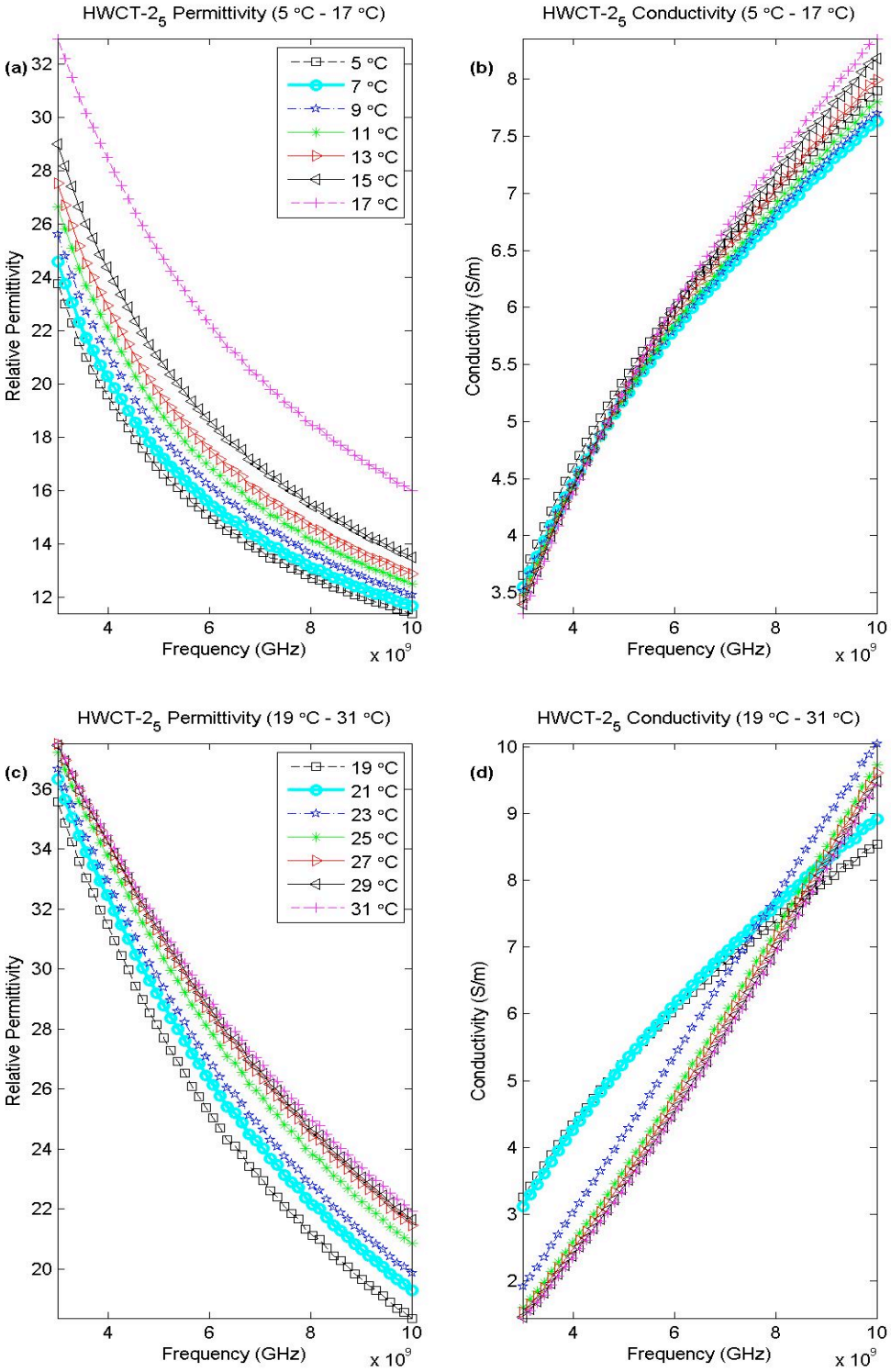
HWCT-2$_5$ Permittivity (5 °C - 17 °C)
(a)
5 °C
7 °C
9 °C
11 °C
13 °C
15 °C
17 °C
Relative Permittivity
Frequency (GHz)
x 10^9
HWCT-2$_5$ Conductivity (5 °C - 17 °C)
(b)
Conductivity (S/m)
Frequency (GHz)
x 10^9
HWCT-2$_5$ Permittivity (19 °C - 31 °C)
(c)
19 °C
21 °C
23 °C
25 °C
27 °C
29 °C
31 °C
Relative Permittivity
Frequency (GHz)
x 10^9
HWCT-2$_5$ Conductivity (19 °C - 31 °C)
(d)
Conductivity (S/m)
Frequency (GHz)
x 10^9

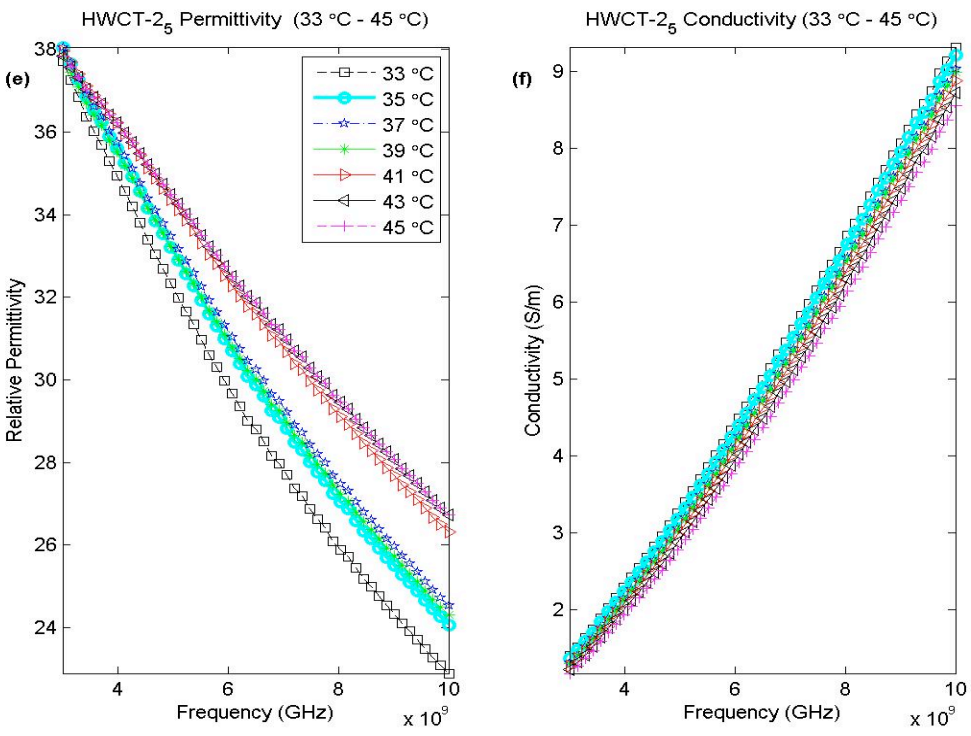

Figure 4.16: Fifth measurement of HWCT-2 phantoms (HWCT-2_5); frequency trends of permittivity ε_r at: *(a)* 5 - 17 °C, *(c)* 19 - 31 °C and *(e)* 33 - 45 °C; and of conductivity σ at: *(b)* 5 - 17 °C, *(d)* 19 - 31 °C and *(f)* 33 - 45 °C.

E. Alginate-based Tumor Phantom

Figure 4.17 *(a) – (j)* show the temperature trends of the relative permittivity ε_r and the conductivity σ of the alginate-based tumor phantoms at 3, 5.1, 7.06, 9.02 and 10 GHz. Each curve represents one of the five measurements, carried out for the alginate-based phantom. Figure 4.18 *(a) – (f)* and Figure 4.19 *(a) – (f)* show the frequency trends at different temperatures of the second and the fifth measurements, respectively. Each curve displays the relative permittivity and the conductivity of the alginate-based tumor phantom from 3 GHz to 10 GHz at each temperature. The figures are divided into three

temperature ranges 5 – 17 °C, 19 – 31 °C and 33 – 45 °C for easier readability. The relative permittivity of this phantom decreases with temperature. The relative permittivity decreases faster at the lower frequencies. It decreases by around 20 units at 3 GHz and by around only 6 units at 10 GHz. The conductivity is relatively constant at lower frequencies and decreases by around 5 S/m at higher frequencies. This trend is consistent with that reported for saline, the solvent of this phantom, at 9.14 GHz and 3.25 GHz in [6].

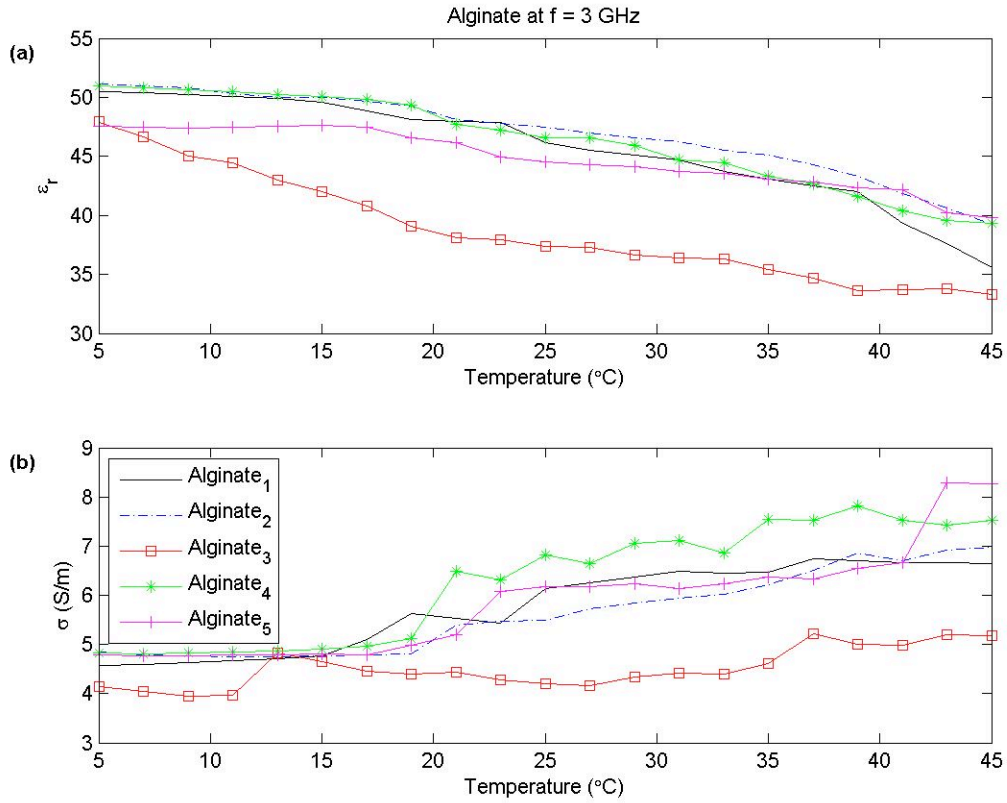

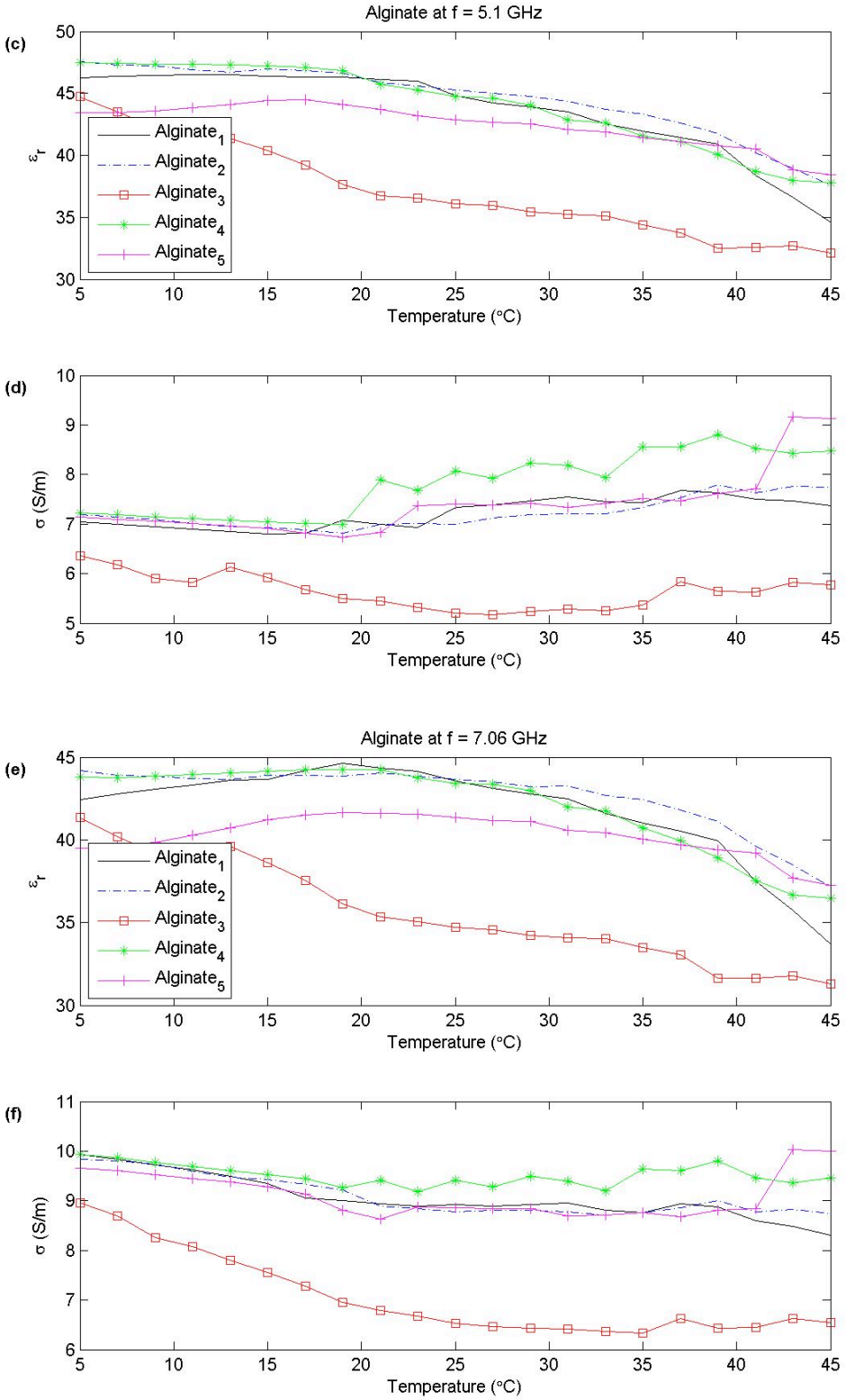
Alginate at f = 5.1 GHz
(c)
ε_r
Alginate$_1$
Alginate$_2$
Alginate$_3$
Alginate$_4$
Alginate$_5$
Temperature (°C)
(d)
σ (S/m)
Temperature (°C)
Alginate at f = 7.06 GHz
(e)
ε_r
Alginate$_1$
Alginate$_2$
Alginate$_3$
Alginate$_4$
Alginate$_5$
Temperature (°C)
(f)
σ (S/m)
Temperature (°C)

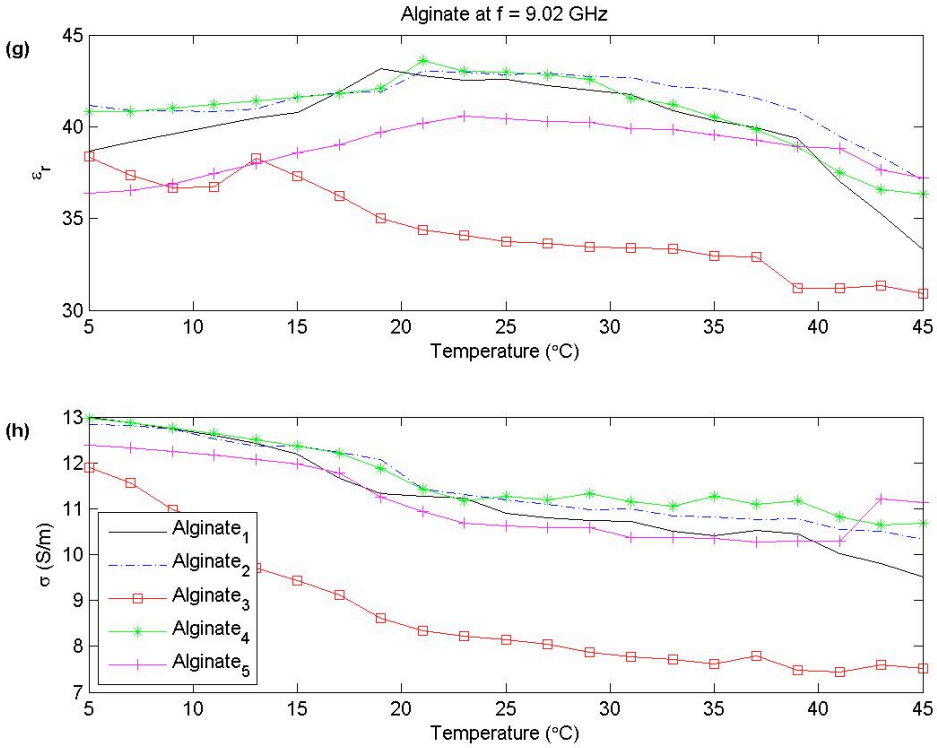
Alginate at f = 9.02 GHz
(g)
ε_r
Temperature (°C)
(h)
σ (S/m)
Alginate$_1$
Alginate$_2$
Alginate$_3$
Alginate$_4$
Alginate$_5$
Temperature (°C)

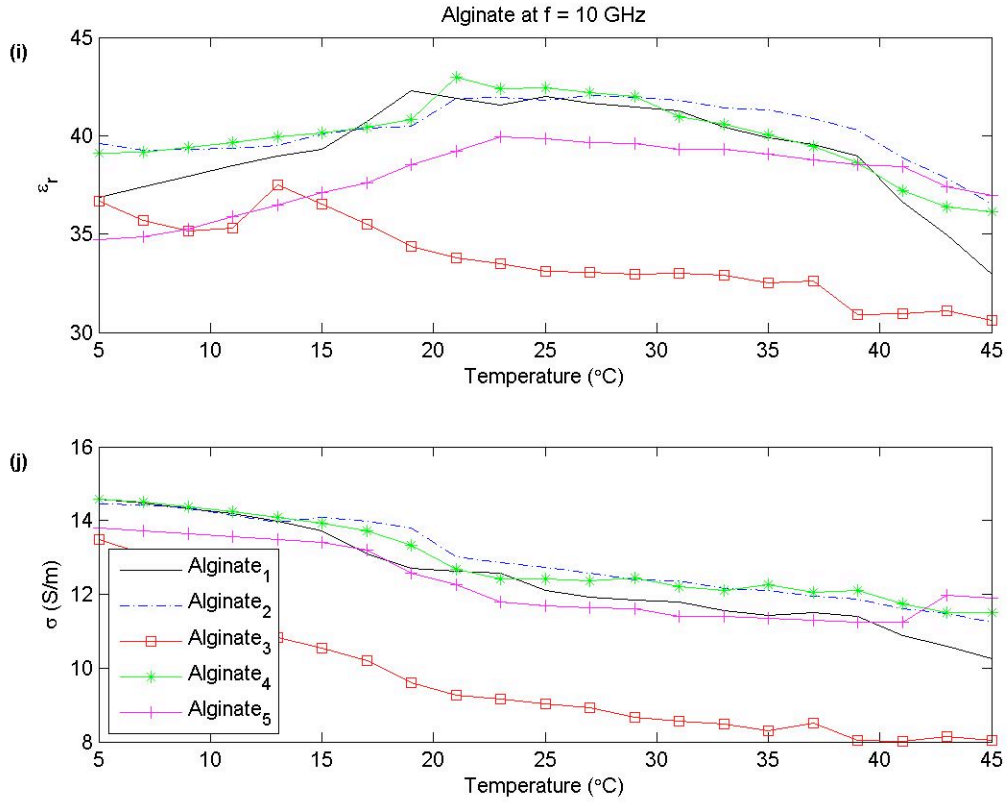

Figure 4.17: Measurements of the alginate-based tumor phantoms; temperature trends of permittivity ε_r at: *(a)* 3 GHz, *(c)* 5.01 GHz, *(e)* 7.06 GHz, *(g)* 9.02 GHz and *(i)* 10 GHz; and of conductivity σ at: *(b)* 3 GHz, *(d)* 5.01 GHz, *(f)* 7.06 GHz, *(h)* 9.02 GHz and *(j)* 10 GHz. The five curves represent the results of the measurements, which were repeated five times.

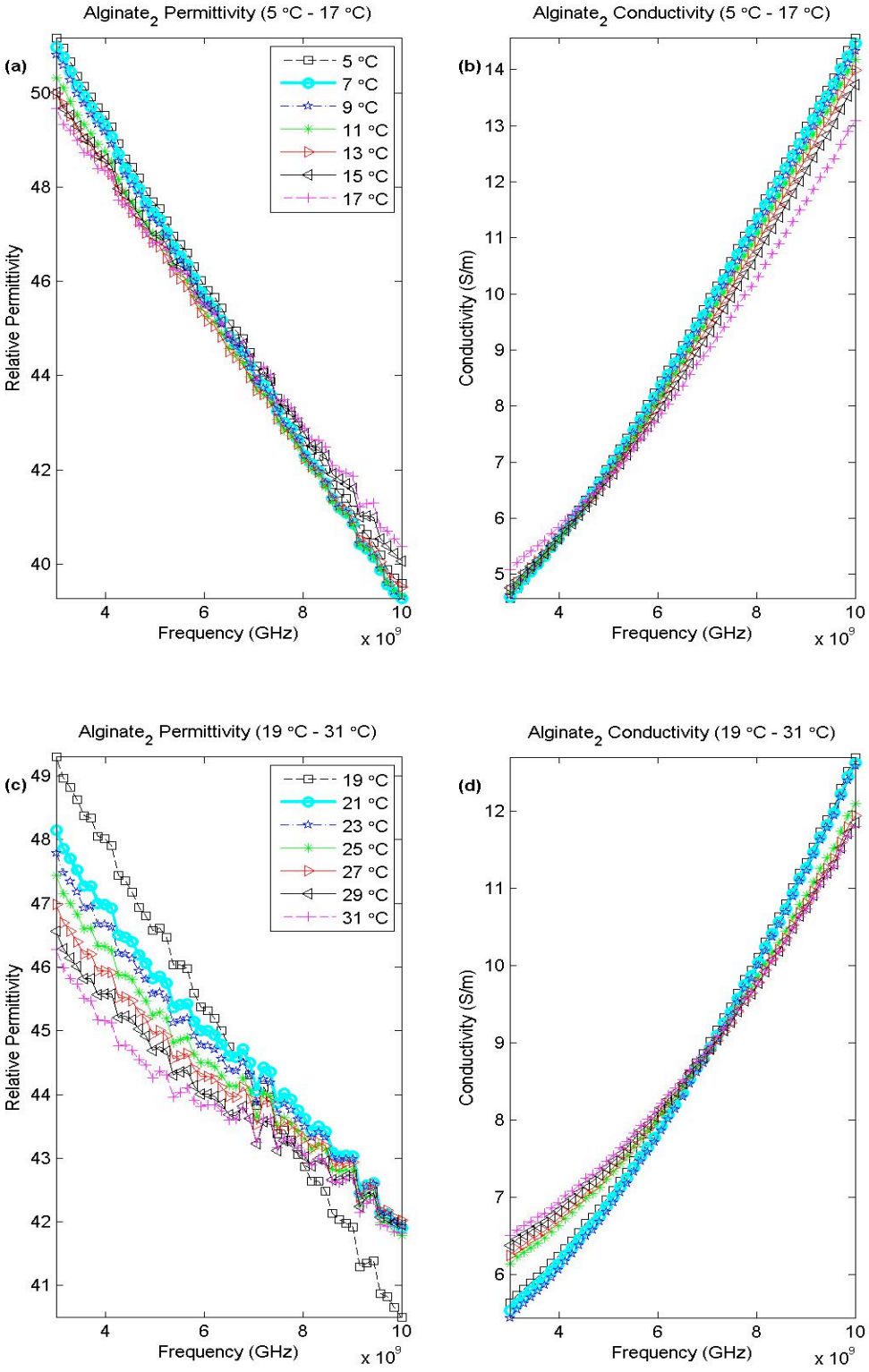
Alginate2 Permittivity (5 °C - 17 °C)
(a)
5 °C
7 °C
9 °C
11 °C
13 °C
15 °C
17 °C
Relative Permittivity
Frequency (GHz)
x 10^9
Alginate2 Conductivity (5 °C - 17 °C)
(b)
Conductivity (S/m)
Frequency (GHz)
x 10^9
Alginate2 Permittivity (19 °C - 31 °C)
(c)
19 °C
21 °C
23 °C
25 °C
27 °C
29 °C
31 °C
Relative Permittivity
Frequency (GHz)
x 10^9
Alginate2 Conductivity (19 °C - 31 °C)
(d)
Conductivity (S/m)
Frequency (GHz)
x 10^9

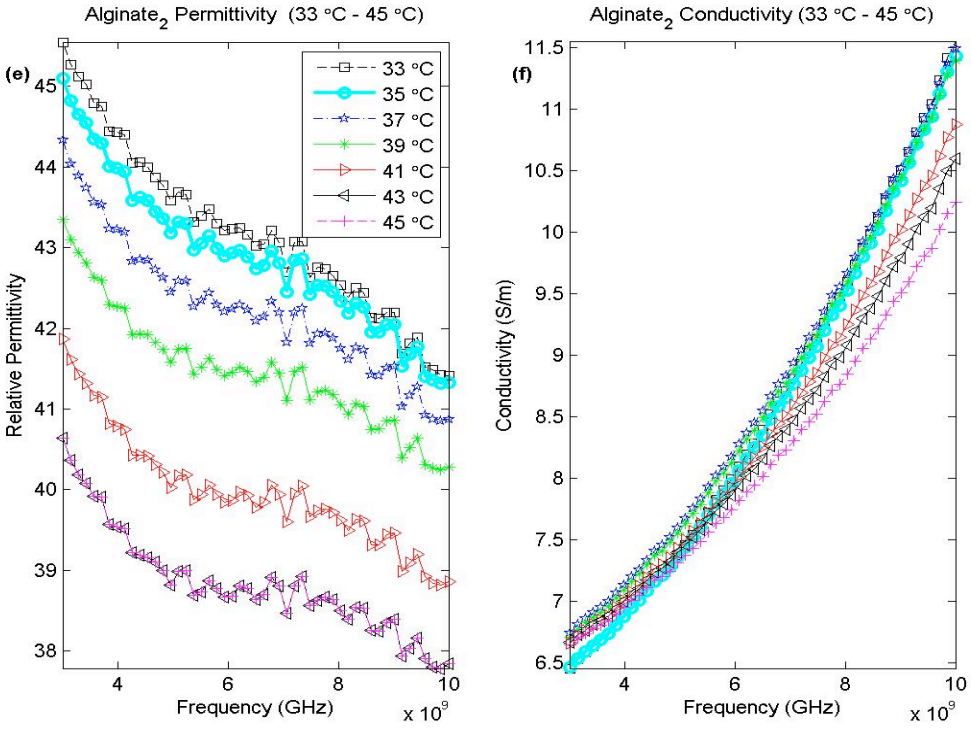

Figure 4.18: Second measurement of alginate-based phantoms (alginate$_2$); frequency trends of permittivity ε_r at: *(a)* 5 - 17 °C, *(c)* 19 - 31 °C and *(e)* 33 - 45 °C; and of conductivity σ at: *(b)* 5 - 17 °C, *(d)* 19 - 31 °C and *(f)* 33 - 45 °C.

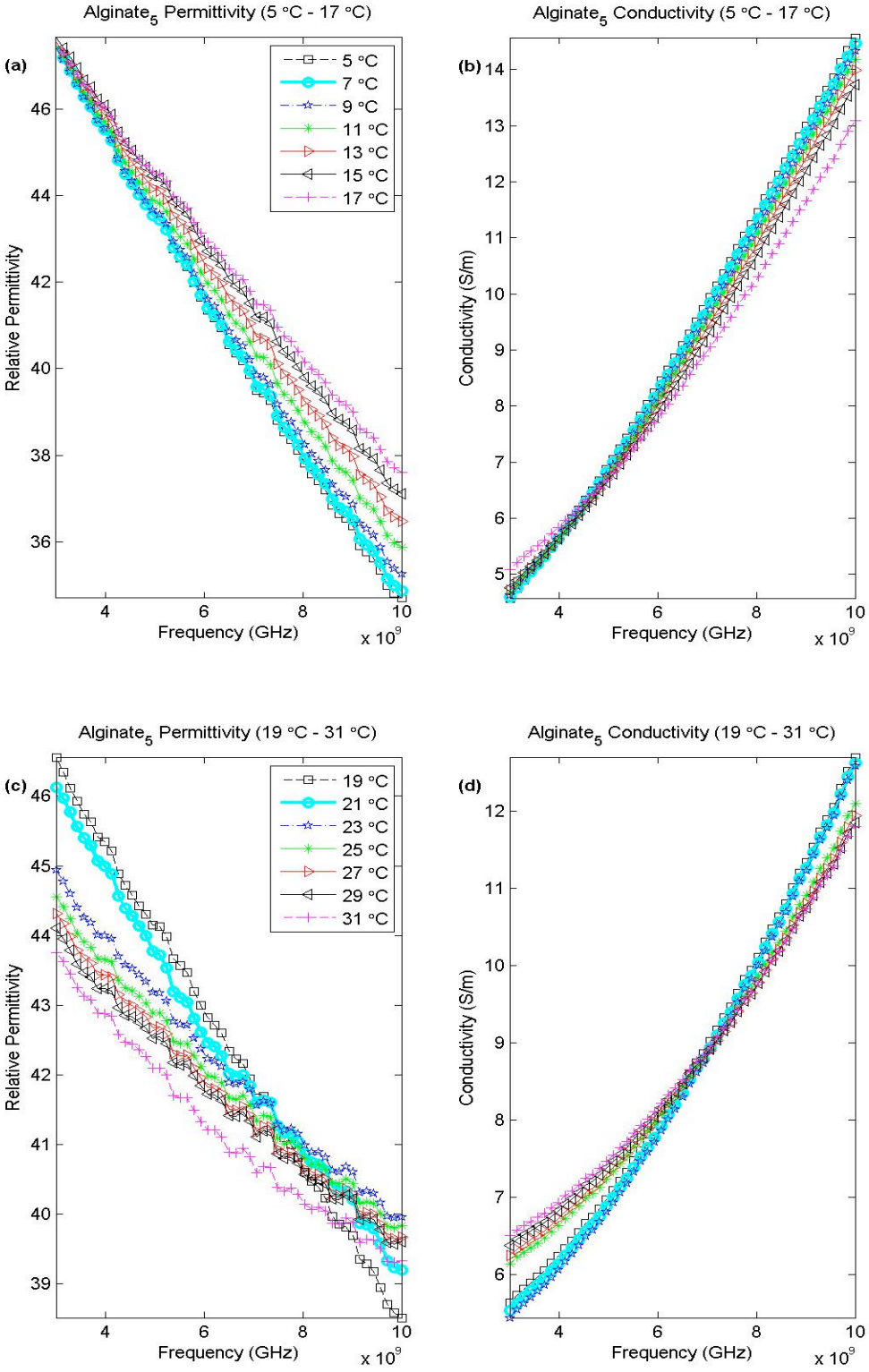
Alginate5 Permittivity (5 °C - 17 °C)
(a)
5 °C
7 °C
9 °C
11 °C
13 °C
15 °C
17 °C
Relative Permittivity
Frequency (GHz)
x 10^9
Alginate5 Conductivity (5 °C - 17 °C)
(b)
Conductivity (S/m)
Frequency (GHz)
x 10^9
Alginate5 Permittivity (19 °C - 31 °C)
(c)
19 °C
21 °C
23 °C
25 °C
27 °C
29 °C
31 °C
Relative Permittivity
Frequency (GHz)
x 10^9
Alginate5 Conductivity (19 °C - 31 °C)
(d)
Conductivity (S/m)
Frequency (GHz)
x 10^9

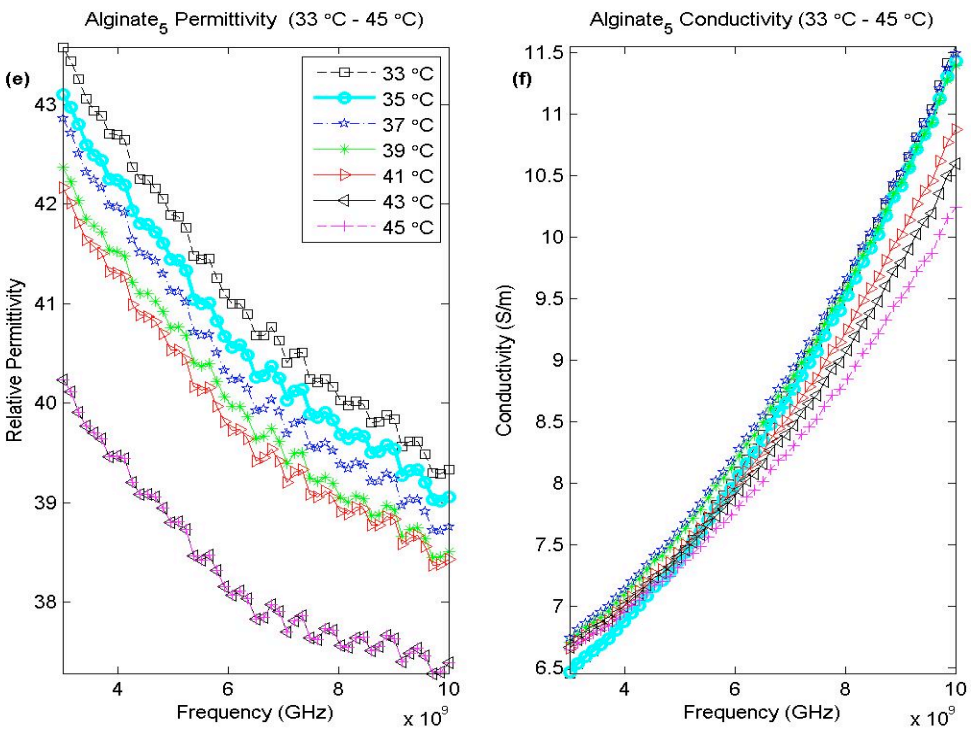

Figure 4.19: Fifth measurement of alginate-based phantoms (alginate$_2$); frequency trends of permittivity ε_r at: *(a)* 5 - 17 °C, *(c)* 19 - 31 °C and *(e)* 33 - 45 °C; and of conductivity σ at: *(b)* 5 - 17 °C, *(d)* 19 - 31 °C and *(f)* 33 - 45 °C.

Tissues

A. Fat

Figure 4.20 *(a)* – *(j)* shows the temperature trends of the relative permittivity ε_r and the conductivity σ of the fat tissue samples at 3, 5.1, 7.06, 9.02 and 10 GHz. Each curve represents the results of one of the five measurements. Figure 4.21 *(a)* – *(f)* and Figure 4.22 *(a)* – *(f)* show the frequency trends at different temperatures of the first and the second measurements, respectively. Each curve displays the relative permittivity and the

conductivity of the fat tissue samples from 3 GHz to 10 GHz at each temperature. The figures are divided into three temperature ranges 5 – 17 °C, 19 – 31 °C and 33 – 45 °C for easier readability. The figures show that the relative permittivity and the conductivity of fat are fairly constant with temperature.

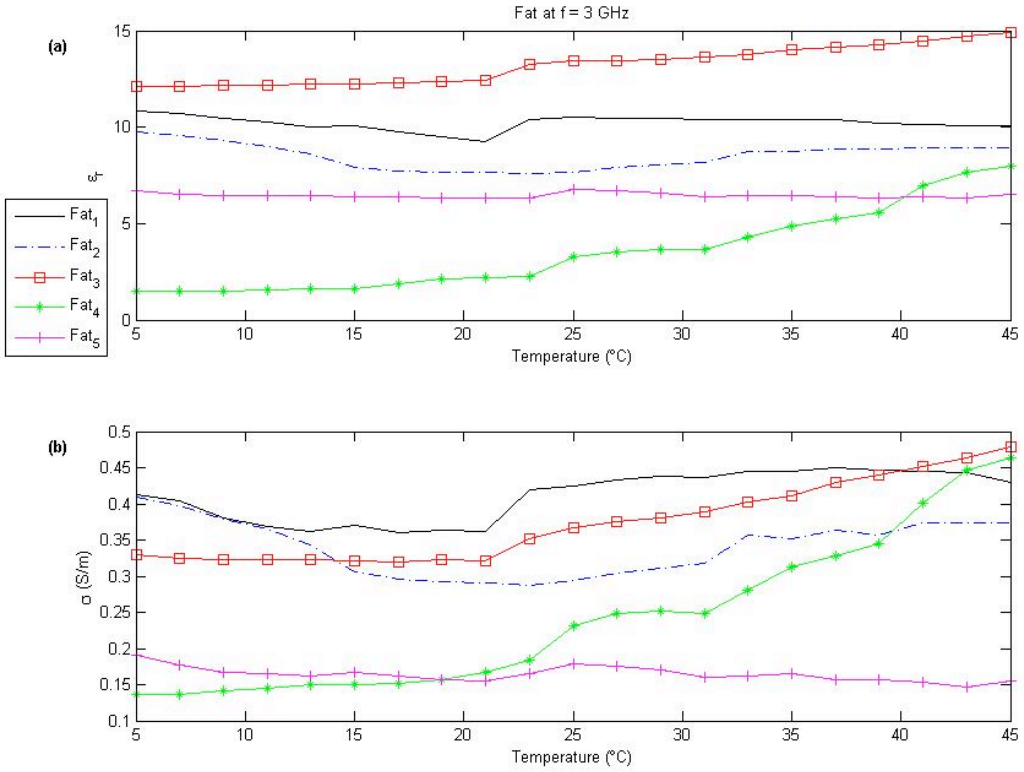

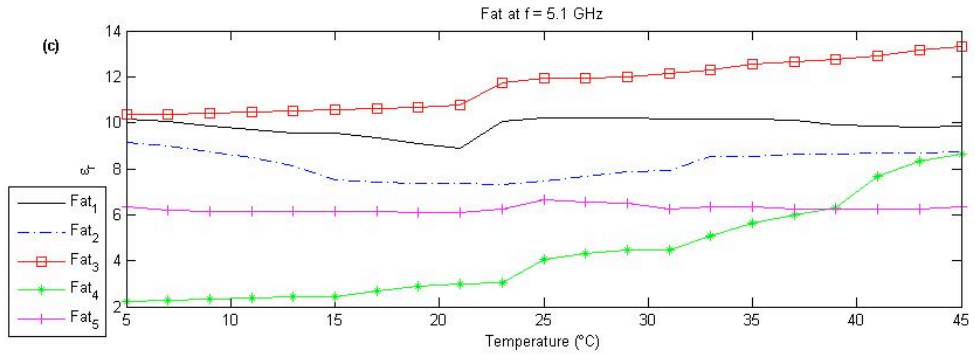
(c)
Fat at f = 5.1 GHz
ε'
Fat1
Fat2
Fat3
Fat4
Fat5
Temperature (°C)

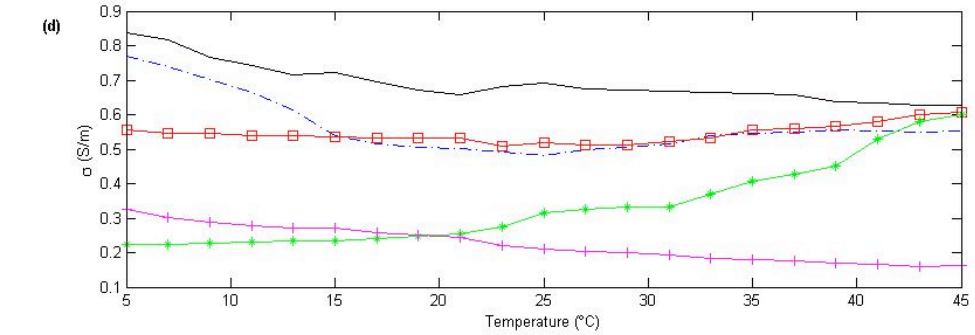
(d)
σ (S/m)
Temperature (°C)

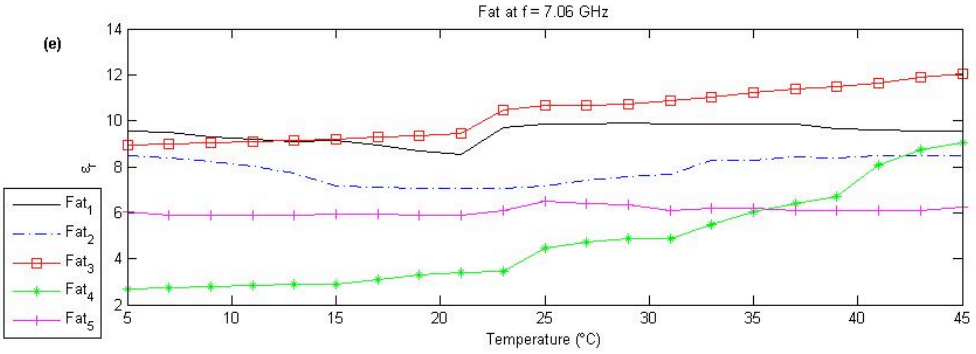
(e)
Fat at f = 7.06 GHz
ε'
Fat1
Fat2
Fat3
Fat4
Fat5
Temperature (°C)

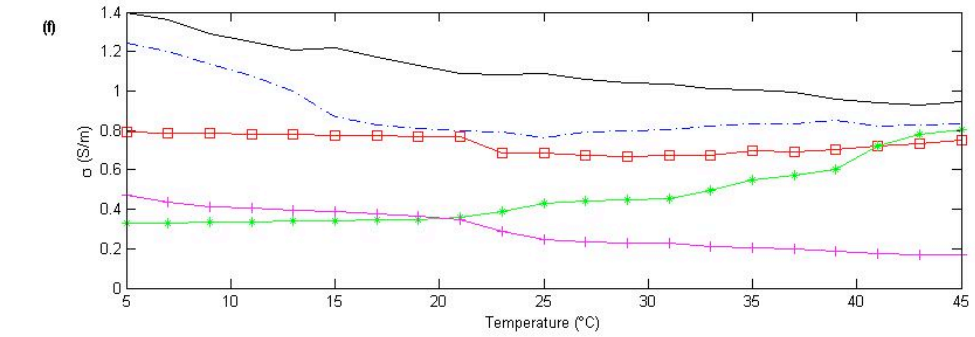
(f)
σ (S/m)
Temperature (°C)

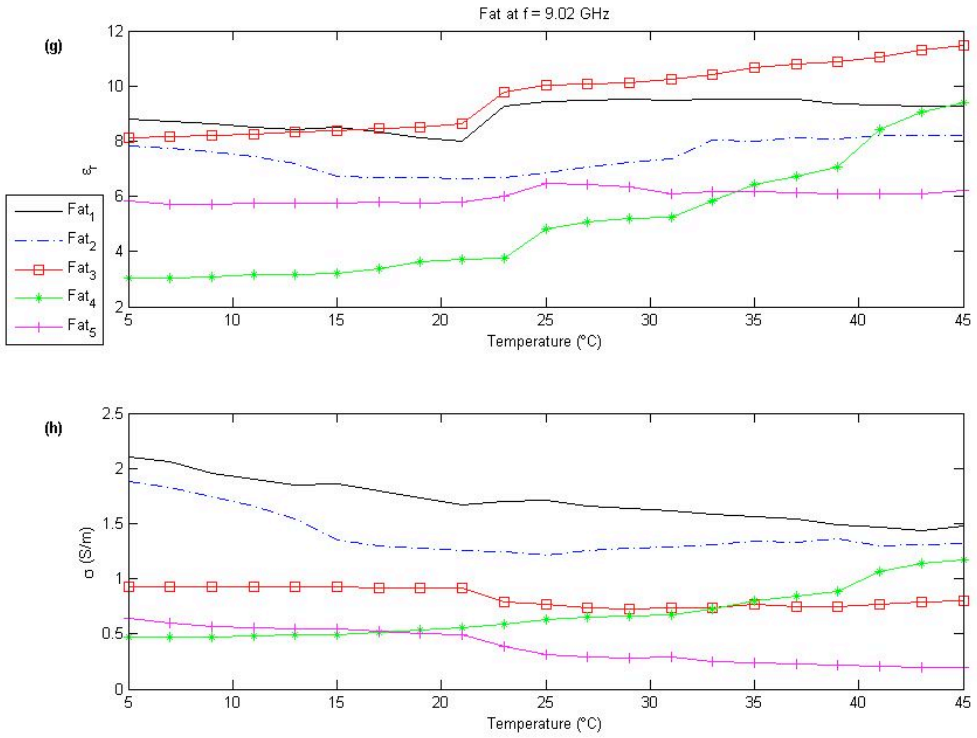
Fat at f = 9.02 GHz
(g)
ε_r
Fat1
Fat2
Fat3
Fat4
Fat5
Temperature (°C)
(h)
σ (S/m)
Temperature (°C)

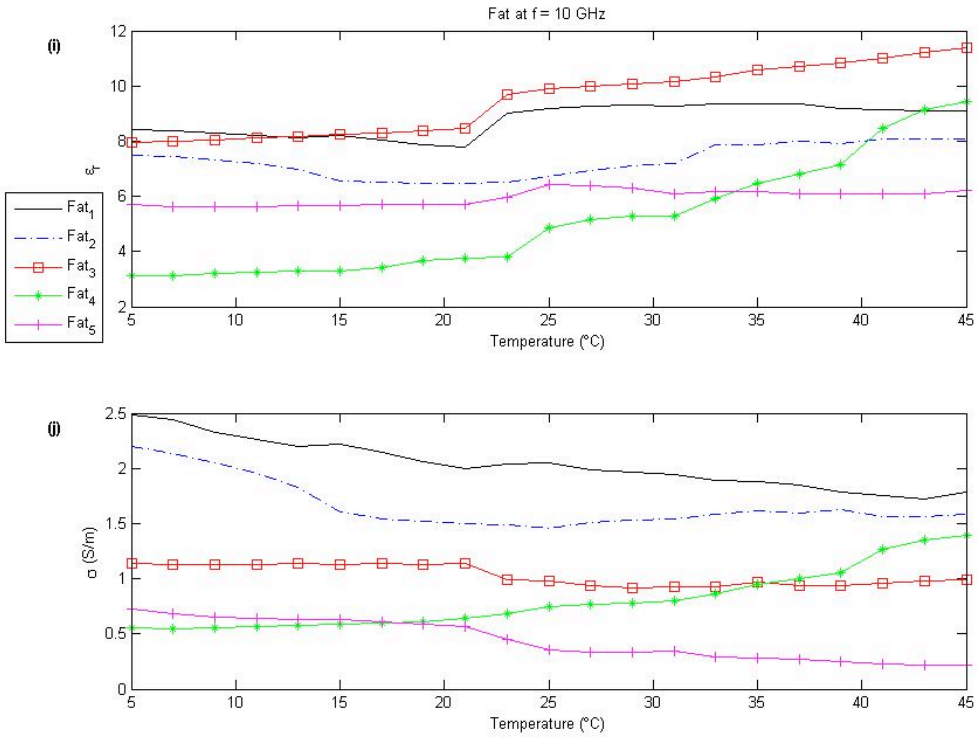

Figure 4.20: Measurements of the fat tissue samples; temperature trends of permittivity ε_r at: *(a)* 3 GHz, *(c)* 5.01 GHz, *(e)* 7.06 GHz, *(g)* 9.02 GHz and *(i)* 10 GHz; and of conductivity σ at: *(b)* 3 GHz, *(d)* 5.01 GHz, *(f)* 7.06 GHz, *(h)* 9.02 GHz and *(j)* 10 GHz. The five curves represent the results of the measurements, which were repeated five times.

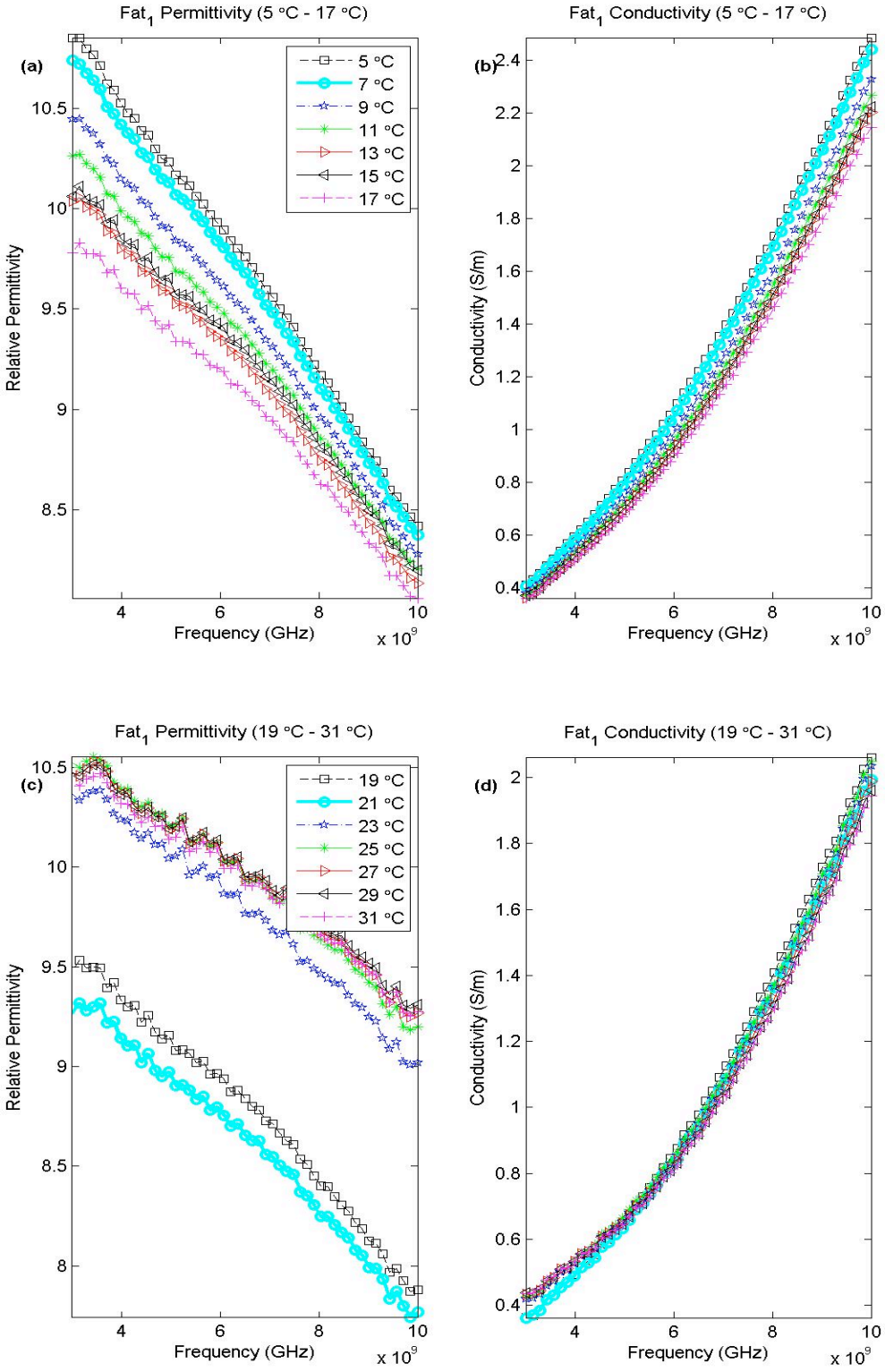
Fat1 Permittivity (5 °C - 17 °C)
(a)
5 °C
7 °C
9 °C
11 °C
13 °C
15 °C
17 °C
Relative Permittivity
Frequency (GHz)
x 10^9
Fat1 Conductivity (5 °C - 17 °C)
(b)
Conductivity (S/m)
Frequency (GHz)
x 10^9
Fat1 Permittivity (19 °C - 31 °C)
(c)
19 °C
21 °C
23 °C
25 °C
27 °C
29 °C
31 °C
Relative Permittivity
Frequency (GHz)
x 10^9
Fat1 Conductivity (19 °C - 31 °C)
(d)
Conductivity (S/m)
Frequency (GHz)
x 10^9

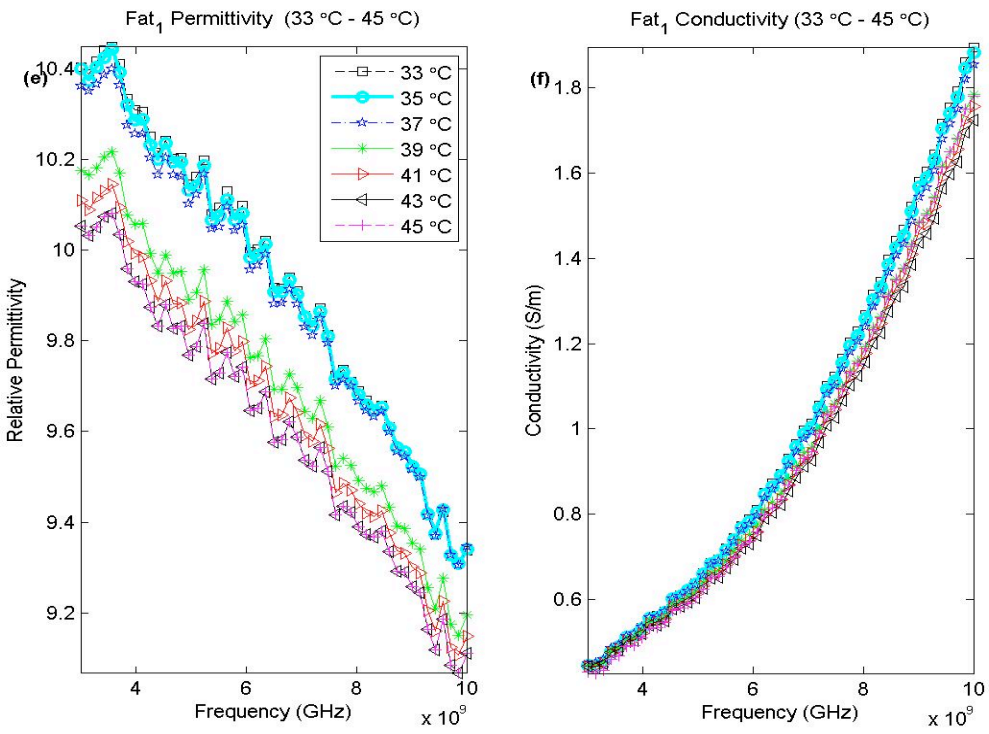

Figure 4.21: First measurement of the fat tissue samples (fat_1); frequency trends of permittivity ε_r at: *(a)* 5 - 17 °C, *(c)* 19 - 31 °C and *(e)* 33 - 45 °C; and of conductivity σ at: *(b)* 5 - 17 °C, *(d)* 19 - 31 °C and *(f)* 33 - 45 °C.

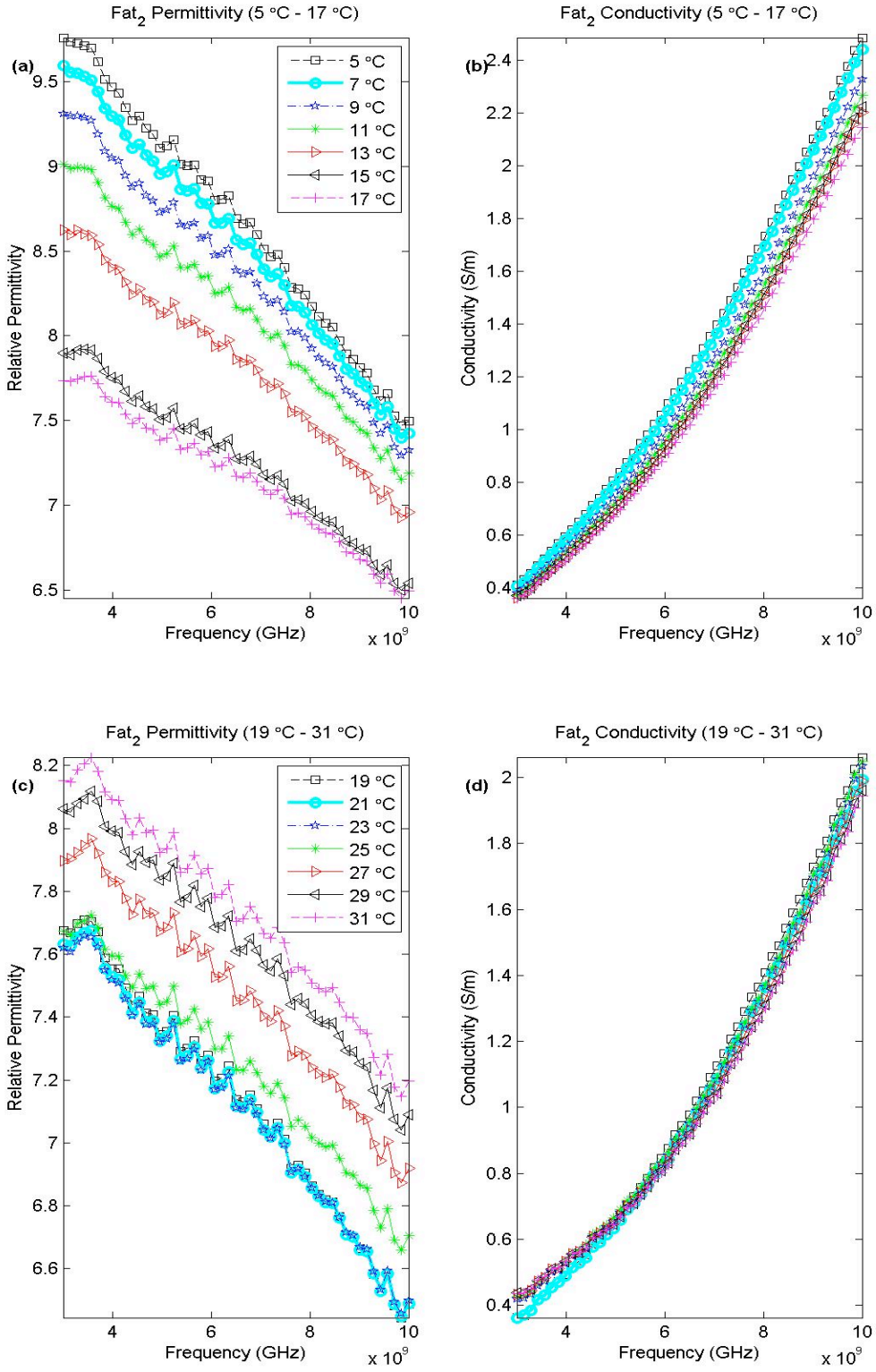
Fat2 Permittivity (5 °C - 17 °C)
(a)
5 °C
7 °C
9 °C
11 °C
13 °C
15 °C
17 °C
Relative Permittivity
Frequency (GHz)
x 10^9
Fat2 Conductivity (5 °C - 17 °C)
(b)
Conductivity (S/m)
Frequency (GHz)
x 10^9
Fat2 Permittivity (19 °C - 31 °C)
(c)
19 °C
21 °C
23 °C
25 °C
27 °C
29 °C
31 °C
Relative Permittivity
Frequency (GHz)
x 10^9
Fat2 Conductivity (19 °C - 31 °C)
(d)
Conductivity (S/m)
Frequency (GHz)
x 10^9

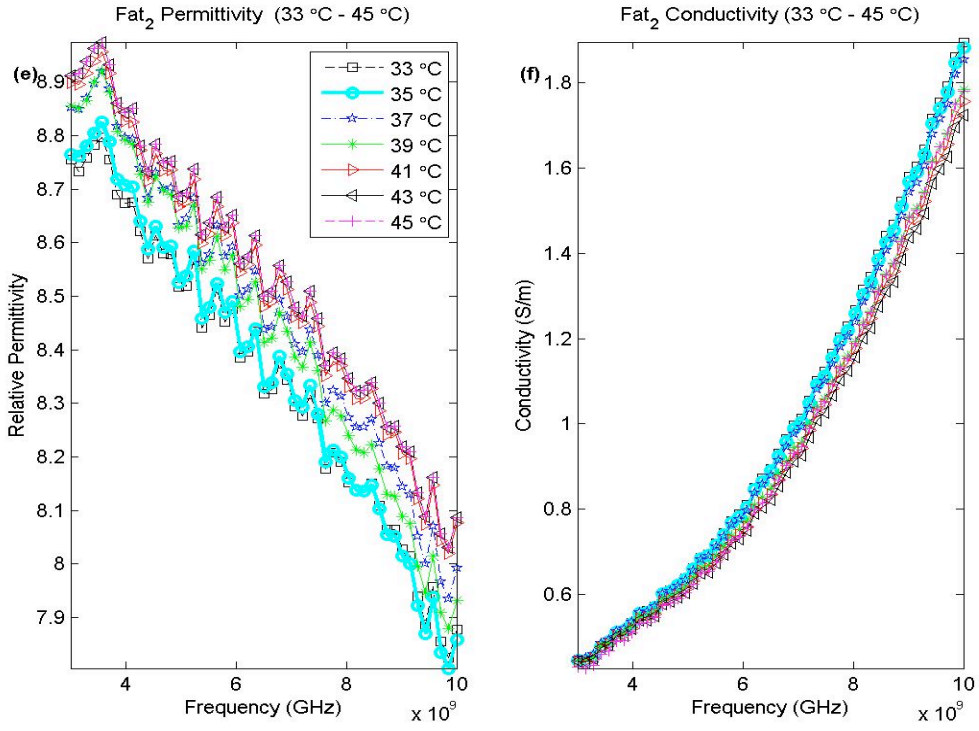

Figure 4.22: Second measurement of the fat tissue samples (fat_2); frequency trends of permittivity ε_r at: *(a)* 5 - 17 °C, *(c)* 19 - 31 °C and *(e)* 33 - 45 °C; and of conductivity σ at: *(b)* 5 - 17 °C, *(d)* 19 - 31 °C and *(f)* 33 - 45 °C.

B. Muscle

Figure 4.23 *(a) – (j)* shows the temperature trends of the relative permittivity ε_r and the conductivity σ of the muscle tissue samples at 3, 5.1, 7.06, 9.02 and 10 GHz. Each curve represents the results of one of the five measurements. Figure 4.24 *(a) – (f)* and Figure 4.25 *(a) – (f)* show the frequency trends at different temperatures of the first and the fourth measurements, respectively. Each curve displays the relative permittivity and the conductivity of the muscle tissue samples from 3 GHz to 10 GHz at each temperature. The figures are divided into three temperature ranges 5 – 17 °C, 19 – 31 °C and 33 – 45

°C for easier readability. The relative permittivity of muscle is fairly constant with temperature at all frequencies. There is a slight decrease in the relative permittivity at lower frequencies and a very small increase at higher frequencies with a cross-over point at around 5.5 GHz. The conductivity of muscle decreases with increasing temperature. It decreases by around a total of 0.8 S/m at 3 GHz and by 3 – 4 S/m at higher frequencies. This trend is consistent with that reported by Lazebnik *et al.* [7] for liver. Lazebnik *et al.* reported that the relative permittivity of liver has a cross-over point at around 4 GHz with the same trends for permittivity and conductivity as those presented in this work. Muscle and liver properties can be compared because both tissues have a high-water content and thus comparable dielectric behavior at microwave frequencies. These trends are similar to those reported for barnacle (a sea creature related to crabs and lobsters) muscle fibres showing a very small change in the relative permittivity and a decrease in the conductivity [8]. The trends are also consistent with those of water [9].

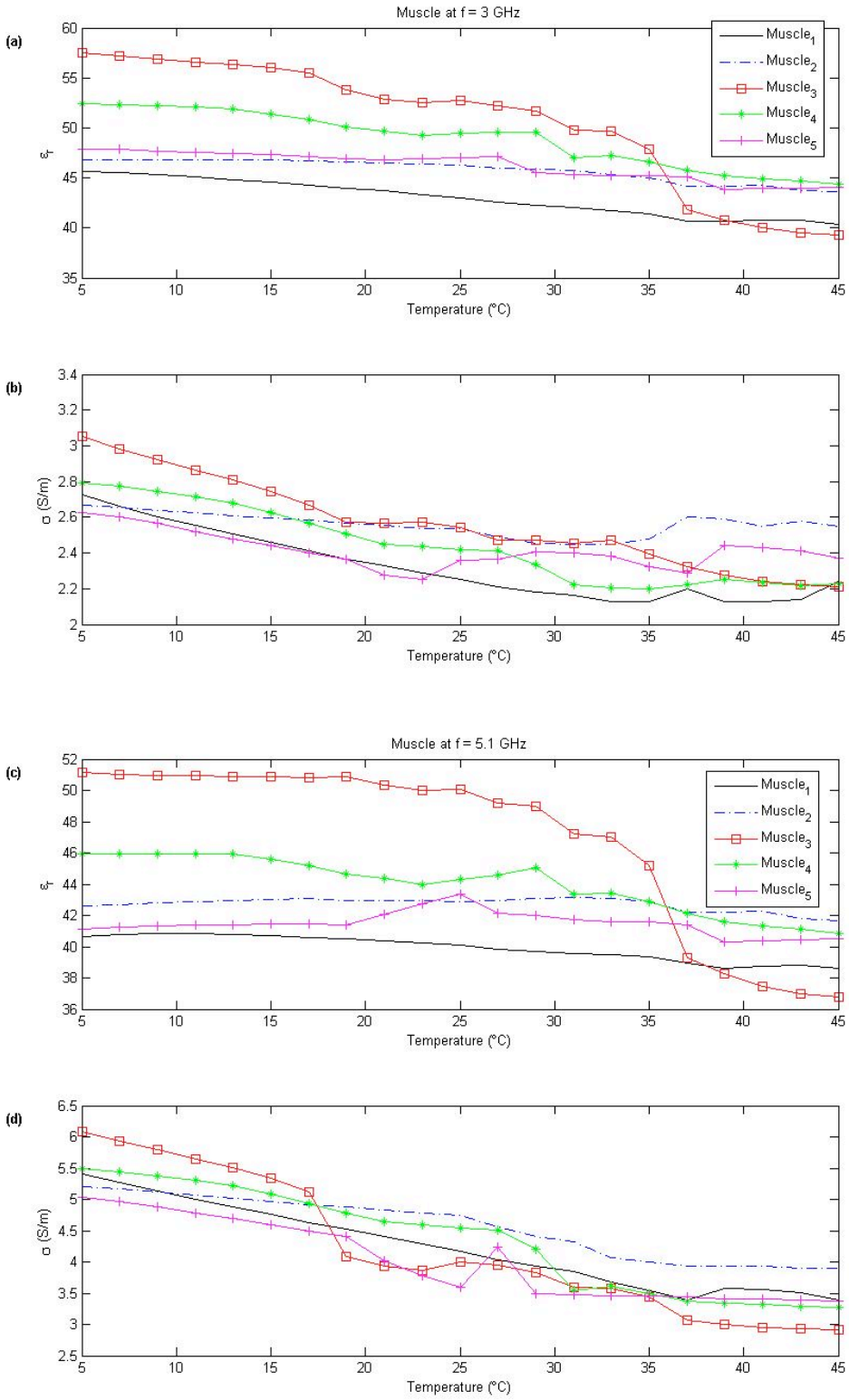
Muscle at f = 3 GHz
(a)
Muscle1
Muscle2
Muscle3
Muscle4
Muscle5
εr
Temperature (°C)
(b)
σ (S/m)
Temperature (°C)
Muscle at f = 5.1 GHz
(c)
Muscle1
Muscle2
Muscle3
Muscle4
Muscle5
εr
Temperature (°C)
(d)
σ (S/m)
Temperature (°C)

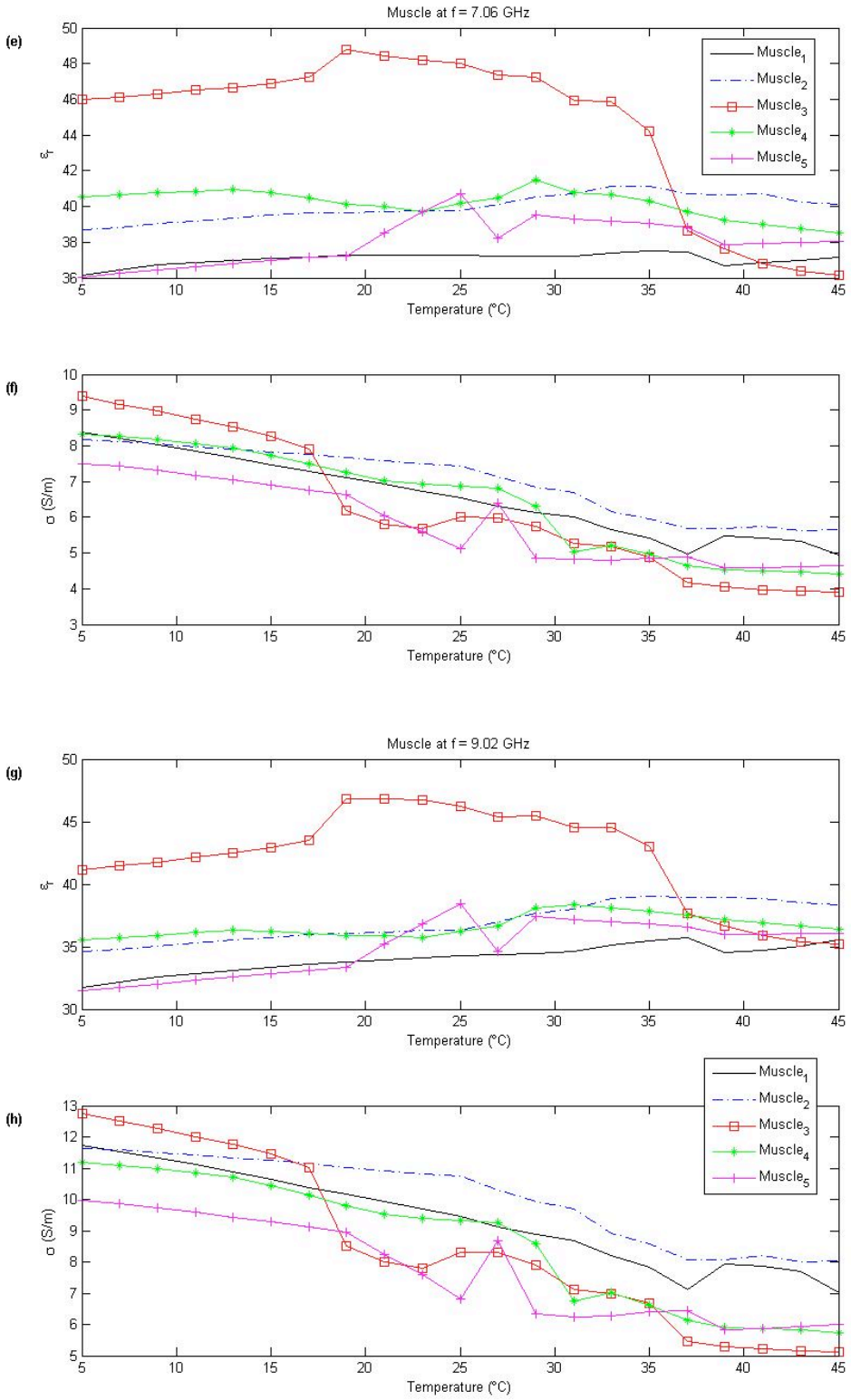
(e)
Muscle at f = 7.06 GHz
Muscle1
Muscle2
Muscle3
Muscle4
Muscle5
εr
Temperature (°C)
(f)
σ (S/m)
Temperature (°C)
(g)
Muscle at f = 9.02 GHz
εr
Temperature (°C)
(h)
Muscle1
Muscle2
Muscle3
Muscle4
Muscle5
σ (S/m)
Temperature (°C)

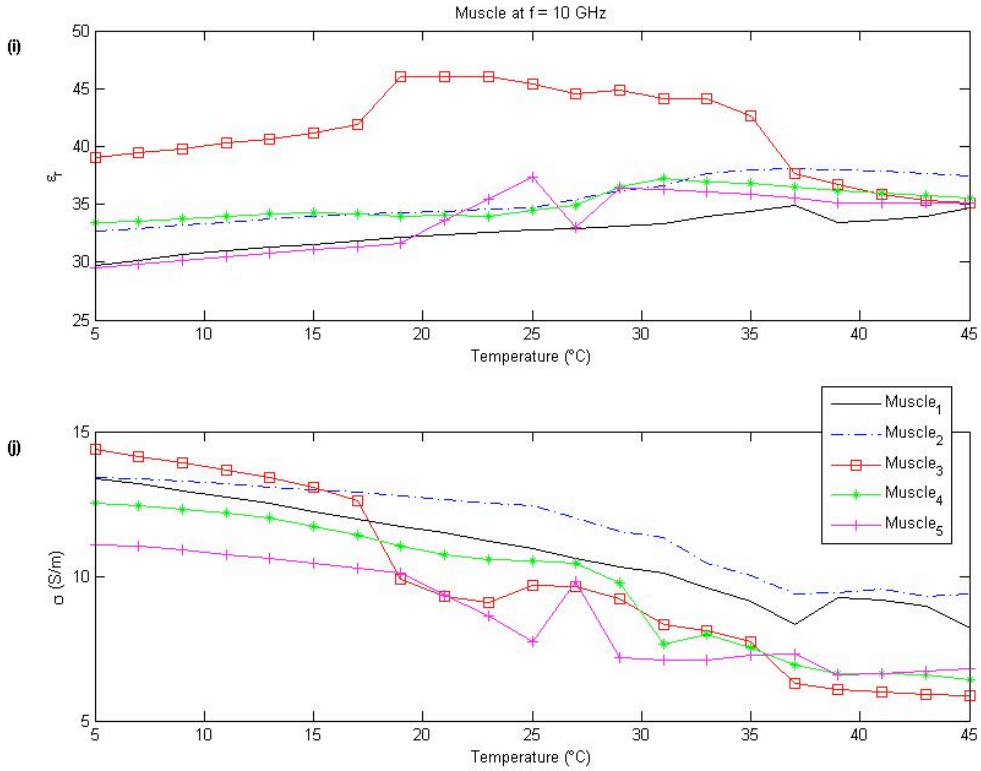

Figure 4.23: Measurements of the muscle tissue samples; temperature trends of permittivity ε_r at: *(a)* 3 GHz, *(c)* 5.01 GHz, *(e)* 7.06 GHz, *(g)* 9.02 GHz and *(i)* 10 GHz; and of conductivity σ at: *(b)* 3 GHz, *(d)* 5.01 GHz, *(f)* 7.06 GHz, *(h)* 9.02 GHz and *(j)* 10 GHz. The five curves represent the results of the measurements, which were repeated five times.

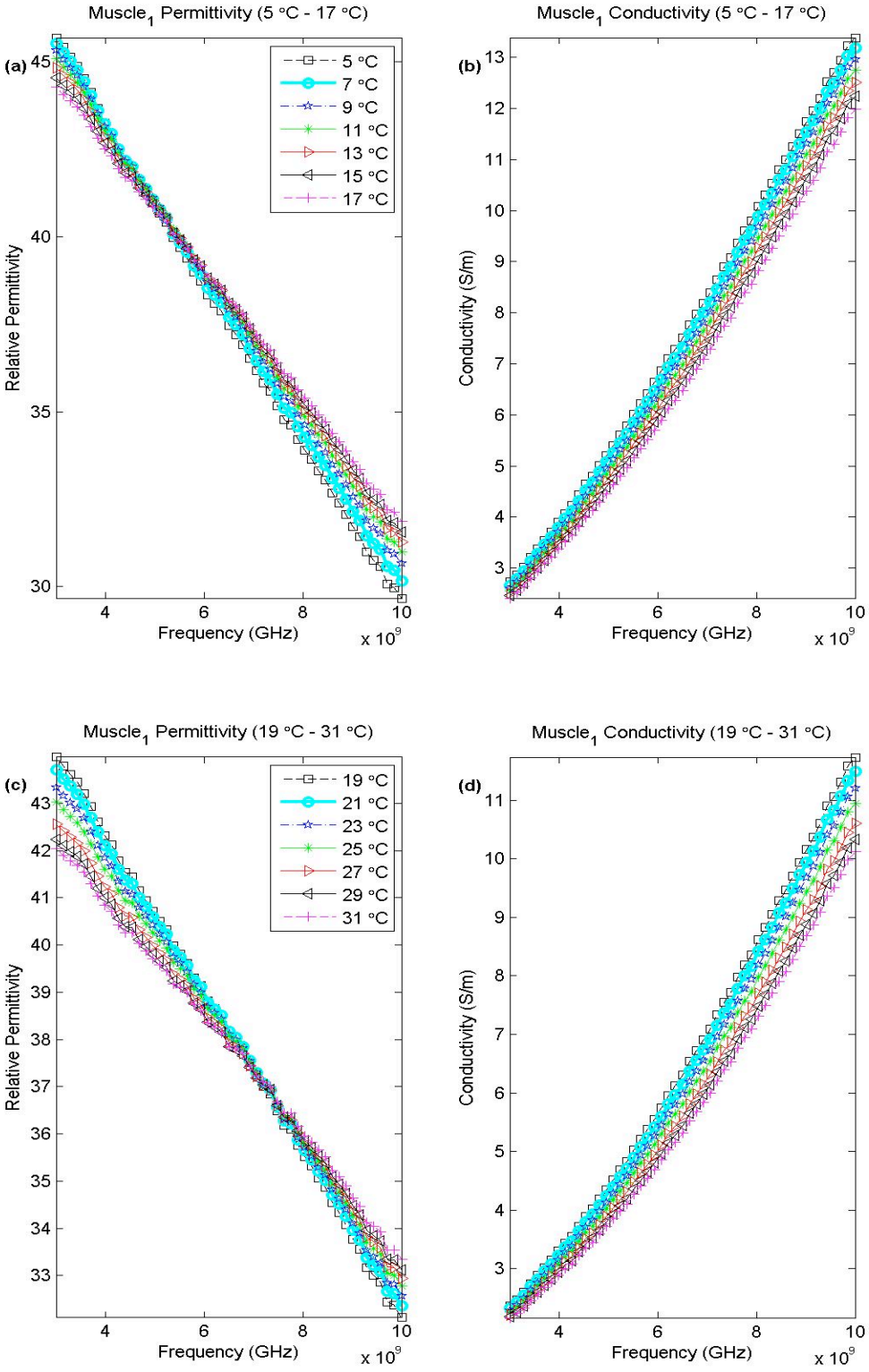
Muscle1 Permittivity (5 °C - 17 °C)
(a)
5 °C
7 °C
9 °C
11 °C
13 °C
15 °C
17 °C
Relative Permittivity
Frequency (GHz)
x 10^9
Muscle1 Conductivity (5 °C - 17 °C)
(b)
Conductivity (S/m)
Frequency (GHz)
x 10^9
Muscle1 Permittivity (19 °C - 31 °C)
(c)
19 °C
21 °C
23 °C
25 °C
27 °C
29 °C
31 °C
Relative Permittivity
Frequency (GHz)
x 10^9
Muscle1 Conductivity (19 °C - 31 °C)
(d)
Conductivity (S/m)
Frequency (GHz)
x 10^9

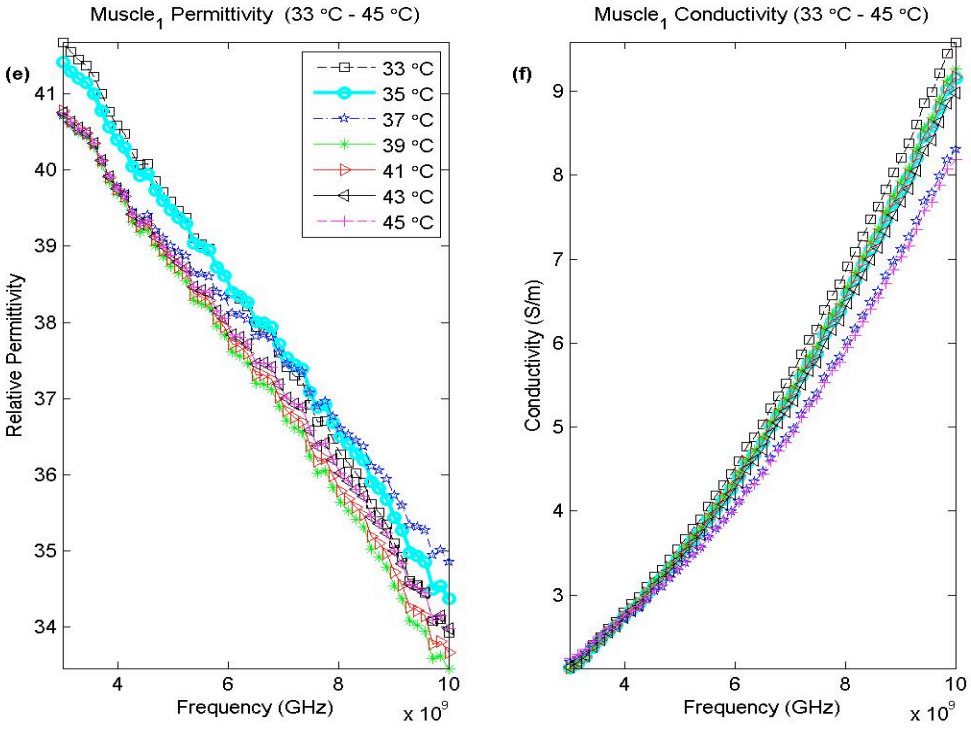

Figure 4.24: First measurement of the muscle tissue samples ($muscle_1$); frequency trends of permittivity ε_r at: *(a)* 5 - 17 °C, *(c)* 19 - 31 °C and *(e)* 33 - 45 °C; and of conductivity σ at: *(b)* 5 - 17 °C, *(d)* 19 - 31 °C and *(f)* 33 - 45 °C.

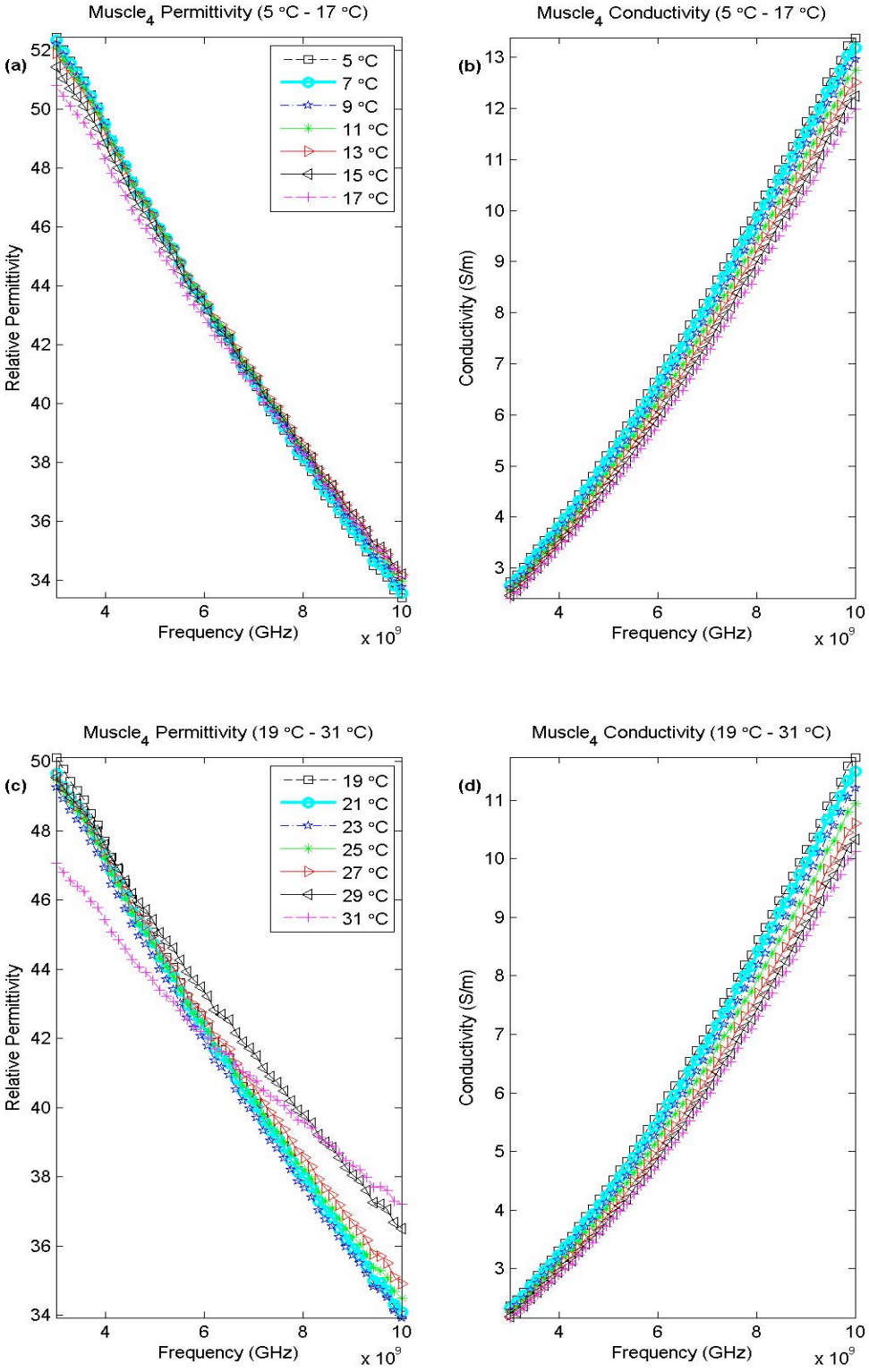
Muscle4 Permittivity (5 °C - 17 °C)
(a)
5 °C
7 °C
9 °C
11 °C
13 °C
15 °C
17 °C
Relative Permittivity
Frequency (GHz)
x 10^9
Muscle4 Conductivity (5 °C - 17 °C)
(b)
Conductivity (S/m)
Frequency (GHz)
x 10^9
Muscle4 Permittivity (19 °C - 31 °C)
(c)
19 °C
21 °C
23 °C
25 °C
27 °C
29 °C
31 °C
Relative Permittivity
Frequency (GHz)
x 10^9
Muscle4 Conductivity (19 °C - 31 °C)
(d)
Conductivity (S/m)
Frequency (GHz)
x 10^9

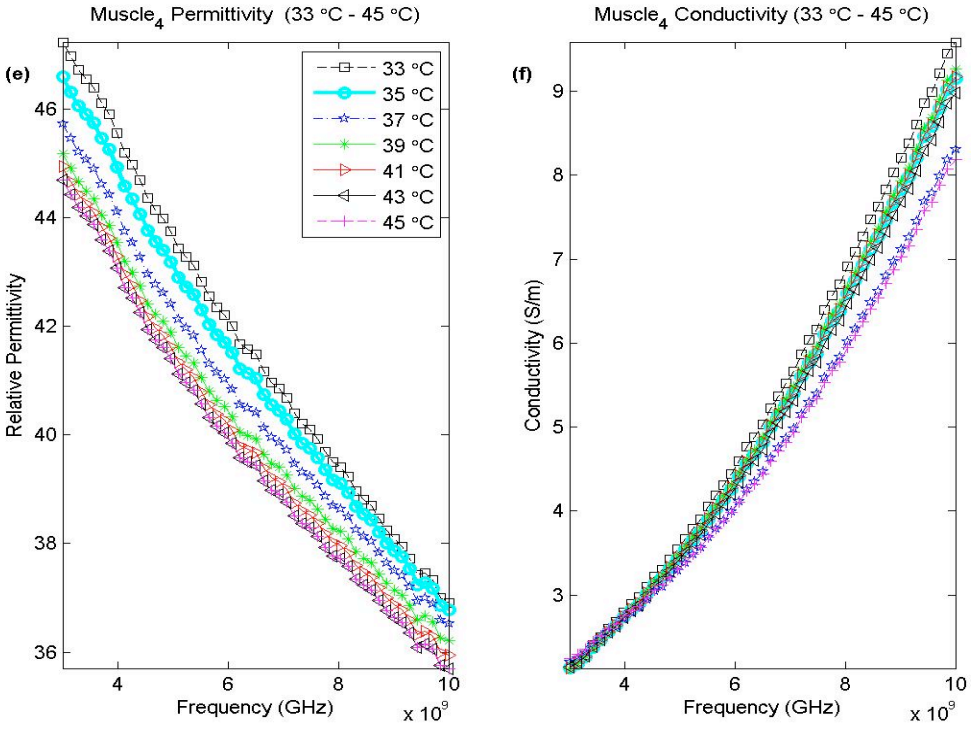

Figure 4.25: Fourth measurement of the muscle tissue samples ($muscle_4$); frequency trends of permittivity ε_r at: *(a)* 5 - 17 °C, *(c)* 19 - 31 °C and *(e)* 33 - 45 °C; and of conductivity σ at: *(b)* 5 - 17 °C, *(d)* 19 - 31 °C and *(f)* 33 - 45 °C.

C. Liver

Figure 4.26 *(a) – (j)* shows the temperature trends of the relative permittivity ε_r and the conductivity σ of the liver tissue samples at 3, 5.1, 7.06, 9.02 and 10 GHz. Each curve represents one of the five measurements carried out for the liver tissue samples. Figure 4.27 *(a) – (f)* and Figure 4.28 *(a) – (f)* shows the frequency trends at different temperatures of the first and the fourth measurements, respectively. Each curve displays the relative permittivity and the conductivity of the liver tissue samples from 3 GHz to 10 GHz at each temperature. The figures are divided into three temperature ranges 5 – 17

°C, 19 – 31 °C and 33 – 45 °C for easier readability. The figures show a slight decrease in permittivity with increasing temperature at 3 GHz, a constant permittivity at 5.1 GHz and a slight increase at 7.06 GHz. The increase becomes more pronounced, yet still small, at higher frequencies. This tend also indicates a cross-over point at around 5 GHz, which is consistent with the results of Lazebnik *et al.* [7] for liver that reported a cross-over point at around 4 GHz with the same trends and similar magnitudes for the relative permittivity. The conductivity of liver decreases with temperature throughout this frequency range. The decrease is higher in magnitude at higher frequencies. This trend is also consistent with the conductivity results of Lazebnik *et al.* [7]. These trends are also consistent with those of water [9].

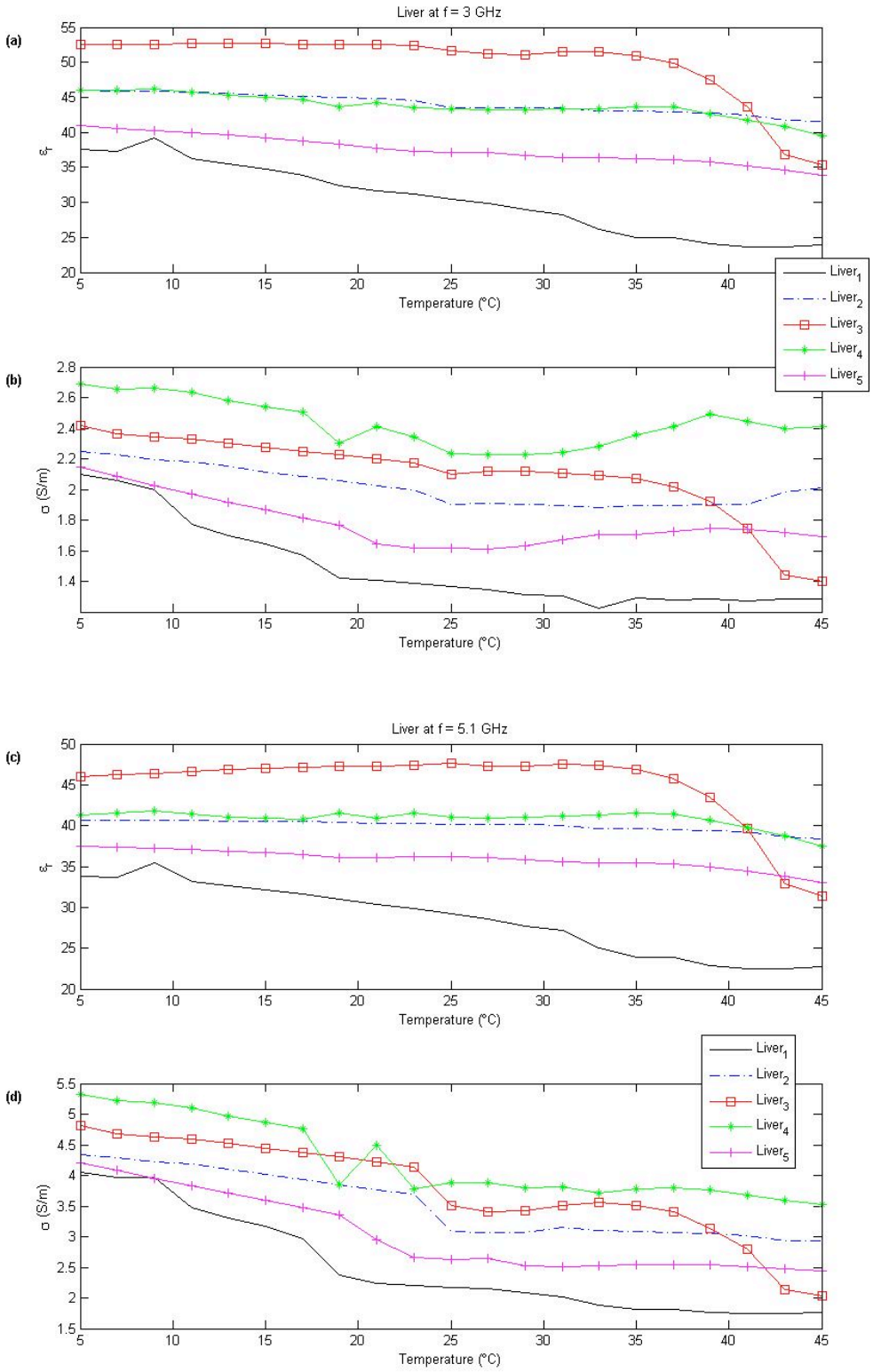
Liver at f = 3 GHz
(a)
ε_r
Temperature (°C)
Liver$_1$
Liver$_2$
Liver$_3$
Liver$_4$
Liver$_5$
(b)
σ (S/m)
Temperature (°C)
Liver at f = 5.1 GHz
(c)
ε_r
Temperature (°C)
(d)
σ (S/m)
Temperature (°C)

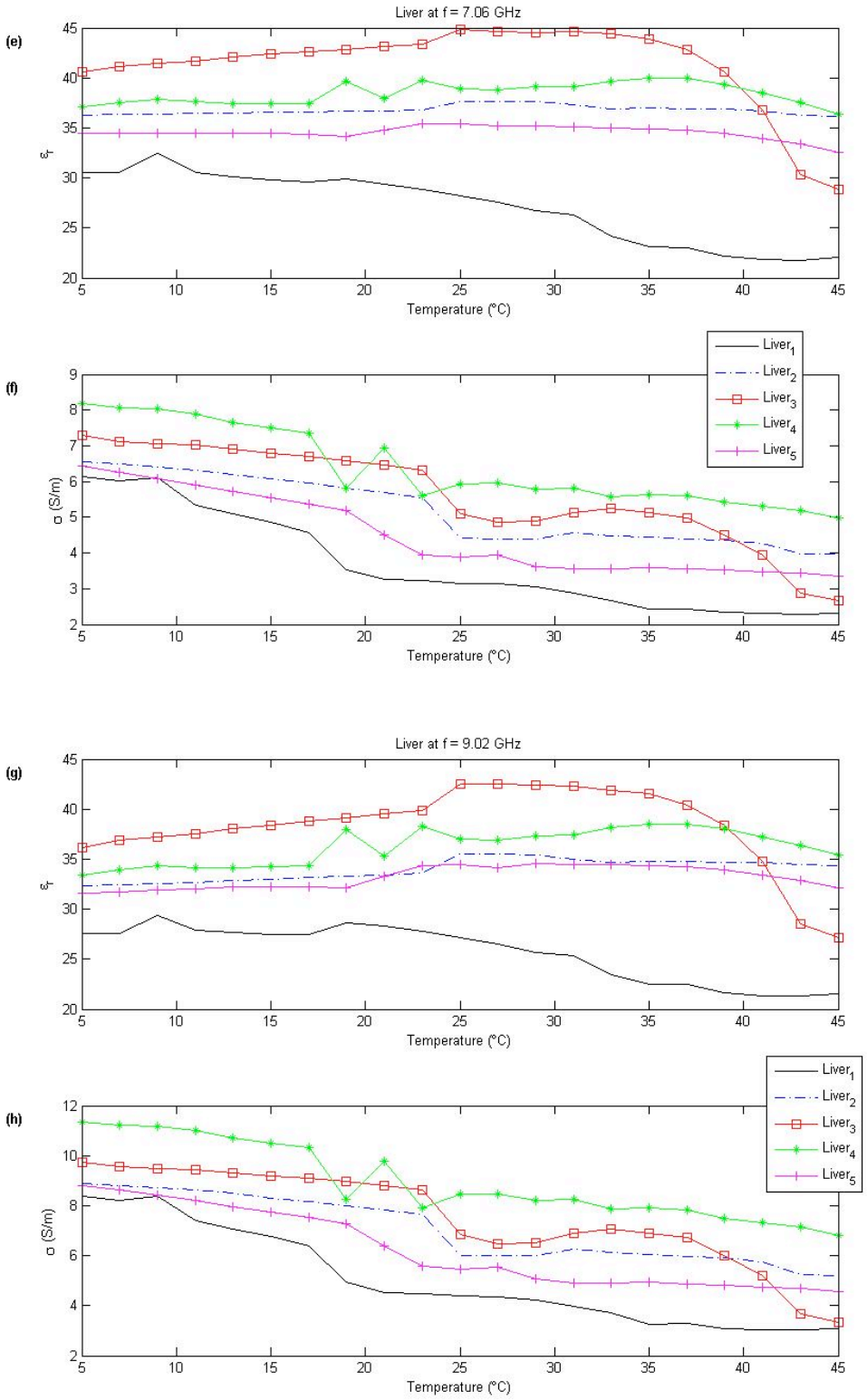
(e)
Liver at f = 7.06 GHz
εr
Temperature (°C)
(f)
σ (S/m)
Temperature (°C)
Liver1
Liver2
Liver3
Liver4
Liver5
(g)
Liver at f = 9.02 GHz
εr
Temperature (°C)
(h)
σ (S/m)
Temperature (°C)
Liver1
Liver2
Liver3
Liver4
Liver5

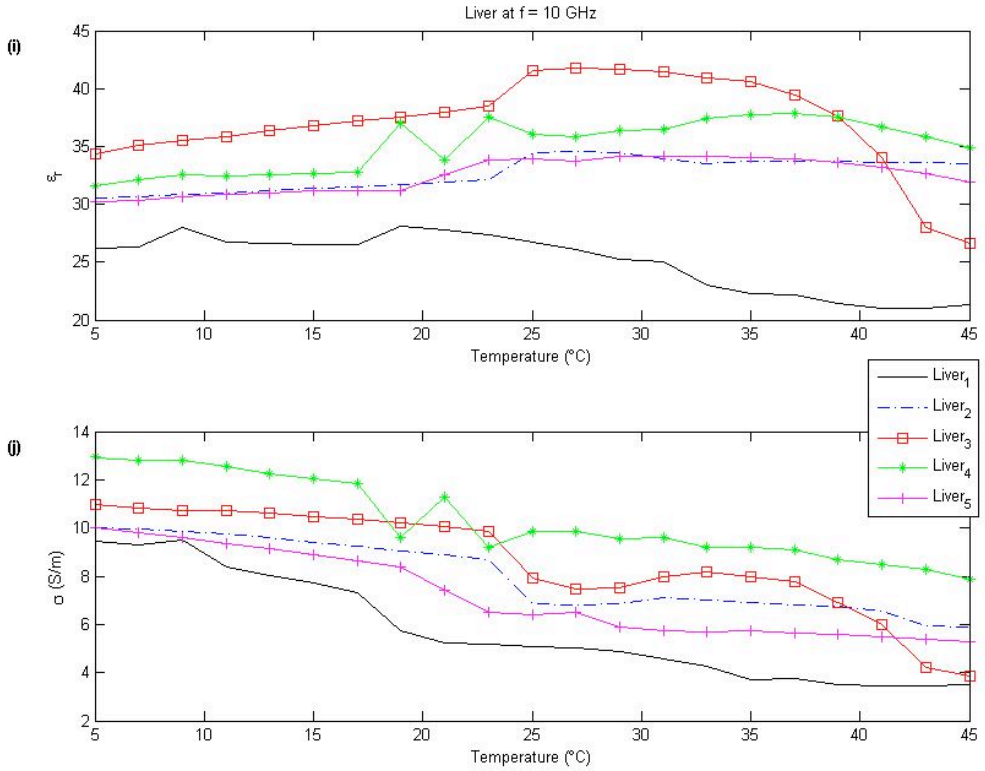

Figure 4.26: Measurements of the liver tissue samples; temperature trends of permittivity ε_r at: *(a)* 3 GHz, *(c)* 5.01 GHz, *(e)* 7.06 GHz, *(g)* 9.02 GHz and *(i)* 10 GHz; and of conductivity σ at: *(b)* 3 GHz, *(d)* 5.01 GHz, *(f)* 7.06 GHz, *(h)* 9.02 GHz and *(j)* 10 GHz. The five curves represent the results of the measurements, which were repeated five times.

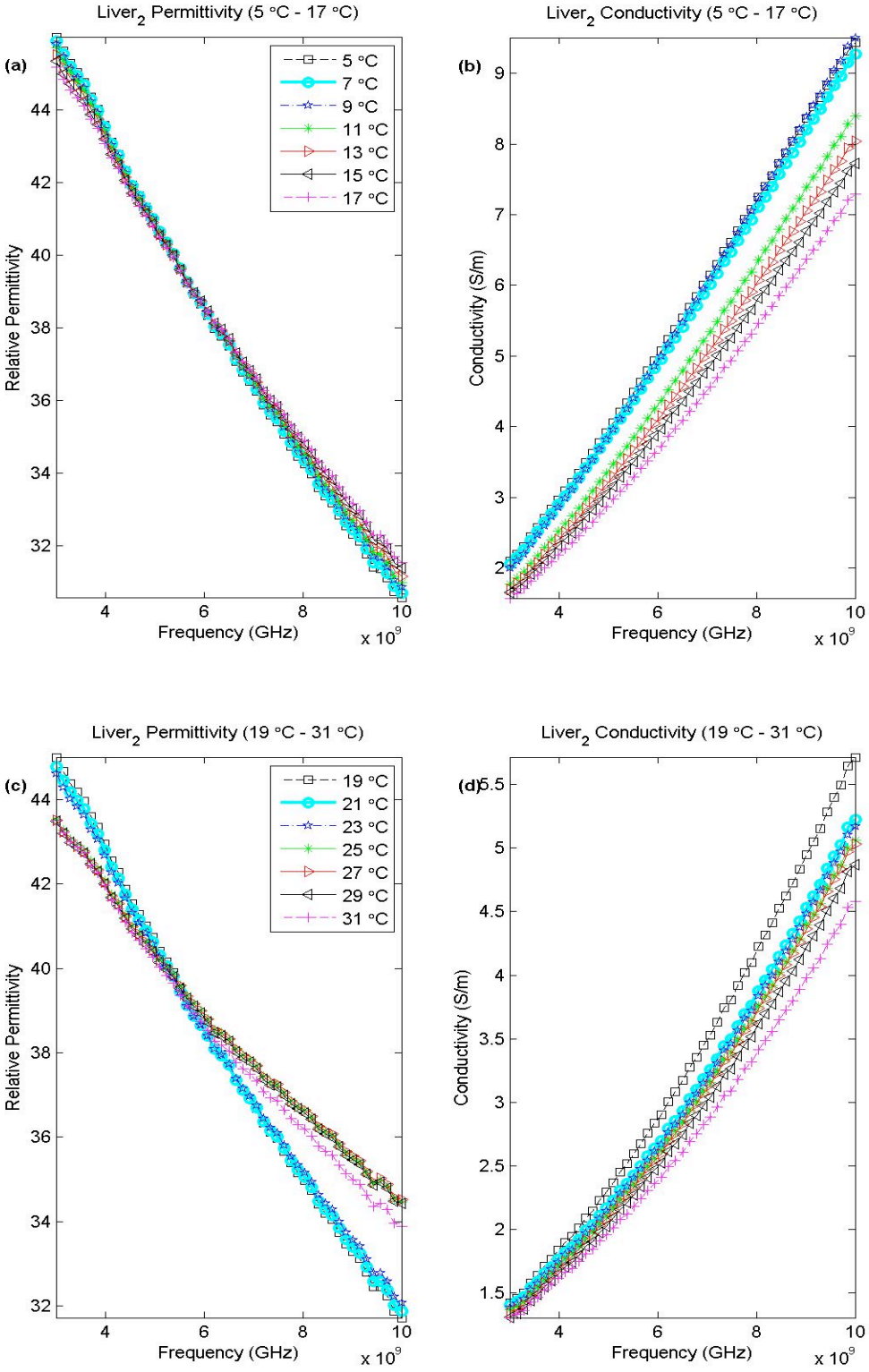
Liver2 Permittivity (5 °C - 17 °C)
(a)
5 °C
7 °C
9 °C
11 °C
13 °C
15 °C
17 °C
Relative Permittivity
Frequency (GHz)
x 10^9
Liver2 Conductivity (5 °C - 17 °C)
(b)
Conductivity (S/m)
Frequency (GHz)
x 10^9
Liver2 Permittivity (19 °C - 31 °C)
(c)
19 °C
21 °C
23 °C
25 °C
27 °C
29 °C
31 °C
Relative Permittivity
Frequency (GHz)
x 10^9
Liver2 Conductivity (19 °C - 31 °C)
(d)
Conductivity (S/m)
Frequency (GHz)
x 10^9

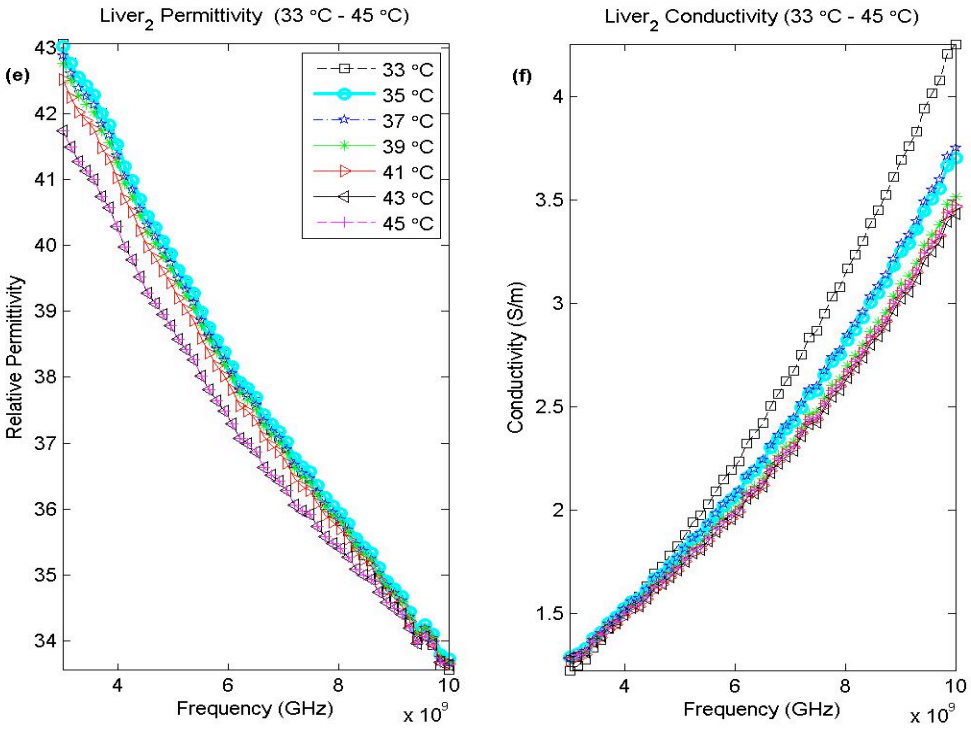

Figure 4.27: Second measurement of the liver tissue samples ($liver_2$); frequency trends of permittivity ε_r at: *(a)* 5 - 17 °C, *(c)* 19 - 31 °C and *(e)* 33 - 45 °C; and of conductivity σ at: *(b)* 5 - 17 °C, *(d)* 19 - 31 °C and *(f)* 33 - 45 °C.

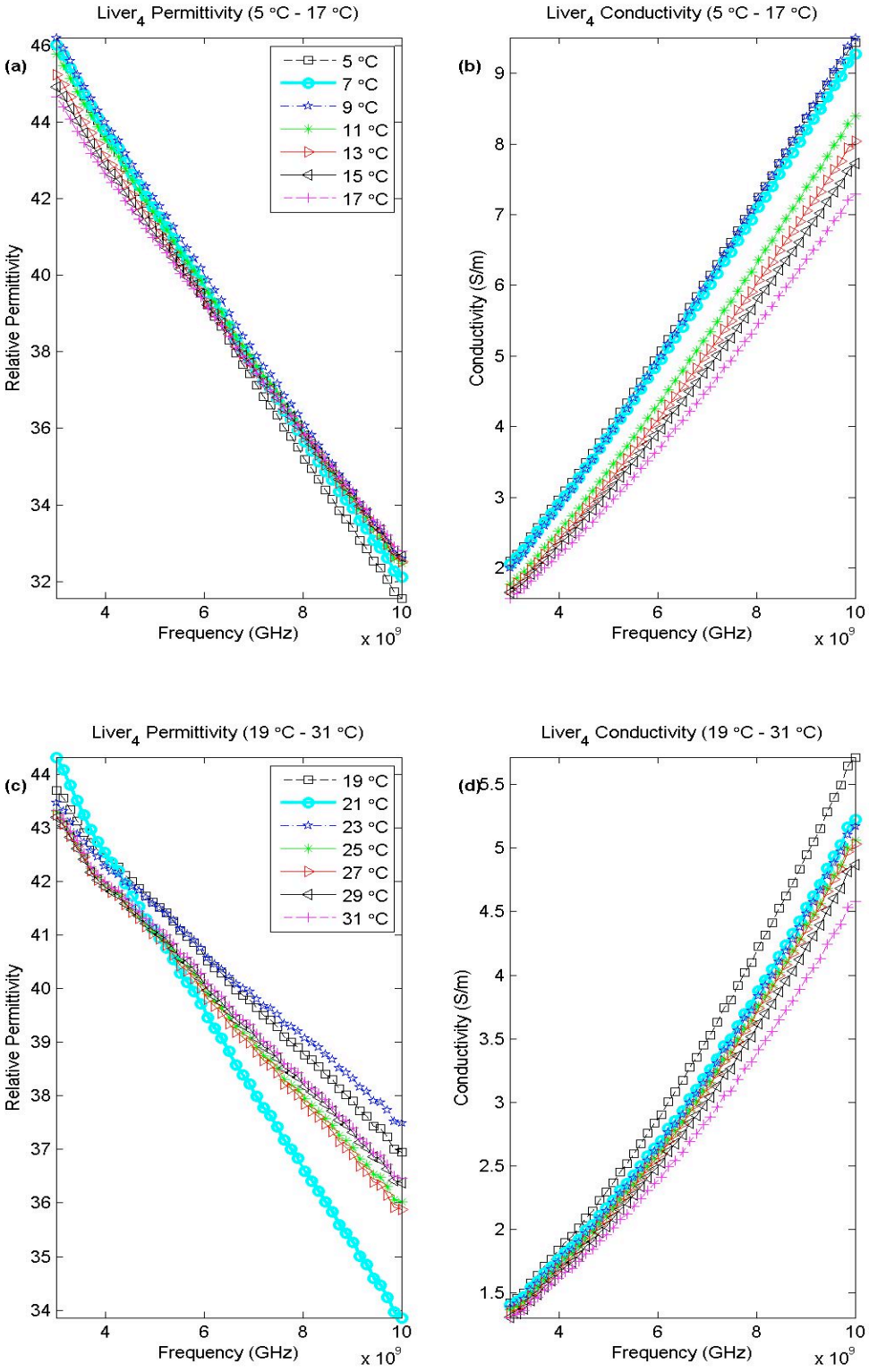
Liver4 Permittivity (5 °C - 17 °C)
(a)
5 °C
7 °C
9 °C
11 °C
13 °C
15 °C
17 °C
Relative Permittivity
Frequency (GHz)
x 10^9
Liver4 Conductivity (5 °C - 17 °C)
(b)
Conductivity (S/m)
Frequency (GHz)
x 10^9
Liver4 Permittivity (19 °C - 31 °C)
(c)
19 °C
21 °C
23 °C
25 °C
27 °C
29 °C
31 °C
Relative Permittivity
Frequency (GHz)
x 10^9
Liver4 Conductivity (19 °C - 31 °C)
(d)
Conductivity (S/m)
Frequency (GHz)
x 10^9

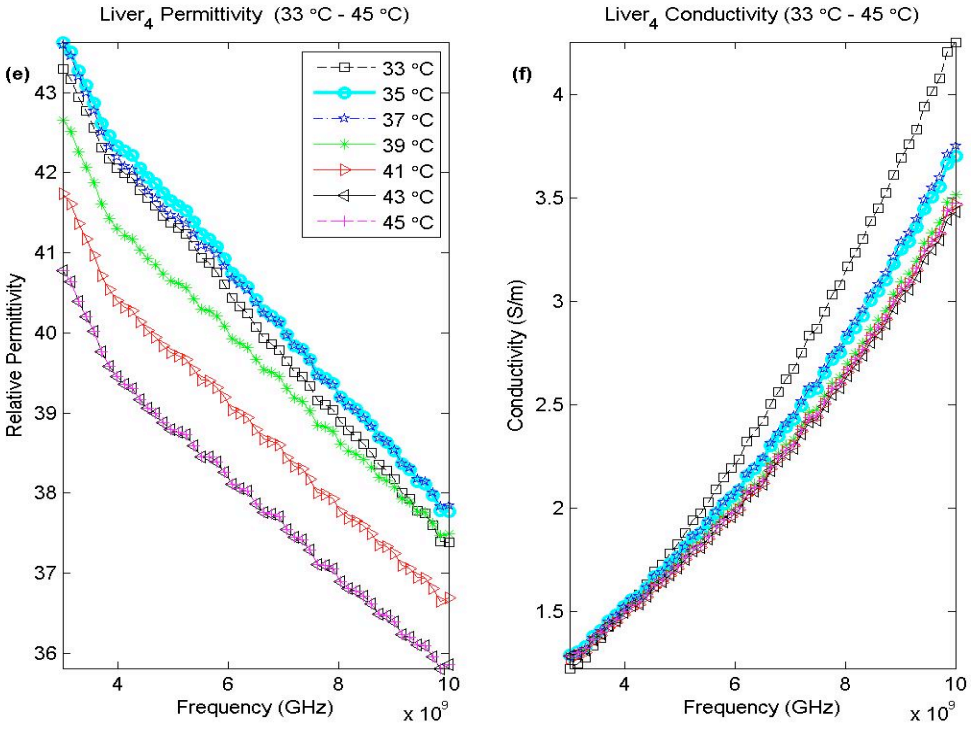

Figure 4.28: Fourth measurement of the liver tissue samples ($liver_4$); frequency trends of permittivity ε_r at: *(a)* 5 - 17 °C, *(c)* 19 - 31 °C and *(e)* 33 - 45 °C; and of conductivity σ at: *(b)* 5 - 17 °C, *(d)* 19 - 31 °C and *(f)* 33 - 45 °C.

The changes of the relative permittivity and the conductivity of the tissue samples are generally not significant at around room temperature indicating that the applied heat did not have a significant effect on the measurement results. The temperature trends of the phantom types and their corresponding tissues (LWCT and fat, HWCT-1 and muscle) do not match, indicating that even though the phantoms follow the frequency trends of their respective tissues, they do not follow their temperature trends. Since the synthesized materials are very different in composition and properties (except the frequency dependence of the dielectric properties) this result was expected.

REFERENCES

[1] Agilent ADS, Agilent Technologies, 1400 Fountaingrove Parkway, Santa Rosa, CA 954031799, USA. [Online] http://www.home.agilent.com/agilent/home.jspx?cc=US&lc=eng.

[2] ThermoWorks, 1762 W. 20 S., Lindon, UT 84042, USA. [Online] http://www.thermoworks.com/index.html.

[3] A. Trehan. *Numerical and Physical Models for Microwave Breast Imaging*, Ch.3. M.A.Sc. Thesis, McMaster University, Ontario, Canada, 2009.

[4] Y. Baskharoun, A. Trehan, N. K. Nikolova, and M. D. Noseworthy, "Physical phantoms for microwave imaging of the breast," *IEEE Conference on BioWireLess*, pp. 73-76, January 2012.

[5] C. L. Brace, "Temperature-dependent dielectric properties of liver tissue measured during thermal ablation: Toward an improved numerical model," *30th Annual IEEE EMBS Conference, Vancouver, British Columbia, Canada*, pp. 230-233, August 2008.

[6] J. B. Hasted and S. H. M. El Sabeh, "The dielectric properties of water in solutions," *Trans. Faraday. Soc.*, vol. 49, pp. 1003-1011, 1953.

[7] M. Lazebnik, M. C. Converse, J. H. Booske and S. C. Hagness, "Ultrawideband temperature-dependent dielectric properties of animal liver tissue in the microwavefrequency range," *Phys. Med. Biol.*, vol. 51, pp. 1941-1955, 2006.

[8] K. R. Foster and H. P. Schwan, "Dielectric properties of tissues and biological materials: a critical review," *Crit. Rev. Biomed. Eng.*, vol. 17, pp. 25-104, 1989.

[9] V. Komarov, S. Wang and J. Tang, "Permittivity and measurements" *Encyclopedia of RF and Microwave Engineering* ed K. Chang, New York: Wiley, 2005.

CHAPTER 5

DATA ANALYSIS AND MODELS

5.1 COLE-COLE MODEL

The first step of the data-fitting algorithm is fitting the frequency dependence of the measured data at each of the measured 21 temperature points. A one-pole Cole-Cole model is used:

$$\varepsilon^*(\omega) = \varepsilon_\infty + \frac{\varepsilon_s - \varepsilon_\infty}{1 + (j\omega\tau)^{1-\alpha}} + \frac{\sigma_i}{j\omega\varepsilon_0} = \varepsilon_\infty + \frac{\Delta\varepsilon}{1 + (j\omega\tau)^{1-\alpha}} + \frac{\sigma_i}{j\omega\varepsilon_0}. \quad (1)$$

The fitting parameters are ε_∞, $\Delta\varepsilon$, τ and σ_i. Here, α is an empirical parameter that accounts for the observed broad distribution of the relaxation-constant values. It does not change with temperature and its constant value is either chosen by trial for the phantoms parameters or is taken from reported data for the tissue parameters. Fitting to the Cole-Cole model is accomplished by minimizing

$$f = \sum \left\| \varepsilon_c^*(\omega) - \varepsilon_m^*(\omega) \right\|^2 \quad (2)$$

where $\varepsilon_c^*(\omega)$ is the complex permittivity of the one-pole Cole-Cole model (1) whose parameters are to be determined and $\varepsilon_m^*(\omega)$ is the measured complex permittivity.

This optimization is achieved by first finding a global minimum of (2) using the 'Global Search' function in MATLAB [1]. The result of this optimization is then used as an initial point for the 'Pattern Search' function of MATLAB. Using either of the methods separately results in inadequate solutions. The lower and upper bounds of the parameters are chosen based on the published Cole-Cole parameters in [2]-[5] in combination with multiple trials to determine the optimum bounds.

Fitting is done for two of the five measurements for each phantom and tissue type because of the difficulty of fitting all the measurements at all temperatures. Measurement errors may also result in frequency dependence that does not obey the Cole-Cole model and such results are discarded. Figure 5.1 shows an example of the fitting result for the LWCT phantom at 45 °C. The measured relative permittivity and conductivity of the two chosen measurements are shown with their average and the resulting Cole-Cole fit. The resulting Cole-Cole model is generated by first fitting the data of each measurement to a Cole-Cole model and then averaging the parameters of both results to obtain the parameters of the Cole-Cole model for this phantom at that temperature. Similar results are obtained for all the phantom and tissue types at all temperatures.

Phantoms

Figure 5.2 – Figure 5.6 show the error between the relative permittivity $\delta\varepsilon_r$ and the error between the conductivity $\delta\sigma$ of the average of the two chosen measurements and the

final Cole-Cole model at each temperature and frequency for the LWCT, IWCT, HWCT-1, HWCT-2 and alginate-based phantoms, respectively. Errors are expressed as absolute differences rather than percentages because the values of the conductivity are very small, which could result in high percent errors that are in fact insignificant. The maximum and the average magnitude of the errors are also shown in the plot inserts. The errors are shown in dimensionless units for the relative permittivity and in S/m for the conductivity.

The maximum error for the relative permittivity of all the models is 1.1 units for the HWCT-2 phantom. Since the relative permittivity of the HWCT-2 phantoms ranges from 30 to 50 units, this error magnitude is acceptable. The maximum error for the relative permittivity of the LWCT phantom is 0.42 units. The relative permittivity of the LWCT phantom is the lowest, being around 5 units at its minimum; yet this maximum error is still a small percentage of the relative permittivity and is acceptable. The maximum average error between the measured and the modeled relative permittivity is also that of HWCT-2 at 0.24 units. All the errors between the measured and the modeled relative permittivities for all the phantom types are within an acceptable range relative to the value of the relative permittivity of their respective phantom types.

The maximum error between the measured and the modeled conductivities is that of the HWCT-1 at 0.45 S/m. However, since the conductivity of the HWCT-1 phantom is relatively high, this error is still acceptable. On the other hand, the maximum error for the conductivity of the LWCT phantom is 0.26. This error is the most alarming because the conductivity of the LWCT phantom at the temperature and the frequency at which this error occurs is around 2.4 S/m. However, the average magnitude of the error for the

LWCT phantom is 0.046, indicating that an error of the magnitude of the maximum rarely occurs. The maximum average of the magnitude of the errors in conductivities occurs for the HWCT-2 phantom at 0.11, which is also acceptable relative to the higher conductivity values of 3 – 10 S/m for this phantom type. All the other errors between the measured and the modeled conductivities for all the phantom types are within an acceptable range relative to the conductivity value of their respective phantom types.

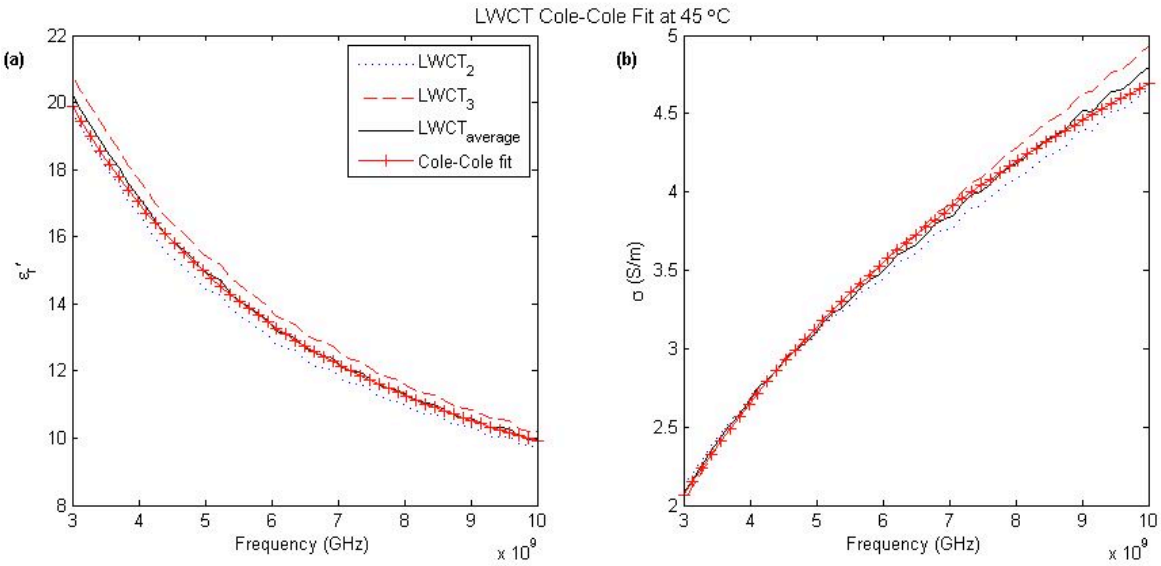

Figure 5.1: *(a)* Relative permittivity and *(b)* conductivity of the second and third LWCT phantom measurements at 45 °C, their average and the resulting one-pole Cole-Cole fit generated from the average parameters of fitting to both measurements.

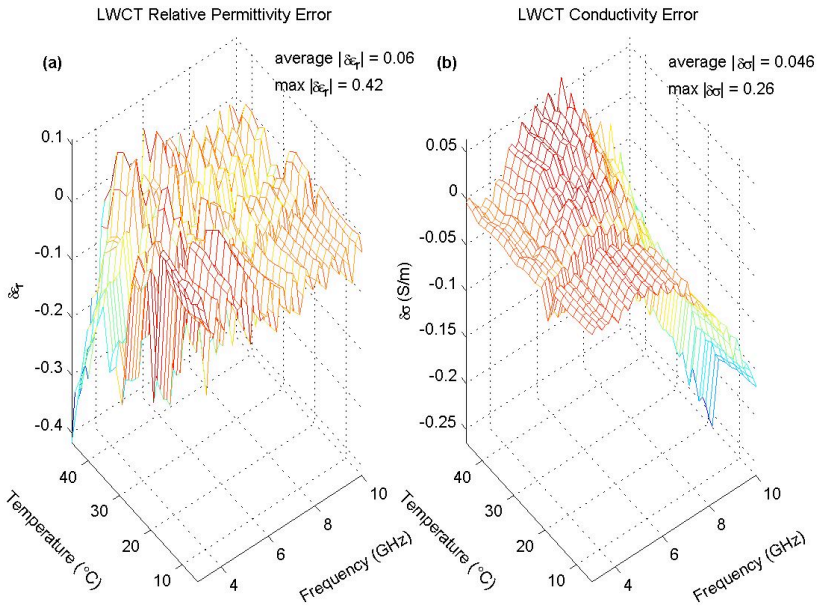

Figure 5.2: Difference between the measured and the one-pole Cole-Cole model values of the LWCT phantoms: *(a)* relative permittivity and *(b)* conductivity. The maximum and the average errors are also shown in the plot insert.

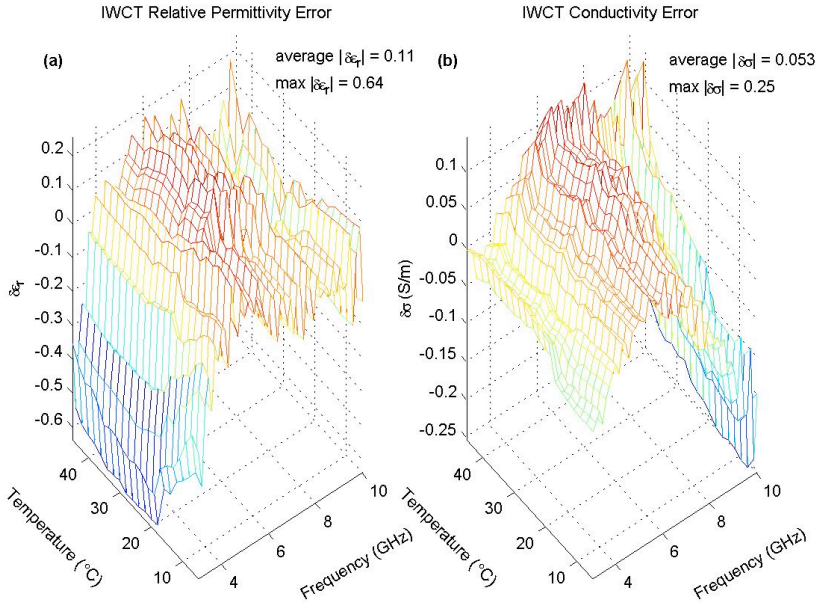

Figure 5.3: Difference between the measured and the one-pole Cole-Cole model values of the IWCT phantoms: *(a)* relative permittivity and *(b)* conductivity. The maximum and the average errors are also shown in the plot insert.

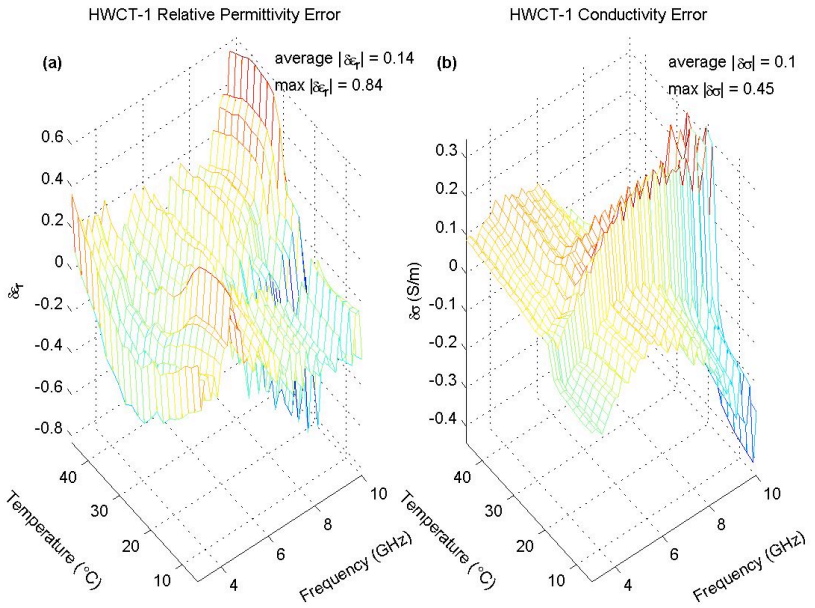

Figure 5.4: Difference between the measured and the one-pole Cole-Cole model values of the HWCT-1 phantoms: *(a)* relative permittivity and *(b)* conductivity. The maximum and the average errors are also shown in the plot insert.

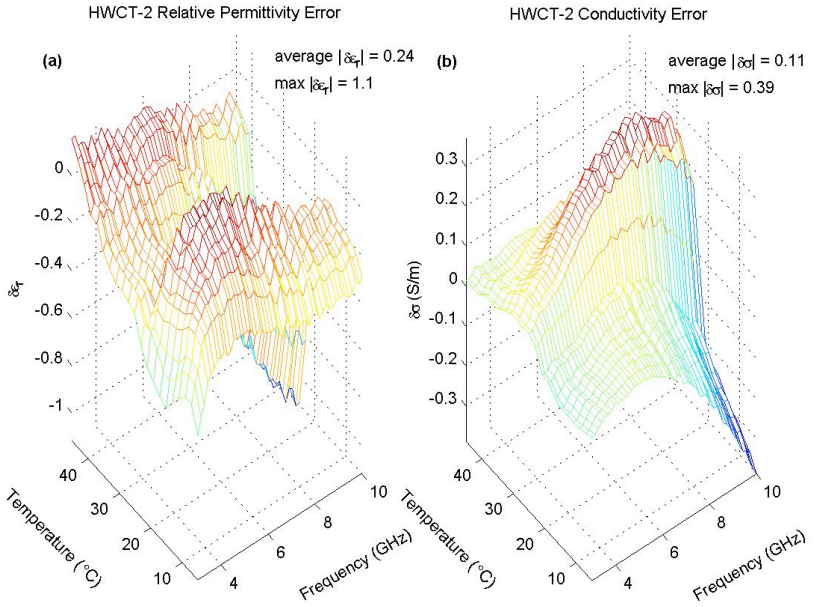

Figure 5.5: Difference between the measured and the one-pole Cole-Cole model values of the HWCT-2 phantoms: *(a)* relative permittivity and *(b)* conductivity. The maximum and the average errors are also shown in the plot insert.

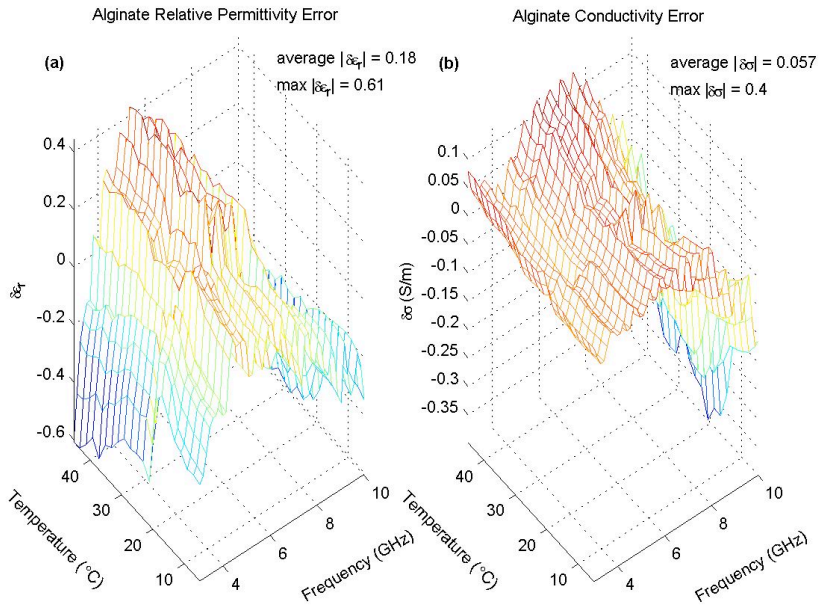

Figure 5.6: Difference between the measured and the one-pole Cole-Cole model values of the alginate-based phantoms: *(a)* relative permittivity and *(b)* conductivity. The maximum and the average errors are also shown in the plot insert.

The empirical parameter α is set to 0.2 for the LWCT phantom and to 0.1 for all the other phantom types. The average parameters of the two measurements for each phantom and tissue type at all temperatures are shown in the figures below. Figure 5.7 shows the average fitted $\boldsymbol{\varepsilon_\infty}$ parameter of the LWCT, IWCT, HWCT-1, HWCT-2 and alginate-based phantoms at all temperatures. The value of ε_∞ decreases gradually with increasing temperature for the LWCT phantom. For the IWCT phantom, it decreases slightly (almost constant) until 19 °C, increases at 21 °C and continues to decrease after. For the HWCT-1 phantom, it decreases slightly (almost constant) until 19 °C, decreases dramatically till 33 °C, and then increases slightly (almost constant) up to 45 °C. For the HWCT-2 phantom, ε_∞ decreases till 33 °C, and then continues to increase up to 45 °C. ε_∞

of the alginate-based tumor phantom remains constant until 19 °C then increases greatly until 45 °C. There is, therefore, a general decreasing trend for ε_∞ for the gelatin-based phantoms, which is consistent with the trend of ε_∞ of water reported in [2].

Figure 5.8 shows the average fitted parameter $\Delta\varepsilon$ of the LWCT, IWCT, HWCT-1, HWCT-2 and alginate-based phantoms at all temperatures**.** $\Delta\varepsilon$ decreases as temperature increases for all the gelatin based phantoms. For the alginate-based tumor phantom, $\Delta\varepsilon$ increases up to 21 °C and then decreases thereafter. The decrease of $\Delta\varepsilon$ of the gelatin-based phantoms is also observed for water [2],[3]. However, the trend of $\Delta\varepsilon$ for the alginate-based phantom, in which saline is the solvent, is not consistent with the decrease of $\Delta\varepsilon$ with temperature for saline [2].

Figure 5.9 shows the average fitted parameter τ for the LWCT phantom at all temperatures. Figure 5.10 shows the average fitted τ parameter (relaxation time) for the IWCT, HWCT-1, HWCT-2 and alginate-based phantoms at all temperatures. τ for the LWCT phantom is an order or magnitude higher than that of the other phantoms. The relaxation times for all the phantoms are in picoseconds. They all decrease, at different rates, with increasing temperature. τ for the LWCT and the IWCT phantoms have the highest rate of decline, while that of the alginate-based phantom has the smallest rate. τ for the HWCT-1 and the HWCT-2 phantoms have similar values and decrease in a similar manner with increasing temperature.

Figure 5.11 shows the average fitted parameter σ_i for the LWCT, IWT, HWCT-1 and HWCT-2 phantoms at all temperatures. Figure 5.12 shows the average fitted parameter σ_i for the alginate-based tumor phantom at all temperatures. σ_i for the LWCT

phantom remains constant at 0.01 S/m, while that of the HWCT-1 and the HWCT-2 is constant at 0.2 S/m. σ_i for the IWCT phantom decreases with increasing temperature. σ_i for the alginate-based phantom is an order of magnitude higher than that of the gelatin-based phantoms and increases with increasing temperature. Since the solvent of this phantom is saline, its high σ_i is a result of the ions formed in the saline. The increase in σ_i can also be explained by the increase in ions with increasing temperature in the saline solution. The exact values of the Cole-Cole parameters at every temperature for the phantoms are given in tables in Appendix I.

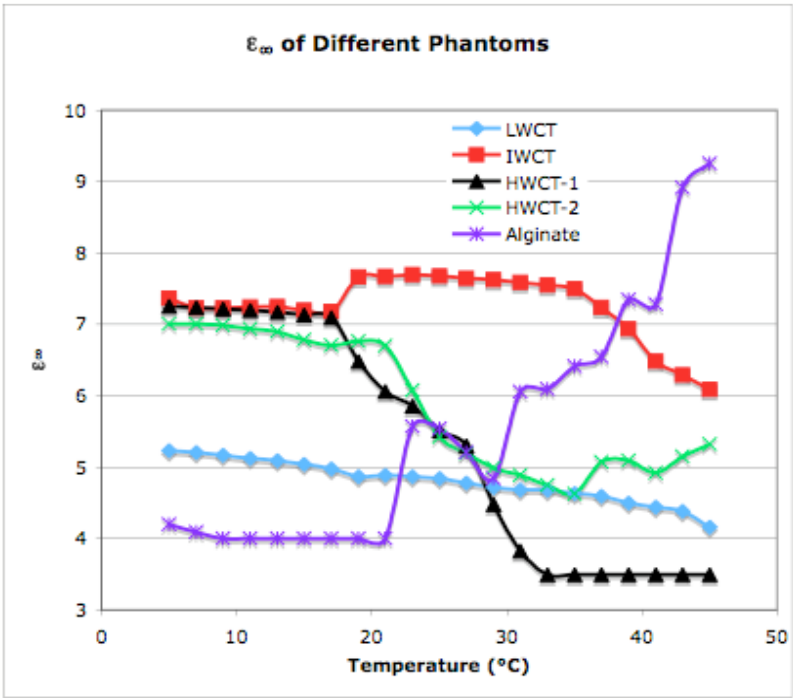

Figure 5.7: Average one-pole Cole-Cole fitted parameter ε_∞ of the LWCT, IWCT, HWCT-1, HWCT-2 and alginate-based phantoms at all temperatures.

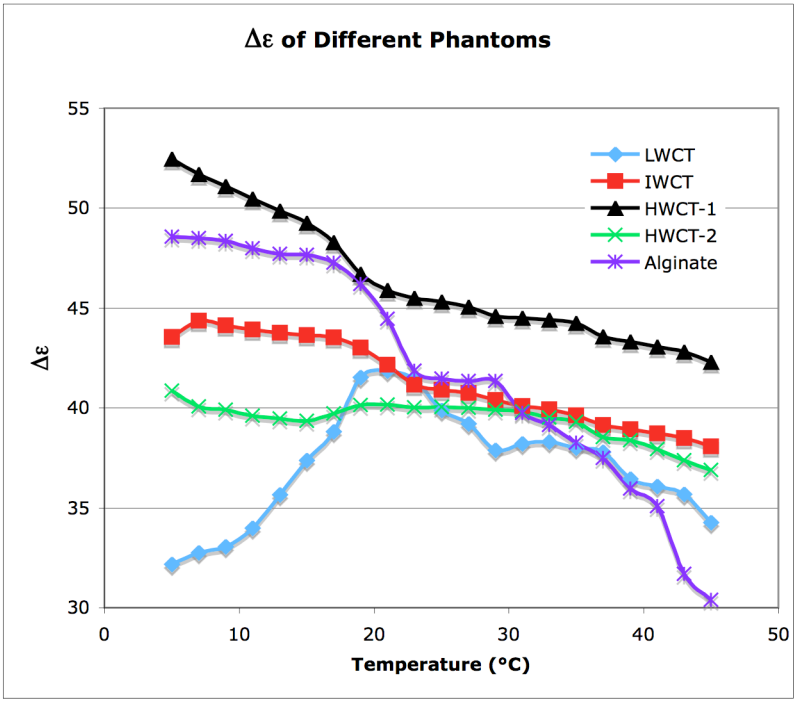

Figure 5.8: Average one-pole Cole-Cole fitted parameter $\Delta\varepsilon$ of the LWCT, IWCT, HWCT-1, HWCT-2 and alginate-based phantoms at all temperatures.

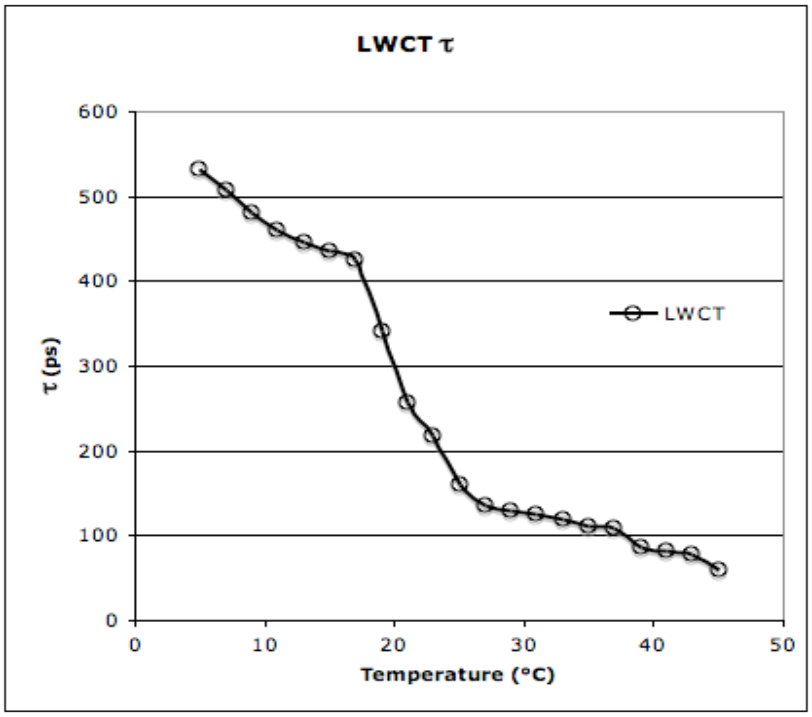

Figure 5.9: Average one-pole Cole-Cole fitted parameter τ for the LWCT phantom at all temperatures.

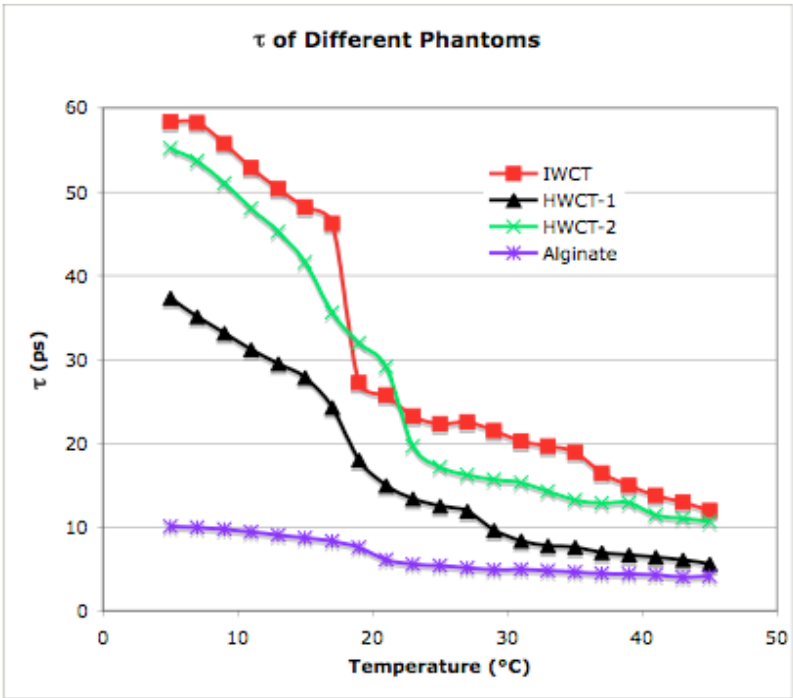

Figure 5.10: Average one-pole Cole-Cole fitted parameter τ for the IWCT, HWCT-1, HWCT-2 and alginate-based phantoms at all temperatures.

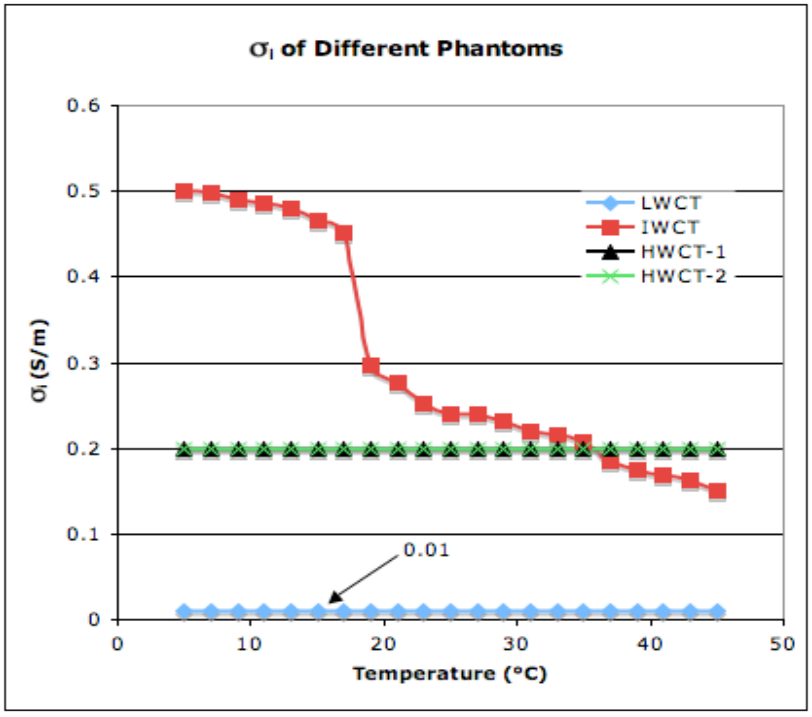

Figure 5.11: Average one-pole Cole-Cole fitted parameter σ_i for the LWCT, IWT, HWCT-1 and HWCT-2 phantoms at all temperatures.

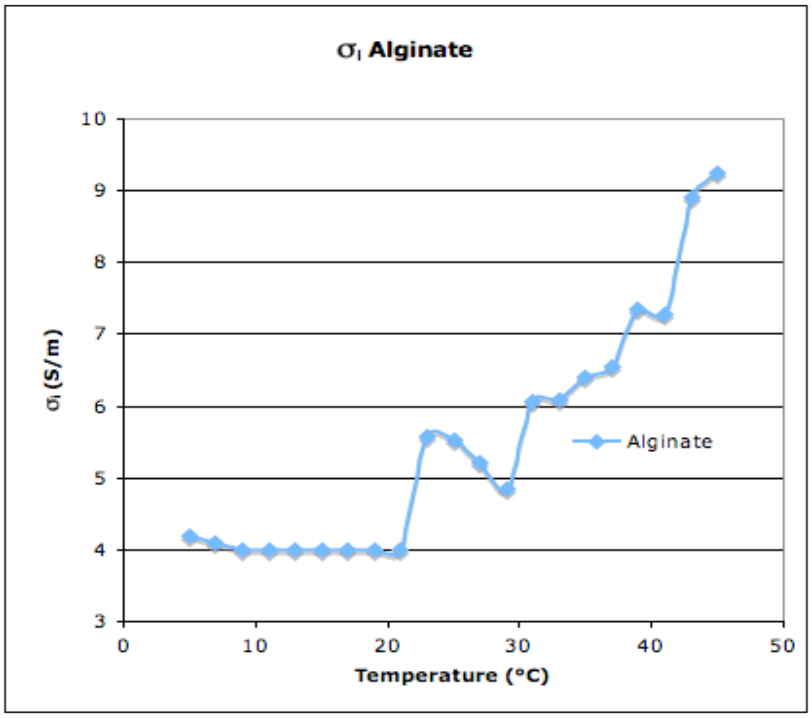

Figure 5.12: Average one-pole Cole-Cole fitted parameter σ_i for the alginate-based phantom at all temperatures.

Tissues

The same fitting procedure to the Cole-Cole model is used to fit the data measured with the tissue sample. For the tissue samples, both α and ε_∞ remain constant with temperature. A small increase in ε_∞ is observed with increasing temperature, which is also observed for water and saline [2]. Those small changes are deemed negligible and ε_∞ are set to a constant value in order to simplify the model. The fitting results for the relative permittivity and the difference between the conductivity of the tissue samples are similar to those in Figure 5.1.

Figure 5.13 – Figure 5.15 show the difference between the relative permittivity $\delta\varepsilon_r$ and the difference between the conductivity $\delta\sigma$ of the average of the two chosen measurements and the final Cole-Cole model at each temperature and frequency for the fat, muscle and liver tissue samples, respectively.

The maximum error for the relative permittivity of the fat tissue samples is 0.14. The minimum relative permittivity of fat is around 6 units; therefore, this maximum error is acceptable. However, the maximum error for the conductivity of fat is 0.16, which is around 25% of the minimum conductivity for fat, which is around 0.3 S/m. Yet, this maximum error occurs at 10 GHz where the conductivity is around 1 S/m, making this error only around 10%. Since the conductivity of fat is very small, the errors seem to be high in term of percentages; however, as Lazebnik *et al.* stated, the conductivity values are very small at low frequencies, possibly resulting in very large, though insignificant, percentage errors [4]. The average of the magnitude of the difference in conductivity for fat is 0.037 indicating satisfactory fitting results overall.

The maximum difference in the relative permittivity of the muscle samples is 1.8 units. Since the relative permittivity of muscle is relatively high, having a minimum of around 35 units, this maximum error is negligible. The maximum difference for the conductivity fit of muscle is 0.67, which occurs at 10 GHz where the conductivity of muscle is around 12 S/m. Thus, this maximum error is tolerable. The average magnitude of the difference in conductivity between the measured and the fitted data is 0.037.

The maximum difference between the measured and the Cole-Cole model relative permittivity of liver is 1.8 units, which, as for muscle, is negligible, compared to the high

relative permittivity values of liver. The average error magnitude for the relative permittivity of liver is also at an insignificant value of 0.24 units. The maximum difference in conductivity values of 0.63 for the liver samples also occurs at 10 GHz where the conductivity of liver is around 10 S/m. The average magnitude of the difference in conductivity values for liver is 0.067. Therefore, the results of the fitting of the Cole-Cole model to the measured data of the tissue samples resulted in generally insignificant or acceptable differences between the measured and the fitted relative permittivities and conductivities.

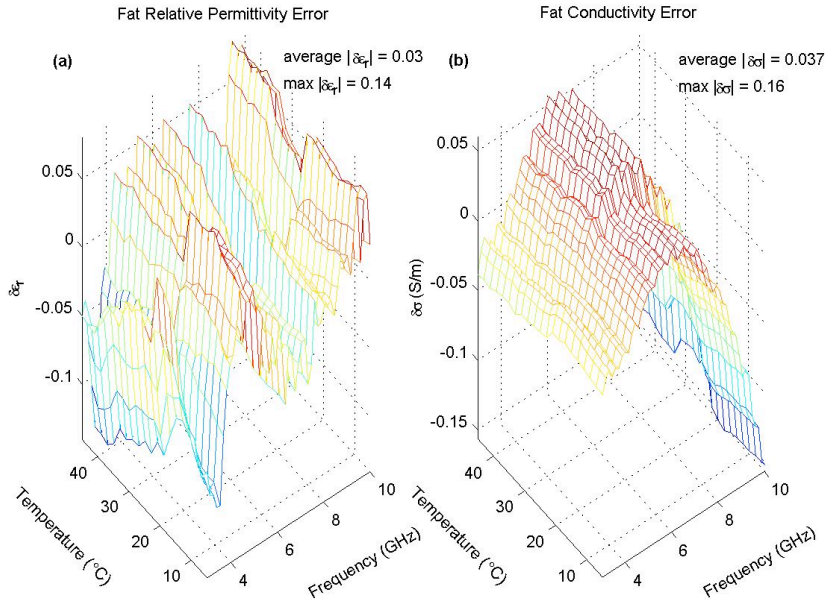

Figure 5.13: Difference between the measured and the one-pole Cole-Cole model values of the fat tissue samples: *(a)* relative permittivity and *(b)* conductivity. The maximum and the average errors are also shown in the plot insert.

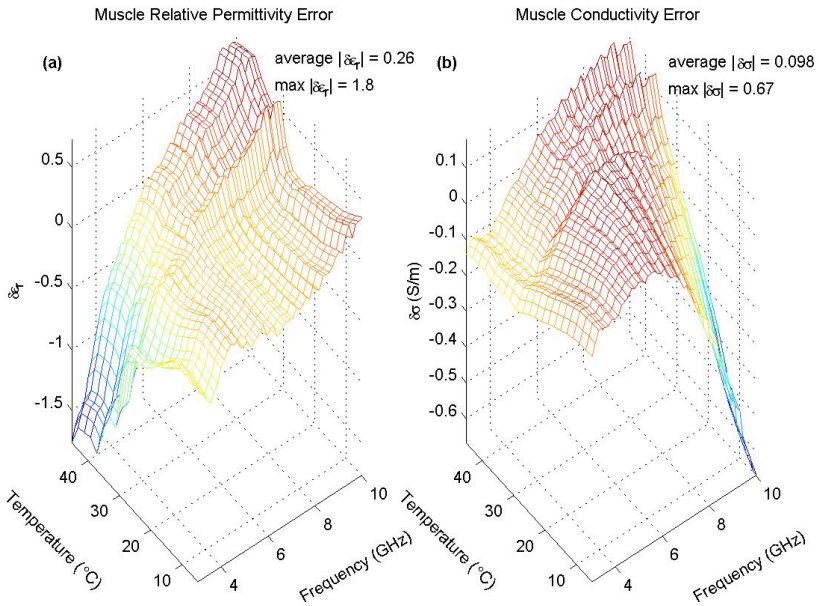

Figure 5.14: Difference between the measured and the one-pole Cole-Cole model values of the muscle tissue samples: *(a)* relative permittivity and *(b)* conductivity. The maximum and the average errors are also shown in the plot insert.

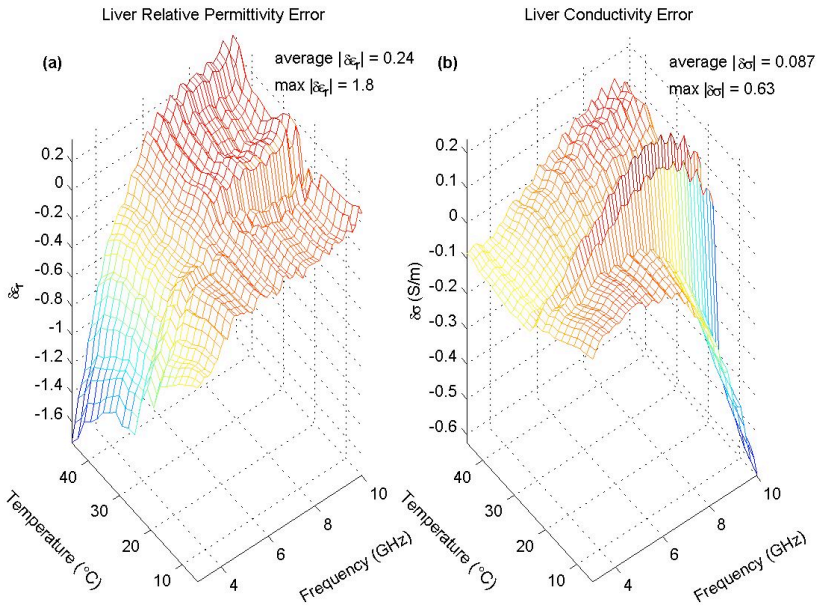

Figure 5.15: Difference between the measured and the one-pole Cole-Cole model values of the liver tissue samples: *(a)* relative permittivity and *(b)* conductivity. The maximum and the average errors are also shown in the plot insert.

The empirical parameter α is set to 0.01 for fat and to 0.1 for muscle and liver. Figure 5.16 shows the average $\Delta\varepsilon$ of the two chosen measurements for each of the three tissue types. The ε_∞ values for the three tissue types are also shown in the figure. Since, as mentioned earlier, the value of ε_∞ changes slightly with temperature, the final ε_∞ value is set equal to the average of the ε_∞ at all temperatures. The value of ε_∞ for fat is 2.54, for muscle is 5.95 and for liver is 7.5. As seen in the figure, the value of $\Delta\varepsilon$ for fat is around 9 units, much smaller than that for muscle and liver, which are 35 and 45, respectively. These values are consistent with the fact that fat is the lowest-water content tissue and has the lowest relative permittivity and conductivity values. Muscle and liver are high-water content tissues and thus have high relative permittivities and conductivities. Muscle has a higher water content than liver and thus has a higher $\Delta\varepsilon$ than liver.

The values of $\Delta\varepsilon$ for all the tissue types decrease as temperature increases. This trend is consistent with that of water and saline [3]. Figure 5.17 shows the average τ values of the two chosen measurements for each of the three tissue types. Same as for $\Delta\varepsilon$, τ of fat is smaller than that of muscle and liver for the lower temperature range; however, as temperature gets higher, the τ values of all three tissue types become almost equal starting at around 30 °C. The decreasing trend of τ as temperature increases is also consistent with that of water and saline [3].

Figure 5.18 shows the average σ_i of the two chosen measurements for each of the three tissue types. σ_i for fat is smaller than that of muscle and liver, which have close values. This is also consistent with the fact that fat has the lowest water content and thus the lowest conductivity values. σ_i of the three tissue types increases as temperature

increases. This trend is also consistent with the increase in σ_i with temperature for liver reported by Lazebnik *et al.* [4]. For all three parameters, $\Delta\varepsilon$, τ and σ_i, the rate of change for fat is smaller than that for muscle and liver. The exact values of the Cole-Cole parameters at every temperature for the tissue samples are given in tables in Appendix I.

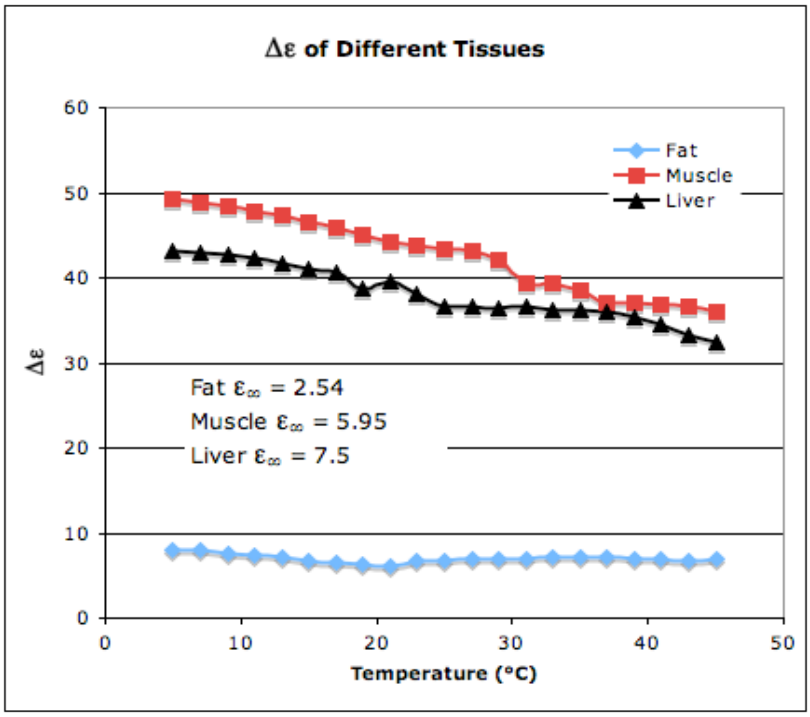

Figure 5.16: Average one-pole Cole-Cole $\Delta\varepsilon$ parameter of the fat, muscle and liver tissue samples at all temperatures. $\Delta\varepsilon = \varepsilon_s - \varepsilon_\infty$ so the ε_∞ values of the three tissue types are also shown in the figure insert.

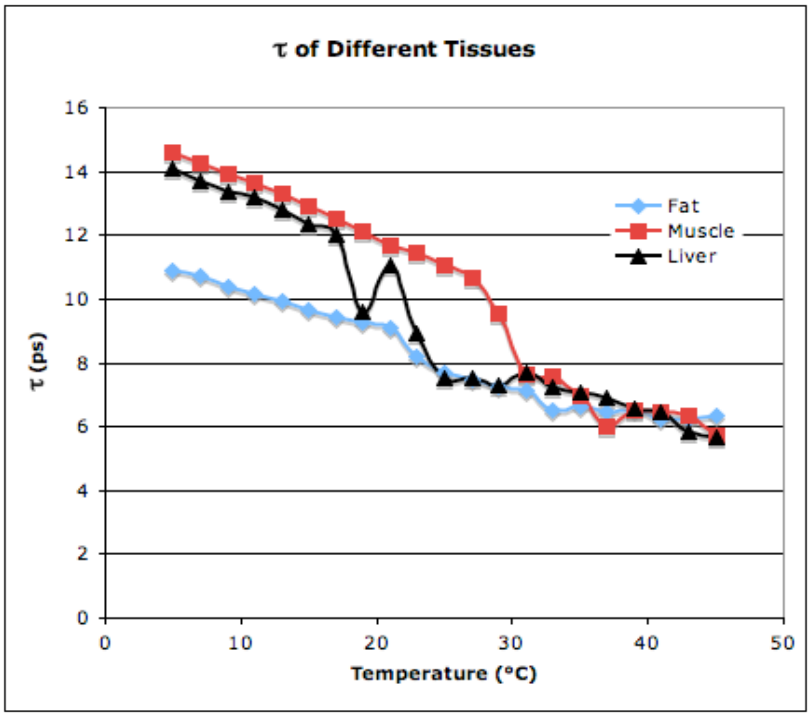

Figure 5.17: Average one-pole Cole-Cole τ parameter for the fat, muscle and liver tissue samples at all temperatures.

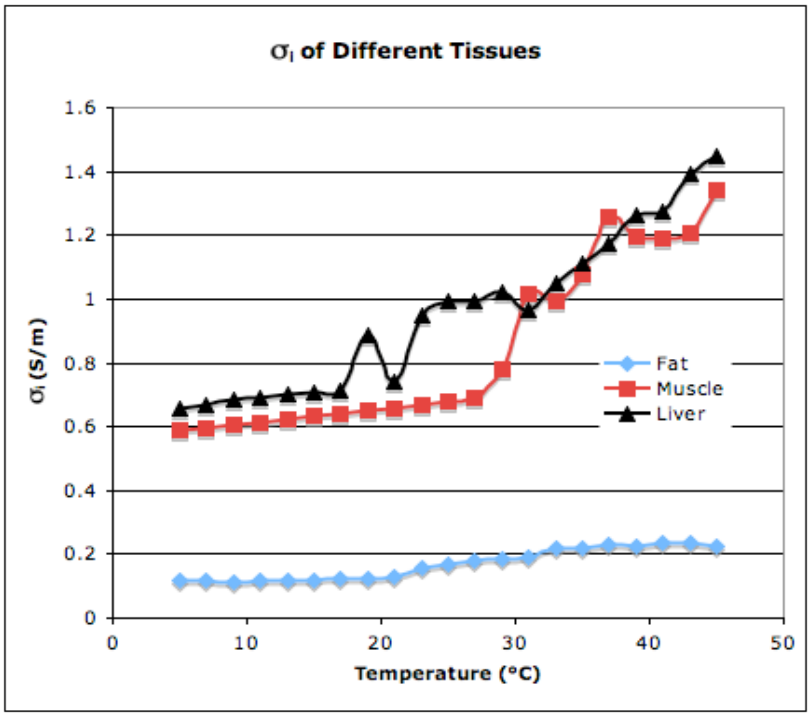

Figure 5.18: Average one-pole Cole-Cole σ_i parameter for the fat, muscle and liver tissue samples at all temperatures.

As Table 5-1 demonstrated, even though the LWCT and the HWCT-1 phantoms were made to mimic the dielectric properties of fat and muscle, respectively, not all one-pole Cole-Cole parameters are similar. This is because the phantoms were created to mimic the frequency trends and the contrast between the various tissues rather than the actual relative permittivity and conductivity values. The relative permittivity and conductivity values of the phantoms and their respective tissues are close and follow similar frequency trends, but are not equal. Moreover, the parameters of the phantoms do not follow the temperature trends of their respective tissues, since their relative permittivities and conductivities do not either.

Table 5-2 shows a comparison between the one-pole Cole-Cole parameters of this work with those of the most relevant pole of the four-pole Cole-Cole model presented by Gabriel *et al.* [5] for fat, muscle and liver, as well as the parameters of the one-pole Cole-Cole model presented by Lazebnik *et al.* for liver [4]. The data sets are reasonably comparable except for two main differences: (i) α for fat of our data is 0.01 compared to a value of 0.2 from Gabriel *et al.*'s data and (ii) σ_i values are very different for all tissue types. The differences in α are due to the necessity to fit our data to a one-pole Cole-Cole model at all temperatures, rather than the single-temperature analysis performed by Gabriel *et al.* However, the value of α is 0.01 for fat , equal to its value in this work, in the fourth pole of the Cole-Cole model provided by Gabriel *et al.* The values of σ_i are very different because Gabriel *et al.* used a four-pole Cole-Cole model to fit their data over a very wide frequency range, and σ_i is an inherently a DC quantity.

This comparison demonstrates that the measurement data obtained in this work truly reproduces previously published data for fat, muscle and liver. It also shows that the one-pole Cole-Cole model is sufficiently accurate.

Table 5-1: Comparison between the one-pole Cole-Cole fitting parameters of the LWCT and the HWCT-1 phantoms at 23 °C and those of fat and muscle at 37 °C. LWCT phantoms are made to mimic the dielectric properties of fat and HWCT-1 phantoms are made to mimic the dielectric properties of muscle.

	Phantoms at 23 °C		**Tissues at 37 °C**	
	LWCT	**HWCT-1**	**Fat**	**Muscle**
ε_∞	4.872	5.859	2.54	5.95
$\Delta\varepsilon$	41.429	45.502	7.063	37.050
α	0.2	0.1	0.01	0.1
τ (ps)	217.971	13.392	6.436	6.012
σ_i	0.010	0.200	0.228	1.257

Table 5-2: Comparison between the one-pole Cole-Cole fitting parameters for the three tissue types in this work and those reported in literature.

	This work's data at 37 °C			**Gabriel *et al.*'s data [5]**			**Lazebnik *et al.*'s data [4]**
	Fat	**Muscle**	**Liver**	**Fat**	**Muscle**	**Liver**	**Liver**
ε_∞	2.54	5.95	7.50	2.5	4.0	4.0	9.1
$\Delta\varepsilon$	7.063	37.050	36.020	6	50.0	39.0	41.1
α	0.01	0.1	0.1	0.2	0.2	0.1	0.1
τ (ps)	6.436	6.012	6.881	7.96	7.23	8.84	9.09
σ_i	0.228	1.257	1.173	0.01	0.2	0.02	0.84

5.2 TEMPERATURE-DEPENDENCE MODEL

The second part of the fitting process is fitting the temperature dependence of the one-pole Cole-Cole model parameters to the measurements. The second-order polynomials:

$$AT^2 + BT + C \tag{3}$$

is chosen to represent this dependence. Whenever a second-order polynomial is insufficient, a third-order polynomial of the form:

$$DT^3 + AT^2 + BT + C \tag{4}$$

is used.

The "add trendline" function of Microsoft Excel [6] is used to complete this part. This function fits the selected data to a chosen function using a least-squares minimization procedure. Therefore, the final model of this work is a one-pole Cole-Cole result whose parameters are functions of temperature. This model is referred to as the final one-pole Cole-Cole model hereafter. The coefficients of the quadratic or cubic polynomial fits are given in Table 5-3 for all the phantom types and in Table 5-4 for all the tissue types.

Table 5-3: Coefficients of the second- or third-order polynomial function from (3) and (4) used to fit the temperature dependence of the one pole Cole-Cole parameters of the different phantom types.

		ε_∞	$\Delta\varepsilon$	τ ($\times 10^{-12}$)	σ_i	α
LWCT	***A***	-0.0002	-0.0186	0.2631	0.01 (constant)	0.2 (constant)
	B	-0.0136	0.9851	-26.314		
	C	5.29	26.921	707.33		
IWCT	***A***	-0.0026	-0.0004	0.03178	0.0002	0.1 (constant)
	B	0.1132	-0.1476	-2.8613	-0.0197	
	C	6.4411	45.375	77.554	0.6496	
HWCT-1	***D***	0.0003	-	-	0.2 (constant)	0.1 (constant)
	A	-0.0224	0.0054	0.0234		
	B	0.3561	-0.517	-2.0193		
	C	5.7851	55.197	49.305		
HWCT-2	***D***	-	-0.0002	-	2.95E-5	0.1 (constant)
	A	0.0012	0.0153	0.03462	-1.99E-03	
	B	-0.1282	-0.2916	-2.9607	2.15E-02	
	C	8.1267	41.552	74.056	4.58E-01	
Alginate	***A***	0.0043	-0.0072	0.00397	0.0009	0.1 (constant)
	B	-0.0933	-0.902	-0.3698	0.0575	
	C	4.5136	49.714	12.641	2.6306	

Phantoms

A. **LWCT Phantom**

Figure 5.19 shows the average one-pole Cole-Cole parameters of the two chosen measurements with the resulting quadratic fits for the LWCT phantom. The temperature dependence of the parameters is not a smooth one, however the resulting second-order polynomials offer a reasonable estimate of the parameters at every temperature. Th values of α and σ_i do not change with temperature and are set to 0.2 and 0.01, respectively.

Figure 5.20 *(a)* – *(j)* shows the relative permittivities and the conductivities calculated from the final Cole-Cole model along with the original five measurements of the LWCT phantom and the average of the two chosen measurements at 3 GHz, 5.1 GHz, 7.06 GHz, 9.02 GHz, 10 GHz. The final one-pole Cole-Cole model follows well the temperature trends of the relative permittivity and the conductivity of the LWCT phantom.

Figure 5.21 shows the absolute differences between the average relative permittivities and the conductivities of the two chosen measurements and the final one-pole Cole-Cole model for the LWCT phantom. The figure also shows the maximum and the average differences for the relative permittivity and the conductivity. The maximum difference in the relative permittivity is 2.3 units at 29 °C and 3 GHz where the relative permittivity is around 15 units. Even though this maximum difference is not small, it is acceptable when compared to the value of the relative permittivity at that point. The

average magnitude of the difference in the relative permittivity is 0.44 units. The maximum difference in conductivity is 0.76 S/m and it occurs at 10 GHz and at 27 °C where the average conductivity of the two chosen measurements is around 3 S/m. Given the generally small values of the conductivity of the LWCT phantom, this maximum error is not within an acceptable range. However, the average difference in conductivities is acceptable at 0.17 S/m.

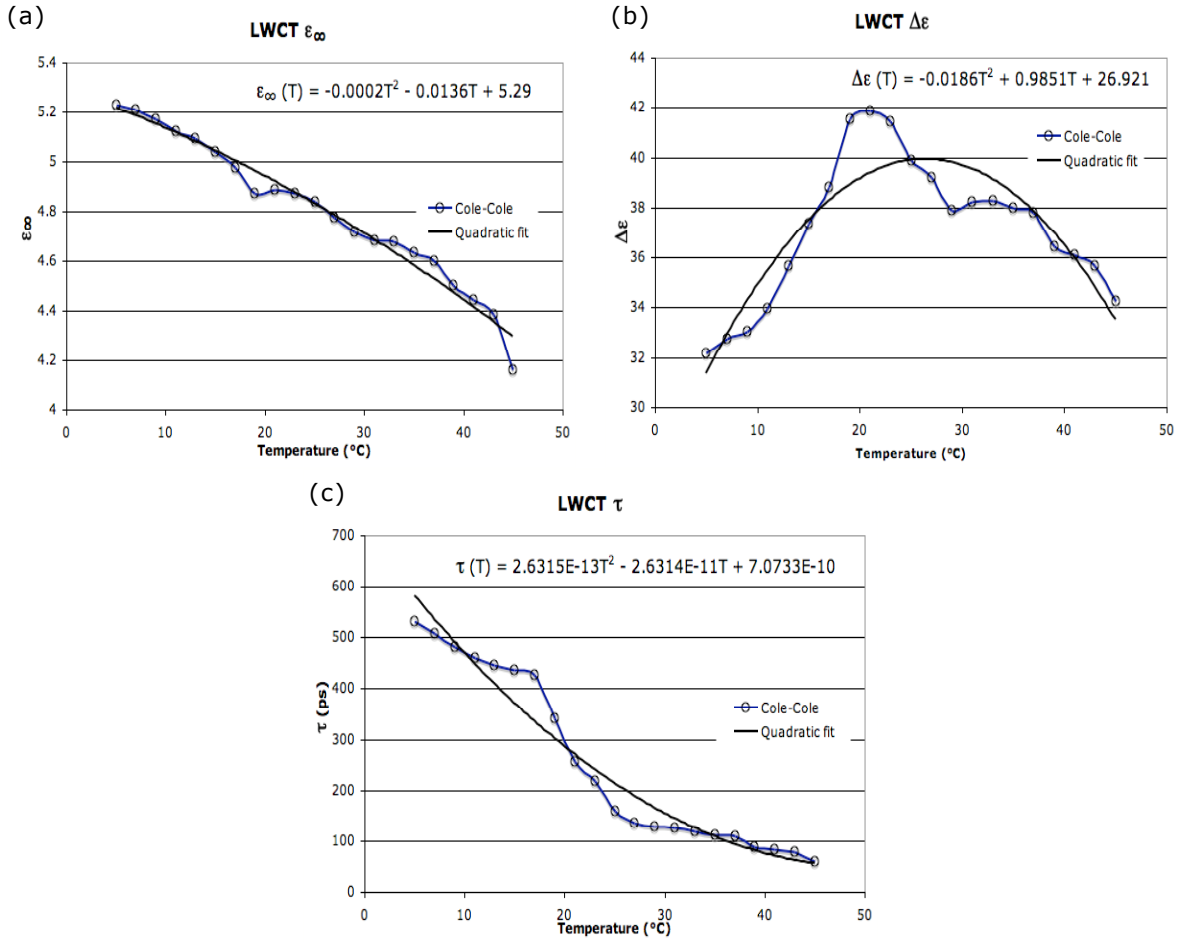

Figure 5.19: LWCT phantom average one-pole Cole-Cole model parameters and their temperature-dependent quadratic fits: *(a)* ε_∞, *(b)* $\Delta\varepsilon$ and *(c)* τ. The resulting temperature equations are also shown in the figure insert.

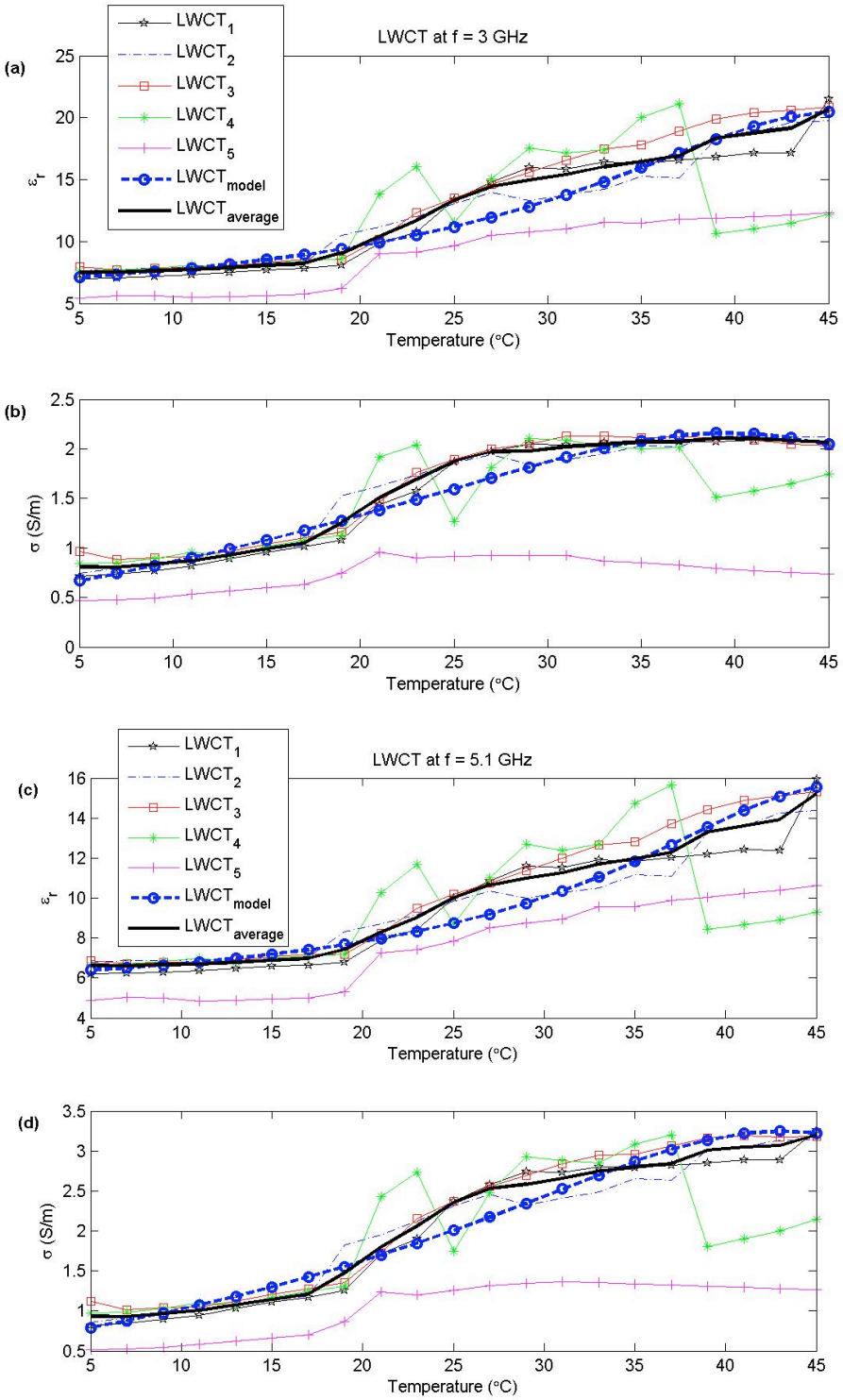
(a)
LWCT at f = 3 GHz
LWCT1
LWCT2
LWCT3
LWCT4
LWCT5
LWCTmodel
LWCTaverage
εr
Temperature (°C)
(b)
σ (S/m)
Temperature (°C)
(c)
LWCT at f = 5.1 GHz
LWCT1
LWCT2
LWCT3
LWCT4
LWCT5
LWCTmodel
LWCTaverage
εr
Temperature (°C)
(d)
σ (S/m)
Temperature (°C)

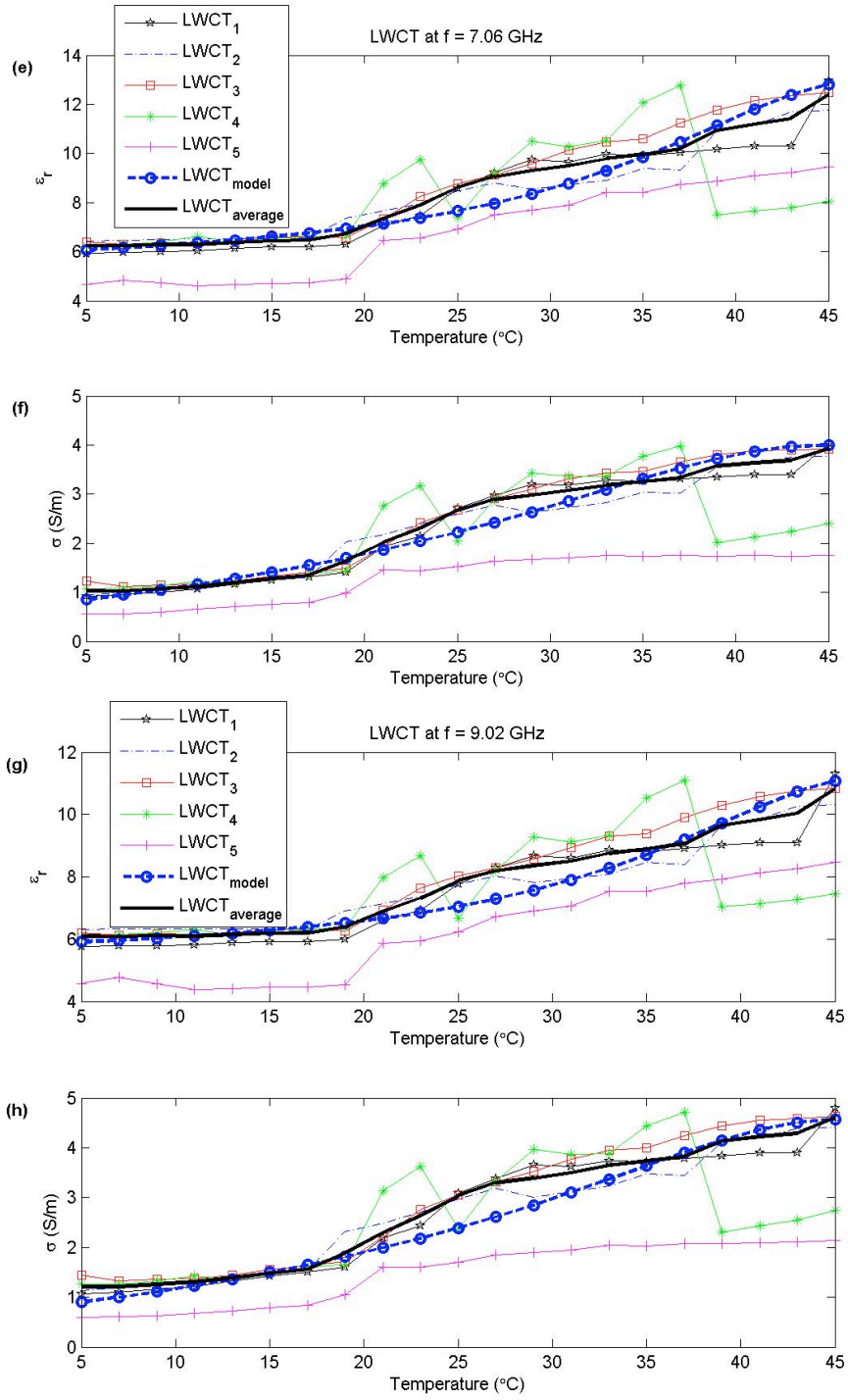
(e)
LWCT at f = 7.06 GHz
LWCT1
LWCT2
LWCT3
LWCT4
LWCT5
LWCTmodel
LWCTaverage
εr
Temperature (°C)
(f)
σ (S/m)
Temperature (°C)
(g)
LWCT at f = 9.02 GHz
LWCT1
LWCT2
LWCT3
LWCT4
LWCT5
LWCTmodel
LWCTaverage
εr
Temperature (°C)
(h)
σ (S/m)
Temperature (°C)

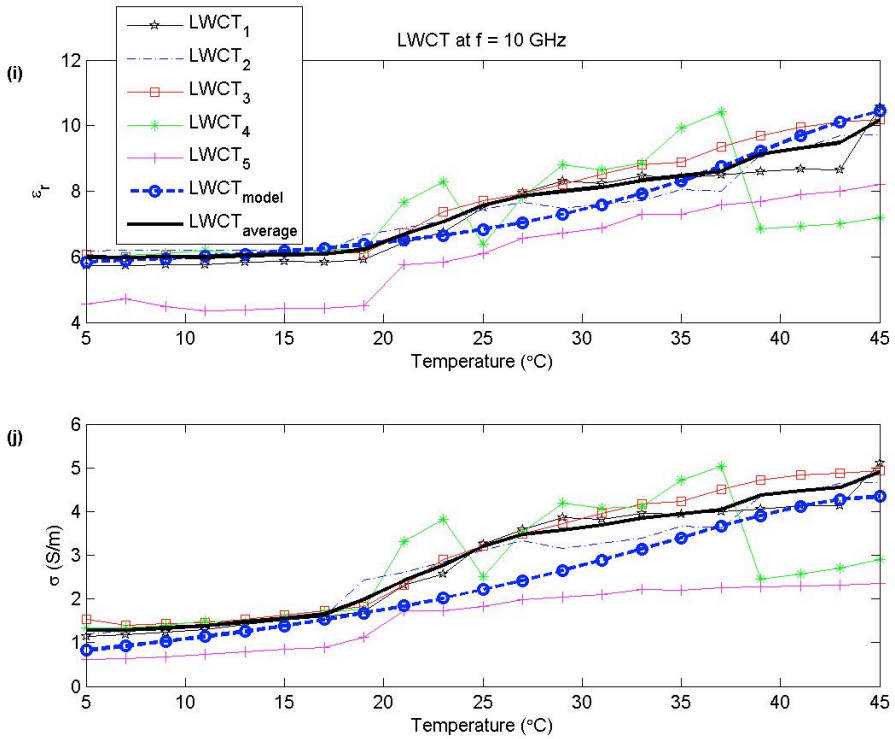

Figure 5.20: Temperature trends of the relative permittivity ε_r of the five measurements of the LWCT phantom, the average of the two chosen measurements and the final one-pole Cole-Cole model at: *(a)* 3 GHz, *(c)* 5.01 GHz, *(e)* 7.06 GHz, *(g)* 9.02 GHz and *(i)* 10 GHz. Temperature trends of the conductivity σ_i at: *(b)* 3 GHz, *(d)* 5.01 GHz, *(f)* 7.06 GHz, *(h)* 9.02 GHz and *(j)* 10 GHz.

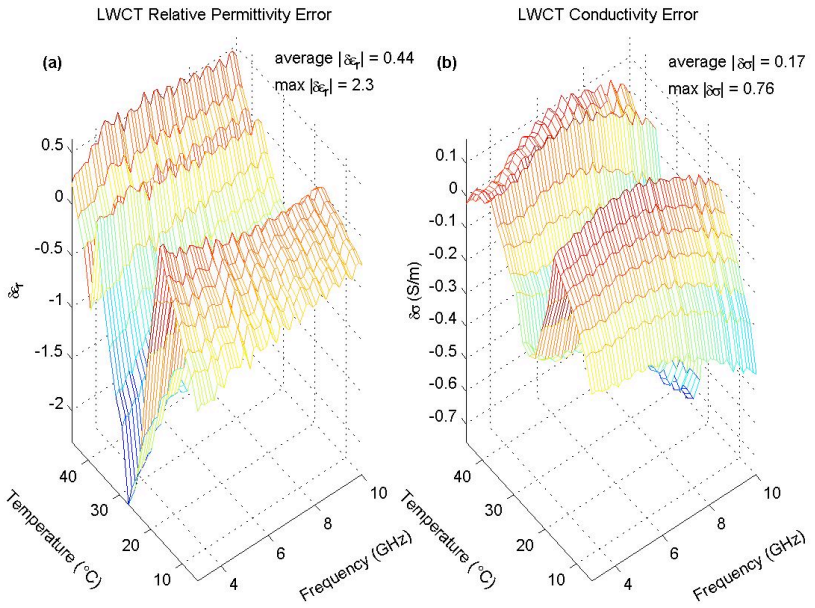

Figure 5.21: Difference between the measured and the final one-pole Cole-Cole model values for the LWCT phantom: *(a)* relative permittivity and *(b)* conductivity. The maximum and the average differences are also shown in the plot insert.

B. IWCT Phantom

Figure 5.22 shows the average one-pole Cole-Cole parameters of the two chosen measurements with the resulting quadratic fits for the IWCT phantom. The temperature dependence of the parameters is not a smooth one, however the resulting second-order polynomials offer a reasonable estimate of the parameters at every temperature. The value of α does not change with temperature and is set to 0.1.

Figure 5.23 *(a)* – *(j)* shows the relative permittivities and the conductivities calculated from the final Cole-Cole model along with the original five measurements of the IWCT phantom and the average of the two chosen measurements at 3 GHz, 5.1 GHz, 7.06 GHz, 9.02 GHz, 10 GHz. The final one-pole Cole-Cole model follows well the

temperature trends of the relative permittivity and the conductivity of the IWCT phantom.

Figure 5.24 shows the absolute differences between the average relative permittivities and the conductivities of the two chosen measurements and the final one-pole Cole-Cole model for the IWCT phantom. The figure also shows the maximum and the average differences for the relative permittivity and the conductivity. The maximum difference between the measured and the modeled the relative permittivities of the IWCT phantom is 4.5 units at 19 °C and at 3 GHz, where the relative permittivity value is around 40 units. Thus this maximum is acceptable. The average difference for the relative permittivity is 1.3 units. The maximum difference for the conductivities is 1.2 S/m at 19 °C and at 10 GHz, where the conductivity is around 9 S/m. This difference is also within an acceptable range. The average magnitude of the difference between the measured conductivity and that of the final Cole-Cole model is 0.14 S/m.

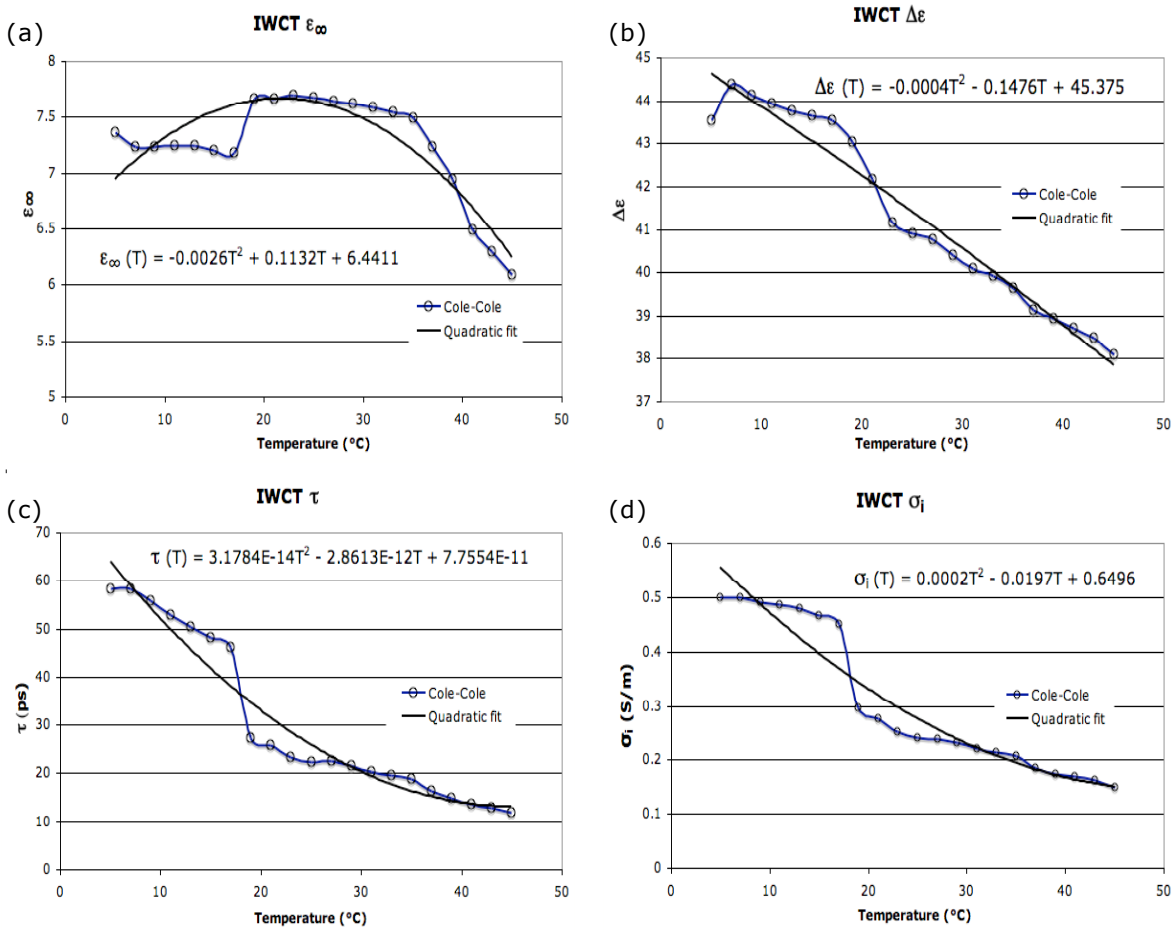

Figure 5.22: IWCT phantom average one-pole Cole-Cole and their temperature-dependent quadratic fits: *(a)* ε_∞, *(b)* $\Delta\varepsilon$, *(c)* τ and *(d)* σ_i. The resulting temperature equations are also shown in the figure insert.

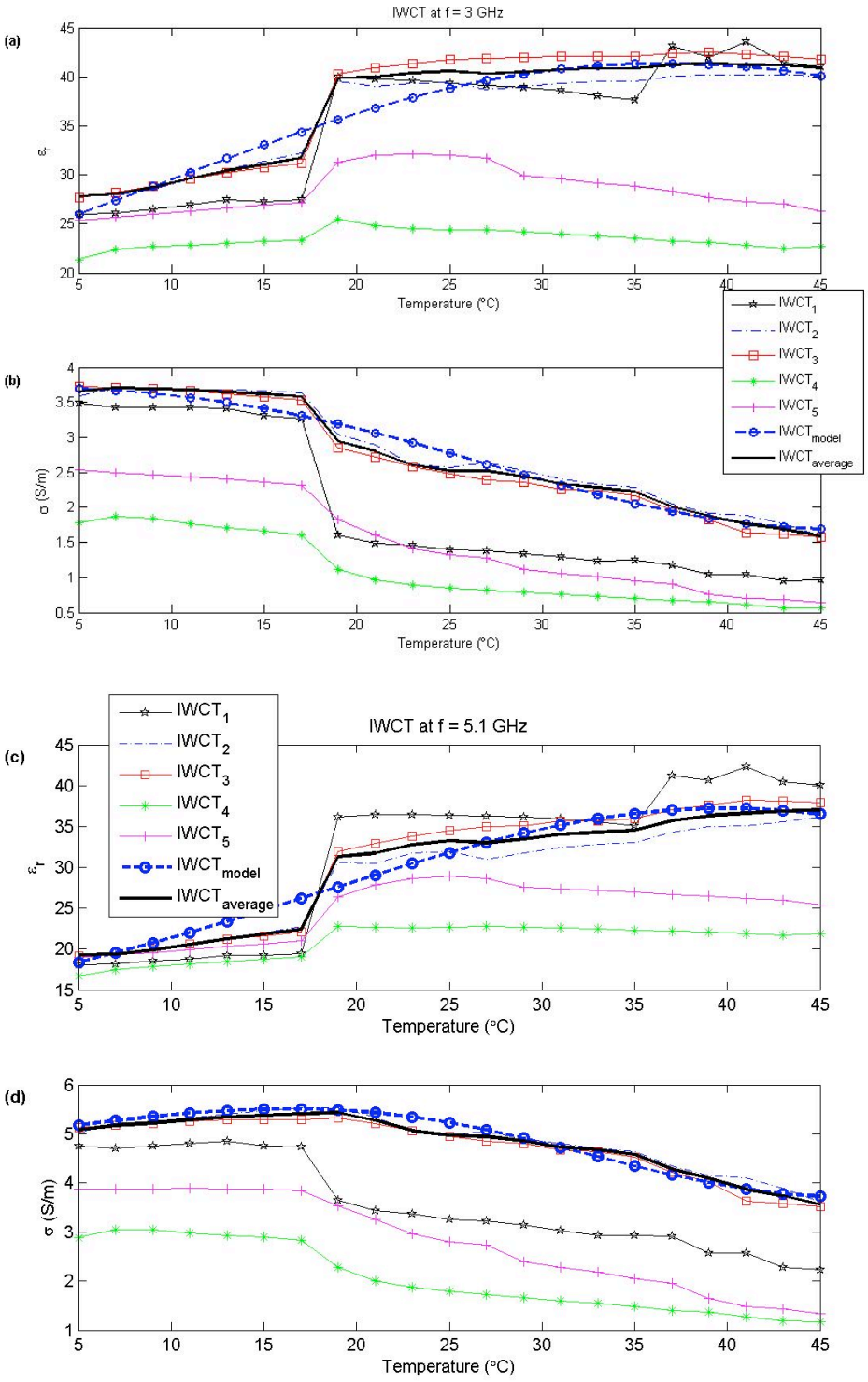
IWCT at f = 3 GHz
(a)
ε_r
Temperature (°C)
(b)
σ (S/m)
Temperature (°C)
IWCT$_1$
IWCT$_2$
IWCT$_3$
IWCT$_4$
IWCT$_5$
IWCT$_{model}$
IWCT$_{average}$
IWCT at f = 5.1 GHz
(c)
ε_r
Temperature (°C)
(d)
σ (S/m)
Temperature (°C)

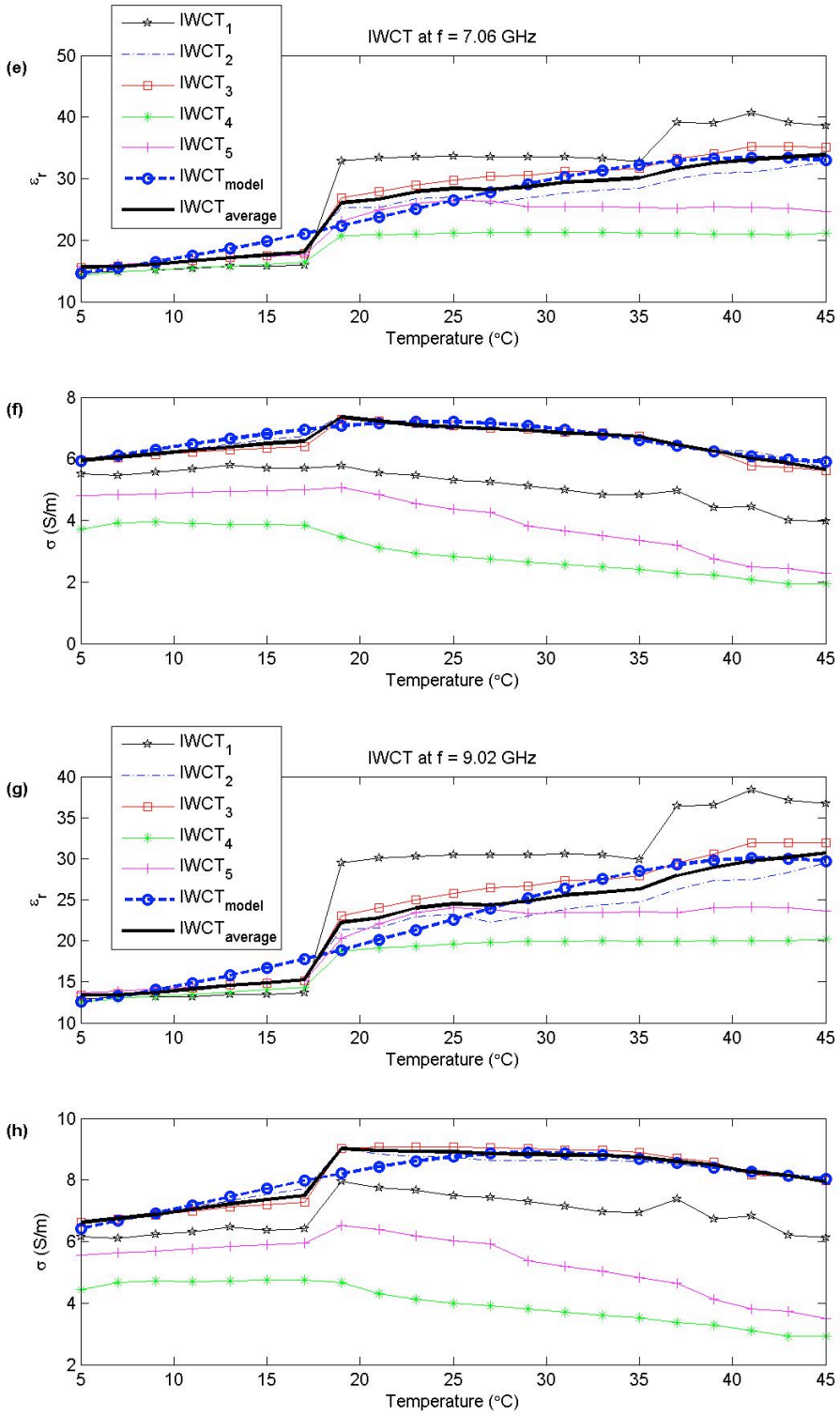
(e)
IWCT at f = 7.06 GHz
IWCT1
IWCT2
IWCT3
IWCT4
IWCT5
IWCTmodel
IWCTaverage
εr
Temperature (°C)
(f)
σ (S/m)
Temperature (°C)
(g)
IWCT at f = 9.02 GHz
IWCT1
IWCT2
IWCT3
IWCT4
IWCT5
IWCTmodel
IWCTaverage
εr
Temperature (°C)
(h)
σ (S/m)
Temperature (°C)

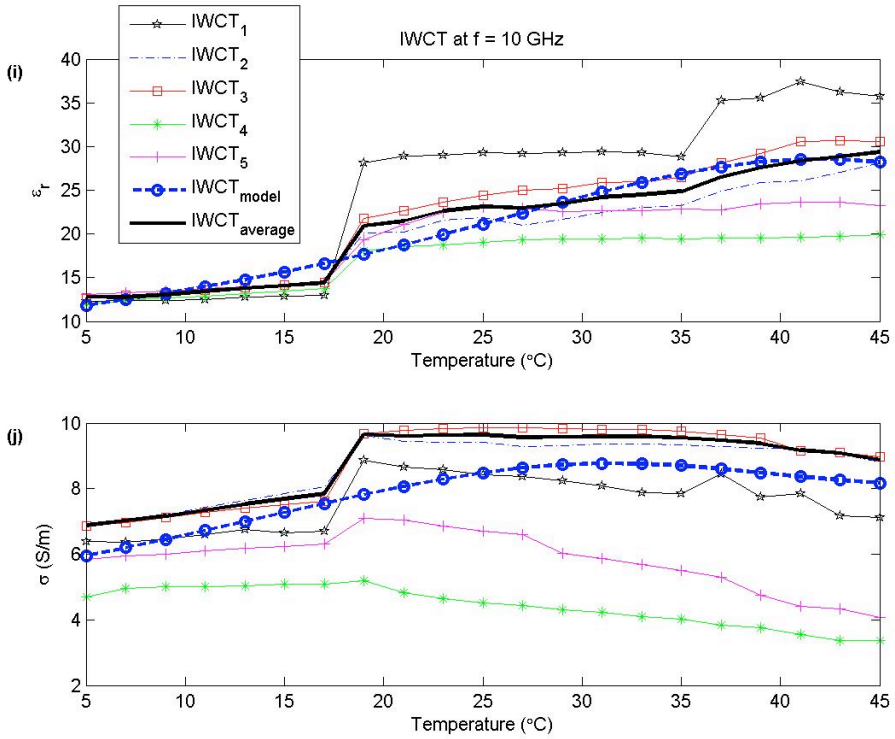

Figure 5.23: Temperature trends of the relative permittivity ε_r of the five measurements of the IWCT phantom, the average of the two chosen measurements and the final one-pole Cole-Cole model at: *(a)* 3 GHz, *(c)* 5.01 GHz, *(e)* 7.06 GHz, *(g)* 9.02 GHz and *(i)* 10 GHz. Temperature trends of the conductivity σ_i at: *(b)* 3 GHz, *(d)* 5.01 GHz, *(f)* 7.06 GHz, *(h)* 9.02 GHz and *(j)* 10 GHz.

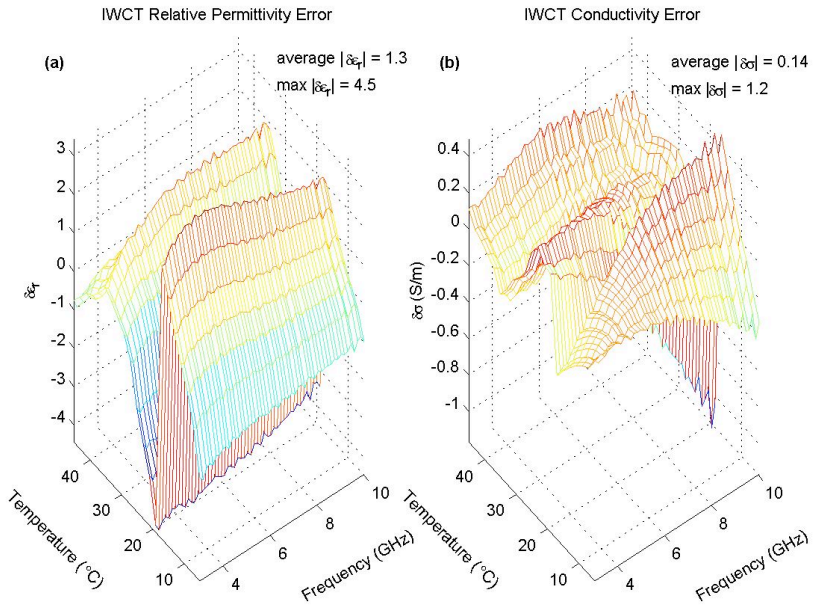

Figure 5.24: Difference between the measured and the final one-pole Cole-Cole model values for the IWCT phantom: *(a)* relative permittivity and *(b)* conductivity. The maximum and the average differences are also shown in the plot insert.

C. HWCT-1 Phantom

Figure 5.25 shows the average one-pole Cole-Cole parameters of the two chosen measurements with the resulting quadratic or cubic fits for the HWCT-1 phantom. The temperature dependence of the parameters is not a smooth one, however the resulting second- and third-order polynomials offer a reasonable estimate of the parameters at every temperature. A third-order polynomial is used for ε_∞. The values of α and σ_i do not change with temperature and are set to 0.1 and 0.2, respectively.

Figure 5.26 *(a)* – *(j)* shows the relative permittivities and the conductivities calculated from the final Cole-Cole model along with the original five measurements of

the HWCT-1 phantom and the average of the two chosen measurements at 3 GHz, 5.1 GHz, 7.06 GHz, 9.02 GHz, 10 GHz. The final one-pole Cole-Cole model follows well the temperature trends of the relative permittivity and the conductivity of the HWCT-1 phantom.

Figure 5.27 shows the absolute differences between the average relative permittivities and the conductivities of the two chosen measurements and the final one-pole Cole-Cole model for the HWCT-1 phantom. The figure also shows the maximum and the average differences for the relative permittivity and the conductivity. The maximum difference between the measured and the modeled the relative permittivities of the HWCT-1 phantom is 2.5 units at 19 °C and at frequencies higher than 5 GHz, where the relative permittivity value is around 35 units. This maximum is acceptable. The average difference in the relative permittivity is 0.82 units.

The maximum difference in the conductivities is 0.76 S/m at 5 °C and at 10 GHz, where the conductivity is around 10 S/m. This difference is also within an acceptable range. The average magnitude of the difference between the measured conductivity and that of the final Cole-Cole model is 0.2 S/m. Overall, the relative permittivity and the conductivity of the final one-pole Cole-Cole model for the HWCT-1 phantom follows well the temperature trends of the measured data.

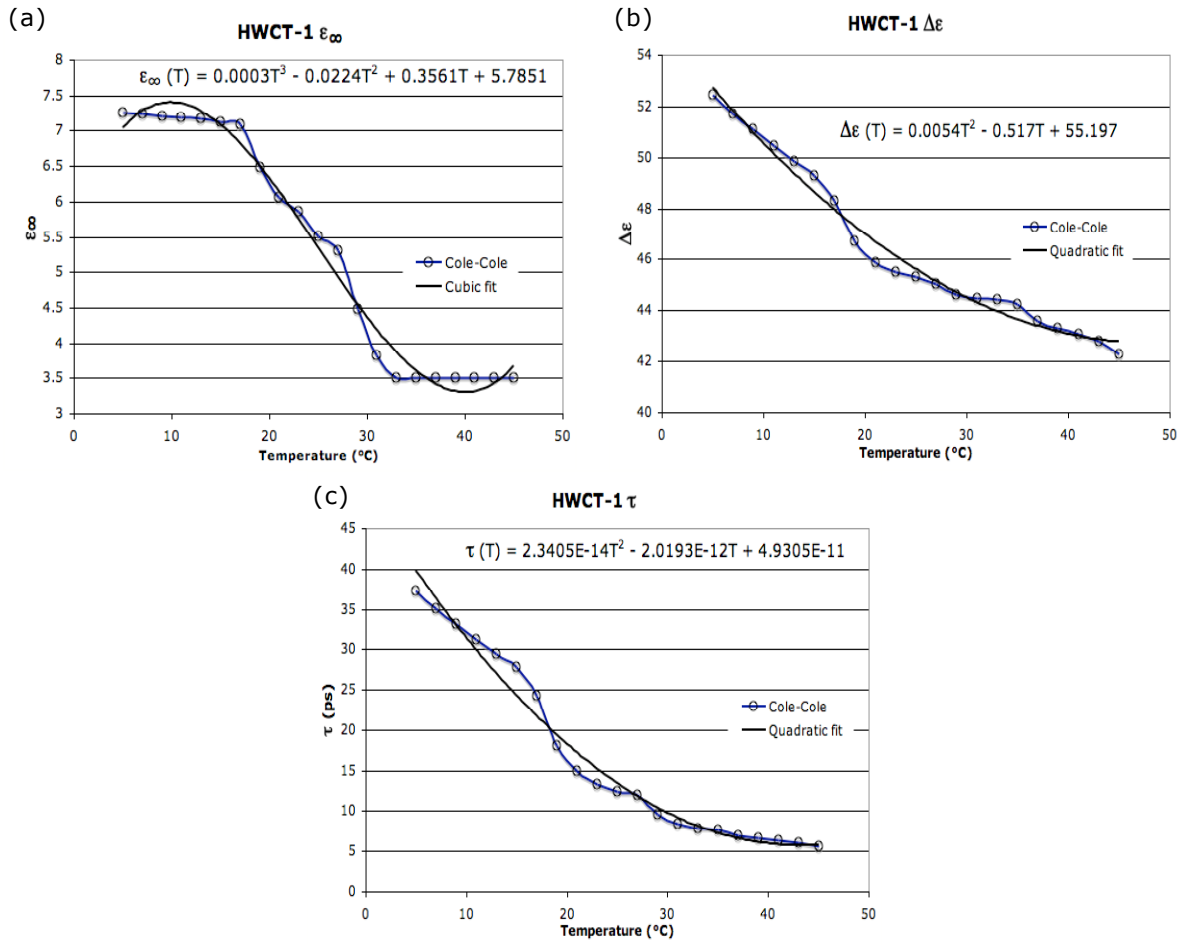

Figure 5.25: HWCT-1 phantom average one-pole Cole-Cole and their temperature-dependent quadratic fits: *(a)* ε_∞, *(b)* $\Delta\varepsilon$ and *(c)* τ. The resulting temperature equations are also shown in the figure insert.

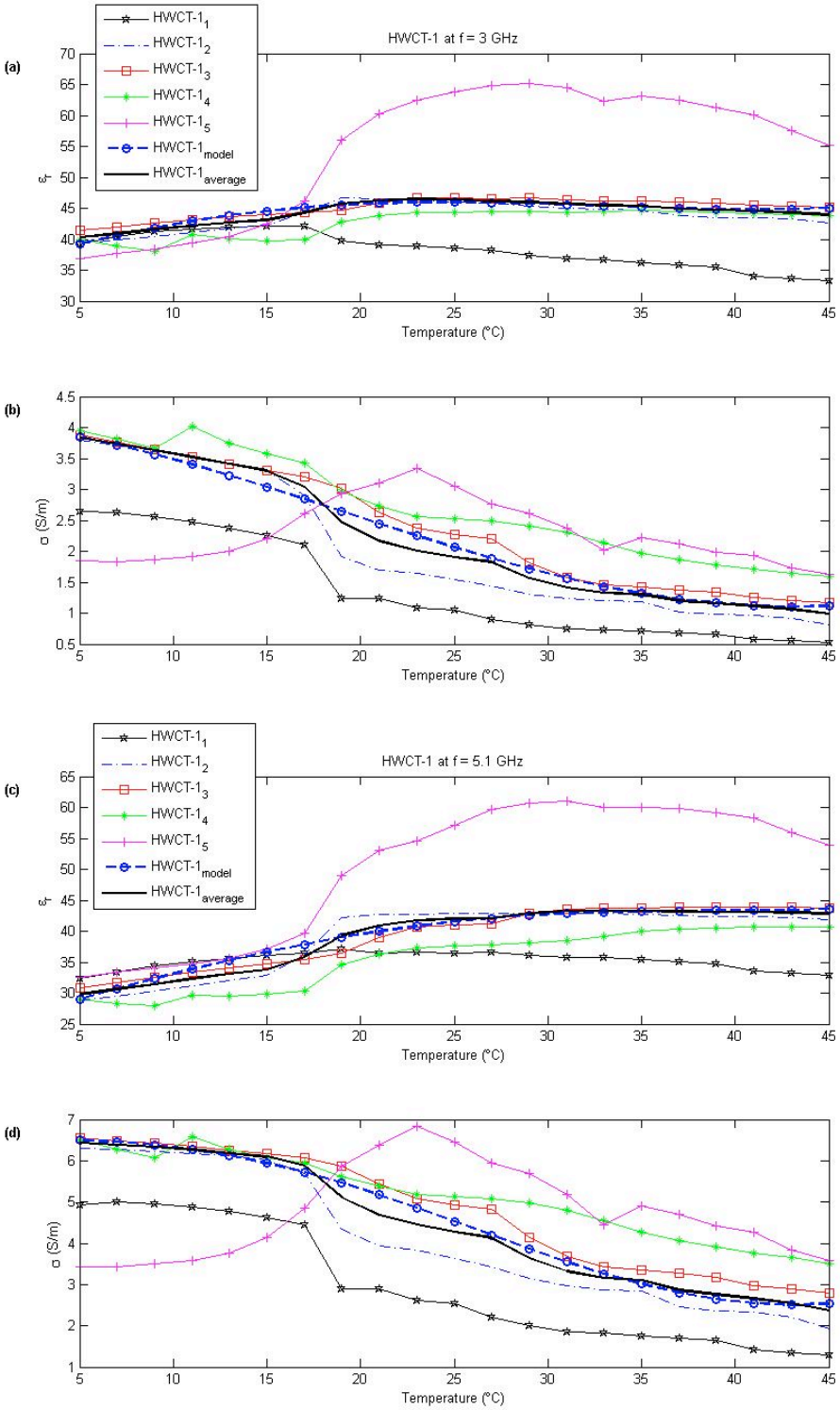
(a)
HWCT-1 at f = 3 GHz
HWCT-1$_1$
HWCT-1$_2$
HWCT-1$_3$
HWCT-1$_4$
HWCT-1$_5$
HWCT-1$_{model}$
HWCT-1$_{average}$
ε_r
Temperature (°C)
(b)
σ (S/m)
Temperature (°C)
(c)
HWCT-1 at f = 5.1 GHz
ε_r
Temperature (°C)
(d)
σ (S/m)
Temperature (°C)

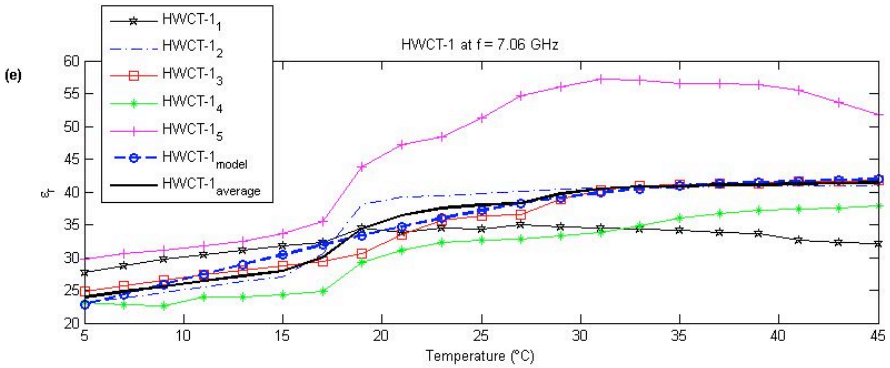
(e)
HWCT-1 at f = 7.06 GHz
HWCT-1$_1$
HWCT-1$_2$
HWCT-1$_3$
HWCT-1$_4$
HWCT-1$_5$
HWCT-1$_{model}$
HWCT-1$_{average}$
ε_r
Temperature (°C)

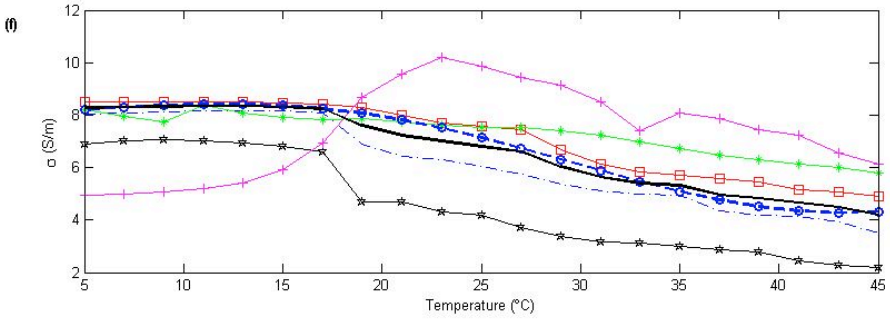
(f)
σ (S/m)
Temperature (°C)

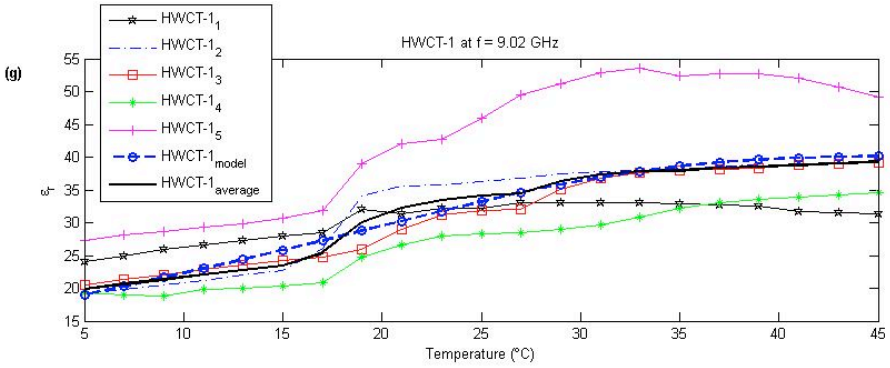
(g)
HWCT-1 at f = 9.02 GHz
HWCT-1$_1$
HWCT-1$_2$
HWCT-1$_3$
HWCT-1$_4$
HWCT-1$_5$
HWCT-1$_{model}$
HWCT-1$_{average}$
ε_r
Temperature (°C)

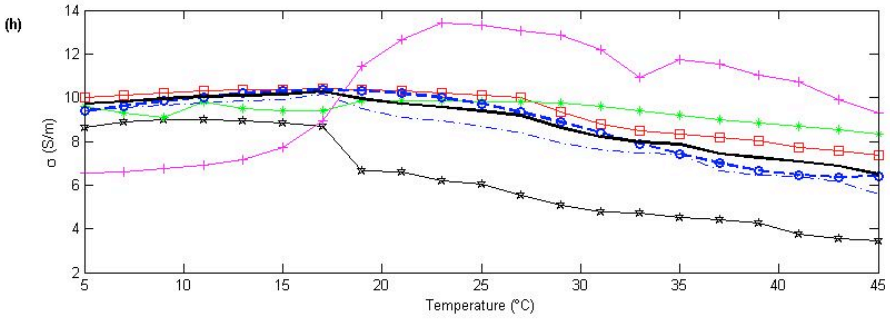
(h)
σ (S/m)
Temperature (°C)

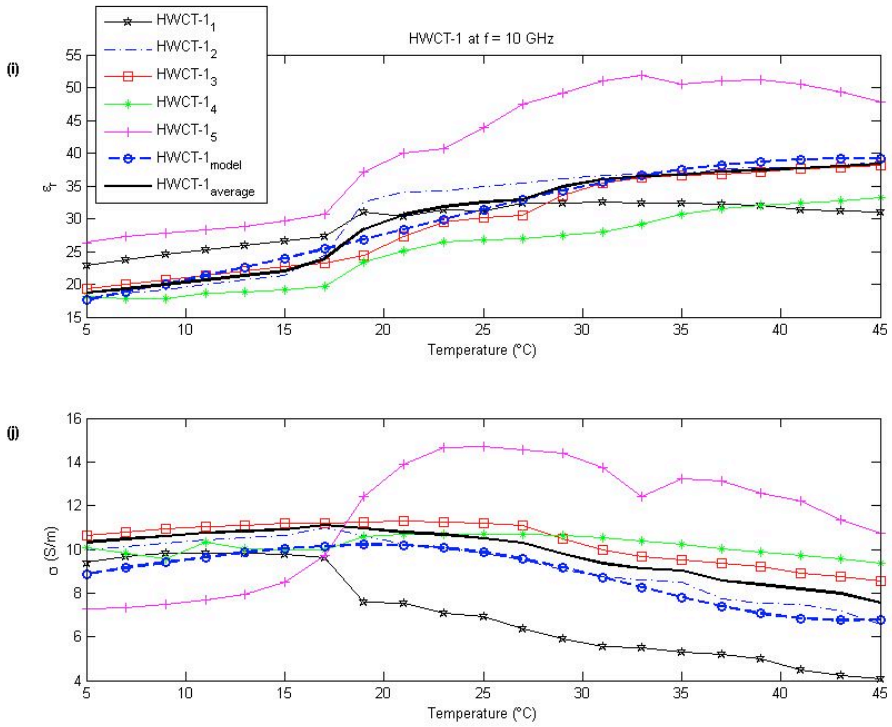

Figure 5.26: Temperature trends of the relative permittivity ε_r of the five measurements of the HWCT-1 phantom, the average of the two chosen measurements and the final one-pole Cole-Cole model at: *(a)* 3 GHz, *(c)* 5.01 GHz, *(e)* 7.06 GHz, *(g)* 9.02 GHz and *(i)* 10 GHz. Temperature trends of the conductivity σ_i at: *(b)* 3 GHz, *(d)* 5.01 GHz, *(f)* 7.06 GHz, *(h)* 9.02 GHz and *(j)* 10 GHz.

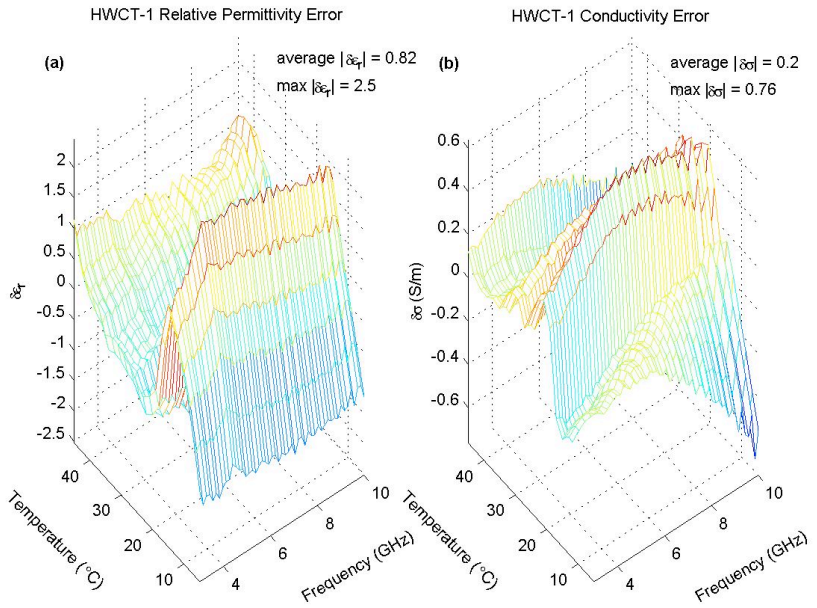

Figure 5.27: Difference between the measured and the final one-pole Cole-Cole model values for the HWCT-1 phantom: *(a)* relative permittivity and *(b)* conductivity. The maximum and the average differences are also shown in the plot insert.

D. HWCT-2 Phantom

Figure 5.28 shows the average one-pole Cole-Cole parameters of the two chosen measurements with the resulting quadratic or cubic fits for the HWCT-2 phantom. The temperature dependence of the parameters is not a smooth one, however the resulting second- and third-order polynomials offer a reasonable estimate of the parameters at every temperature. A third-order polynomial is used for $\Delta\varepsilon$ and σ_i. The value of α does not change with temperature and is set to 0.1.

Figure 5.29 *(a)* – *(j)* shows the relative permittivities and the conductivities calculated from the final Cole-Cole model along with the original five measurements of

the HWCT-2 phantom and the average of the two chosen measurements at 3 GHz, 5.1 GHz, 7.06 GHz, 9.02 GHz, 10 GHz. The final one-pole Cole-Cole model follows well the temperature trends of the relative permittivity and the conductivity of the HWCT-2 phantom.

Figure 5.30 shows the absolute differences between the average relative permittivities and the conductivities of the two chosen measurements and the final one-pole Cole-Cole model for the HWCT-2 phantom. The figure also shows the maximum and the average differences for the relative permittivity and the conductivity. The maximum difference between the measured and the modeled the relative permittivities of the HWCT-2 phantom is 4.2 units at 27 °C and at 10 GHz, where the relative permittivity value is around 22 units. The maximum difference in the conductivities is 0.97 S/m at 39 °C and 3 GHz where the conductivity is around 2 S/m. This difference is also within an acceptable range. These maximum differences for the relative permittivity and the conductivity make up a significant percentage of their original values; however, the results of the final Cole-Cole model still follow the temperature trends of the measured data, which originally spans a wide range. The final Cole-Cole model of the HWCT-2 phantom is the least accurate between all the other models. The average difference in the relative permittivity is 1.6 units. The average magnitude of the difference between the measured conductivity and that of the final Cole-Cole model is 0.34 S/m.

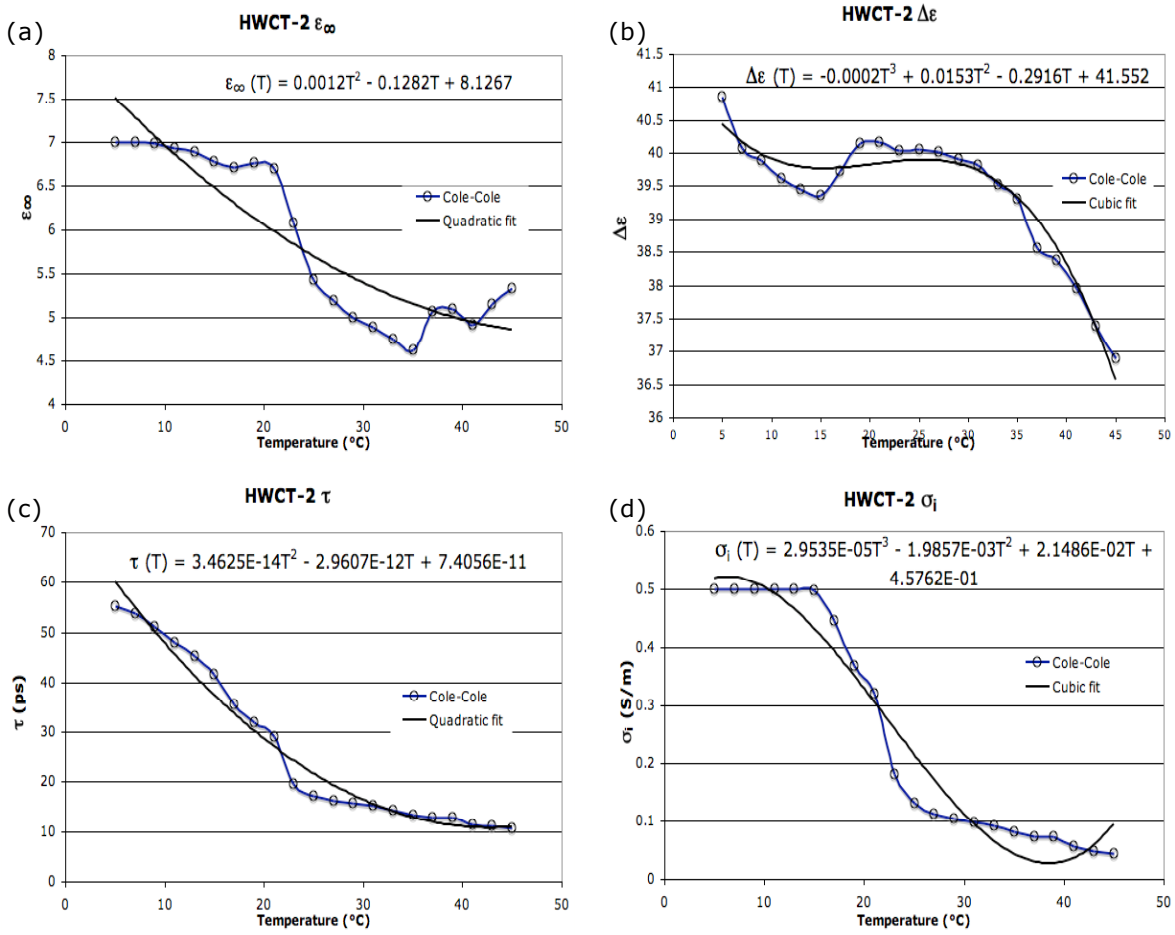

Figure 5.28: HWCT-2 phantom average one-pole Cole-Cole and their temperature-dependent quadratic fits: *(a)* ε_∞, *(b)* $\Delta\varepsilon$, *(c)* τ and *(d)* σ_i. The resulting temperature equations are also shown in the figure insert.

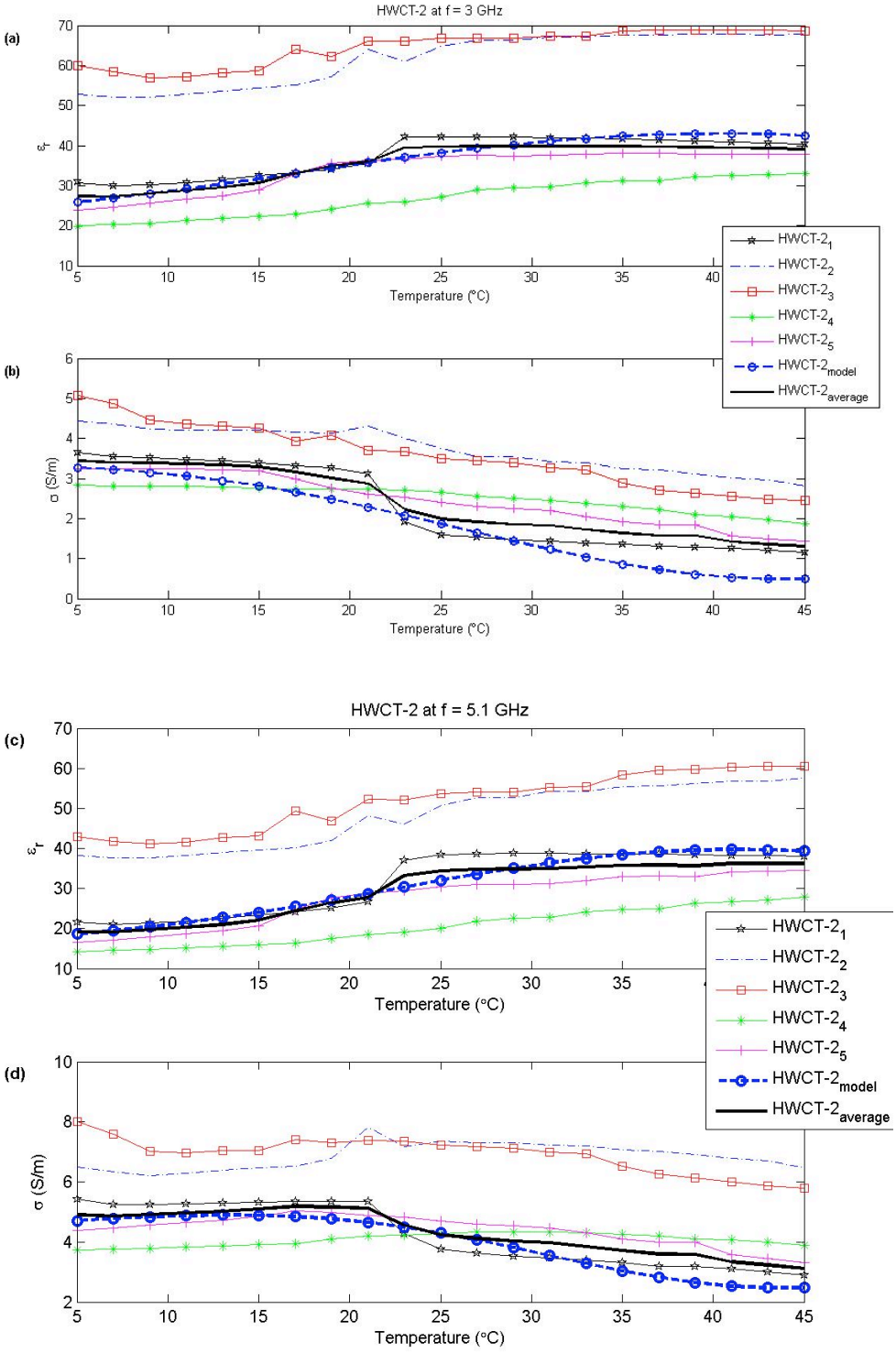
HWCT-2 at f = 3 GHz
(a)
ε_r
Temperature (°C)
(b)
σ (S/m)
Temperature (°C)
HWCT-2 at f = 5.1 GHz
(c)
ε_r
Temperature (°C)
(d)
σ (S/m)
Temperature (°C)
HWCT-2$_1$
HWCT-2$_2$
HWCT-2$_3$
HWCT-2$_4$
HWCT-2$_5$
HWCT-2$_{model}$
HWCT-2$_{average}$

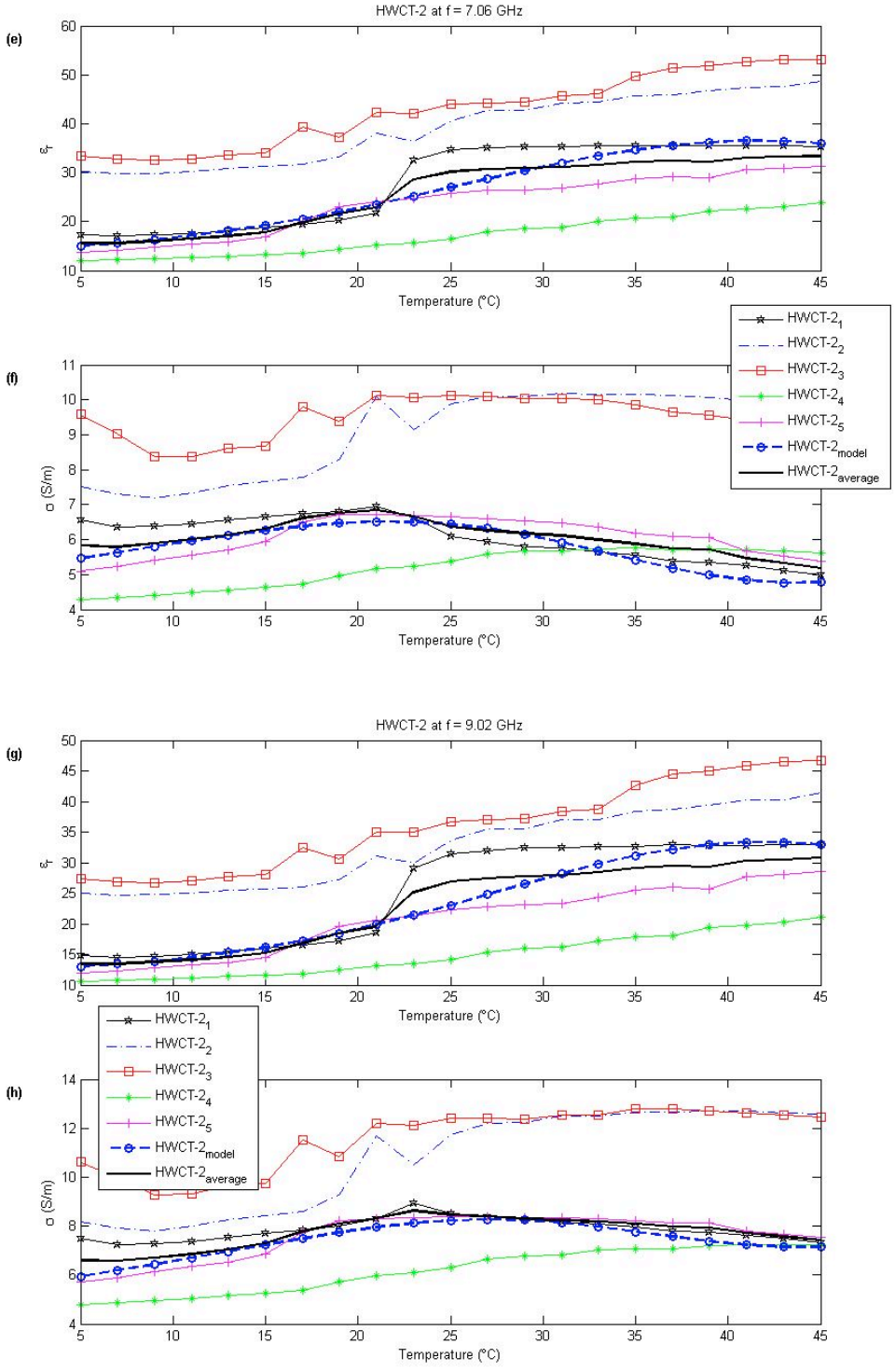
(e)
HWCT-2 at f = 7.06 GHz
ε_r
Temperature (°C)
(f)
σ (S/m)
Temperature (°C)
HWCT-2$_1$
HWCT-2$_2$
HWCT-2$_3$
HWCT-2$_4$
HWCT-2$_5$
HWCT-2$_{model}$
HWCT-2$_{average}$
(g)
HWCT-2 at f = 9.02 GHz
ε_r
Temperature (°C)
(h)
σ (S/m)
Temperature (°C)

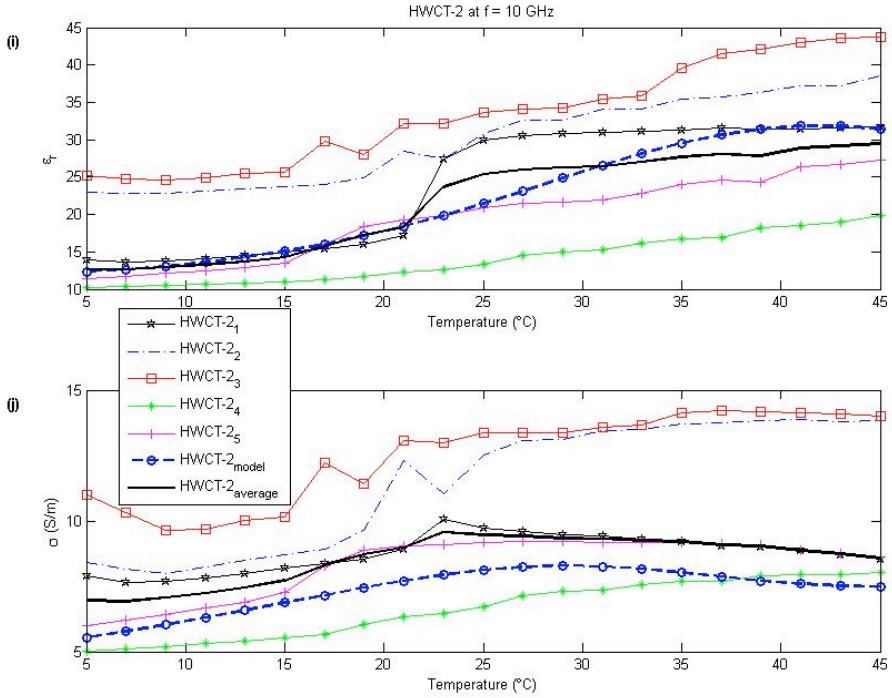

Figure 5.29: Temperature trends of the relative permittivity ε_r of the five measurements of the HWCT-2 phantom, the average of the two chosen measurements and the final one-pole Cole-Cole model at: *(a)* 3 GHz, *(c)* 5.01 GHz, *(e)* 7.06 GHz, *(g)* 9.02 GHz and *(i)* 10 GHz. Temperature trends of the conductivity σ_i at: *(b)* 3 GHz, *(d)* 5.01 GHz, *(f)* 7.06 GHz, *(h)* 9.02 GHz and *(j)* 10 GHz.

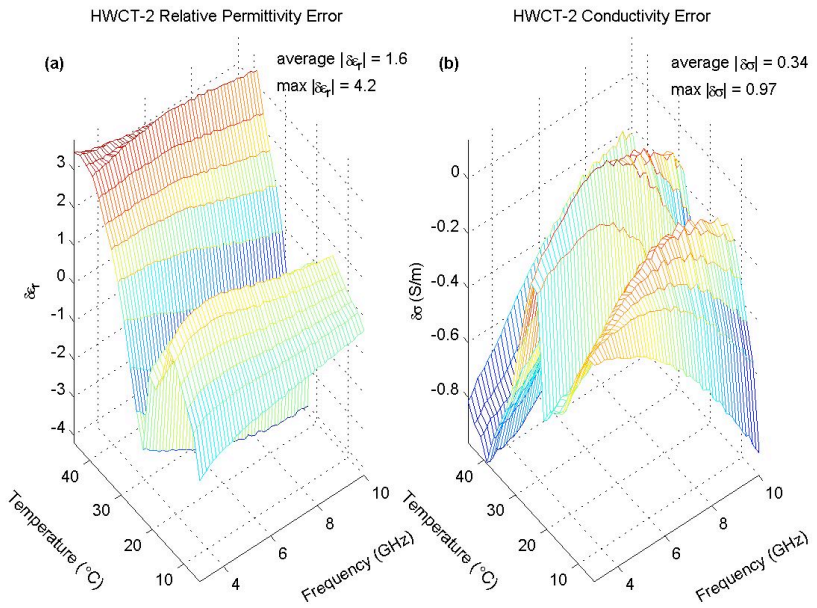

Figure 5.30: Difference between the measured and the final one-pole Cole-Cole model values for the HWCT-2 phantom: *(a)* relative permittivity and *(b)* conductivity. The maximum and the average differences are also shown in the plot insert.

E. Alginate-Based Phantom

Figure 5.32 shows the average one-pole Cole-Cole parameters of the two chosen measurements with the resulting quadratic or cubic fits for the alginate-based phantom. The temperature dependence of the parameters is not a smooth one, however the resulting second-order polynomials offer a reasonable estimate of the parameters at every temperature. The value of α does not change with temperature and is set to 0.1.

Figure 5.33 *(a)* – *(j)* shows the relative permittivities and the conductivities calculated from the final Cole-Cole model along with the original five measurements of the alginate-based phantom and the average of the two chosen measurements at 3 GHz,

5.1 GHz, 7.06 GHz, 9.02 GHz, 10 GHz. The final one-pole Cole-Cole model follows well the temperature trends of the relative permittivity and the conductivity of the alginate-based phantom.

Figure 5.34 shows the absolute differences between the average relative permittivities and the conductivities of the two chosen measurements and the final one-pole Cole-Cole model for the alginate-based phantom. The figure also shows the maximum and the average differences for the relative permittivity and the conductivity. The maximum difference between the measured and the modeled the relative permittivities of the alginate-based phantom is 1.4 units at 5 °C and at 10 GHz, where the relative permittivity value is around 37 units. This maximum is acceptable. The average difference between the relative permittivities is 0.33 units. The maximum difference in the conductivities is 0.63 S/m at 17 °C and at 10 GHz, where the conductivity is around 12 S/m. This difference is also within an acceptable range. The average magnitude of the difference between the measured conductivity and that of the final Cole-Cole model is 0.2 S/m. Overall, the final Cole-Cole model follows well the measured dielectric properties of the alginate-based phantom.

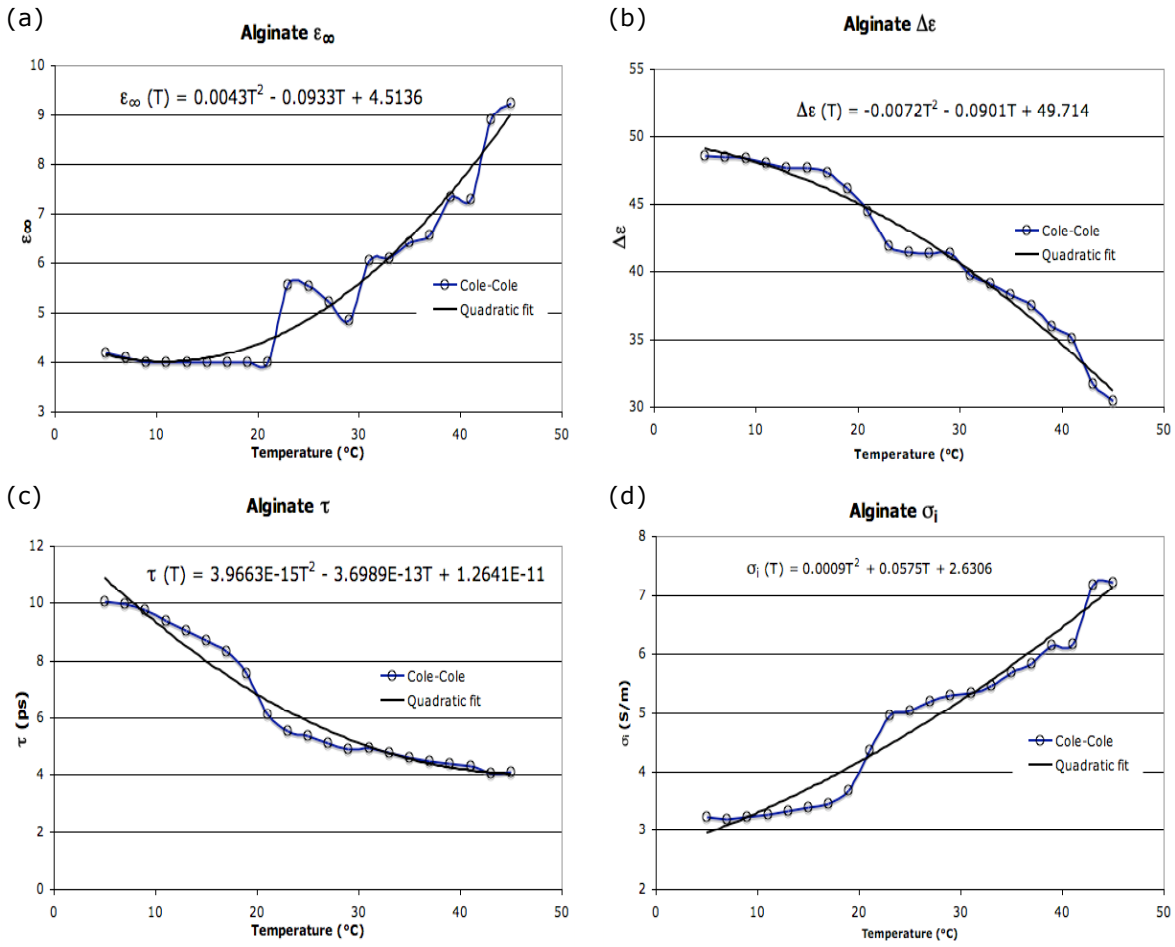

Figure 5.31: Alginate-based phantom average one-pole Cole-Cole and their temperature-dependent quadratic fits: *(a)* ε_∞, *(b)* $\Delta\varepsilon$, *(c)* τ and *(d)* σ_i. The resulting temperature equations are also shown in the figure insert.

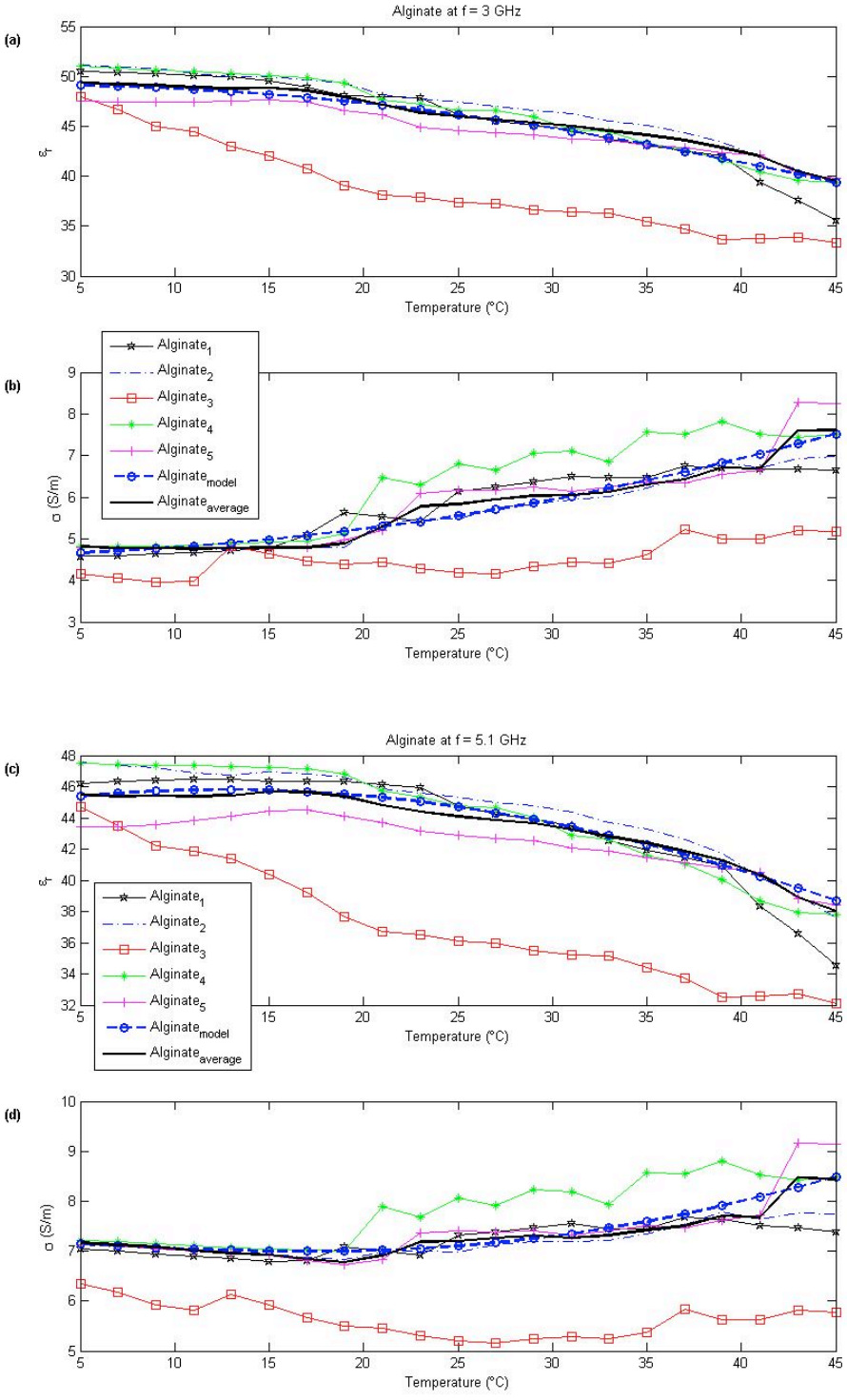
Alginate at f = 3 GHz
(a)
ε_r
Temperature (°C)
(b)
σ (S/m)
Temperature (°C)
Alginate$_1$
Alginate$_2$
Alginate$_3$
Alginate$_4$
Alginate$_5$
Alginate$_{model}$
Alginate$_{average}$
Alginate at f = 5.1 GHz
(c)
ε_r
Temperature (°C)
(d)
σ (S/m)
Temperature (°C)

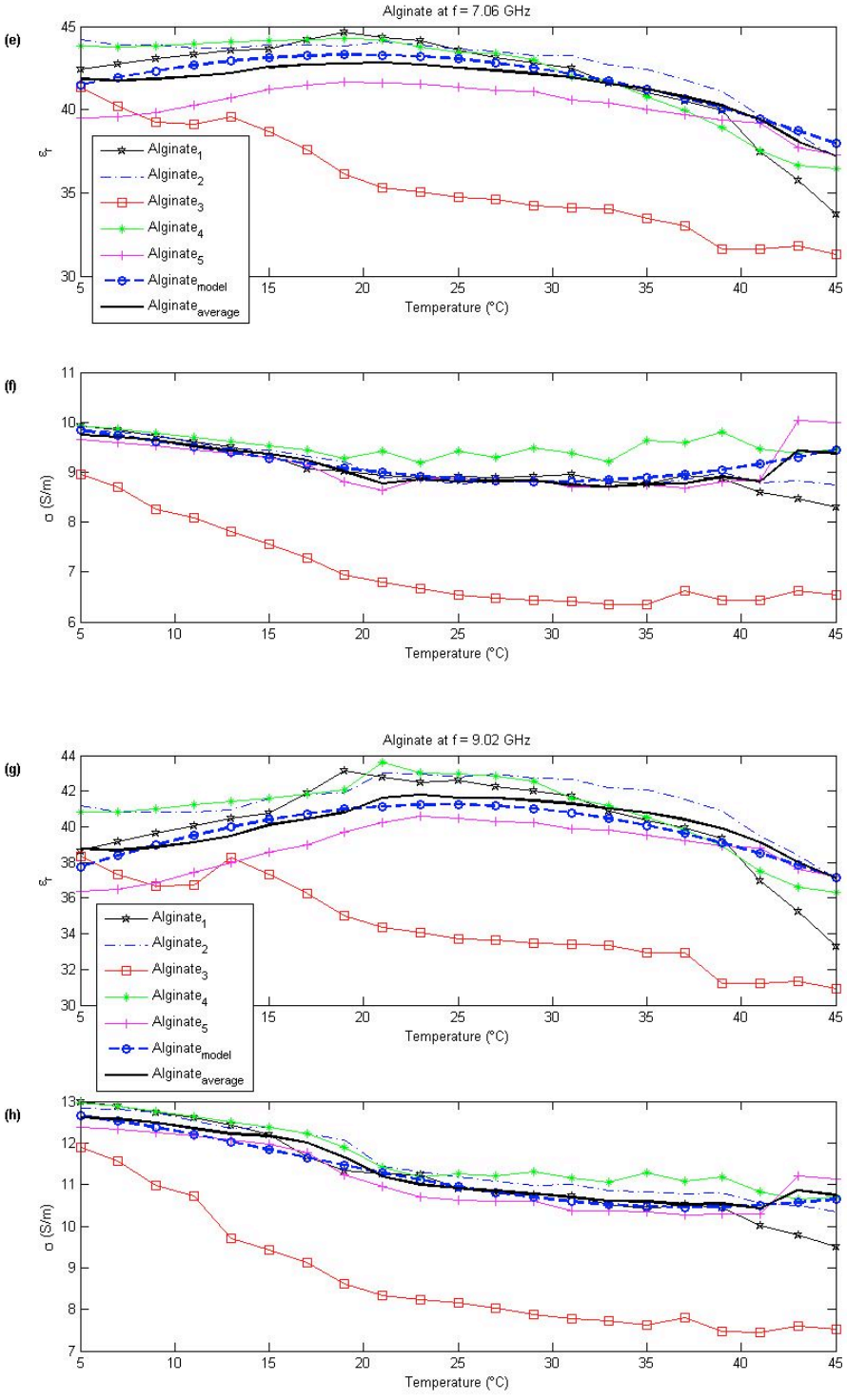
(e)
Alginate at f = 7.06 GHz
ε_r
Temperature (°C)
Alginate$_1$
Alginate$_2$
Alginate$_3$
Alginate$_4$
Alginate$_5$
Alginate$_{model}$
Alginate$_{average}$
(f)
σ (S/m)
Temperature (°C)
(g)
Alginate at f = 9.02 GHz
ε_r
Temperature (°C)
(h)
σ (S/m)
Temperature (°C)

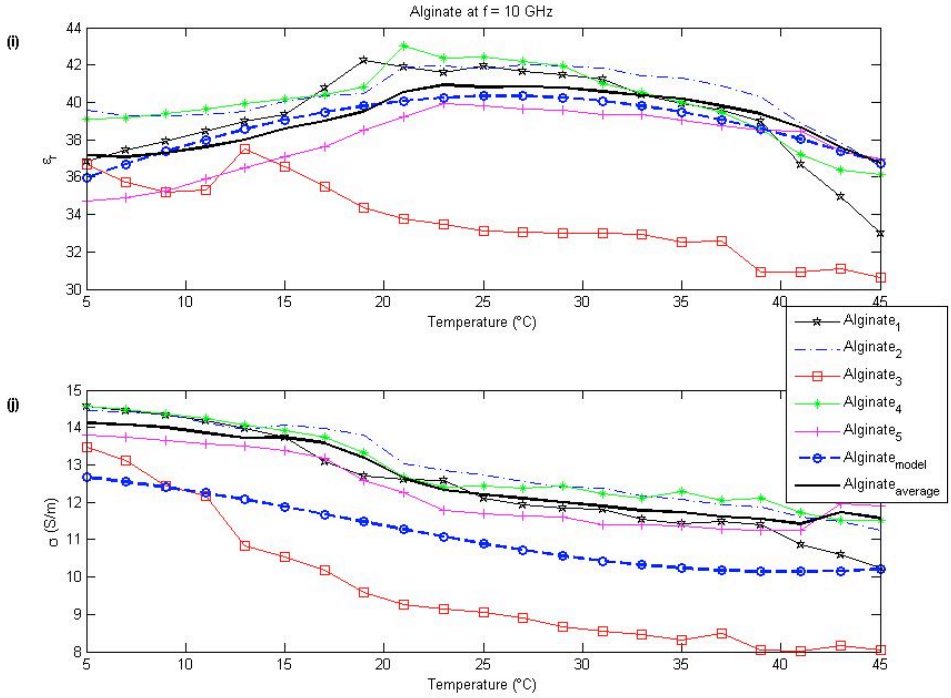

Figure 5.32: Temperature trends of the relative permittivity ε_r of the five measurements of the alginate-based phantom, the average of the two chosen measurements and the final one-pole Cole-Cole model at: *(a)* 3 GHz, *(c)* 5.01 GHz, *(e)* 7.06 GHz, *(g)* 9.02 GHz and *(i)* 10 GHz. Temperature trends of the conductivity σ_i at: *(b)* 3 GHz, *(d)* 5.01 GHz, *(f)* 7.06 GHz, *(h)* 9.02 GHz and *(j)* 10 GHz.

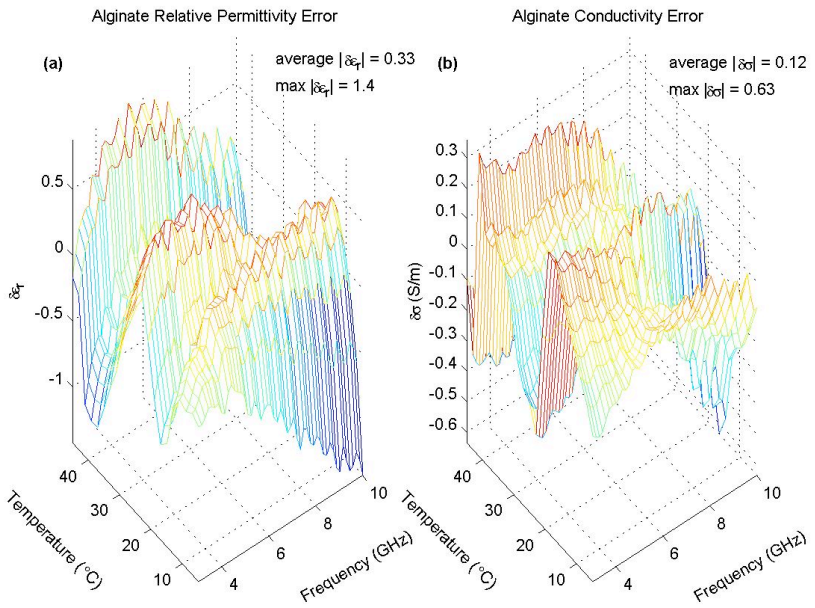

Figure 5.33: Difference between the measured and the final one-pole Cole-Cole model values for the alginate-based tumor phantom: *(a)* relative permittivity and *(b)* conductivity. The maximum and the average differences are also shown in the plot insert.

Tissues

The same procedure used to fit the one-pole Cole-Cole parameters of the phantoms to a temperature model is used for the tissue samples. Table 5-4 shows the temperature coefficients of the one-pole Cole-Cole model for fat, muscle and liver. As mentioned earlier, ε_∞ changes slightly with temperature, therefore, the value of ε_∞ is assumed constant and set to its the average value. The value of α is also constant with temperature. Overall, the final one-pole Cole-Cole models for the tissue samples are more accurate than those for the phantoms. In Lazebnik *et al.*'s study of the temperature dependence of the dielectric properties of liver, the maximum difference due to the reconstruction was

approximately 5.6 units for the relative permittivity and 5.4 S/m for the conductivity [4]. The maximum differences in this study are always less than these values.

Table 5-4: Coefficients of the second or third order polynomial function from (3) and (4) used to fit the temperature-dependence of the one-pole Cole-Cole parameters of the different tissue types.

		ε_∞ (constant)	$\Delta\varepsilon$	τ ($\times 10^{-12}$)	σ_i	α (constant)
Fat	***D***	2.54	-0.0002			0.01
	A		0.0155	0.00152	3.00E-05	
	B		-0.4135	-0.2133	0.0023	
	C		10.058	12.278	0.0879	
Muscle	***D***	5.95		0.00028		0.1
	A		-0.0009	-0.0221	0.0006	
	B		-0.3194	0.2534	-0.0092	
	C		51.592	13.435	0.6247	
Liver	***A***	7.5	0.0013	0.0036	0.0003	0.1
	B		-0.3224	-0.4089	0.0035	
	C		45.205	16.819	0.6213	

A. **Fat**

Figure 5.34 shows the temperature trends of the one-pole Cole-Cole model with their second- or third- order polynomial fits. A third-order polynomial is used to model the temperature dependence of $\Delta\varepsilon$. The resultant polynomial is also displayed in its corresponding figure. Figure 5.35 *(a) – (j)* shows the relative permittivities and the conductivities calculated from the final Cole-Cole model along with the original five

measurements of the fat tissue samples and the average of the two chosen measurements at 3 GHz, 5.1 GHz, 7.06 GHz, 9.02 GHz, 10 GHz.

Figure 5.36 shows the absolute differences in the relative permittivities and conductivities of the measured data and the final one-pole Cole-Cole model. The maximum difference in the relative permittivity is 2.5 units at 45 °C and at 3 GHz, where the relative permittivity is around 10 units. This error is not an insignificant one, however, in general the model follows well the trends of the relative permittivity of fat except at 45 °C where the Cole-Cole model results in a decrease in the relative permittivity, which in the measured data remains equal to the value at 43 °C. The maximum difference in the measured and the modeled conductivities for fat is 0.59 S/m at 45 °C and at 10 GHz, where the conductivity is around 2 S/m. Therefore, this model for fat would best be used up to only 43 °C instead of 45 °C. The average magnitude of the difference between the measured and the modeled relative permittivities for fat is 0.67 units. The average difference between the conductivities is 0.078 S/m.

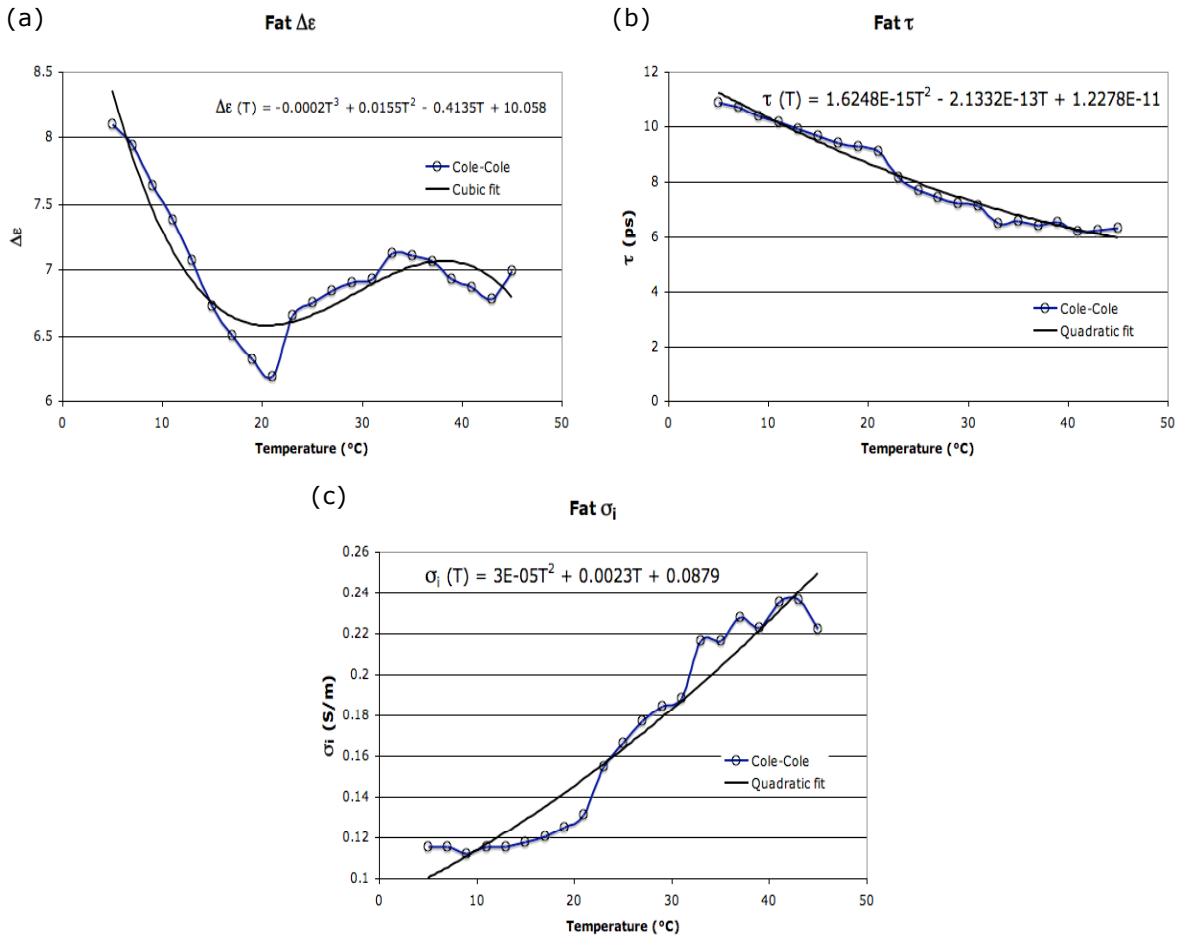

Figure 5.34: Fat tissue samples average one-pole Cole-Cole and their temperature-dependent quadratic fits: *(a)* $\Delta\varepsilon$, *(b)* τ and *(c)* σ_i. The resulting temperature equations are also shown in the figure insert.

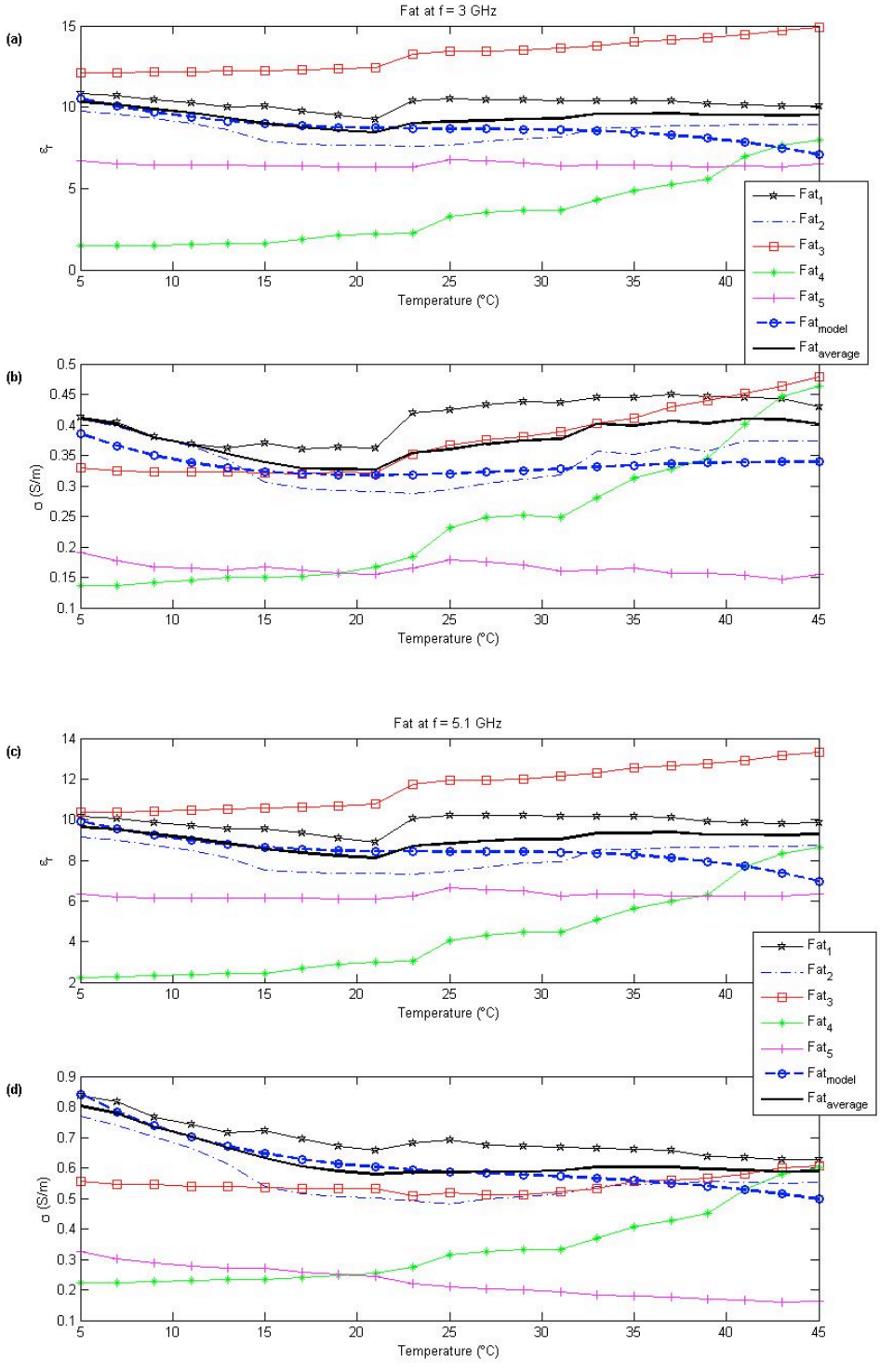
Fat at f = 3 GHz
(a)
ε_r
Temperature (°C)
Fat_1
Fat_2
Fat_3
Fat_4
Fat_5
Fat_{model}
$Fat_{average}$
(b)
σ (S/m)
Temperature (°C)
Fat at f = 5.1 GHz
(c)
ε_r
Temperature (°C)
(d)
σ (S/m)
Temperature (°C)

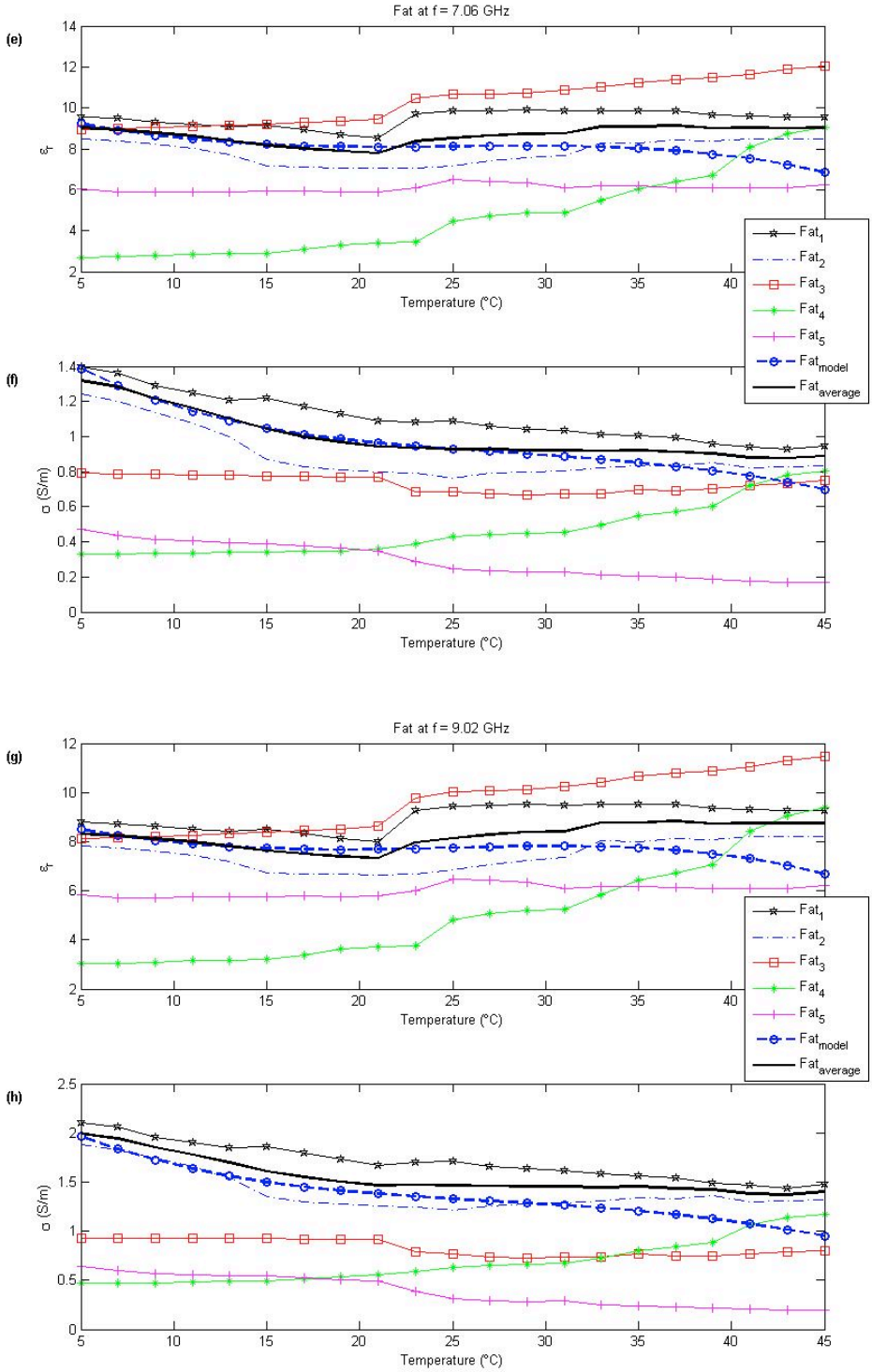
(e)
Fat at f = 7.06 GHz
ε_r
Temperature (°C)
(f)
σ (S/m)
Temperature (°C)
(g)
Fat at f = 9.02 GHz
ε_r
Temperature (°C)
(h)
σ (S/m)
Temperature (°C)
Fat_1
Fat_2
Fat_3
Fat_4
Fat_5
Fat_{model}
$Fat_{average}$

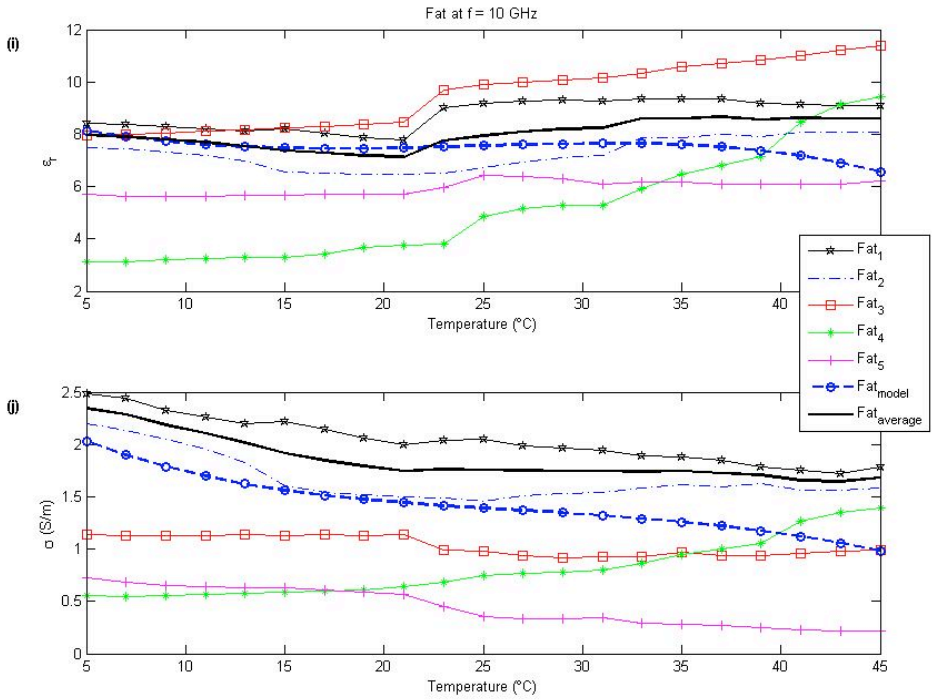

Figure 5.35: Temperature trends of the relative permittivity ε_r of the five measurements of the fat tissue, the average of the two chosen measurements and the final one-pole Cole-Cole model at: *(a)* 3 GHz, *(c)* 5.01 GHz, *(e)* 7.06 GHz, *(g)* 9.02 GHz and *(i)* 10 GHz. Temperature trends of the conductivity σ_i at: *(b)* 3 GHz, *(d)* 5.01 GHz, *(f)* 7.06 GHz, *(h)* 9.02 GHz and *(j)* 10 GHz.

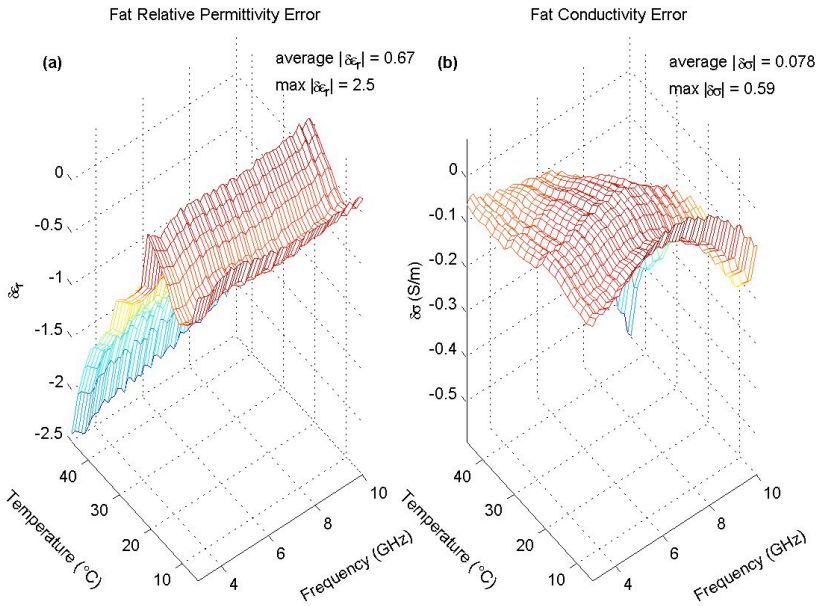

Figure 5.36: Difference between the measured and the final one-pole Cole-Cole model values for the fat tissue samples: *(a)* relative permittivity and *(b)* conductivity. The maximum and the average differences are also shown in the plot insert.

B. Muscle

Figure 5.37 shows the temperature trends of the one-pole Cole-Cole model with their second- or third- order polynomial fits for the muscle samples. A third-order polynomial is used to model the temperature dependence of τ. The resultant polynomial is also displayed in its corresponding figure. Figure 5.38 *(a)* – *(j)* shows the relative permittivities and the conductivities calculated from the final Cole-Cole model along with the original five measurements of the muscle tissue samples and the average of the two chosen measurements at 3 GHz, 5.1 GHz, 7.06 GHz, 9.02 GHz, 10 GHz.

Figure 5.39 shows the absolute differences in the relative permittivities and conductivities of the measured data and the final one-pole Cole-Cole model. The maximum difference in the relative permittivity is 2.6 units at 45 °C and at 3 GHz, where the value is 45 permittivity units. The maximum difference between the conductivity values is 0.71 S/m at 5 °C and at 10 GHz, where the conductivity value is 13 S/m. These maximum differences are within an acceptable range. The average differences between the measured and the modeled relative permittivities and conductivities are 0.46 units and 0.15 S/m, respectively. In general, the relative permittivity and the conductivity of the final one-pole Cole-Cole model follows well the temperature dependence of the measured relative permittivity and conductivity of the muscle samples.

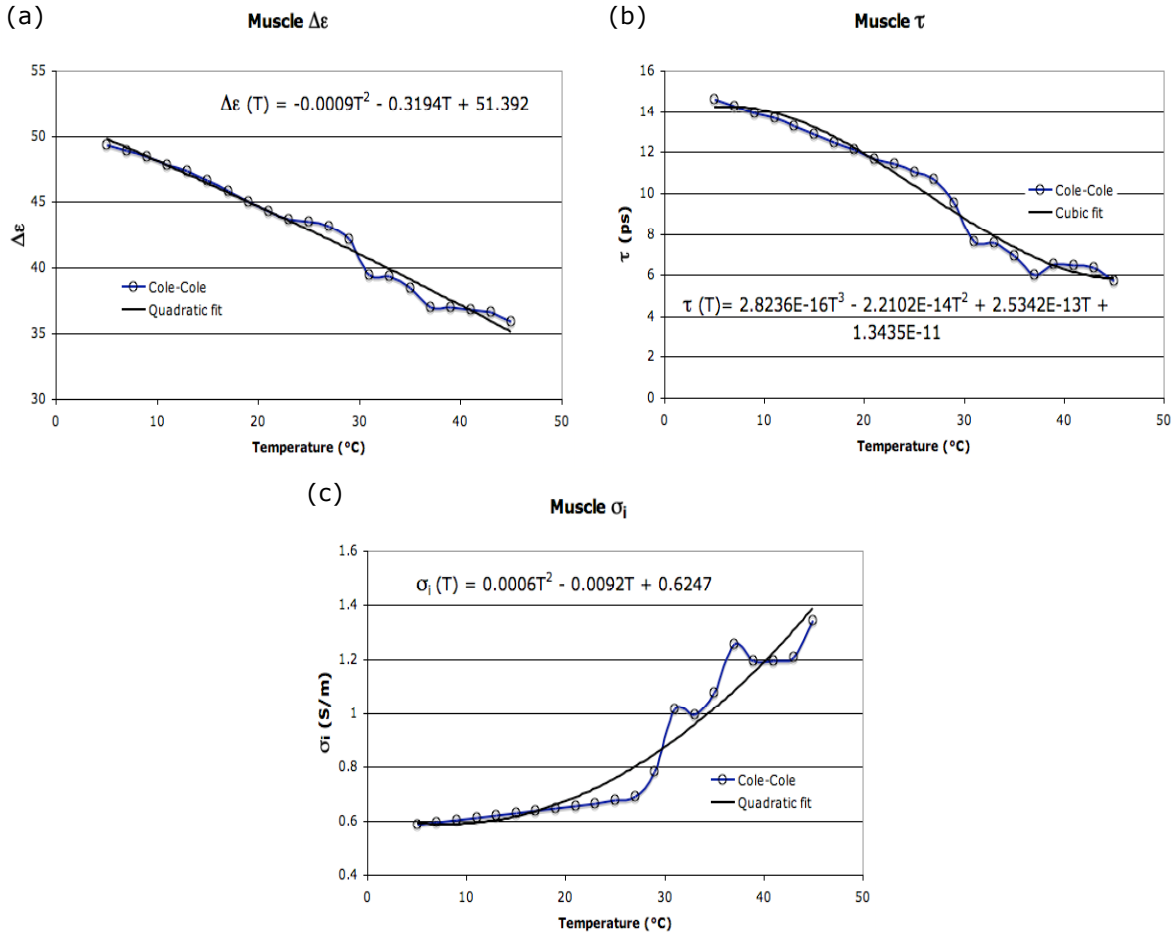

Figure 5.37: Muscle tissue samples average one-pole Cole-Cole and their temperature-dependent quadratic fits: *(a)* $\Delta\varepsilon$, *(b)* τ and *(c)* σ_i. The resulting temperature equations are also shown in the figure insert.

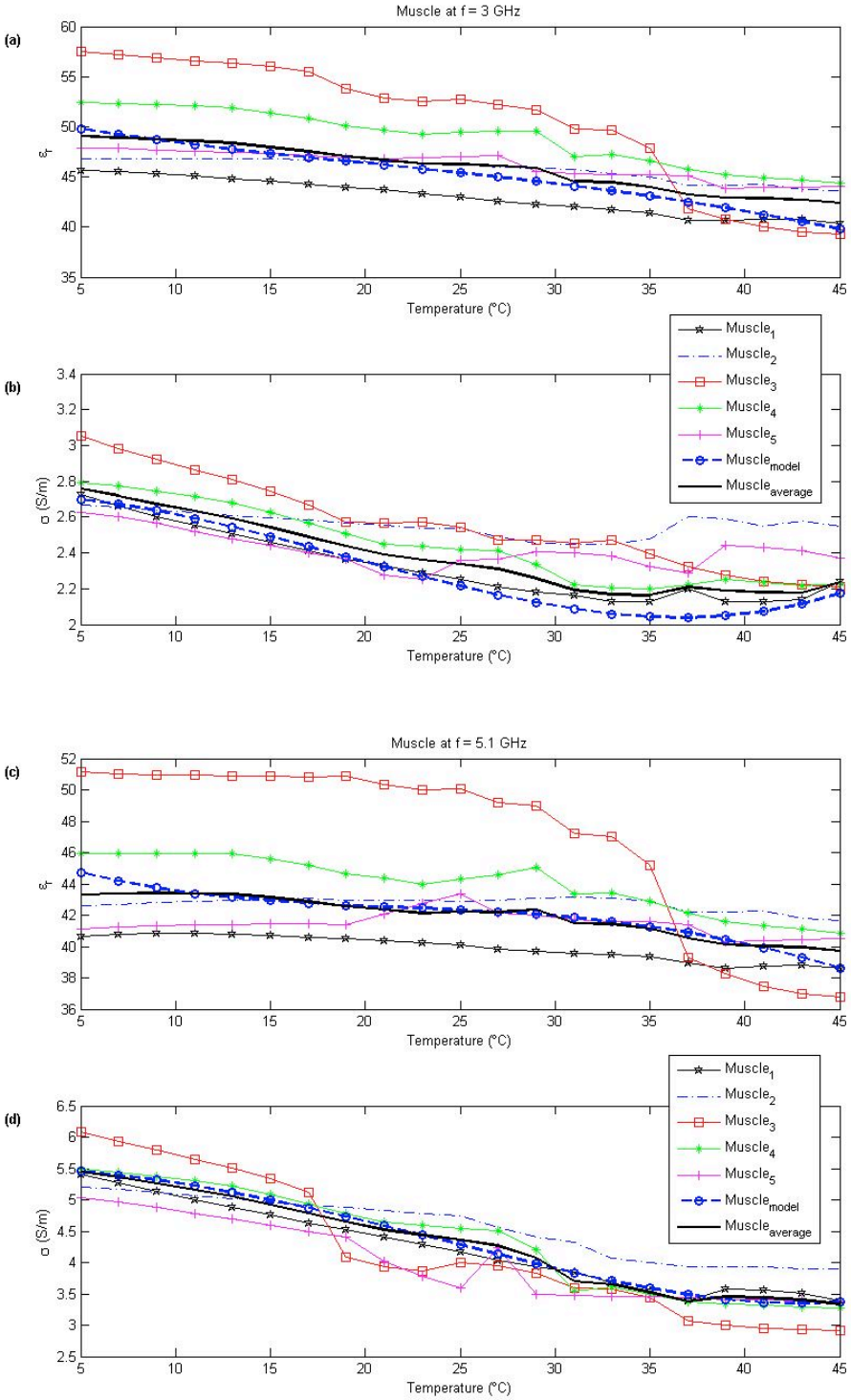
Muscle at f = 3 GHz
(a)
ε_r
Temperature (°C)
(b)
σ (S/m)
Temperature (°C)
Muscle$_1$
Muscle$_2$
Muscle$_3$
Muscle$_4$
Muscle$_5$
Muscle$_{model}$
Muscle$_{average}$
Muscle at f = 5.1 GHz
(c)
ε_r
Temperature (°C)
(d)
σ (S/m)
Temperature (°C)

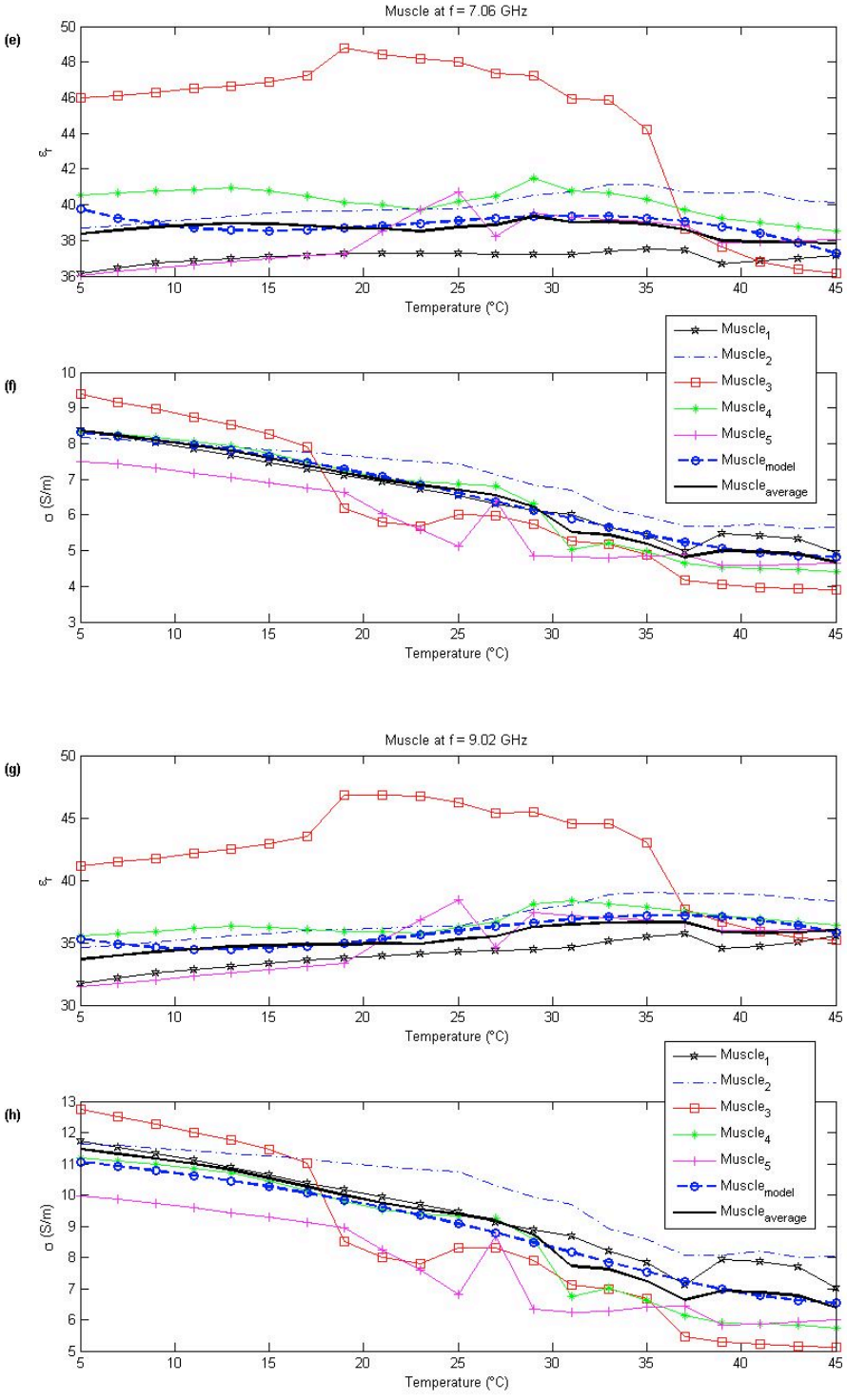
(e)
Muscle at f = 7.06 GHz
ε_r
Temperature (°C)
(f)
Muscle$_1$
Muscle$_2$
Muscle$_3$
Muscle$_4$
Muscle$_5$
Muscle$_{model}$
Muscle$_{average}$
σ (S/m)
Temperature (°C)
(g)
Muscle at f = 9.02 GHz
ε_r
Temperature (°C)
(h)
Muscle$_1$
Muscle$_2$
Muscle$_3$
Muscle$_4$
Muscle$_5$
Muscle$_{model}$
Muscle$_{average}$
σ (S/m)
Temperature (°C)

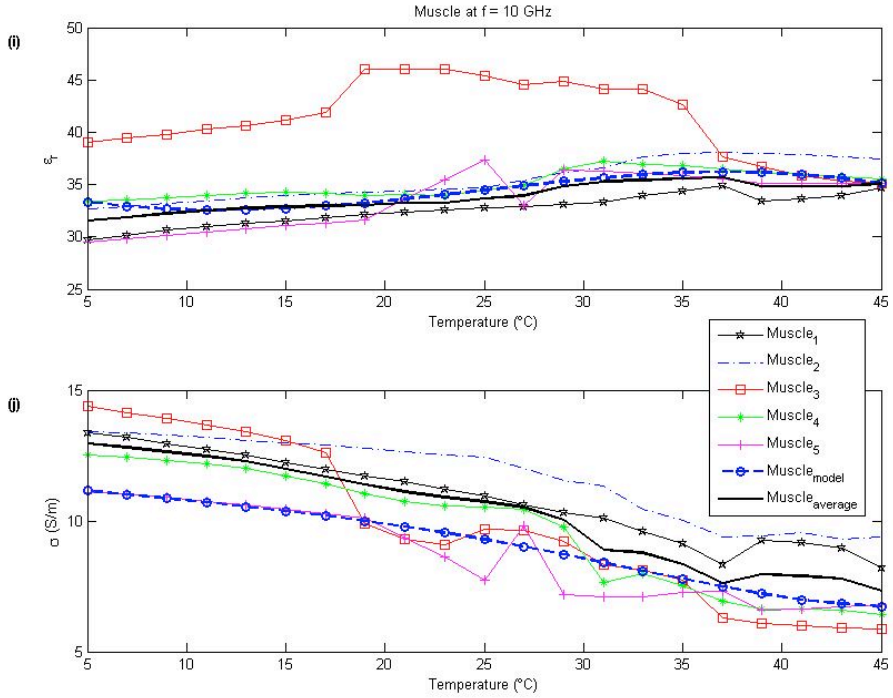

Figure 5.38: Temperature trends of the relative permittivity ε_r of the five measurements of the muscle tissue, the average of the two chosen measurements and the final one-pole Cole-Cole model at: *(a)* 3 GHz, *(c)* 5.01 GHz, *(e)* 7.06 GHz, *(g)* 9.02 GHz and *(i)* 10 GHz. Temperature trends of the conductivity σ_i at: *(b)* 3 GHz, *(d)* 5.01 GHz, *(f)* 7.06 GHz, *(h)* 9.02 GHz and *(j)* 10 GHz.

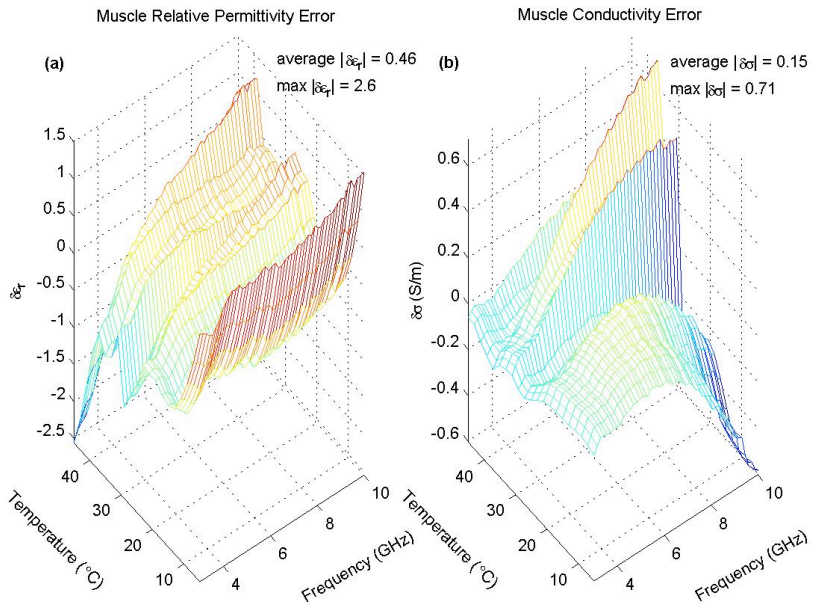

Figure 5.39: Difference between the measured and the final one-pole Cole-Cole model values for the muscle tissue samples: *(a)* relative permittivity and *(b)* conductivity. The maximum and the average differences are also shown in the plot insert.

C. Liver

Figure 5.40 shows the temperature trends of the one-pole Cole-Cole model with their second- or third- order polynomial fits for the liver samples. A third-order polynomial is used to model the temperature dependence of τ. The resultant polynomial is also displayed in its corresponding figure. Figure 5.41 *(a)* – *(j)* shows the relative permittivities and the conductivities calculated from the final Cole-Cole model along with the original five measurements of the muscle tissue samples and the average of the two chosen measurements at 3 GHz, 5.1 GHz, 7.06 GHz, 9.02 GHz, 10 GHz.

Figure 5.42 shows the absolute differences between the relative permittivities and conductivities of the measured data and the final one-pole Cole-Cole model for the liver samples. The maximum difference between the measured and the modeled relative permittivity values is 2.2 units at 39 °C and at 3 GHz, where the relative permittivity value is around 45 units. The maximum difference in the conductivity is 0.7 S/m at 11 °C and at 10 GHz, where the conductivity is 11 S/m. These maximum errors are relatively insignificant. The average differences between the measured and the modeled relative permittivity values and conductivity values are 0.46 permittivity units and 0.18 S/ m, respectively. The final one-pole Cole-Cole model for liver models well the measured data.

Table 5-5 shows a comparison between the coefficients of the quadratic fits for the Cole-Cole parameters of liver in this work and those reported by Lazebnik *et al.* [4]. The values are not comparable and it is difficult to identify the differences or similarities by observing the coefficients. Therefore, Figure 5.43 shows the resulting Cole-Cole parameters of these quadratic equations for both works. The optimization used in fitting the Cole-Cole model to the measured data is non-unique, resulting in various possible solutions. Therefore, the curves of the temperature dependence of the Cole-Cole parameters for both works are not expected to be equal. The measurement setup used as well as the different frequency and temperature ranges also affect the final results.

Since the value of ε_∞ in this work is set to a constant value for all temperatures, while it is used as a fitting parameter in [4], its temperature trends are different. As a result, the temperature trends of $\Delta\varepsilon$ are also not the same for all temperatures. They are

similar only up to around 37 °C, after which $\Delta\varepsilon$ for liver in this work continues to decrease while that in [4] increases. Since $\Delta\varepsilon = \varepsilon_s - \varepsilon_\infty$, the temperature trend of ε_s can be used to show the temperature dependence of $\Delta\varepsilon$ independently of ε_∞. In fact, the temperature trends of the resulting ε_s of both works are similar. The temperature trends of the resultant quadratic fits to both the values of τ and σ_i are also consistent with those reported in [4]. This comparison validates the truthfulness of the measured data and the models used in this work.

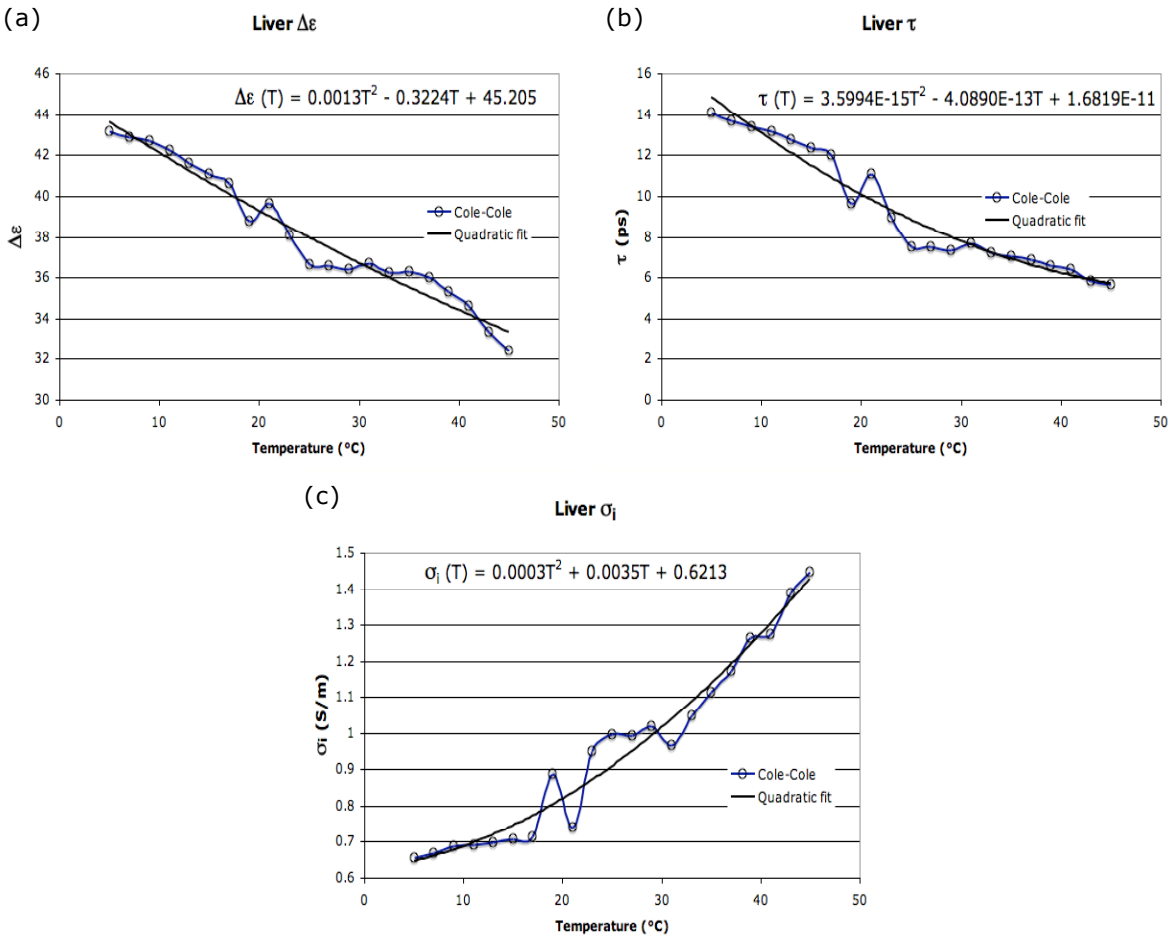

Figure 5.40: Liver tissue samples average one-pole Cole-Cole and their temperature-dependent quadratic fits: *(a)* $\Delta\varepsilon$, *(b)* τ and *(c)* σ_i. The resulting temperature equations are also shown in the figure insert.

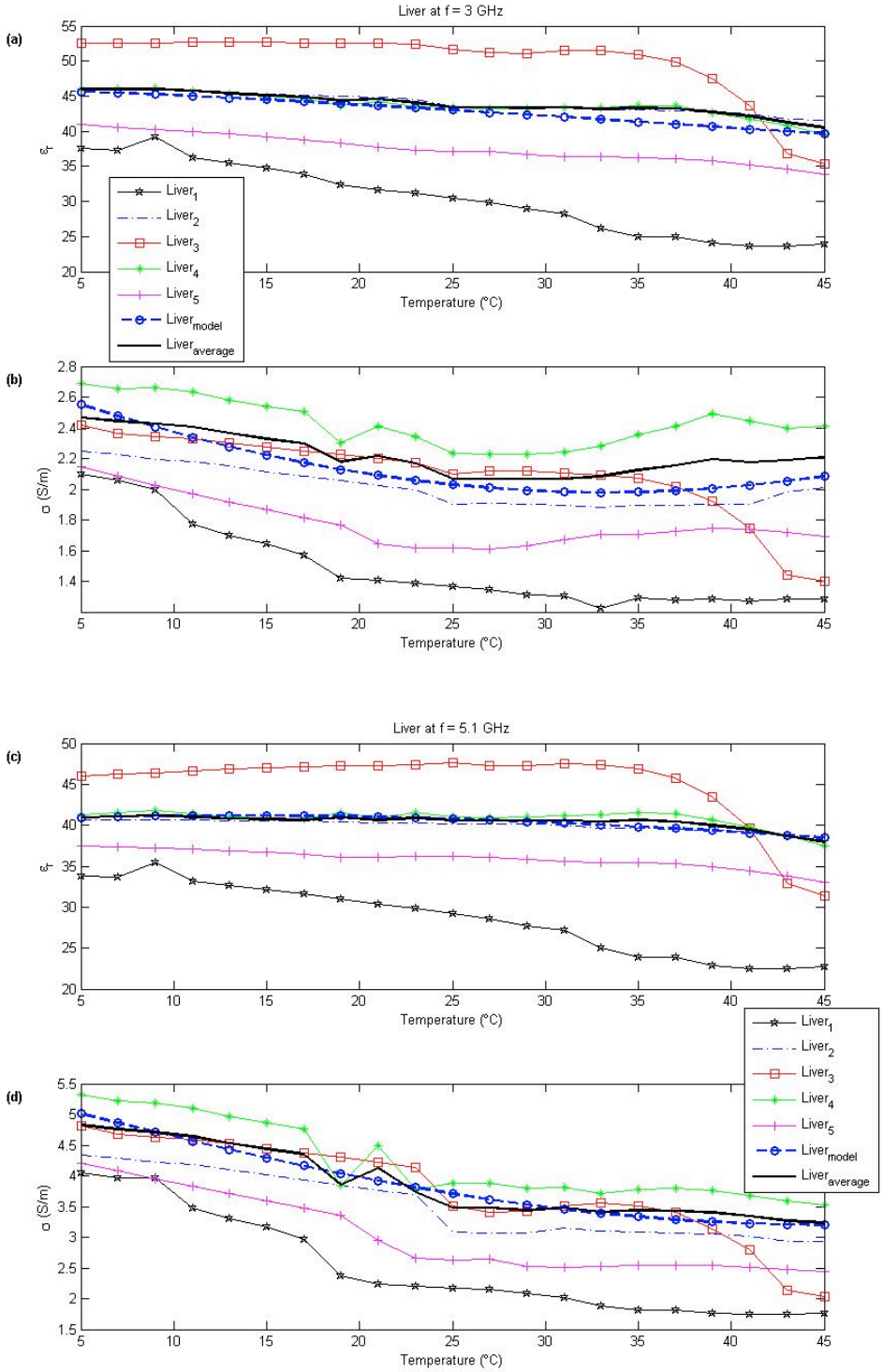
Liver at f = 3 GHz
(a)
ε_r
Temperature (°C)
Liver$_1$
Liver$_2$
Liver$_3$
Liver$_4$
Liver$_5$
Liver$_{model}$
Liver$_{average}$
(b)
σ (S/m)
Temperature (°C)
Liver at f = 5.1 GHz
(c)
ε_r
Temperature (°C)
(d)
σ (S/m)
Temperature (°C)

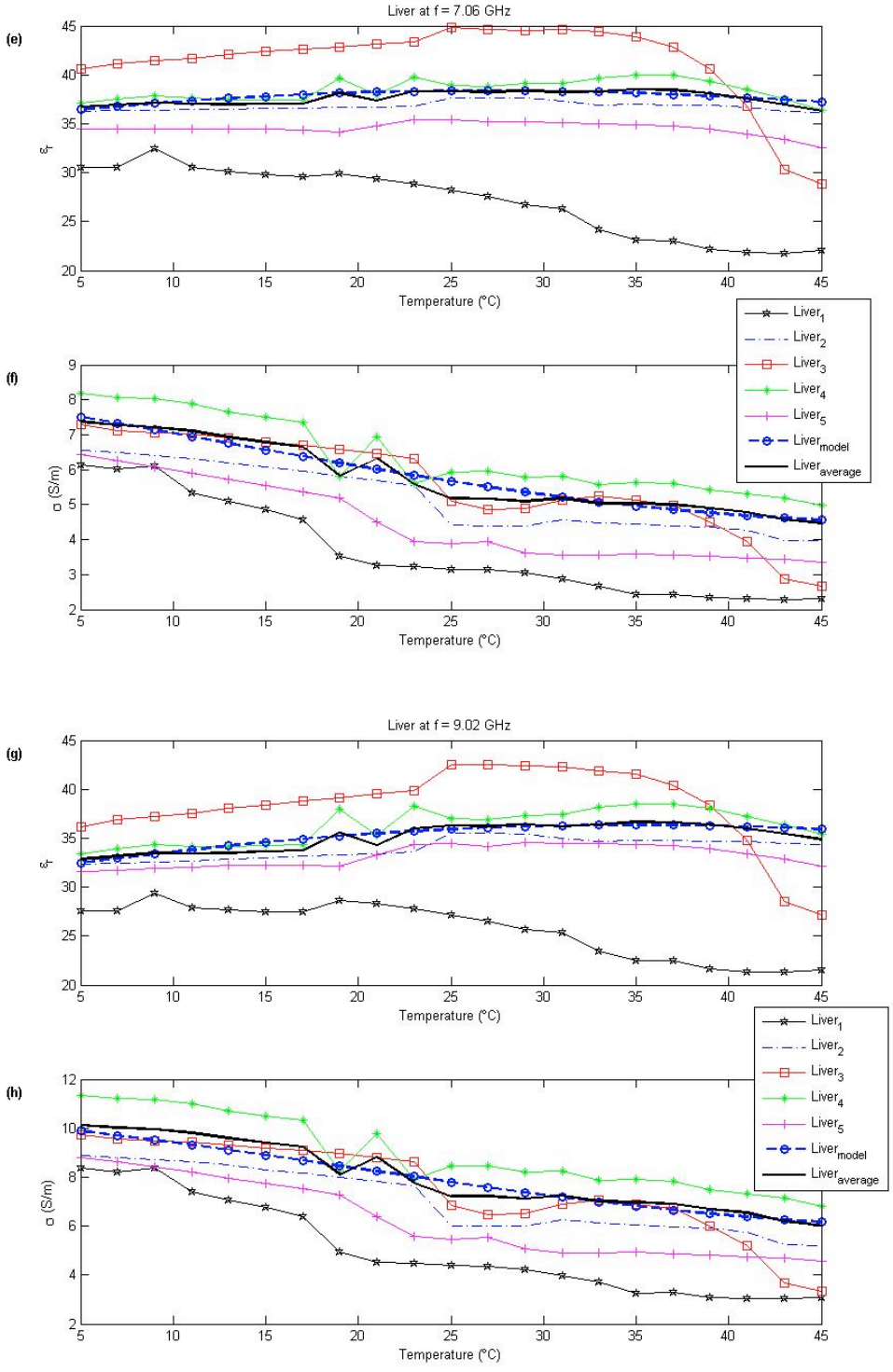
(e)
Liver at f = 7.06 GHz
ε_r
Temperature (°C)
(f)
σ (S/m)
Temperature (°C)
Liver$_1$
Liver$_2$
Liver$_3$
Liver$_4$
Liver$_5$
Liver$_{model}$
Liver$_{average}$
(g)
Liver at f = 9.02 GHz
ε_r
Temperature (°C)
(h)
σ (S/m)
Temperature (°C)

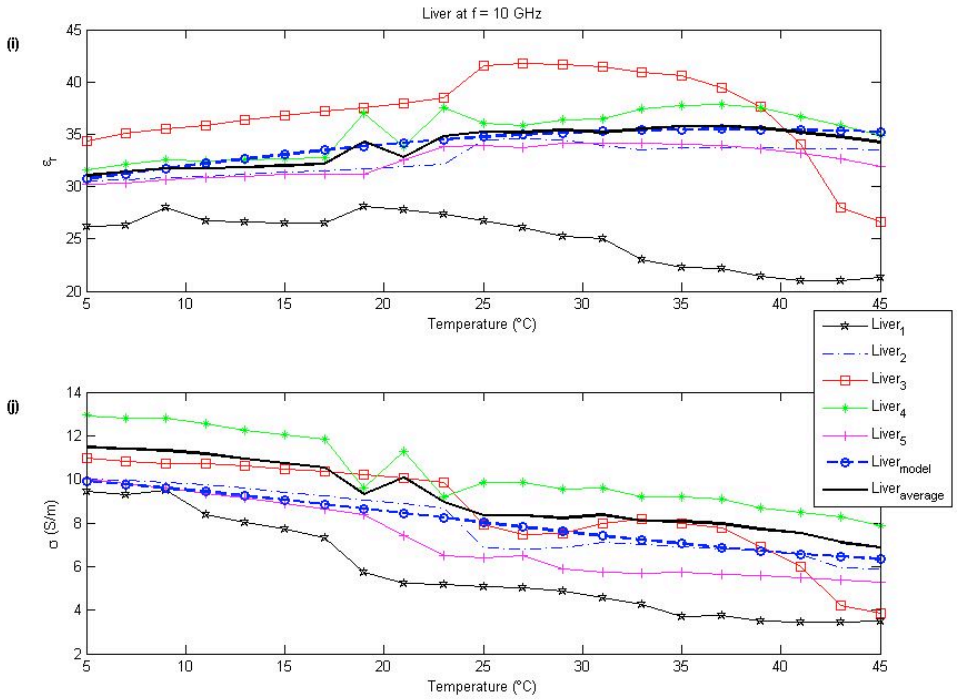

Figure 5.41: Temperature trends of the relative permittivity ε_r of the five measurements of the liver tissue, the average of the two chosen measurements and the final one-pole Cole-Cole model at: *(a)* 3 GHz, *(c)* 5.01 GHz, *(e)* 7.06 GHz, *(g)* 9.02 GHz and *(i)* 10 GHz. Temperature trends of the conductivity σ_i at: *(b)* 3 GHz, *(d)* 5.01 GHz, *(f)* 7.06 GHz, *(h)* 9.02 GHz and *(j)* 10 GHz.

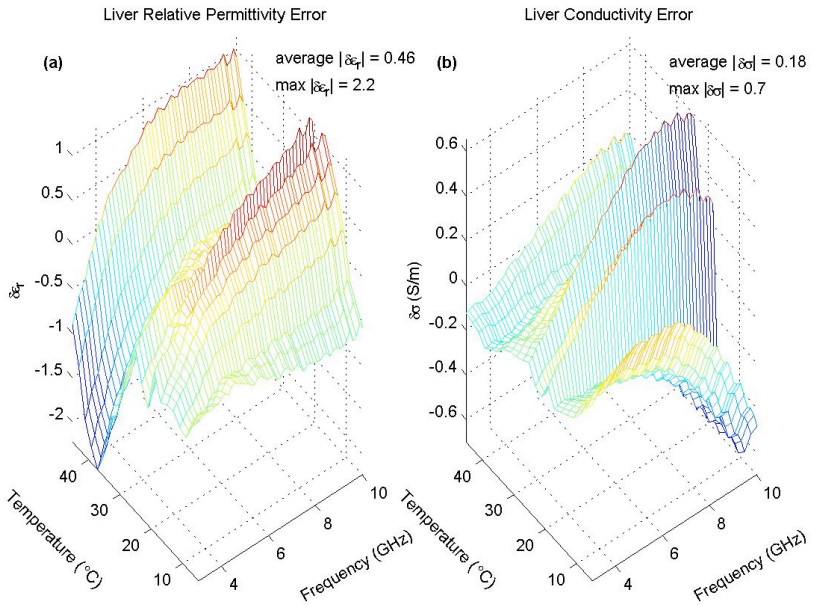

Figure 5.42: Difference between the measured and the final one-pole Cole-Cole model values for the liver tissue samples: *(a)* relative permittivity and *(b)* conductivity. The maximum and the average differences are also shown in the plot insert.

Table 5-5: Comparison between the coefficients of the quadratic fits to the temperature-dependent Cole-Cole model in this work and those reported by Lazebnik *et al.* for liver [4].

	This work's liver parameters (5 - 45 °C), (3 - 10 GHz)			**Lazebnik *et al.*'s liver parameters [4] (23 - 60 °C), (0.5 - 20 GHz)**		
	A	***B***	***C***	***A***	***B***	***C***
ε_∞	7.5 (constant)			-0.0127	0.861	5.411
$\Delta\varepsilon$	0.0013	-0.3224	45.205	0.0115	-0.893	58.36
α	0.1 (constant)			0.1 (constant)		
τ **(ps)**	0.0036	-0.4089	16.819	-1.40E-03	-0.064	13.4
σ_i	0.0003	0.0035	0.6213	1.85E-04	3.49E-04	0.57

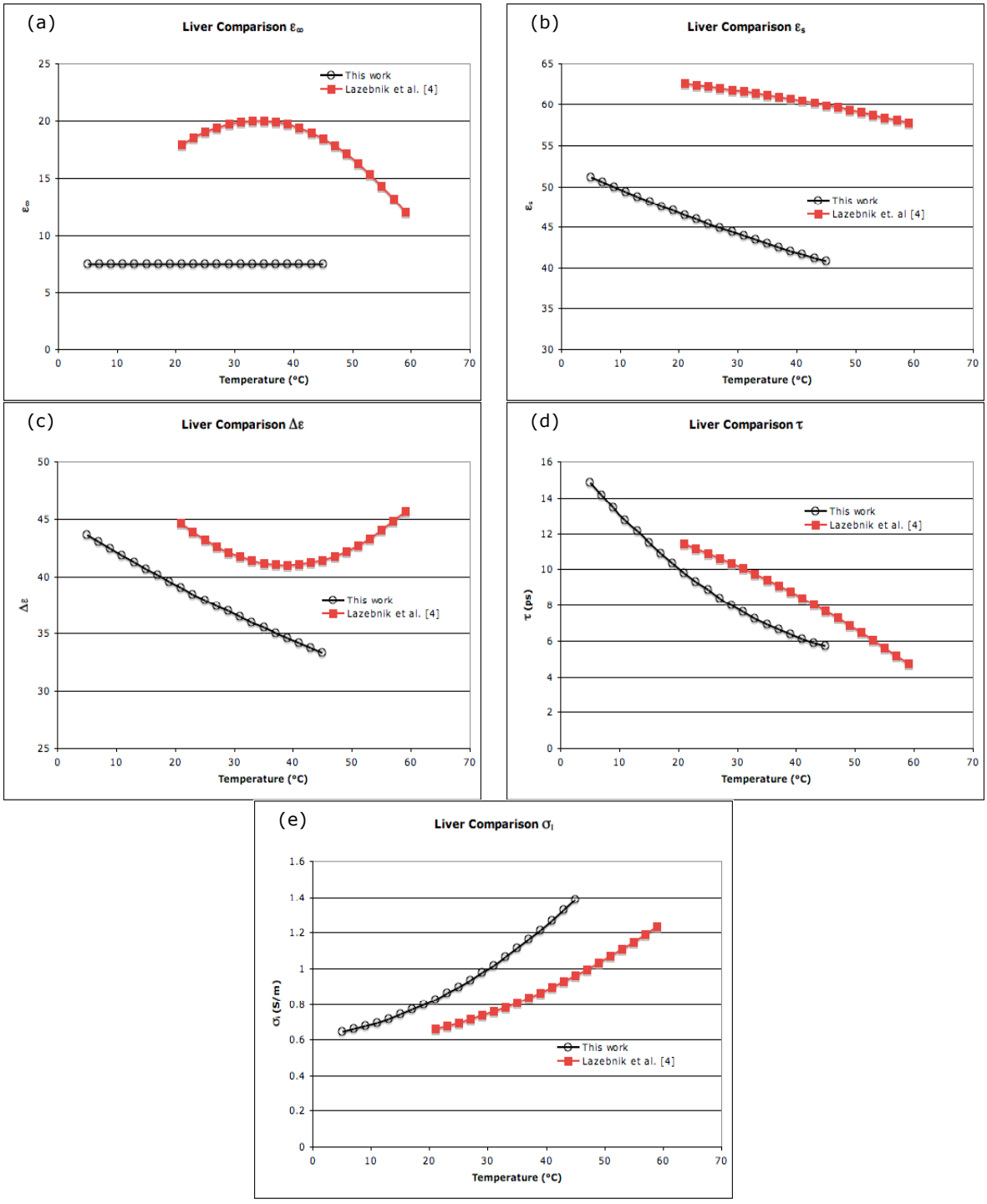

Figure 5.43: Comparison between the temperature trends of *(a)* ε_∞, *(b)* ε_s, *(c)* $\Delta\varepsilon$, *(d)* τ and *(e)* σ_i quadratic fits to the temperature-dependent Cole-Cole model in this work and those reported by Lazebnik *et al.* for liver [4].

REFERENCES

[1] MATLAB version 7.10.0. Natick, Massachusetts: The MathWorks Inc., 2010.

[2] N. E. Hill, "The temperature dependence of the dielectric properties of water," *J. Phys. C: Solid State Phys.*, vol. 3, pp. 238-239, 1970.

[3] J. B. Hasted and S. H. M. El Sabeh, "The dielectric properties of water in solutions," *Trans. Faraday. Soc.*, vol. 49, pp. 1003-1011, 1953

[4] M. Lazebnik, M. C. Converse, J. H. Booske and S. C. Hagness, "Ultrawideband temperature-dependent dielectric properties of animal liver tissue in the microwave frequency range," *Phys. Med. Biol.*, vol. 51, pp. 1941-1955, 2006.

[5] S. Gabriel, R. W. Lau and C. Gabriel, "The dielectric properties of biological tissues: II. Measurements in the frequency range 10 Hz to 20 GHz*," Phys. Med. Biol.*, vol. 41, pp. 2251-2269, 1996.

[6] Microsoft Excel 2004 for Mac version 11.6. Redmond, Washington: Microsoft Corporation, 2004.

CHAPTER 6

CONCLUSION

6.1 SUMMARY OF WORK

In this work, the temperature dependence of the dielectric properties of the five difference physical phantom types (LWCT, IWCT, HWCT-1, HWCT-2 and alginate-based) developed by our group, as well as porcine fat, muscle and liver samples were systematically measured over a wide frequency range (3 GHz – 10 GHz) and for temperatures ranging from 5 °C to 45 °C. A simple and methodological heating and measurement setup and procedure were used. The temperature trends of the different phantom and tissue types were investigated. A compact numerical model for all the measured phantom and tissue types over the measured frequency and temperature ranges was presented. Namely, a one-pole Cole-Cole model was used to model the frequency dependence of the dielectric properties of the measured samples at every temperature point and a second- or third-order polynomial was used to model the temperature dependence of the Cole-Cole parameters. The final result is a model that is a function of

both frequency and temperature for every phantom and tissue type. The models can be used to calculate the dielectric properties of the measured phantom and tissue types at every frequency and for every temperature in the frequency range from 3 GHz to 10 GHz and for temperatures ranging from 5 °C to 45 °C.

6.2 SUMMARY OF RESULTS

The temperature trends are different for the different phantom and tissue types. The temperature trends are also, as expected, frequency-dependent. For all the gelatin-based phantoms (LWCT, IWCT, HWCT-1, HWCT-2) the relative permittivity increases with temperature. The conductivity of the LWCT phantom increases almost constantly as temperature increases. The conductivity of the IWCT phantom decreases with temperature at lower frequencies and increases with temperature at higher frequencies; however, this change in conductivity is small and can be considered negligible. The conductivity of the HWCT-1 decreases constantly with temperature by a total of around 3 S/m over the entire temperature range at lower frequencies with a slightly smaller magnitude at higher frequencies. The conductivity of the HWCT-1 phantom is fairly constant at 10 GHz. The conductivity of the HWCT-2 phantom decreases by a total of around 2 S/m with temperature at lower frequencies and increases also by around 2 S/m with temperature at higher frequencies with a cross-over point at around 5.5 GHz. The relative permittivity of the alginate-based tumor phantom decreases with temperature. It decreases at a higher rate at lower frequencies. For the alginate-based phantom, the conductivity is relatively constant at lower frequencies and decreases by a total of around

5 S/m over the entire temperature range at higher frequencies.

The relative permittivity and the conductivity of fat are fairly constant with temperature. The relative permittivity of muscle is almost constant with temperature at all frequencies. It shows a very small decreasing trend at lower frequencies and a very small increasing trend at higher frequencies with a cross-over point at around 5.5 GHz. The conductivity of muscle decreases with increasing temperature. Over the whole temperature range, it decreases by around 0.8 S/m at 3 GHz and by 3 – 4 S/m at higher frequencies. For liver, there is a slight decrease in permittivity with increasing temperature at 3 GHz, a constant permittivity at 5.1 GHz and a slight increase at 7.06 GHz. The conductivity of liver decreases with temperature over the whole frequency range. The decrease rate is higher at higher frequencies.

The temperature trends of the phantom types and their corresponding tissues (LWCT and fat, HWCT-1 and muscle) do not match. This indicates that even though the phantoms follow the frequency trends of their respective tissues, they do not follow their temperature trends.

The effectiveness of the Cole-Cole model at every temperature is assessed based on the maximum differences between the measured and the modeled relative permittivities and conductivities. The maximum difference between the measured and the modeled relative permittivity and conductivity for the phantoms is 1.1 permittivity units and 0.45 S/m, respectively. The maximum difference between the measured and the modeled relative permittivity and conductivity for the tissue samples is 1.8 permittivity units and 0.67 S/m, respectively. Similarly, the accuracy of the final one-pole Cole-Cole model

whose parameters are second- or third-order polynomial functions of temperature is also assessed. The maximum difference between the measured and the modeled relative permittivity and conductivity for the phantoms is 4.5 permittivity units and 1.2 S/m, respectively. The maximum difference between the measured and the modeled relative permittivity and conductivity of the tissue samples is 2.6 permittivity units and 0.71 S/m, respectively.

6.3 RECOMMENDATIONS AND FUTURE WORK

The limitations of this study include: the small number of samples used, the exclusive use of *ex vivo* animal tissue samples and the possible effects of the heating method on the results of the tissue phantoms.

Using microwave power to heat the samples could yield more reliable results in which the humidity caused by the steam used to heat the samples in this study is not a factor.

There is always room for improvement in the numerical models presented. More accurate Cole-Cole models can be investigated. The use of non-polynomial functions or neural networks to model the temperature dependence of the Cole-Cole parameters could also yield more accurate final models that accurately follow the temperature trends of the dielectric properties of the phantoms and the tissues samples.

A large-scale study with a larger number of human tissue samples in which statistical analysis of the data is conducted would provide more reliable results. The heterogeneity of the tissue samples also plays a role in the wide range of relative

permittivity and conductivity results; therefore, a histological assessment of the tissue samples, especially the area in direct contact with the dielectric probes, would yield more reliable results.

Such studies also need to be performed on the variety of tissues available in the body, and specifically in the breast, such as the fibroglandular tissue. A similar investigation of the temperature dependence of the dielectric properties of benign and malignant tumors would also add more insight into the properties of cancerous cells and thus have an impact on the future research in cancer detection and treatment. Wider frequency and temperature ranges would also make such data more comprehensive. More studies are also necessary to determine the contributions of the difference physical mechanisms such as cellular changes and dehydration on temperature trends of biological tissues. Extensive studies in this area should be geared towards a comprehensive data source, which is available to the research communities in relevant fields.

APPENDIX I.

Tables Showing the Values of the Cole-Cole Parameters for All Phantom and Tissue Types at Every Temperature

A. LWCT Phantom

Constant parameters: $\alpha = 0.1$, $\sigma_i = 0.2$ S/m

Temperature (°C)	$\Delta\varepsilon$	ε_∞	τ (ps)
5	32.18169265	5.230471784	532.41
7	32.77086053	5.207445722	508.41
9	33.05826698	5.171909331	481.34
11	33.98805439	5.122620352	460.38
13	35.66768634	5.092772778	445.72
15	37.38616328	5.040589368	436.60
17	38.81832302	4.976937211	426.24
19	41.54576128	4.87150186	340.56
21	41.87314393	4.885811467	255.98
23	41.42907053	4.872046031	217.97
25	39.87978615	4.841124255	159.78
27	39.21849646	4.777171124	136.34
29	37.90187951	4.716991503	128.67
31	38.21745513	4.685051409	126.09
33	38.30312613	4.676261388	119.79
35	38.01360225	4.63620845	110.77
37	37.79089582	4.59817799	109.26
39	36.4415062	4.500639134	87.21
41	36.08333002	4.44336903	82.72
43	35.68618772	4.387273649	78.36
45	34.26610704	4.162852599	58.75

B. IWCT Phantom

Constant parameter: $\alpha = 0.1$

Temperature (°C)	$\Delta\varepsilon$	ε_∞	τ (ps)	σ_i
5	43.54969876	7.366767752	58.37	0.5
7	44.37489273	7.231959527	58.26	0.498543187
9	44.13356109	7.232109347	55.76	0.489927246
11	43.92156873	7.244157934	52.87	0.485322901
13	43.75511719	7.246883929	50.34	0.479546699
15	43.64475173	7.197913689	48.18	0.465989488
17	43.54368802	7.178342464	46.20	0.450881278
19	43.0236296	7.665838709	27.25	0.296536612
21	42.15366152	7.670565179	25.75	0.276710638
23	41.16322695	7.694138124	23.24	0.252460235
25	40.90014585	7.679880076	22.30	0.240440926
27	40.75166404	7.646498218	22.52	0.239663749
29	40.39882186	7.627628161	21.50	0.232621354
31	40.09521087	7.586721058	20.26	0.219922616
33	39.92445213	7.546586319	19.64	0.214581891
35	39.6333599	7.497350043	18.96	0.208316462
37	39.13769565	7.237747643	16.46	0.184747798
39	38.93678749	6.937574437	14.97	0.174922528
41	38.71825492	6.486367195	13.75	0.168770345
43	38.49302979	6.294298126	12.93	0.162132739
45	38.08480446	6.086070456	11.98	0.150082913

C. HWCT-1 Phantom

Constant parameters: $\alpha = 0.1$, $\sigma_i = 0.2$ S/m

Temperature (°C)	$\Delta\varepsilon$	ε_∞	τ (ps)
5	52.46692511	7.254933163	37.34
7	51.69336001	7.235186219	35.12
9	51.08937477	7.216105643	33.17
11	50.46698388	7.199292156	31.21
13	49.8693318	7.170301108	29.50
15	49.2684973	7.132680815	27.89
17	48.29216134	7.097099057	24.27
19	46.72367425	6.486737763	18.02
21	45.896675	6.064246096	14.96
23	45.50241332	5.858761173	13.39
25	45.32639073	5.515914258	12.51
27	45.05368031	5.301351524	11.93
29	44.60576921	4.480923106	9.66
31	44.49842845	3.832154344	8.37
33	44.42113696	3.5	7.79
35	44.24785749	3.5	7.63
37	43.58881356	3.5	6.95
39	43.33363635	3.5	6.71
41	43.06914873	3.5	6.40
43	42.82079262	3.5	6.11
45	42.29350038	3.5	5.62

D. HWCT-2 Phantom

Constant parameters: $\alpha = 0.1$

Temperature (°C)	$\Delta\varepsilon$	ε_∞	τ (ps)	σ_i
5	40.8612748	7.008040415	55.21	0.5
7	40.08255501	7.008832325	53.67	0.5
9	39.90050453	6.990005405	51.00	0.5
11	39.61092023	6.940016204	48.03	0.5
13	39.4615514	6.896111388	45.22	0.5
15	39.36559879	6.781939878	41.60	0.498209969
17	39.73507111	6.709436468	35.63	0.445813661
19	40.14940273	6.765172597	31.97	0.367711472
21	40.1728638	6.700960608	29.15	0.320826762
23	40.03501688	6.078159192	19.65	0.180409022
25	40.04945886	5.426156509	17.14	0.13172786
27	40.01386816	5.197067178	16.24	0.111879826
29	39.90787609	4.993558415	15.70	0.10488761
31	39.8189876	4.890705385	15.31	0.097812883
33	39.52227861	4.750120047	14.28	0.092535784
35	39.29921782	4.624140082	13.23	0.080847816
37	38.54998436	5.072114811	12.83	0.073715728
39	38.37562958	5.092579552	12.92	0.072951424
41	37.95003205	4.918764737	11.41	0.055263798
43	37.3849048	5.152558296	11.05	0.047337026
45	36.89064316	5.324472402	10.66	0.042811263

E. Alginate-based Phantom

Constant parameters: $\alpha = 0.1$, $\sigma_i = 0.2$ S/m

Temperature (°C)	$\Delta\varepsilon$	ε_∞	τ (ps)	σ_i
5	48.56450345	4.198730101	10.05	3.226934137
7	48.50202681	4.093949745	9.99	3.197388104
9	48.36479965	4	9.75	3.223122139
11	47.99279701	4	9.40	3.272011739
13	47.71131406	4	9.06	3.32968856
15	47.66997858	4	8.71	3.396035675
17	47.28094811	4	8.33	3.454488164
19	46.20357079	4	7.55	3.689630425
21	44.46908745	4.000036035	6.12	4.360962919
23	41.87230649	5.570044161	5.55	4.952430652
25	41.46698768	5.53985471	5.38	5.03967327
27	41.35338733	5.207751179	5.10	5.196535526
29	41.35070433	4.844324516	4.91	5.304015659
31	39.74672361	6.057954469	4.95	5.350931608
33	39.13745524	6.097284969	4.77	5.481445321
35	38.27368632	6.410860241	4.60	5.693226435
37	37.49945253	6.548931069	4.47	5.852647553
39	35.95689249	7.344141469	4.40	6.160367311
41	35.08441211	7.280661982	4.31	6.174227194
43	31.6885713	8.913929637	4.05	7.183151852
45	30.40613211	9.255844061	4.12	7.209549748

F. Fat Tissue

Constant parameters: $\alpha = 0.1$, $\varepsilon_\infty = 2.54$

Temperature (°C)	$\Delta\varepsilon$	τ (ps)	σ_i
5	8.105085327	10.90	0.115465427
7	7.938936105	10.73	0.115316506
9	7.6418875	10.40	0.111990352
11	7.382471963	10.15	0.115513715
13	7.074356323	9.92	0.115308713
15	6.729807297	9.66	0.117431225
17	6.505606691	9.41	0.120741431
19	6.321230659	9.26	0.125400539
21	6.185609763	9.11	0.131212834
23	6.655698999	8.17	0.154733099
25	6.75173661	7.71	0.166284033
27	6.844033356	7.46	0.177182075
29	6.907149643	7.25	0.184559861
31	6.92652508	7.16	0.188437667
33	7.126023469	6.51	0.216656685
35	7.106236653	6.60	0.216610676
37	7.062613967	6.44	0.227848616
39	6.932498917	6.54	0.222601838
41	6.867493444	6.22	0.235302188
43	6.782128184	6.25	0.236586797
45	6.994742333	6.33	0.222533853

G. Muscle Tissue

Constant parameters: $\alpha = 0.1$, $\varepsilon_\infty = 5.95$

Temperature (°C)	$\Delta\varepsilon$	τ (ps)	σ_i
5	49.35134394	14.60	0.5889584
7	48.91798462	14.28	0.59658292
9	48.39939109	13.95	0.606319698
11	47.84703784	13.67	0.613896959
13	47.33882191	13.31	0.621775013
15	46.59784346	12.90	0.63260815
17	45.80993757	12.50	0.64157241
19	44.98923072	12.11	0.649437709
21	44.29031861	11.68	0.658565292
23	43.70766655	11.44	0.667094924
25	43.46638654	11.05	0.680168271
27	43.10004262	10.67	0.692924459
29	42.14131729	9.52	0.782375489
31	39.40652307	7.63	1.013563949
33	39.31105145	7.57	0.992716284
35	38.44308785	6.95	1.078508209
37	37.04967032	6.01	1.256790893
39	37.00105101	6.52	1.195857917
41	36.87702211	6.48	1.192680939
43	36.67885857	6.35	1.2058264
45	35.93137684	5.72	1.341080657

H. Liver Tissue

Constant parameters: $\alpha = 0.1$, $\varepsilon_\infty = 7.5$

Temperature (°C)	$\Delta\varepsilon$	τ (ps)	σ_i
5	43.15136036	14.09	0.657121891
7	42.87944782	13.70	0.668390085
9	42.71229237	13.38	0.686777535
11	42.25075296	13.17	0.693135647
13	41.60072344	12.78	0.699438978
15	41.07460707	12.37	0.706953986
17	40.61246632	12.03	0.713409128
19	38.75183209	9.62	0.888209216
21	39.65999652	11.06	0.739830746
23	38.07730843	8.93	0.949295148
25	36.62092605	7.52	0.994421522
27	36.56880416	7.52	0.993277956
29	36.42974249	7.31	1.019023297
31	36.68213529	7.68	0.966968437
33	36.22035178	7.24	1.047831183
35	36.27020577	7.05	1.113146981
37	36.01961213	6.88	1.172801515
39	35.30510032	6.58	1.26289368
41	34.60540925	6.44	1.274182618
43	33.35575813	5.85	1.390030618
45	32.44690102	5.66	1.448564439

BIBLIOGRAPHY

Agilent ADS, Agilent Technologies, 1400 Fountaingrove Parkway, Santa Rosa, CA 954031799, USA. [Online] http://www.home.agilent.com/agilent/home.jspx?cc=US&lc=eng.

R. K. Amineh, M. Ravan, N. K. Nikolova, and A. Khalatpour, "Three-dimensional near-field microwave holography using reflected and transmitted signals," *IEEE Trans. Antennas Propagat.*, vol. 59, no. 12, pp. 4777-4789, December 2011.

Y. Baskharoun, A. Trehan, N. K. Nikolova, and M. D. Noseworthy, "Physical phantoms for microwave imaging of the breast," *IEEE Conference on BioWireLess*, pp. 73-76, January 2012.

C. Bircan and S. A. Barringer, "Determination of protein denaturation of muscle foods using the dielectric properties," *J. Food Sci.*, vol. 67, pp. 202-205, 2002.

B.Bocquet, J.C. van deVelde, A. Mamouni, Y. Leroy, G. Giaux, J. Delannoy, and D. DelValee, "Microwave radiometric imaging at 3 GHz for the exploration of breast tumors," *IEEE Trans. Microw. Theory Tech.*, vol. 38, pp. 791-793, June 1990.

E. J. Bond, S. C. Hagness, and B. D. Van Veen, "Microwave imaging via space-time beamforming for early detection of breast cancer," *IEEE Trans. Antennas Propagat.*, vol. 51, no. 8, pp. 1690-1705, 2003.

B.Bocquet, J.C. van deVelde, A. Mamouni, Y. Leroy, G. Giaux, J. Delannoy, and D. DelValee, "Microwave radiometric imaging at 3 GHz for the exploration of breast tumors," *IEEE Trans. Microw. Theory Tech.*, vol. 38, pp. 791-793, June 1990.

J. D. Bronzino, *The Biomedical Engineering Handbook.* 2nd ed, vol. 1, Florida: CRC Press, 2000, pp. 89.

C. L. Brace, "Temperature-dependent dielectric properties of liver tissue measured during thermal ablation: Toward an improved numerical model," *30th Annual IEEE EMBS Conference, Vancouver, British Columbia, Canada*, pp. 230-233, August 2008.

(October 2009). Breast Cancer. WebMD Health News. [Online]. http://www.medicinenet.com/script/main/art.asp?articlekey=150356.

(March 2011). Breast Cancer: Early Detection. National Cancer Institute. [Online].

http://www.cancer.org/Cancer/BreastCancer/MoreInformation/BreastCancerEarlyDetection/breast-cancer-early-detection-toc.

(June 2012). Breast Cancer Information. Canadian Breast Cancer Foundation, Toronto, ON. [Online]. http://www.cbcf.org/central/AboutBreastCancerMain/AboutBreastCancer/Pages/default.aspx.

(May 2012). Breast Cancer Statistics 2012. Canadian Cancer Society. [Online]. http://www.cancer.ca/canada-wide/about%20cancer/cancer%20statistics/stats%20at%20a%20glance/breast%20cancer.aspx.

A. E. Bulyshev, S. Y. Semenov, A. E. Souvorov, R. H. Svenson, A. G. Nazarov, Y.E. Sizov and G. P. Tatsis, "Computational modeling of three-dimensional microwave tomography of breast cancer," *IEEE Trans. Biomed. Eng.*, vol. 48, no. 9, pp. 1053-1056, September 2001.

E. C. Burdette, F. L. Cain and J. Seals, "*In situ* tissue permittivity at microwave frequencies: perspective, techniques, results," *Medical Applications of Microwave Imaging ed. L. E. Larsen and J. H. Jacobi,* New York: IEEE, 1985, pp. 13-40.

A. M. Campbell and D. V. Land, "Dielectric properties of female human breast tissue measured *in vitro* at 3.2 GHz," *Phys. Med. Biol.*, vol. 37, pp. 193-210, 1992.

(May 2012). Cancer Statistics 2012. Canadian Cancer Society, pp. 11, 28. [Online]. http://www.cancer.ca/~/media/CCS/Canada%20wide/Files%20List/English%20files%20heading/PDF%20-%20Policy%20-%20Canadian%20Cancer%20Statistics%20-%20English/Canadian%20Cancer%20Statistics%202012%20-%20English.ashx.

K. L. Carr, "Microwave radiometry: its importance to the detection of cancer," *IEEE Trans. Microw. Theory Tech.*, vol. 37, pp. 1862-1869, December 1989.

K. L. Carr, P.Cevasco, P.Dunlea, and J. Shaeffer, "Radiometric sensing: An adjuvant to mammography to determine breast biopsy*," IEEE MTT-S Int. Microwave Symp. Dig.*, vol. 2, 2000, pp. 929-932.

S. S. Chaudhary, R. K. Mishra, A. Swarup and J. M. Thomas, "Dielectric properties of normal and malignant human breast tissues at radiowave and microwave frequencies," *Indian J. Biochem. Biophys.*, vol.21, pp. 76-79, 1984.

L. Chin and M. Sherar, "Changes in dielectric properties of ex vivo bovine liver at 915 MHz during heating," *Phys. Med. Biol.,* vol. 46, no. 1, pp. 197-211, 2001.

L. Chin and M. Sherar, "Changes in the dielectric properties of rat prostate ex vivo at 915 MHz during heating," *Int. J. Hyperthermia*, vol. 20, no. 5, pp. 517-27, 2004.

J. W. Choi *et al.*, "Microwave detection of metastasized breast cancer cells in the lymph node; potential applications for sentinel lymphadenectomy," *Breast Cancer Res. Treat.*, vol. 86, pp. 107-115, 2004.

M. C. Converse, E. J. Bond, S. C. Hagness and B. D. Van Veen "Ultrawideband microwave space-time beamforming for hyperthermia treatment of breast cancer: a computational feasibility study," *IEEE Trans. Microw. Theory Tech.,* vol. 52, no. 8, pp. 1876-89, 2004.

J. Croteau, J. Sill, T. Williams, and E. Fear, "Phantoms for testing radar-based microwave breast imaging," Presented at the 13th International Symposium on Antenna Technology and Applied Electromagnetics and Canadian Radio Sciences Meeting, 2009.

(June 2012). Detecting Breast Cancer Earlier. Canadian Breast Cancer Foundation, Toronto, ON. [Online]. http://www.cbcf.org/central/AboutBreastHealth/EarlyDetection/Pages/default.aspx.

F. A. Duck, Physical Properties of Tissue: A Comprehensive Reference Book. London: Academic Press, 1990.

J. G. Elmore, K. Armstrong, C. D. Lehman, S.W. Fletcher, "Screening for breast cancer," *JAMA*, vol. 293, no. 10, pp. 1245-1256, 2005.

M. Elsdon, D. Smith, M. Leach, and S. J. Foti, "Experimental investigation of breast tumor imaging using indirect microwave holography," *Microwave Opt. Technol. Lett.*, vol. 48, no. 3, pp. 480-482, March 2006.

T. S. England N. A. and Sharples, "Dielectric properties of the human body in the microwave region of the spectrum," *Nature*, vol. 163, pp. 487-488, 1949.

(February 2011). FDA approves first 3D mammogram device. Bloomberg Business Week, New York, USA. [Online]. http://www.businessweek.com/lifestyle/content/healthday/649867.html.

E. C. Fear, S. C. Hagness, P. M. Meaney, M. Okoniewski, and M. A. Stuchly, "Enhancing breast tumor detection with near field imaging," *IEEE Microw. Mag.*, vol.3, pp. 8-56, March 2002.

E. C. Fear, X. Li, S. C. Hagness, and M. A. Stuchly, "Confocal microwave imaging for breast cancer detection: Localization of tumors in three dimensions," *IEEE Trans. Biomed. Eng.*, vol. 49, pp. 812-822, August 2002.

E. C. Fear, J. Sill, and M. A. Stuchly, "Experimental feasibility study of confocal microwave

imaging for breast tumor detection," *IEEE Trans. Microw. Theory Tech.*, vol. 51, no. 3, pp. 887-892, March 2003.

K. R. Foster, J. L. Schepps, R. D. Stoy and H. P. Schwan, "Dielectric properties of brain tissue between 0.01 and 10 GHz," *Phys. Med. Biol.*, vol. 24, no. 6, pp. 1177-87, 1979.

K. R. Foster and H. P. Schwan, "Dielectric properties of tissues and biological materials: a critical review," *Crit. Rev. Biomed. Eng.*, vol. 17, pp. 25-104, 1989.

C. Gabriel, T. Y. A. Chan and E. H. Grant, "Admittance models for open ended coaxial probes and their place in dielectric spectroscopy," *Phys. Med. Biol.*, vol. 39, pp. 2183-2200, 1994.

C. Gabriel, S. Gabriel and E. Corthout, "The dielectric properties of biological tissues: I. Literature survey," *Phys. Med. Biol.*, vol. 41, pp. 2231-2249, 1996.

S. Gabriel, R. W. Lau and C. Gabriel, "The dielectric properties of biological tissues: II. Measurements in the frequency range 10 Hz to 20 GHz*," Phys. Med. Biol.*, vol. 41, pp. 2251-2269, 1996.

S. Gabriel, R. W. Lau, and C. Gabriel, "The dielectric properties of biological tissues: III. Parametric models for the dielectric spectrum of tissues," *Phys. Med. Biol*., vol. 41, pp. 2271-2293, April 1996.

E. Grant, T. Buchanan, and H. Cook, "Dielectric behavior of water at microwave frequencies," *J. Chem. Phys.*, vol. 26, pp. 156-161, 1957.

S. C. Hagness, A. Taflove, and J. E. Bridges, "Two-dimensional FDTD analysis of a pulsed microwave confocal system for breast cancer detection: Fixed-focus and antenna-array sensors," *IEEE Trans. Biomed. Eng*., vol. 45, pp. 1470-1479, Dec. 1998.

R. J. Halter *et al.*, "The correlation of in vivo and ex vivo tissue dielectric properties to validate electromagnetic breast imaging: initial clinical experience," *Physiol. Meas.,* vol. 30, pp. S121-S136, June 2009.

J. B. Hasted and S. H. M. El Sabeh, "The dielectric properties of water in solutions," *Trans. Faraday. Soc.*, vol. 49, pp. 1003-1011, 1953.

N. E. Hill, "The temperature dependence of the dielectric properties of water," *J. Phys. C: Solid State Phys.*, vol. 3, pp. 238-239, 1970.

(January 2010). Information on Mammography for Women Aged 40 and Older - A Decision Aid for Breast Cancer Screening in Canada. Public Health Agency of Canada. [Online]. http://www.phac-aspc.gc.ca/cd-mc/mammography-mammographie-eng.php.

F. Jaspard and M. Nadi, "Dielectric properties of blood: an investigation of temperature dependence," *Physiol. Meas.*, vol. 23, pp. 547-554, 2002.

C. C. Johnson, A. W. Guy, "Nonionizing electromagnetic wave effects in biological materials and systems," *Proc. IEEE*, vol. 60, no. 6, pp. 692-718, 1972.

W. T. Joines, Y. Zhang, C. Li and R. L. Jirtle, "The measured electrical properties of normal and malignant human tissues from 50 to 900 MHz," *Med. Phys.*, vol. 21, pp. 547-550, 1994.

J. Jossinet, "The impedivity of freshly excised human breast tissue," *Phys. Meas.*, vol. 19, pp. 61-75, 1998.

M. Kerr. (November 2007). 3-D mammography cuts false-positive rates by half. Reuter Health, Chicago. [Online]. http://www.reuters.com/article/healthNews/idUSCOL97439820071129.

M. Klemm, J. A. Leendertz, D. Gibbins, I. J. Craddock, A. Preece, and R. Benjamin, "Microwave radar-based breast cancer detection: Imaging in inhomogeneous breast phantoms," *IEEE Antennas Wireless Propag. Lett.*, vol. 8, pp. 1349-1352, 2009.

M. Klemm, J. A. Leendertz, D. Gibbins, I. J. Craddock, A. Preece, and R. Benjamin, "Microwave radar-based differential breast cancer imaging: imaging in homogeneous breast phantoms and low contrast scenarios," *IEEE Trans. Antennas Propagat.*, vol. 58, no. 7, pp. 2337-2344, July 2010.

V. Komarov, S. Wang and J. Tang, "Permittivity and measurements" *Encyclopedia of RF and Microwave Engineering* ed K. Chang, New York: Wiley, 2005.

R. A. Kruger, W. L. Kiser Jr, D. R. Reinecke, G. A. Kruger, R. L. Eisenhart, "Thermoacoustic Computed Tomography of the Breast at 434 MHz," *IEEE MlT-S Digest*, vol. 2, pp. 591-594, 1999.

G. Ku and L. V. Wanga, "Scanning thermoacoustic tomography in biological tissue," *Med. Phys.*, vol. 27, no. 5, pp. 1195-1202, May 2000.

J. Kyber, H. Hansgen and F. Pliquett, "Dielectric properties of biological tissues at low temperatures demonstrated on fatty tissue," *Phys. Med. Biol.*, vol. 37, no. 8, pp. 1675-1688, 1992.

J. C. Y. Lai, C. B. Soh, E. Gunawan, and K. S. Low, "UWB microwave imaging for breast cancer detection – experiments with heterogeneous breast phantoms," *Prog. Electromagn. Res.M.*, vol. 16, pp. 19-29, 2011.

B. Lambert. (April 2008). Dr. K. A. Mauritz Research Group - Dielectric spectroscopy. [Online]. http://www.psrc.usm.edu/mauritz/dilect.html.

J. Lane and J. Saxon, "Dielectric dispersion in pure polar liquids at very high frequencies. III. The effect of electrolytes in solution, " *Proc. Roy. Sot.*, vol. A213, pp. 531-545, 1952.

M. Lazebnik, E.L. Madsen, G.R. Frank, and S.C. Hagness, "Tissue-mimicking phantom materials for narrowband and ultrawideband microwave applications," *Phys. Med. Biol.*, vol. 50, pp. 4245-4258, 2005.

M. Lazebnik, M. C. Converse, J. H. Booske and S. C. Hagness, "Ultrawideband temperature-dependent dielectric properties of animal liver tissue in the microwave frequency range," *Phys. Med. Biol.*, vol. 51, pp. 1941-1955, 2006.

M. Lazebnik, L. McCartney, D. Popovic, C. B. Watkins, M. J. Lindstorm, J. Harter, S. Sewall, A. Magliocco, J. H. Brooske, M. Okoniewski and S. C. Hagness, " A large - scale study of the ultra wideband microwave dielectric properties of normal breast tissue obtained from reduction surgeries*," Phys. Med. Biol*., vol. 52, pp. 2637-2656, April 2007.

M. Lazebnik, L. McCartney, D. Popovic, C. B. Watkins, M. J. Lindstorm, J. Harter, S. Sewall, A. Magliocco, J. H. Brooske, M. Okoniewski and S. C. Hagness, "A large-scale study of the ultrawideband microwave dielectric properties of normal, benign and malignant breast tissues obtained from cancer surgeries," *Phys. Med. Biol*., vol. 52, pp. 6093-6115, October 2007.

M. Lazebnik, M. Okoniewski, J. H. Brooske, S. C. Hagness, "Highly accurate Debye models for normal and malignant breast tissue dielectric properties at microwave frequencies," *IEEE Microw. Wireless Comp. Lett.*, vol. 17, no. 12, pp. 822-824, December 2007.

D. Li, P. M. Meaney, T. D. Tosteson, S. Jiang, T. E. Kerner, T. O. McBride, B. W. Pogue, A. Hartov, and K. D. Paulsen, "Comparisons of three alternative breast modalities in a common phantom imaging experiment," *Med. Phys.*, vol. 30, pp. 2194-2205, 2003.

X. Li and S. C. Hagness, "A confocal microwave imaging algorithm for breast cancer detection," *IEEE Microwave Wireless Compon. Lett.*, vol. 11, no. 3, pp. 130-132, 2001.

X. Li, S. K. Davis, S. C. Hagness, D. W. Weide and B. D. Van Veen, "Microwave imaging via space–time beamforming: experimental investigation of tumor detection in multilayer breast phantoms," *IEEE Trans. Microw. Theory Tech.*, vol. 52, pp. 1856-1865, August 2004.

X. Li, E. J. Bond, B. D. Van Veen and S. C. Hagness, "An overview of ultra-wideband

microwave imaging via space-time beamforming for early- stage breast-cancer detection," *IEEE Antennas Propagat. Mag.*, vol. 47, pp. 19-34, February 2005.

Q. H. Liu, Z. Q. Zhang, T. T. Wang, J. A. Bryan, G. A. Ybarra, L. W. Nolte, and W. T. Joines, "Active microwave imaging I — 2-D forward and inverse scattering methods," *IEEE Trans. Microw. Theory Tech.*, vol. 50, no. 1, pp. 123-133, January 2002.

H. Maeda, "The enhanced permeability and retention (EPR) effect in tumor vasculature: the key role of tumor selective macromolecular drug targeting," *Advan. Enzyme Regul.,* vol. 41, pp. 189-207, 2001.

C. Malmberg and A. Maryott, "Dielectric constant of water from 0° to 100 °C," *J. Res. Nat. Bur. Stand.*, vol. 56, pp. 1-8, 1956.

(September 2010). Mammograms. National Cancer Institute (NCI). [Online]. http://www.cancer.gov/cancertopics/factsheet/detection/mammograms.

Mammograms and Other Breast Imaging Procedures. American Cancer Society (ACS). [Online]. http://www.cancer.org/Healthy/FindCancerEarly/ExamandTestDescriptions/MammogramsandOtherBreastImagingProcedures/index.

A. Mashal, F. Gao, and S. C. Hagness, "Heterogeneous anthropomorphic phantoms with realistic dielectric properties for microwave breast imaging experiments," *Microw. Opt. Techn. Let.*, vol. 53, no. 8, pp. 1896-1902, August 2011.

MATLAB version 7.10.0. Natick, Massachusetts: The MathWorks Inc., 2010.

D. A. McRae and M. A. Esrick, "The dielectric parameters of excised EMT-6 tumours and their change during hyperthermia," *Phys. Med. Biol.*, vol. 37, no. 11, pp. 2045-2058, 1992.

P. M. Meaney, M. W. Fanning, D. Li, S. P. Poplack, and K. D. Paulsen, "A clinical prototype for active microwave imaging for the breast," *IEEE Trans. Microw. Theory Tech.*, vol. 48, no. 11, pp. 1841-1853, November 2000.

Microsoft Excel 2004 for Mac version 11.6. Redmond, Washington: Microsoft Corporation, 2004.

D. Miklavčič, N. Pavšelj, and F. X. Hart, Electric Properties of Tissues. Wiley Encyclopedia of Biomedical Engineering, 2006.

M. Miyakawa, S. Takata, and K. Inotsume, "Development of non-uniform breast phantom

and its microwave imaging for tumor detection by CP-MCT," *Proceedings of the Annual International Conference of the IEEE Engineering in Medicine and Biology Society*, pp. 2723-2726, 2009.

T. Morimoto *et al.*, "A study of the electrical bioimpedance of tumors," *J. Invest. Surg.*, vol. 6, pp. 25-32, 1993.

S. Mouty, B. Bocquet, R. Ringot, N. Rocourt, and P. Devos, "Microwave radiometric imaging for the characterisation of breast tumors," *Eur. Phys. J.: Appl. Phys.*, vol. 10, pp. 73-78, 2000.

(March 2010). National Breast and Ovary Cancer Center, Australia. [Online]. http://canceraustralia.nbocc.org.au/breast-cancer/about-breast-cancer/about.

L. Nie, D. Xing, Q. Zhou, D. Yang, and H. Guo, "Microwave-induced thermoacoustic scanning CT for high-contrast and noninvasive breast cancer imaging," *Med. Phys.*, vol. 35, no. 9, pp. 4026-4032, September 2008.

N. K. Nikolova, "Microwave imaging for breast cancer," *IEEE Microw. Mag.*, vol. 12, no. 7, pp. 78-94, December 2011.

M. Ostadrahimi, R. Reopelle, S. Noghanian, S. Pistorius, A. Vahedi, and F. Safari, "A heterogeneous breast phantom for microwave breast imaging," *Proceedings of the Annual International Conference of the IEEE Engineering in Medicine and Biology Society*, pp. 2727-2730, 2009.

R. Peloso, D. T. Tuma and R. K. Jain, Dielectric properties of solid tumors during nonhyperthermia and hyperthermia," *IEEE Trans. Biomed. Eng.*, vol. BME-31, no. 11, pp. 725-728, November 1984.

R. Pethig, "Dielectric properties of body tissues," *Clin. Phys. Physol. Meas.*, vol. 8, suppl. A., pp. 5-12, 1987.

S. P. Poplack *et al.*, "Electromagnetic breast imaging: average tissue property values in women with negative clinical findings," *Radiology*, vol. 231, pp. 571-580, 2004.

D. Popovic, L. McCartney, C. Beasley, M. Lazebnik, M. Okoniewski, S. C. Hagness and J. Booske, "Precision open-ended coaxial probes for *in vivo* and *ex vivo* dielectric spectroscopy of biological tissues at microwave frequencies," *IEEE Trans. Microw. Theory Tech.*, vol. 53, pp. 1713-1722, 2005.

E. Porter, A. Santorelli, A. Bourdon, D. Coulibaly, M. Coates, M. Popovi, "Time-domain microwave breast cancer detection: Experiments with comprehensive glandular phantoms," *Proceedings of the Asia-Pacific Microwave Conference*, pp. 203-206, 2011.

(August 2009). Questions and Answers on Gadolinium-Based Contrast Agents. FDA Drug Safety Newsletter, Maryland, USA. [Online]. http://www.fda.gov/Drugs/DrugSafety/DrugSafetyNewsletter/ucm142889.htm.

M. Ravan, R. K. Amineh, and N. K. Nikolova, "Two-dimensional near-field microwave holography," *Inverse Prob.*, vol. 26, no. 5, May 2010.

J. Reichman. (April 2007). MRI vs. Mammography: Which is better for screening women at high risk of breast cancer? National Cancer Institute (NCI). [Online]. http://www.cancer.gov/clinicaltrials/results/mri-vs-mammography0603.

R. F. Reinoso, B. A. Telfer and M. Rowland, "Tissue water content in rats measured by dessication," *J. Pharmacol. Toxicol. Methods*, vol. 38, pp. 87-92, 1997.

A. Rosen, M. A. Stuchly and A. Vander Vorst, "Applications of RF/microwaves in medicine," *IEEE Trans. Microw. Theory Tech.*, vol. 50, no.3, pp. 963-74, 2002.

T. Rubæk, P. M. Meaney, P. Meincke, and K. D. Paulsen, "Nonlinear microwave imaging for breast-cancer screening using gauss–newton's method and the CGLS inversion algorithm," *IEEE Trans. Antennas Propagat.*, vol. 55, no. 8, pp. 2320-2331, 2007.

S. Ryynanen, "The electromagnetic properties of food materials: a review of basic properties" *J. Food Eng.*, vol. 26, pp. 409-429, 1995.

S. M. Salvador and G. Vecchi, "Experimental tests of microwave breast cancer detection on phantoms," *IEEE Trans. Antennas Propag.*, vol. 57, pp. 1705-1712, 2009.

A. Samani, J. Zubovits, D. Plewes, "Elastic moduli of normal and pathological human breast tissues: an inversion-technique-based investigation of 169 samples," *Phys. Med. Biol.*, vol. 52, pp. 1565-1576, February 2007.

S. Y. Semenov, R. H. Svenson and G. P. Tatsis, "Microwave spectroscopy of myocardial ischemia and infarction. 1. Experimental study," *Ann. Biomed. Eng.*, vol. 28, pp. 48-54, 2000.

J. L. Schepps and K. R. Foster, "The UHF and microwave dielectric properties of normal and tumour tissues: variation in dielectric properties with tissue water content," *Phys. Med. Biol.*, vol. 25, no. 6, pp. 1149-1160, 1980.

H. P. Schwan, "Electrical properties of tissue and cell suspensions," *Adv. Biol. Med. Phys.*, vol. 5, pp. 147-209, 1957.

H. P. Schwan and K. R. Foster, "Rf-field interactions with biological systems: electrical

properties and biophysical mechanisms," *Proc. IEEE*, vol. 68, pp. 104-113, 1980.

H. P. Schwan, "Electrical properties of tissues and cell suspensions: mechanisms and models," *Engineering in Medicine and Biology Society. Engineering Advances: New Opportunities for Biomedical Engineers. Proceedings of the 16th Annual International Conference of the IEEE*, vol. 1, pp. A70-A71, November 1994.

L. Sha, E. R. Ward, B. Story, "A review of dielectric properties of normal and malignant breast tissue," *Proc. IEEE Southeast Conf.*, pp. 457-462, 2002.

M. D. Sherar, J. Trachtenberg, S. R. H. Davidson and M. R. Gertner, "Interstitial microwave thermal therapy and its application to the treatment of recurrent prostate cancer," *Int. J. Hyperthermia*, vol. 20, no. 7, pp. 757-68, 2004.

J. M. Sill and E. C. Fear, "Tissue sensing adaptive radar for breast cancer detection—experimental investigation of simple tumor models," *IEEE Trans. Microw. Theory Tech.*, vol. 53, pp. 3312-3319, November 2005.

J. da Silva, J. de Sa and J. Jossinet, "Classification of breast tissue by electrical impedance spectroscopy," *Med. Biol. Eng. Comput.*, vol. 38, pp. 26-30, 2000.

O. Sipahioglu, S. A. Barringer and C. Bircan, "The dielectric properties of meats as a function of temperature and composition," *J. Microw. Power Electr. Energy*, vol. 38, pp. 161-9, 2003.

P. R. Stauffer, F. Rossetto, M. Prakash, D. G. Neuman and T. Lee, "Phantom and animal tissues for modeling the electrical properties of human liver," *Int. J. Hyperthermia*, vol. 19, no. 1, pp. 89-101, 2003.

A. Stogryn, "Equations for calculating the dielectric constant of saline water," *IEEE Trans. Microw. Theory and Tech.*, vol. , pp. 733-376, August 1971.

A. J. Surowiec, S. S. Stuchly, J. R. Barr and A. Swarup, "Dielectric properties of breast carcinoma and the surrounding tissues," *IEEE Trans. Biomed. Eng.*, vol. 35, pp. 257-263, 1988.

(November 2011). The American College of Radiology BI-RADS® ATLAS and MQSA: Frequently Asked Questions. American College of Radiology (ACR). [Online]. http://www.acr.org/~/media/ACR/Documents/PDF/QualitySafety/Resources/BIRADS/BIRADSFAQs.pdf.

The Canadian Task Force on Preventive Health Care, "Recommendations on screening for breast cancer in average-risk women aged 40–74 years," *CMAJ*, vol. 183, no. 17, pp. 1991-2001, November 2011.

ThermoWorks, 1762 W. 20 S., Lindon, UT 84042, USA. [Online] http://www.thermoworks.com/index.html.

V. N. Tran and S. S. Stuchly, "Dielectric properties of beef, beef liver, chicken and salmon at frequencies from 100 to 200 MHz," *J. Microw. Power*, vol. 22, pp. 29-33, 1987.

A. Trehan. *Numerical and Physical Models for Microwave Breast Imaging*, Ch.3. M.A.Sc. Thesis, McMaster University, Ontario, Canada, 2009.

W. E. Vaughan, "Dielectric relaxation," *Ann. Rev. Phys. Chem.*, vol. 30, pp. 103-124, October 1979.

D. W. Winters, J. D. Shea, E. L. Madsen, G. R. Frank, B. D. Van Veen, and S. C. Hagness, "Estimating the breast surface using UWB microwave monostatic backscatter measurements," *IEEE Trans. Biomed. Eng.*, vol. 55, pp. 247-256, 2008.

D. Yang *et al.*, "A floating sleeve antenna yields localized hepatic microwave ablation," *IEEE Trans. Biomed. Eng.*, vol. 53, no. 3, pp. 533-7, 2005.

Z. Q. Zhang, Q. H. Liu, C. Xiao, E. Ward, G. Ybarra, and W. T. Joines, "Microwave breast imaging: 3-D forward scattering simulation," *IEEE Trans. Biomed. Eng.*, vol. 50, no. 10, pp. 1180-1189, 2003.